Implementation of wall functions to bridge the low-Re academic/high-Re industrial gap in large-eddy-simulation predictions

A thesis submitted to The University of Manchester for the degree of
Doctor of Philosophy (PhD)
in the Faculty of Science and Engineering

2022

Brendan Ehimen Omozopia Iyamabo

Department of Mechanical, Aerospace and Civil Engineering

Table of Contents

Final word count: 72737

List of Figures

List of Tables

List of Publications and Awards

The following listed papers form part of this alternate format thesis:

(I) **The Subdomain Wall Function for Large Eddy Simulation**:
B.E.O. Iyamabo, D. Laurence, A. Revell, and I. Afgan. *International Journal of Heat and Fluid Flow*, Submitted 2020

(II) **Large Eddy Simulation of Turbulent Heat Transfer through a Circular 90-deg Pipe Bend**:
B.E.O. Iyamabo, A. Revell, D. Laurence, and I. Afgan. *International Journal of Heat and Mass Transfer*, Submitted 2020

(III) **Implementing Numerical Wall Function for Large Eddy Simulation in OpenFOAM**:
B.E.O. Iyamabo, and I. Afgan. In *the 5th MACE PGR Conference*, 2018

The following conference paper was also published during the course of the PhD project:

(I) **An Improved Wall Function for Large Eddy Simulation**:
B.E.O. Iyamabo, I. Afgan, D. Laurence, and A. Revell. In *12th Engineering Turbulence Modelling and Measurement Conference (ETMM12)*, 2018

Furthermore, the following paper was published during the course of the PhD project:

(I) **Coupled Hybrid RANS-LES Research at The University of Manchester**:
A. Revell, I. Afgan, A. E. A. Ali, M. Camps Santasmasas, T. Craft, A. De Rosis, J. Holgate, D. Laurence, B. E. O. Iyamabo, and A. Mole, B. Owen, M. Savoie, A. Skillen, J. Wang, and X. Zhang. *ERCOFTAC Bulletin.* European Research Community on Flow, Turbulence And Combustion. Progress in RANS-based Scale-Resolving Flow Simulation Methods, 120:67, 2020

Two academic awards were received during the PhD programme, these are listed below:

1. First prize for the best paper at the 5th MACE PGR Conference, 2018.
2. First prize for best poster at the 16th EFCOFTAC Osborne Reynolds Day, 2018.

Abstract

Turbulent flows occur over a wide range of scales; this wide range becomes a challenge to resolve all the scales in turbulence for high Reynolds number industrial flows as required by direct numerical simulation (DNS) because the process is prohibitively computationally expensive.

Large eddy simulation (LES) resolves the large energy-carrying scales in a turbulent flow, while the smallest scales, which can make up to 90% of the computational effort in DNS, are modelled. Consequently, LES is cheaper computationally than DNS, and a wall-resolved LES is used to investigate the development of heat transfer properties through a 90° pipe bend. The heat transfer along the outer wall of the bend is in good agreement with the mass transfer experimental data. However, the traditional correlation between heat and mass transfer breaks down along the inner wall due to the difference in the evolution of the flow and thermal fields.

Despite the efficiency gains of LES against DNS, the computational cost remains very high for a fully wall-resolved LES. This work develops a wall function approach that allows for the deliberate reduction of the near-wall grid resolution for LES. A separate but smaller grid, which solves Reynolds-averaged Navier-Stokes equations (RANS) overlaps the near-wall LES domain to support the LES grid, where it is expected to be weak. Two variants of this approach have been tested.

The more simple of the two variants, termed the numerical wall function for LES, is similar to the wall-modelled LES devised by Balaras et al. (1996) as the RANS grid computes a wall shear stress to correct the first cell at the wall of the under-resolved LES grid. The numerical wall function makes improvements over the wall-modelled LES by coupling consistent information at the interface between the LES grid and the top boundary of the secondary RANS grid. This procedure enables the computation of the full RANS equations, without simplification as done in traditional wall function approaches, and the specification of any advanced turbulence model in the RANS domain. The numerical wall function has been tested for a plane channel flow and a pipe bend flow.

The second variant, which forms the major contribution of this project, has been the development of the subdomain wall function for LES to correct the under-resolved near-wall LES coarse grid beyond the first cell at the wall as is done in traditional wall function approaches. This method has a similar setup to the numerical wall function but uses ideas of the dual-mesh hybrid LES/RANS framework proposed by Xiao and Jenny (2012) to specify a weak source term in the LES momentum equation. The source term acts to readjust the partial mean LES fields in the near-wall near-wall region towards the equivalent fields in the RANS secondary grid. Predictions of the flow through numerous plane channels configurations, and flow through periodic hills and an asymmetric plane diffuser are in excellent agreement with reference data.

Declaration

I hereby declare that no portion of the work referred to in this thesis has been submitted in support of an application for another degree or qualification of this or any other university or other institute of learning.

Brendan Ehimen Omozopia Iyamabo
2022

Copyright

i. The author of this thesis (including any appendices and/or schedules to this thesis) owns certain copyright or related rights in it (the “Copyright”) and s/he has given The University of Manchester certain rights to use such Copyright, including for administrative purposes.

ii. Copies of this thesis, either in full or in extracts and whether in hard or electronic copy, may be made only in accordance with the Copyright, Designs and Patents Act 1988 (as amended) and regulations issued under it or, where appropriate, in accordance with licensing agreements which the University has from time to time. This page must form part of any such copies made.

iii. The ownership of certain Copyright, patents, designs, trade marks and other intellectual property (the “Intellectual Property”) and any reproductions of copyright works in the thesis, for example graphs and tables (“Reproductions”), which may be described in this thesis, may not be owned by the author and may be owned by third parties. Such Intellectual Property and Reproductions cannot and must not be made available for use without the prior written permission of the owner(s) of the relevant Intellectual Property and/or Reproductions.

iv. Further information on the conditions under which disclosure, publication and commercialisation of this thesis, the Copyright and any Intellectual Property University IP Policy (see http://documents.manchester.ac.uk/DocuInfo.aspx?DocID=24420), in any relevant Thesis restriction declarations deposited in the University Library, The University Library’s regulations (see http://www.library.manchester.ac.uk/about/regulations/) and in The University’s policy on Presentation of Theses.

To my beloved wife, cherished sister and my dear parents

Acknowledgements

I would like to thank my supervisor Professor Dominique Laurence for his support and valuable feedback throughout my PhD. His generosity with his time and extensive knowledge helped me to navigate the turbulent moments of my research. I am also grateful to the guidance and support provided by my co-supervisor Professor Alistair Revell. I would like to acknowledge the Department of Mechanical, Aerospace and Civil Engineering of The University of Manchester for funding my PhD.

I would like to thank my fellow PhD colleague Abdelmagid Ali, my comrade in the numerous late nights in the office, for all the invaluable discussions that we had throughout our research, and for those moments that we helped each when we were stuck. Learning and utilising OpenFOAM would have been a much difficult task without you. Thanks to Khalil, Firas, Ioannis Bageris, Diego, Marta, Maxim and the rest of the George Begg crew for their friendship and encouragement outside the daily research slog. I must also appreciate Dr Tim Craft for the tutorials that he gave me during my MSc course, which opened my mind to the world of turbulence modelling.

It goes without saying, but all this would not have been possible without my supportive family, particularly my wife, parents and sister. They have helped, inspired and encouraged me throughout my studies and also in life. I am deeply grateful for the love and patience they have given me.

Nomenclature

Roman Symbols

a_{ij}	Turbulent stress anisotrophy tensor, $a_{ij} = u'_i u'_j / k - \frac{2}{3}\delta_{ij}$
C_D	Dynamic Smagorinsky constant
C_f	Skin friction coefficient
C_{ij}	Cross-stress tensor
C_μ	RANS model constant
C_S	Smagorinsky constant
De	Dean number
D^p_{ij}	Turbulent diffusion of the $u'_i u'_j$ stress tensor by pressure fluctuations
D^t_{ij}	Turbulent diffusion of the $u'_i u'_j$ stress tensor due to velocity fluctuations
D^ν_{ij}	Molecular diffusion of the $u'_i u'_j$ stress tensor
$G()$	LES filter kernal
h	Convective heat transfer coefficient
h	Height of interface of RANS subdomain
k	Turbulent kinetic energy
L	Length
l	Eddy length-scale
L_{ij}	Leonard Stress
Nu	Nusselt number, hL/γ
P	Pressure

P_{ij}	Turbulent production of the $u_i'u_j'$ stress tensor due to mean velocity gradient
P_k	Production of the turbulent kinetic energy due to mean velocity gradient
q	Heat flux vector
Q_{ij}	Drift term in subdomain wall function
Re	Reynolds number
Re_D	Reynolds number based on bulk velocity and pipe diameter
Re_τ	Friction velocity based Reynolds number, $Re_\tau = U_\tau \delta / \nu$
Re_y	Turbulent Reynolds number, $Re_t = k^2/(\varepsilon \nu)$
R_{ij}	Reynolds-stress tensor
Sh	Sherwood number
S_{ij}	Strain rate tensor
T	Temperature
t	Time
t_η	Kolmogorov time scale
T_{ij}	Time Period
T^+	Non-dimensional temperature, $(T - T_w)/T_\tau$
T_τ	Friction temperature, $q_w''/\rho c_p U_\tau$
U	Velocity
u	Velocity
u'	Velocity fluctuation
U_B	Bulk velocity
u_η	Kolmogorov velocity scale
U^+	Non-dimensional velocity, U/u_τ
U_τ	Friction velocity, $U_\tau = \sqrt{\tau_w/\rho}$
v'^2/k	Ratio of normal Reynolds stress to the turbulent kinetic energy

W_{ij}	Rotation rate tensor
y^+	Non-dimensional wall normal distance

Greek Symbols

α	Elliptic blending parameter in the elliptic blending model
α	Thermal diffusivity
Δ	LES grid filer
δ	Channel half height
δ_{ij}	Kronecker delta
δ_ν	Viscous length-scale in a boundary layer
ε	Dissipation rate of the turbulent kinetic energy
ε_{ij}	Reynolds stresses dissipation rate tensor
ε_h	Homogeneous dissipation rate of the turbulent kinetic energy
$\tilde{\varepsilon}$	Quasi-homogeneous dissipation rate of the turbulent kinetic energy
η	Kolmogorov length scale
κ	Von-Karman constant
κ_h	Thermal Von-Karman constant
λ	Thermal conductivity of the fluid
l_m	Mixing length
μ	Dynamic viscosity
μ_t	Turbulent dynamic viscosity
ν	Kinematic viscosity
ν_t	Turbulent kinematic viscosity
ν_{SGS}	Subgrid scale viscosity
Ω_{ij}	Rotation tensor
π	$\simeq 3.14\ldots$

∂	Partial derivative
ϕ	Ratio of normal Reynolds stress to the turbulent kinetic energy, v'^2/k
Φ_{ij}	Pressure-strain correlation in $u'_i u'_j$
ρ	Density
σ_t	Turbulent Prandtl number
τ	Turbulent time scale
τ_{ij}	Viscous stress
τ^r_{ij}	Residual stress tensor
τ_w	Wall shear stress
θ	Fluctuating temperature
$u'_i\theta$	Scalar heat flux vector

Subscripts

b, B	Bulk quantity
in	Value at the inlet
mean	Mean quantity
r	radial or cross-stream direction in pipe bend flow
SGS	Subgrid scale
Θ	Streamwise direction in pipe bend flow
w	Value at the wall
z	Spanwise direction in the pipe bend flow

Acronyms / Abbreviations

CFD	Computational Fluid Dynamics
DES	Detached Eddy Simulation
DNS	Direct Numerical Simulation
ERCOFTAC	European Research Community on Flow, Turbulence and Combustion

ETMM	Engineering Turbulence Modelling and Measurements
EVM	Eddy Viscosity Model
EWA	Exponentially Weighted Average
GGDH	Generalised Gradient Diffusion Hypothesis
IDDES	Improved Delayed Detached Eddy Simulation
LES	Large Eddy Simulation
MPI	Message Passing Interface
NWF	Numerical Wall Function for Large Eddy Simulation
RANS	Reynolds-Averaged Navier-Stokes
RSM	Reynolds Stress Model
SGS	Sub-Grid Scale
SWF	Subdomain Wall Function for Large Eddy Simulation
TLM	Two Layer Model for Large Eddy Simulation
WMLES	Wall-Modelled Large Eddy Simulation

Chapter 1

Introduction

Most flows in engineering that are of practical importance are turbulent. This is due to the ability of turbulent flows to mix and transport fluid more effectively than laminar flows. Turbulent flows contain unsteady vortices with a wide range of length and time scales. The small-scale motions or eddies are influenced by the viscous forces of the flow and obtain most of their energy from large-scale motions. This feature leads to the small-scale dissipative motions having a universal character that is independent of the geometry of the flow. However, the boundaries of the flow domain strongly determine the behaviour of the large integral length-scales, which are chiefly responsible for turbulent transport.

The increased availability of computational resources and improved speed of computational analysis over recent decades has led to an increased usage of computational fluid dynamics (CFD) as an engineering tool to perform parametric analysis for turbulent flow phenomena. CFD simulations enable the analysis of fluid problems of applications in power generation, aerospace, refrigeration and other industries. Solutions provided for the CFD analysis to describe the flow physics are resolved through the direct numerical computation of the Navier Stokes equations. However, highly turbulent flows, especially flows bounded by a solid wall, impose severe computational costs when the Navier Stokes equations are numerically solved directly. The high computational costs are due to the requirement of a fine grid resolution to resolve all the scales of motion in the flow. Hence, the direct numerical simulation (DNS) of the Navier Stokes equations is limited to relatively simple low-Reynolds number academic test cases. However, industrial applications tend to be focused on more complex high-Reynolds number simulations such as flows around a cascade of turbine blades or through complicated pipe networks in a power plant.

The Reynolds-averaged Navier Stokes equations (RANS) are widely used in industry. RANS equations do not resolve any scale of motion in the flow. Consequently, the grid requirements for RANS are much lower than that of DNS, making the RANS method suitable for high-Reynolds number computations. However, the formulation of RANS involves many modelling assumptions developed using simple academic test cases. These assumptions often become inaccurate when tested with complex flow phenomena typically found in industrial applications.

There is a disparity between the high accuracy of approaches used to implement and validate scale-resolving methods for low-Reynolds number flows in academia and the low accuracy of RANS models used to study high-Reynolds number engineering flows in industry. Large Eddy Simulation (LES) was designed to bridge the gap between the Reynolds number disparity where the large-scale motions of a turbulent flow are resolved, but the mostly isotropic small length-scales are modelled with a RANS-type approach. This method made LES for a homogeneous turbulent flow cheaper to run computationally than the DNS while still providing excellent description and accuracy of the flow. Recently, LES has replaced RANS in the global approach to turbulence research in academia. Nevertheless, LES is rarely used in the industrial design process. This rarity is because in the inner layer of a wall-bounded turbulent flow, the large eddies scale with the viscous length scale. The implication is that the separation of sizes between the integral and dissipative length-scales is no longer distinct in the inner layer. Hence, for the LES approach, where only the small – scale motions are modelled, a computational grid approaching the requirements of DNS must be employed for the inner layer of the wall-bounded turbulent flow where viscous forces are dominant. A 'wall-resolved' LES limits the application of the scale-resolving method to moderate Reynolds numbers.

This project aims to develop novel techniques for large eddy simulation to extend the applicability of the scale-resolving method to a much higher Reynolds number range while maintaining a high level of detail and accuracy. Wall functions are used to overcome the expensive grid requirements of LES. The resolution of the near-wall grid is deliberately reduced to achieve significant savings in computational cost. The coarse near-wall grid can no longer resolve the unsteady vortices in the flow and must be supported by corrections. Previous researchers have used standard wall function approaches for RANS, where the wall shear stress is related to the velocity in the log-layer, to derive empirical corrections for the LES grid. These empirical corrections are applicable for relatively simple flows that are not far from local equilibrium but fail for more complex flows.

Furthermore, peak production of turbulence occurs in the area of the flow next to the wall where viscous forces are dominant. This area, also known as the viscous sublayer, influences the large turbulent structures found in the outer region for moderate-Reynolds number flows. The influence of the viscous sublayer reduces as the Reynolds number increases. For very high Reynolds numbers, the thickness of the viscous near-wall region becomes very thin compared to the rest of the flow domain and the bulk contribution of the production of turbulence shifts to the log-layer (Marusic et al., 2010).

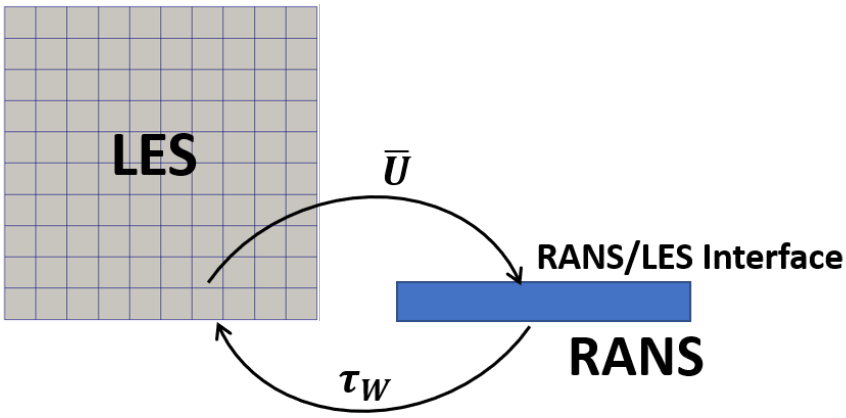

Fig. 1.1 Schematic showing the setup of the wall-modelled large eddy simulation.

Also, the large-scale superstructures in the log-layer become increasingly influential on the near-wall flow dynamics for high Reynolds numbers. These observations justify the approach of modelling the thin near-wall region for LES in high Reynolds number flows.

This PhD utilises the setup of the wall-modelled LES of Balaras et al. (1996) as the springboard for the development of new wall function ideas for LES. The wall-modelled LES embeds a separate RANS grid that covers the first cell at the wall of the LES grid, as seen in Figure 1.1. The RANS grid solves simplified boundary layer equations and computes a wall shear stress that corrects the first cell of the coarse LES grid. On the other hand, the LES grid sends instantaneous filtered velocity to the interface between LES and RANS domains to complete the boundary conditions of the RANS grid. There are several drawbacks of the wall-modelled LES approach. First, the correction of the LES grid is done for only the first cell at the wall, but the under-resolution of the LES grid goes beyond the first cell. Second, the coupling of the instantaneous unsteady information of the LES grid with the time-average information of the RANS grid at the interface is inconsistent and has led to researchers developing empirical corrections in the equations in the RANS grid to reduce this inconsistency. Finally, the simple mixing length model is typically used to represent turbulence in the RANS grid. This algebraic model limits the usage of the modelled LES for complex flow phenomena.

The new wall function method developed by this project will utilise the domain setup of the wall-modelled LES but will improve how the wall function is applied in the LES grid. This project investigates extending the height of the RANS subdomain to overlap the low-resolution near-wall LES grid beyond the first cell. Also, the wall function will not be applied at the wall of the coarse LES domain as a wall shear stress, like it is done for the wall-modelled LES approach. Rather, it will be specified as a source term in the LES momentum equation in the near-wall region. This approach ensures that the correction of the under-resolved near-wall coarse LES grid extends beyond the first cell at the wall. Consistent coupling at the interface between the LES and RANS grids is investigated. This PhD aims to make the new technique for LES suitable for complex turbulent flows, and hence, the utilisation of advanced turbulence models in the secondary RANS grid is studied. This new method developed by the project is termed the subdomain wall function for LES.

The development of the subdomain wall function is carried out in the open-source code OpenFOAM (Weller et al., 1998). To enable a seamless implementation of the code structure of the subdomain wall function in OpenFOAM, a simpler method termed the numerical wall function for LES is created by this project. The numerical wall function method includes the overlapping method by the RANS domain like the subdomain wall function approach, the utilisation of advanced turbulence models in the secondary RANS grid and the consistent coupling of the quantities at the interface between the RANS and LES grids. However, the wall function approach for the numerical wall function is akin to the wall-modelled LES method, where the wall shear stress is specified at the first cell of the coarse LES grid. The implementation of the numerical wall function serves as a stepping stone for the development of the subdomain wall function of LES, which is the main task of this research.

1.1 Study of Turbulent Heat Transfer of Flow through 90° Pipe Bend

The application of turbulent flow through pipe bends is relevant in nuclear reactor and refrigeration systems. The fluid encounters a combination of forces as it moves around the pipe bend. A radial pressure gradient, which balances the centrifugal forces, moves low momentum fluid from the side walls of the pipe towards the inner wall region of the bend. On the other hand, centrifugal forces transport high momentum fluid along the symmetry plane towards the bend outer wall. The secondary flow movement of the fluid leads to the formation of a pair of counter-rotating vortices, also known as the Dean vortices. A number of numerical and experimental studies have been done for the hydrodynamics properties of the pipe bend. However, the study of the heat transfer characteristics in pipe bends has not received the same attention. This author investigated the suitability of RANS models in predicting the flow and thermal properties for a pipe bend flow, which was reported in the author's Master of Science dissertation. The heat transfer coefficient results were validated with mass transfer experimental data due to insufficient heat transfer data available. An early discovery was made where there was a breakdown of the well-established correlation between heat transfer and mass transfer along the inner wall of the bend. The trend of heat transfer and skin friction also diverged along the inner wall. This project intends to use scale-resolving techniques to confirm these findings and gain insight into the mechanisms that affect heat transfer in 90° bends.

1.2 Objectives

The present work aims to extend the usage of large eddy simulation for high-Reynolds number industrial applications. The tools developed by the PhD should maintain the ability of LES to accurately predict complex flow phenomena that are typically encountered in engineering. A deeper understanding of the effect of the curved geometry and evolution of the flow field on heat transfer parameters in a pipe bend is sought. The PhD project's aims can be accomplished by meeting the following objectives:

- To remove the constraints in utilising advanced turbulence models in the RANS secondary grid of implemented wall function methods.
- To develop a new wall function approach for LES, without highly empirical assumptions, that is capable of simulating challenging flow regimes and overcoming the problems encountered with the wall-modelled LES method.
- To gain an improved understanding of the physics of heated flows through a 90° pipe bend.

1.3 Thesis Outline

The thesis encompasses all the work accomplished during the PhD and is presented in the alternative format. This format means that the numerical implementations, validation of methods, results, discussions and major findings are illustrated in the form of academic papers that are appended to this thesis. The author of this thesis wrote three papers with advice from the academic supervisors, Professor Dominique Laurence and Professor Alistair Revell.

The 2^{nd} chapter in the main body of the thesis provides information on the CFD methods used to represent turbulence and describes the characteristics of turbulence near the wall. Chapter 3 presents a review of relevant literature on the evolution of wall function approaches for large eddy simulation. Chapter 4 expands on the methodology on the numerical wall function for LES demonstrated in Paper III, whose code structure becomes the stepping stone for the development of the main wall function of this project - the subdomain wall function. The strengths and limitations of implementing the simpler method in an open-source toolbox are discussed in this chapter. In Chapter 5, the contributions to the field resulting from the PhD project are summarised. Finally, Chapter 6 concludes the thesis and provides suggestions for future work.

The first two papers, included at the end of the thesis, are to be issued in journal publications and are currently under review. The third paper was presented at the 5th MACE PGR Conference.

Paper I: *The subdomain wall function for large eddy simulation.* This paper reports the development and testing of a new wall function framework for large eddy simulation. The paper outlines the mathematical formulation of the approach and the improvements made in coupling the LES and RANS domains. The wall function uses a volumetric source term in the LES momentum equation to correct the under-resolved near-wall fields of the LES domain. The new method has been successfully validated with three test cases. This paper has been submitted to the International Journal of Heat and Fluid Flow.

A paper was presented at the 12^{th} International ERCOFTAC Symposium on Engineering Turbulence Modelling and Measurements (ETMM12), which reports on the early implementation of the subdomain wall function. This conference paper is not included in the present thesis as the work covered by it has been broadened and incorporated into Paper I.

Paper II: *Large eddy simulation of turbulent heat transfer through a circular 90-deg pipe bend.* This paper reported the findings of a 30-million cell wall-resolved LES of a 90° pipe bend. The evolution of the flow and thermal fields and their effect on the heat transfer coefficient are investigated. The heat transfer results of the paper are compared against an experimental mass transfer dataset. An interesting discovery was made where the well-known correlation between heat and mass transfer broke down for a section of the pipe bend. This paper has been submitted to the International Journal of Heat and Mass Transfer.

Paper III: *Implementing numerical wall function for large eddy simulation in OpenFOAM.* The improvements on the classic wall-modelled LES is illustrated in this paper published in the proceedings in the 5th MACE PGR Conference. The numerical wall function for LES successfully implements advanced turbulence models in RANS secondary grid, thereby accomplishing the prediction of a challenging test case.

Chapter 2

Turbulence Modelling

This chapter introduces the physics and theoretical background of turbulent flows. The popular CFD techniques used in academia and industry to model the flow of turbulent flows are described. The turbulence modelling approaches described are Direct Numerical Simulation, Reynolds-Averaged Navier-Stokes and Large Eddy Simulation. Wall function approaches for the Reynolds-Averaged Navier-Stokes method and the flow dynamics in the near-wall region of a turbulent flow are also explored.

2.1 Some Key Characteristics of Turbulence

The Reynolds number is a non-dimensional parameter that helps establish the nature of the flow, whether it is turbulent or laminar. It is defined as the ratio between inertial forces and viscous forces:

$$Re = \frac{UL}{\nu}, \tag{2.1}$$

where U and L are characteristic velocity and length scales, and ν is the kinematic viscosity. The concept was introduced by Reynolds (1883) from his famous experiment of the flow of a dye stream through a straight pipe. Laminar flows are dominated by viscous forces at low Reynolds numbers, while the inertia forces are relatively low. When the Reynolds number is increased to a sufficient level, instabilities as a result of the interaction between the viscous and inertia forces in the fluid instigates turbulence. Turbulence leads to the formation of chaotic, unsteady and rotational motions with significant levels of fluctuating vorticity in the flow. Hence, turbulence is three dimensional in nature. Vortex stretching sustains the turbulent vortical motions which lead to the breaking down of large scale eddies into smaller motions and so on in a continuous process. The perpetual breakdown of eddies leads to a wide range of length and time scales of the motions in a turbulent flow.

Turbulence is dissipative as viscous effects in the fluid change the turbulent kinetic energy to internal thermal energy. This characteristic leads to a decay of turbulent kinetic energy in due course unless there is a continuous energy source to sustain turbulence (Pope, 2000). A cascading process usually transfers the required energy from the mean flow to the large-scale integral eddies; this cascading process continues by transferring energy from the large eddies to smaller ones and so forth. However, the turbulent length scale of the smallest dissipative eddies is larger than any molecular length scale in spite of the significant viscous forces at this level. Consequently, the governing fluid mechanics equations of turbulence can still be represented as a continuum phenomenon (Tennekes and Lumley, 1972).

The Navier-Stokes equations are a set of governing equations that represent the motion of a fluid. The Navier-Stokes equation consists of the continuity equation, which governs the conservation of mass, and the momentum transport equation. For an incompressible flow with constant fluid properties, the continuity equation is defined in Cartesian form as:

$$\frac{\partial U_i}{\partial x_i} = 0, \tag{2.2}$$

where U_i is the i$^{\text{th}}$ component of the flow velocity vector.

The transport equation for momentum is derived from applying Newton's second law with the assumption that the stress in the fluid is the sum of the diffusing viscous term and the pressure term, which is in balance with the non-linear convection of velocity. The momentum transport equation for an incompressible flow is defined as:

$$\frac{\partial U_i}{\partial t} + U_j \frac{\partial U_i}{\partial x_j} = -\frac{1}{\rho}\frac{\partial P}{\partial x_i} + \frac{\partial \tau_{ij}}{\partial x_j}, \tag{2.3}$$

where the term τ_{ij} represents the viscous stress, which is written as:

$$\tau_{ij} = \nu \left(\frac{\partial U_i}{\partial x_j} + \frac{\partial U_j}{\partial x_i} \right). \tag{2.4}$$

2.2 Scales of Turbulence

Beyond a critical Reynolds number, laminar flow transitions into turbulence as a consequence of the complex interactions between the viscous and the inertia effects on the flow. As identified in the previous sections, the resulting flow turbulent flow exhibits fluctuating and chaotic behaviour leading to the generation of unsteady motions known as eddies. These eddies are moderately coherent structures in their localised region; the size of the eddies ranges from the width of the flow to minuscule scales with a local characteristic length l, velocity $u(l)$ and timescale $\tau(l) \equiv l/u(l)$. Turbulence also significantly augments mixing, and increases the rates of momentum, heat and mass transfers due to it diffusive attribute.

Despite the chaotic and irregular behaviour of turbulence, it is possible to correlate turbulent quantities, such as velocity in space and time. Also, such flow quantities like the instantaneous velocity and pressure fluctuate around a local average value. Richardson (1922) theorized that turbulence can be arranged into an order of eddies of different sizes. There is an energy cascade process that transfers generated energy through various scales of the eddies in the flow. The geometry of the flow determines the size of the largest eddies. These large motions are unstable and break down, distributing their turbulent kinetic energy to eddies that are continually decreasing in size. This inertial process continues until the turbulent motions become small enough at a low Reynolds number for viscous effects to become significant and effectively dissipates the turbulent kinetic energy into heat. The dissipation rate is determined by the rate of transfer of the turbulent kinetic energy in the cascade process as the rate of energy transfer from the large eddies is balanced by the rate of dissipation ε. The dissipation rate scales with $u_0^2/\tau_0 = u_0^3/l_0$, where the subscript 0 represents the values of the largest eddies.

Kolmogorov (1941) gave more details of the energy cascade in three hypotheses. The large scale chaotic structures are affected by the boundaries of the flow domain and are anisotropic. The first hypothesis states that the large eddies lose their directional biases as they are broken up through the energy cascade process leading to the small scales reaching a local isotropic state. As the large scale motions lose information of direction during the energy cascade process, information about the geometry and mean flow field are also lost.

This loss of information of the mean flow by the small scales leads to Kolmogorov's second hypothesis and the first of the similarity hypotheses. Since the small scale eddies are independent of flow geometry, the statistics of the small-scale eddies are universal and are depended on the kinematic viscosity ν and the dissipation rate. Hence, universal forms of length, time and velocity for the small scale motions can be defined, and the forms are known as Kolmogorov scales. The Kolmogorov length η, velocity u_η and time τ_η scales are defined respectively as:

$$\eta = \left(\frac{\nu^3}{\varepsilon}\right)^{1/4}, \tag{2.5}$$

$$u_\eta = (\varepsilon\nu)^{1/4}, \tag{2.6}$$

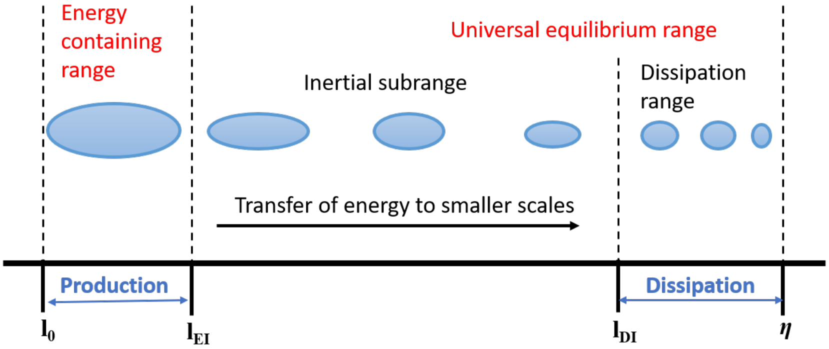

Fig. 2.1 Schematic showing the length scales and ranges of the energy cascade for high Reynolds number flows.

$$\tau_\eta = \left(\frac{\nu}{\varepsilon}\right)^{1/2}. \tag{2.7}$$

The second similarity hypothesis and the final of the three hypotheses state that for sufficiently high Reynolds number turbulent flow, there exists a range of scales l that is much smaller than the size of the energy-carrying motions l_0 but greater than the Kolmogorov scales. The Reynolds number $lu(l)/\nu$ for this range is large enough to ensure that the eddies are not affected by viscosity. These motions with length scale l have a universal form that depends on the dissipation rate but are large enough to be independent of the kinematic viscosity. The hypothesis defines the universal equilibrium range as $l < l_{EI}$, where the length scale $l_{EI} \approx 1/6l_0$ represents the largest isotropic eddy length scale. The universal equilibrium range is split into two subranges by the lengthscale l_{DI}: the dissipative range $l < l_{DI}$ and the inertial subrange $l_{EI} > l > l_{DI}$. The length scale l_{DI} represents the largest dissipative scales. Additional scale ranges are defined with the universal range splitting into the inertial subrange, where inertial forces dominate the motions, but the viscous forces are negligible, and the dissipation range where the motions are chiefly dominated by viscous forces. The ranges motions in the energy cascade process are shown in Figure 2.1.

The velocity and time scales in the inertial subrange can be defined given an eddy size l and viscosity ε as:

$$u(l) = (\varepsilon l)^{1/3} = u_\eta \, (l/\eta)^{1/3} \sim u_0 \, (l/l_0)^{1/3}, \tag{2.8}$$

$$\tau(l) = \left(l^2/\varepsilon\right)^{1/3} = \tau_\eta \, (l/\eta)^{2/3} \sim \tau_0 \, (l/l_0)^{2/3}. \tag{2.9}$$

Equations 2.8 and 2.9 show that the velocity and time scales are in proportion with the size of the eddy in the inertial subrange, and decrease as the length scale of the eddies reduces.

2.3 Direct Numerical Simulation

Direct numerical simulation (DNS) solves the Navier-Stokes equations by resolving all the temporal and spatial scales of motion of the flow. The Navier-Stokes equations are solved numerically without utilising any modelling approaches. The level of information and accuracy provided by DNS is comprehensive; hence, DNS is used to supplement measurements of quantities that are not easily obtained through experiments. Furthermore, DNS data is frequently used to validate new approaches to turbulence modelling. DNS is conceptually the most straightforward approach to simulate a turbulent flow. However, the computational costs of performing a DNS are significantly high. The high cost of DNS arises from the need to resolve all the length and time scales of all the eddies identified in Section 2.2. The grid spacing of the computational domain must be small enough to capture the smallest scales of motion in the dissipative range given by the Kolmogorov length η to perform a valid DNS. Furthermore, the size of the computational domain must be big enough to capture the largest energy-carrying eddy size l. Ferziger and Perić (2002) computed the number of nodes required to resolve each direction of a DNS computational box to scale to the order of $Re_l^{3/4}$. Hence, the total number of cells for a three-dimensional box N^3 needed for a DNS calculation scales with $Re_l^{9/4}$. This correlation shows that the number of grid points needed to resolve a turbulent flow increases exponentially with a moderate increase in Reynolds number. This constraint severely constricts the applicability of DNS to basic geometries with low or moderate Reynolds numbers despite the rapid advances in computing technology.

2.4 Reynolds-Averaged Navier-Stokes Models

The high computational cost of DNS for industrial applications of interest requires a different approach to simulating turbulent flows. The Reynolds – Averaged Navier-Stokes equations (RANS) model all the scales of motion in a turbulent flow. This approach drastically reduces the required computational time and resources compared to scale-resolving methods. A time-averaging of the Navier-Stokes equation is done which leads to the appearance of an additional term in the RANS equation known as the turbulent Reynolds stress. The Reynolds stress tensor needs to be modelled to close the RANS equations. The closure of the turbulent Reynold stress can be done using two approaches. The first approach assumes that the Reynolds stresses are related to the mean rate of strain tensor through a turbulent viscosity. The turbulent viscosity is computed from the product of the length and velocity scales of the mean turbulent motions. The scales can either be algebraically prescribed based on the geometry of the flow (however mostly inaccurate for a variety of turbulent flows) or by solving transport equations of turbulent quantities such as the turbulent kinetic energy to obtain the required scales. This approach forms the basis of the turbulent viscosity hypothesis. On the other hand, the second approach involves directly solving a transport equation for each component of the Reynolds stress tensor. This approach overcomes many of the deficiencies of the turbulent viscosity hypothesis. Although there are additional transport equations needed to be solved, which add to the computational costs compared to the first approach.

Reynolds (1883) proposed the decomposition of an instantaneous field $\Phi_i(x_i,t)$ into $\langle\Phi_i(x_i,t)\rangle$ and fluctuating components $\phi\prime_i(x_i,t)$:

$$\Phi_i(x_i,t) = \phi\prime_i(x_i,t) + \langle\Phi_i(x_i,t)\rangle. \tag{2.10}$$

The angled brackets represent the Reynolds operator for averaging the instantaneous field. The type of Reynolds operator used depends on the characteristic of the turbulent flow. For statistically steady flows, the terms in the Navier-Stokes equations are averaged over time, and the operator is defined as:

$$\langle\Phi_i(x_i,t)\rangle = \lim_{T\to\infty}\int_t^{t+T}\Phi_i(x_i,t)\,\mathrm{dt}, \tag{2.11}$$

where T is a long-time period that is much larger than the time scale of the fluctuating component. The time average of a time-averaged field is equivalent to itself $\langle\Phi_i(x_i,t)\rangle = \langle\langle\Phi_i(x_i,t)\rangle\rangle$. This identity leads to the time average of the fluctuating component of the instantaneous field in Equation 2.10 being zero i.e. $\langle\phi\prime_i(x_i,t)\rangle = 0$.

Substituting the decomposed terms into the variables of the Navier-Stokes equations of Equations 2.3, 2.4 and 2.5 leads to the derivation of the Reynolds-averaged Navier-Stokes equations. The RANS equations for an incompressible flow are defined below:

$$\frac{\partial\langle U_i\rangle}{\partial x_i} = 0, \tag{2.12}$$

$$\frac{\partial\langle U_i\rangle}{\partial t} + \langle U_j\rangle\frac{\partial\langle U_i\rangle}{\partial x_j} = -\frac{1}{\rho}\frac{\partial\langle P\rangle}{\partial x_i} + \frac{\partial}{\partial x_j}\left[\nu\left(\frac{\partial\langle U_i\rangle}{\partial x_j} + \frac{\partial\langle U_j\rangle}{\partial x_i}\right)\right] - \frac{\partial\langle u_i'u_j'\rangle}{\partial x_j}, \tag{2.13}$$

where $\langle u_i'u_j'\rangle$ is the Reynolds stress tensor that is introduced into the momentum transport equation. The Reynolds stress is a symmetric tensor field; hence six additional unknown variables are introduced to the system of equations. The six terms of the Reynolds stress tensor and the four terms from the velocity vector field and pressure scalar field lead to the system of four equations having ten unknowns. The system needs to be closed, which is a problem associated with the RANS method. The turbulent stress is modelled for the system to be solved. Modelling of the Reynolds stresses has been a keen research interest for the past 60 years. The following sections present the various approaches to modelling the turbulent Reynolds stress term in the RANS equations.

2.4.1 Turbulent Viscosity Models

Boussinesq (1868) proposed the turbulent – viscosity hypothesis that the deviatoric part of the turbulent Reynolds stress tensor is linearly proportional to the mean rate of strain tensor. This definition is similar to the relation between molecular stress and the rate of strain in Newtonian fluids. The turbulent – viscosity hypothesis is defined as:

$$-\langle u_i' u_j' \rangle + \frac{2}{3} k \delta_{ij} = \nu_t \left(\frac{\partial \langle U_i \rangle}{\partial x_j} + \frac{\partial \langle U_j \rangle}{\partial x_i} \right) = 2 \nu_t S_{ij}, \tag{2.14}$$

where ν_t is the turbulent eddy viscosity, which is the coefficient of proportionality, k is the turbulent kinetic energy defined as:

$$k = \frac{1}{2} \langle u_i' u_i' \rangle, \tag{2.15}$$

and S_{ij} is the Reynolds averaged rate of strain which is defined as:

$$S_{ij} = \frac{1}{2} \left(\frac{\partial \langle U_i \rangle}{\partial x_j} + \frac{\partial \langle U_j \rangle}{\partial x_i} \right). \tag{2.16}$$

The only remaining unknown term is the turbulent eddy viscosity, and the system of equations is closed by the specification of the turbulent viscosity. The turbulent viscosity can be formed from a combination of a length l, velocity u or time τ scales. From dimensional analysis, the turbulent viscosity can be written as:

$$\nu_t = c_1 u l = c_2 \frac{l^2}{\tau}, \tag{2.17}$$

where c_1 and c_2 are constants.

The turbulent scales can be prescribed to obtain the turbulent viscosity. However, this method suffers from the difficulty of prescribing scales, such as the length, in complex geometries. Another approach to defining the eddy viscosity is computing the transport equations of turbulent quantities. These turbulent quantities are combined to derive the required scales to compute the turbulent viscosity. This approach overcomes the problems associated with prescribing the required turbulent scales.

The accuracy of the turbulent viscosity hypothesis is inadequate for many flows of engineering interest despite the convenience of the approach. There are many eddy viscosity models in literature. This work focuses on the models used in this project, which are described in the next sections.

Mixing – Length Model or Zero – Equation Model

The mixing length model does not require any transport equation for a turbulent property to obtain the turbulent viscosity. Instead, the turbulent viscosity is determined from the algebraic relationship of a prescribed length scale and the product of the given length scale and the mean flow velocity gradient. The turbulent length scale or the mixing length *lm* is specified as a function of position or distance from the wall. The mixing length for a two-dimensional boundary layer flow is determined by:

$$l_m = \kappa y, \tag{2.18}$$

where κ is the von Karman constant usually taken as 0.41, while the velocity scale is defined as:

$$u_m = l_m \left| \frac{\mathrm{d}\langle U \rangle}{\mathrm{d}y} \right|, \tag{2.19}$$

Hence, the turbulent viscosity is specified as:

$$\nu_t = l_m^2 \left| \frac{\mathrm{d}\langle U \rangle}{\mathrm{d}y} \right|. \tag{2.20}$$

The mixing-length varies linearly with wall distance y in the overlap region. However, as the wall is approached, the shear stress is overpredicted using the linear correlation between the mixing length and wall distance of Equation 2.18. van Driest (1956) proposed damping the mixing-length close to the wall with viscosity in the viscous sublayer to reduce the rate at which the shear stress is increased in the near-wall vicinity. The equation is stated as:

$$l_m^+ = \kappa y^+ \left[1 - exp\left(-y^+/A^+\right)\right], \tag{2.21}$$

where the value of the constant A^+ is specified as 26.

While the mixing-length model is the simplest turbulence model, the mixing length $l_m(x)$ always has to be specified. This process is empirical and becomes harder to determine when prescribing the length scales for flows in complex geometries. Another shortcoming of the model is that the existence of turbulence is linked to the presence of mean velocity gradients, as seen in Equation 2.19 for the velocity scale. Hence, the velocity scale tends to zero if the mean velocity gradient is zero. There are situations, such as the centreline of the round jet, where the turbulent viscosity is non-zero despite the zero mean velocity gradient.

One – Equation Models

Prandtl (1945) proposed basing the velocity scale on the turbulent kinetic energy $u_m = ck^{1/2}$. This approach accounts for the non-local and time changes to the turbulent viscosity. Hence, the turbulent viscosity can be specified as:

$$\nu_t = ck^{1/2} l_m, \tag{2.22}$$

where c is a constant approximated as 0.55. Basing the velocity scale on the turbulent kinetic energy resolves the non-physical problem in the mixing-length model in certain turbulent flows where the turbulent viscosity becomes zero, when the mean velocity gradient is also zero. A transport equation is solved for the variable to compute the turbulent kinetic energy. The transport equation of k is defined as:

$$\frac{\partial k}{\partial t} + \langle U_j \rangle \frac{\partial k}{\partial x_j} = -\langle u_i' u_j' \rangle \frac{\partial \langle U_i \rangle}{\partial x_j} + \frac{\partial}{\partial x_j}\left[\left(\nu + \frac{\nu_t}{\sigma_k}\right)\frac{\partial k}{\partial x_j}\right] - \varepsilon, \tag{2.23}$$

where σ_k is the turbulent Prandtl number which is usually specified as 1.0 and the rate of dissipation of the turbulent kinetic energy ε is unknown. The Prandtl one-equation model estimates the rate of dissipation ε, which is a sink term in Equation 2.23 as:

$$\varepsilon = C_D k^{3/2} / l_m, \tag{2.24}$$

where C_D is a model constant. The one-equation model shows improvements in predicting a selection of flow regimes over the mixing length model (Wilcox, 2006). However, as with the zero – equation model, the mixing-length must be specified prior to the simulation. This specification is a considerable weakness when handling turbulent flows in complex geometries.

Equation 2.24 can be substituted into Equation 2.22 to eliminate the mixing length term and yield a new formulation of the turbulent viscosity, which is defined as:

$$\nu_t = C_\mu \frac{k^2}{\varepsilon}, \tag{2.25}$$

where the constant $C_\mu = cC_D$. From a DNS dataset of a plane channel flow, the value of C_μ is estimated as 0.09. The value remains approximately constant for C_μ for most regions of the turbulent channel flow except close to the wall, $y^+ < 50$.

Further, one-equation models based on the transport equation of the turbulent kinetic energy have been developed, most notably the method of Wolfshtein (1969) and the improved approach of Goldberg (1991). Recent developments have focused on solving directly the transport equation of the turbulent viscosity rather than the turbulent kinetic energy. Two examples of this approach are the model of Baldwin and Barth (1991) and the method of Spalart and Allmaras (1992). The Spalart – Allmaras model is the most widely used one-equation model in industry. However, turbulent viscosity based one-equation models suffer the need for empirical damping functions and closure constants to complete the system of equations.

The $k-\varepsilon$ Models

The $k-\varepsilon$ turbulence models are a class of methods that solve at least two transport equations for turbulent quantities. The two main quantities that are solved are the turbulent kinetic energy k and the dissipation rate ε. From these two quantities, the turbulent length scale and the time scale can be defined as:

$$l = \frac{k^{3/2}}{\varepsilon}, \tag{2.26}$$

$$\tau = \frac{k}{\varepsilon}. \tag{2.27}$$

The computation of the turbulence scales overcome the weakness of prescribing the length scales as featured from the mixing length and one-equation models. Hence, the $k-\varepsilon$ turbulence model can be used for flows in complex geometries. Also, the turbulent length scales vary in space and time for most engineering flows, and this variation is captured better by models that automatically compute the turbulent scales.

The development of the standard $k-\varepsilon$ model is accredited to Jones and Launder (1972). The standard model defines the turbulent viscosity as:

$$\nu_t = C_\mu \frac{k^2}{\varepsilon}, \tag{2.28}$$

where $C_\mu = 0.09$ is a constant that is tuned to return the expected behaviour of the ratio $\bar{uv}/k$ in the logarithmic layer of a channel flow. The transport equation for the turbulent kinetic energy remains the same as that of the one-equation model in Equation 2.23. The transport equation for the dissipation rate is defined as:

$$\frac{\partial \varepsilon}{\partial t} + \langle U_j \rangle \frac{\partial \varepsilon}{\partial x_j} = -C_{\varepsilon 1} \frac{\varepsilon}{k} \langle u_i' u_j' \rangle \frac{\partial}{\partial x_j} - C_{\varepsilon 2} \frac{\varepsilon^2}{k} + \frac{\partial}{\partial x_j} \left[\left(\nu + \frac{\nu_t}{\sigma_\varepsilon} \right) \frac{\partial \varepsilon}{\partial x_j} \right]. \tag{2.29}$$

The transport equation for the dissipation rate is completely empirical as the exact equation includes a number of terms with high order unknown correlations that are difficult to accurately model. The constants C_{ε_1} and C_{ε_2} are tuned using the decaying homogeneous isotropic turbulence flow. Launder and Sharma (1974) modelled the constants in Equations 2.23, 2.28 and 2.29 as:

$$C_\mu = 0.09,\ C_{\varepsilon 1} = 1.44,\ C_{\varepsilon 2} = 1.92,\ \sigma_k = 1.0,\ \sigma_\varepsilon = 1.3. \tag{2.30}$$

The standard $k-\varepsilon$ model does not integrate down to the wall. Wall functions are used with the model to account for the physics in the near-wall region. Hence, the correct near-wall behaviour may not be captured with the use of the standard wall function approach for flows where the log-law assumption is no longer valid.

Launder and Sharma (1974) $k-\varepsilon$ Model

Launder and Sharma (1974) updated the standard $k-\varepsilon$ model by including damping functions to account for the diffusion of both the turbulent kinetic energy and its dissipation rate due to molecular viscosity in the near-wall region. Prescribing the correct wall damping behaviour allows the low-Reynolds region to be properly solved by the model without the need for wall functions. The definitions of the turbulent viscosity and the transport equations for the turbulent kinetic energy and its dissipation rate are shown as follows:

$$\nu_t = C_\mu f_\mu \frac{k^2}{\widetilde{\varepsilon}}, \tag{2.31}$$

$$\begin{aligned}\frac{\partial k}{\partial t} + \langle U_j\rangle \frac{\partial k}{\partial x_j} = -\langle u_i' u_j'\rangle \frac{\partial \langle U_i\rangle}{\partial x_j} + \frac{\partial}{\partial x_j}\left[\left(\nu + \frac{\nu_t}{\sigma_k}\right)\frac{\partial k}{\partial x_j}\right] \\ -\underbrace{\left[\widetilde{\varepsilon} + 2\nu\left(\frac{\partial k^{\frac{1}{2}}}{\partial x_j}\right)^2\right]}_{\varepsilon},\end{aligned} \tag{2.32}$$

$$\begin{aligned}\frac{\partial \widetilde{\varepsilon}}{\partial t} + \langle U_j\rangle \frac{\partial \widetilde{\varepsilon}}{\partial x_j} = -C_{\varepsilon_1} f_1 \frac{\widetilde{\varepsilon}}{k}\langle u_i' u_j'\rangle \frac{\partial \langle U_i\rangle}{\partial x_j} - C_{\varepsilon_2} f_2 \frac{\widetilde{\varepsilon}^2}{k} \\ + \frac{\partial}{\partial x_j}\left[\left(\nu + \frac{\nu_t}{\sigma_\varepsilon}\right)\frac{\partial \widetilde{\varepsilon}}{\partial x_j}\right] \\ + 2\nu\nu_t\left(\frac{\partial^2 \langle U_i\rangle}{\partial x_j \partial x_k}\right)^2.\end{aligned} \tag{2.33}$$

The values of the constants C_{ε_1}, C_{ε_2}, C_μ, σ_ε and σ_k are the same for the standard $k-\varepsilon$ model shown in (30). The coefficients f_μ and f_2 depend on the turbulent Reynolds number, $\widetilde{R}_t = k^2/(\nu\widetilde{\varepsilon})$, to yield the correct wall damping behaviour (Jones and Launder 1972), while $f_1 = 1.0$. The coefficients f_μ and f_2 are defined as $f_\mu = \exp\left[-3.4/\left(1+\widetilde{R}_t/50\right)^2\right]$ and $f_2 = 1.0-0.3\exp\left(-\widetilde{R}_t^2\right)$.

The term $\widetilde{\varepsilon}$ is the quasi-homogeneous dissipation rate of the turbulent kinetic energy which is defined as:

$$\widetilde{\varepsilon} = \varepsilon - 2\nu\left(\frac{\partial k^{\frac{1}{2}}}{\partial x_j}\right)^2. \tag{2.34}$$

The term $\widetilde{\varepsilon}$ tends to zero at the wall $(\widetilde{\varepsilon}|_w = 0.0)$ which is the preferable boundary condition to specify at wall compared to ε, which is a non-zero value at the wall.

The Elliptic Blending $k-\varepsilon-\overline{v^2}/k$ Model

Billard and Laurence (2012) developed a three-equation transport equation for turbulent kinetic energy, its dissipation rate and the ratio of the wall-normal fluctuating velocity variance to the turbulent kinetic energy $\overline{v^2}/k$. There is an additional elliptic equation for the blending parameter α to produce the parabolic decay of $\overline{v^2}/k$ in the near-wall region without having to use wall-distance or low-Reynolds number related damping functions like the Launder and Sharma (1974) $k-\varepsilon$ model. The additional variable $\overline{v^2}/k$ acts as an anisotropy sensor and blends the high Reynolds region and the near-wall regions of the flow. Hence, the elliptic blending $k-\varepsilon$ model integrates the transported quantities down to the wall without the use of wall or damping functions. The model is also an improvement of the $k-\varepsilon-\overline{v^2}-f$ method, first proposed by Durbin (1991), as the problem of numerical stiffness is reduced.

The elliptic equation for the blending parameter is defined as:

$$\alpha - L^2\frac{\partial^2\alpha}{\partial x_j^2} = 1, \tag{2.35}$$

where L is the turbulent length scale defined as:

$$L = C_L \max\left[\frac{k^{\frac{3}{2}}}{\varepsilon_h}, C_\eta\left(\frac{\nu^3}{\varepsilon_h}\right)^{1/4}\right]. \tag{2.36}$$

The blending parameter is $\alpha = 0$ near the wall and at the wall boundary, while $\alpha = 1$ far from the wall. The transport equation for the turbulent kinetic energy is defined as:

$$\begin{aligned}\frac{\partial k}{\partial t} + \langle U_j \rangle \frac{\partial k}{\partial x_j} = -\langle u_i' u_j' \rangle \frac{\partial \langle U_i \rangle}{\partial x_j} + \frac{\partial}{\partial x_j}\left[\left(\frac{\nu}{2} + \frac{\nu_t}{\sigma_k}\right)\frac{\partial k}{\partial x_j}\right] - \varepsilon_h \\ + C_{\varepsilon_3}\left(1-\alpha\right)^3 \frac{k}{\varepsilon_h} 2\nu\nu_t \left(\frac{\partial^2 \langle U_i \rangle}{\partial x_j \partial x_k}\right)^2\end{aligned} \tag{2.37}$$

This model adopts the homogeneous dissipation rate as it is less sensitive to Reynolds number effects. The transport equation for the homogeneous dissipation rate is defined as:

$$\frac{\partial \varepsilon_h}{\partial t} + \langle U_j \rangle \frac{\partial \varepsilon_h}{\partial x_j} = \frac{C_{\varepsilon_1} \langle u_i' u_j' \rangle \frac{\partial \langle U_i \rangle}{\partial x_j} - C_{\varepsilon_2}^* \varepsilon_h}{T} + \frac{\partial}{\partial x_j}\left[\left(\frac{\nu}{2} + \frac{\nu_t}{\sigma_{\varepsilon_h}}\right)\frac{\partial \varepsilon_h}{\partial x_j}\right] \tag{2.38}$$

with the variable $C_{\varepsilon_2}^*$ and the turbulent timescale T defined respectively as:

$$C_{\varepsilon_2}^* = C_{\varepsilon_2} + \alpha^3 (C_{\varepsilon_4} - C_{\varepsilon_2}) \tan\left(\left|\frac{\frac{\partial}{\partial x_j}\left(\frac{\nu_t}{\sigma_k}\frac{\partial k}{\partial x_j}\right)}{\varepsilon_h}\right|^{3/2}\right), \tag{2.39}$$

$$T = \max\left[\frac{k}{\varepsilon_h}, C_T \left(\frac{\nu}{\varepsilon_h}\right)^{1/2}\right]. \tag{2.40}$$

The rate of dissipation is defined as:

$$\varepsilon = \varepsilon_h + \frac{1}{2}\nu \frac{\partial^2 k}{\partial x_j \partial x_j}. \tag{2.41}$$

Finally, the transport equation for the anisotropic $\phi = \overline{v^2}/k$ is shown as follows:

$$\begin{aligned}\frac{\partial \phi}{\partial t} + \langle U_j \rangle \frac{\partial \phi}{\partial x_j} = \left(1-\alpha^3\right) f_w + \alpha^3 f_h - \langle u_i' u_j' \rangle \frac{\partial \langle U_i \rangle}{\partial x_j}\frac{\phi}{k} \\ + \frac{\partial}{\partial x_j}\left[\left(\frac{\nu}{2} + \frac{\nu_t}{\sigma_\phi}\right)\frac{\partial \phi}{\partial x_j}\right] \\ + \frac{2}{k}\frac{\nu_t}{\sigma_k}\frac{\partial \phi}{\partial x_j}\frac{\partial k}{\partial x_j},\end{aligned} \tag{2.42}$$

where f_w and f_h are defined respectively as:

$$f_w = -\frac{\varepsilon_h}{2}\frac{\phi}{k}, \tag{2.43}$$

$$f_h = -\frac{1}{T}\left(C_1 - 1 + C_2 \frac{\langle u_i' u_j' \rangle \frac{\partial \langle U_i \rangle}{\partial x_j}}{\varepsilon_h}\right)\left(\phi - \frac{2}{3}\right). \tag{2.44}$$

The values of all the constants for the model are shown in Table 2.1.

Table 2.1 Constants of the elliptic blending $k-\varepsilon$ model

C_{ε_1}	C_{ε_2}	C_{ε_3}	C_{ε_4}	σ_k	σ_{ε_h}	C_μ	C_T	C_L	C_η	C_1	C_2	σ_ϕ
1.44	1.83	2.3	0.4	1.0	1.5	0.22	4	0.164	75	1.7	0.9	1.0

The elliptic blending $k-\varepsilon$ model reproduces the variation of turbulence terms in the near-wall region excellently. This model has been used extensively in this project.

2.4.2 Reynolds Stress Transport Models

The turbulent – viscosity hypothesis is inadequate for many types of turbulent flows such as secondary motions in ducts, flows with sudden changes in the mean strain rate and flows over curved surfaces. This inadequacy stems from the Reynolds stress anisotropy tensor being linearly related to the mean rate-of-strain tensor through the isotropy of the turbulent viscosity. In the absence of mean velocity gradients, the linear eddy viscosity model leads to isotropic turbulence. Moreover, linear eddy viscosity models tend to overpredict the lengthscales in impinging flows. This overprediction leads to much higher levels of turbulence and heat transfer. Also, linear eddy viscosity models tend not to capture the effect of stream curvature.

Reynolds stress transport models (RSM) overcome the difficulties of the turbulent viscosity hypothesis. Transport equations are solved for each component of the Reynolds stress tensor and the dissipation rate. The transport equations for the Reynolds stresses are defined as:

$$\begin{aligned}\frac{\mathrm{D}\langle u_i' u_j' \rangle}{\mathrm{D}t} = &\underbrace{-\left(\langle u_i' u_k' \rangle \frac{\partial \langle U_j \rangle}{\partial x_k} + \langle u_j' u_k' \rangle \frac{\partial \langle U_i \rangle}{\partial x_k}\right)}_{P_{ij}} \underbrace{-2\nu \frac{\partial \langle u_i' \rangle}{\partial x_k}\frac{\partial \langle u_i' \rangle}{\partial x_k}}_{\varepsilon_{ij}} \\ &\underbrace{-\frac{1}{\rho}\langle u_i' \rangle \frac{\partial \langle p' \rangle}{\partial x_j} - \frac{1}{\rho}\langle u_j' \rangle \frac{\partial \langle p' \rangle}{\partial x_i}}_{\Phi_{ij}^*} \underbrace{-\frac{\partial \langle u_i' u_j' u_k' \rangle}{\partial x_k}}_{D_{ij}^t} \\ &\underbrace{+\nu \frac{\partial^2 \langle u_i' u_j' \rangle}{\partial x_k^2}}_{D_{ij}^\nu},\end{aligned} \tag{2.45}$$

where P_{ij} is the production of Reynolds stress tensor, ε_{ij} represents the viscous dissipation of the Reynolds stress tensor, Φ^*_{ij} accounts for the pressure rate of strain, and D^t_{ij} and D^ν_{ij} are stress diffusion due to turbulent and viscous effects, respectively. The production term and the viscous diffusion can be treated exactly as they contain only the Reynolds stress tensor or the mean strain rates. The terms that are modelled are ε_{ij}, Φ^*_{ij} and D^t_{ij} as the derived equations of the terms are very complex. The next subsection discusses how the elliptic blending Reynolds stress model (EBRSM) of Manceau and Hanjalić (2002) represents the dissipation, pressure-strain and turbulent diffusion terms.

The Elliptic Blending Reynolds Stress Model

The EBRSM of Manceau and Hanjalić (2002) is devised to extend the standard RSM to the wall without the need for wall functions. The elliptic blending parameter of Equation 2.35 switches the asymptotic behaviour of the pressure-strain term between the far-wall region to the near-wall region. The elliptic blending parameter also accounts for the nonlocal blocking effect of the wall on the dissipation rate tensor. The elliptic blending parameter α is defined as the same as the parameter of the elliptic blending $k-\varepsilon$ model of Section 2.4.1.

The dissipation rate tensor is modelled to be isotropic for high Reynolds number flows in standard RSM approaches. However, close the wall, the dissipation rate tensor becomes anisotropic. The algebraic correlation for the dissipation rate tensor ε_{ij} is defined as:

$$\varepsilon_{ij} = \left(1-\alpha^3\right)\frac{\langle u'_i u'_j\rangle}{k}\varepsilon + \alpha^3 \frac{2}{3}\varepsilon\delta_{ij}. \tag{2.46}$$

The blending parameter switched the dissipation rate tensor ε_{ij} between the isotropic stress dissipation in the far-wall region $\varepsilon_{ij} = \frac{2}{3}\varepsilon$ and the non-isotropic stress dissipation $\varepsilon_{ij} = \frac{\langle u'_i u'_j\rangle}{k}\varepsilon$. The transport equation for the dissipation rate ε is defined as:

$$\begin{aligned}\frac{\partial \varepsilon}{\partial t} + \langle U_j\rangle \frac{\partial \varepsilon}{\partial x_j} = \frac{C'_{\varepsilon 1}\langle u'_i u'_j\rangle \frac{\partial \langle U_i\rangle}{\partial x_j} - C_{\varepsilon 2}\varepsilon}{T} &+ \nu\frac{\partial}{\partial x_k}\left(\frac{C_\mu}{\sigma_\varepsilon}\langle u'_l u'_m\rangle T \frac{\partial \varepsilon}{\partial x_m}\right) \\ &+ \nu\frac{\partial^2 \varepsilon}{\partial x_k x_k},\end{aligned} \tag{2.47}$$

where

$$C'_{\varepsilon 1} = C_{\varepsilon 1}\left[1 + A_1\left(1-\alpha^3\right)\frac{\langle u'_i u'_j\rangle \frac{\partial \langle U_i\rangle}{\partial x_j}}{\varepsilon}\right]. \tag{2.48}$$

The pressure-strain tensor term or the velocity-pressure gradient correlation Φ^*_{ij} is split between the homogeneous pressure-strain Φ^h_{ij} and the wall pressure-strain Φ^w_{ij} due to near-wall viscous effects and damping of the wall-normal velocity fluctuations. The algebraic correlation of the pressure-strain tensor Φ^*_{ij} is defined as:

$$\Phi^*_{ij} = \left(1-\alpha^3\right)\Phi^w_{ij} + \alpha^3\Phi^h_{ij}. \tag{2.49}$$

The homogeneous pressure-strain is obtained from the SSG model of Speziale et al. (1991) and is defined as:

$$\begin{aligned}\Phi^h_{ij} = &-\left(g_1 + g_1^*\frac{P}{\varepsilon}\right)\varepsilon b_{ij} + g_2\varepsilon\left(b_{ik}b_{kj} - \frac{1}{3}b_{kl}b_{kl}\delta_{ij}\right)\\ &+\left(g_3 - g_3^*\sqrt{b_{kl}b_{kl}}\right)kS_{ij} + g_4k\left(b_{ik}S_{jk} + b_{jk}S_{ik} - \frac{2}{3}b_{lm}S_{lm}\delta_{ij}\right)\\ &+g_5k\left(b_{ik}\Omega_{jk} + b_{jk}\Omega_{ik}\right).\end{aligned} \tag{2.50}$$

where the turbulence anisotropy tensor b_{ij}, the mean strain rate tensor S_{ij} and the mean vorticity tensor Ω_{ij} are defined as:

$$b_{ij} = \frac{\langle u'_iu'_j\rangle}{2k} - \frac{1}{3}\delta_{ij}, \tag{2.51}$$

$$S_{ij} = \frac{1}{2}\left(\frac{\partial\langle U_i\rangle}{\partial x_j} + \frac{\partial\langle U_j\rangle}{\partial x_i}\right), \tag{2.52}$$

$$\Omega_{ij} = \frac{1}{2}\left(\frac{\partial\langle U_i\rangle}{\partial x_j} - \frac{\partial\langle U_j\rangle}{\partial x_i}\right). \tag{2.53}$$

The wall pressure-strain term Φ^w_{ij} is defined as:

$$\Phi^w_{ij} = \frac{-5\varepsilon}{k}\left(\left\langle u'_iu'_k\right\rangle n_jn_k + \left\langle u'_ju'_k\right\rangle n_in_k - \frac{1}{2}\left\langle u'_ku'_l\right\rangle n_kn_l\left(n_in_j - \delta_{ij}\right)\right), \tag{2.54}$$

where the unit vector field for the wall-normal direction n_i is evaluated as:

$$n_i = \frac{\nabla\alpha}{|\nabla\alpha|}. \tag{2.55}$$

Finally, the turbulent diffusion D^t_{ij} term in the transport equations of $u'_iu'_j$ is modelled using the generalised gradient diffusion hypothesis (GGDH) proposed by Daly and Harlow (1970) as:

$$D^t_{ij} = \frac{\partial}{\partial x_l}\left(\frac{C_\mu}{\sigma_k}\langle u'_lu'_m\rangle T\frac{\partial\langle u'_iu'_j\rangle}{\partial x_m}\right) \tag{2.56}$$

The turbulent time T and length L scales are computed as the respective scales for the elliptic blending $k-\varepsilon$ model in Equations 2.36 and 2.40. The model constants are shown in Table 2.2.

Table 2.2 Constants of the elliptic blending RSM model

C_{ε_1}	C_{ε_2}	C_T	C_L	C_η	C_μ	A_1	σ_k
1.44	1.83	6	0.1333	80	0.22	0.065	1.0

σ_ε	g_1	g_1^*	g_2	g_3	g_3^*	g_4	g_5
1.15	3.4	1.8	0.0	0.8	1.3	1.25	0.4

2.5 Large Eddy Simulation

LES directly solves the large-scale motions that carry the most energy in a turbulent flow. These large scale motions are affected by the geometry of the flow. However, the dissipative and isotropic small-scale motions are modelled, unlike in DNS. The smallest dissipative scales are universal and independent of the boundary conditions of the flow geometry. This universality makes modelling of the small scales favourable as the potential modelling errors will be relatively low. Furthermore, most of the effort in DNS is spent resolving the dissipation range, making up for 99% of the total computational costs (Pope, 2000). Consequently, the cost of LES is significantly less than DNS as a relatively coarser grid can be employed to resolve the flow. The computational effort of LES is still more than that of RANS methods, but LES offers levels of information and accuracy that is unmatched by RANS.

2.5.1 Numerical Method of Large Eddy Simulation

The DNS operation resolves the velocity field $U_i(x,t)$ on all the lengthscales down to the Kolmogorov scale. On the other hand, the instantaneous velocity field of the LES goes through a low-pass filtering process. Hence, the resulting filtered velocity $\overline{U}_i(x,t)$ can be explicitly solved on a grid that is coarser than a typical DNS grid. The filter width Δ is generally linked with grid resolution and should be smaller than the length scale of the smallest energy-carrying eddy l_{EI} in the inertial subrange. The lengthscales that are a larger size than Δ are resolved while a subgrid-scale (SGS) model models the eddies smaller than the filter width. Leonard (1975) defined the filtering process as:

$$\overline{U}_i\,(x_i,t) = \int G\,(r_i,x_i)\,U_i\,(x_i - r_i,t)\,dr_i, \tag{2.57}$$

where G is the special filter function that satisfies the following normalisation condition:

$$\int G\,(r_i,x_i)\,dr_i = 1. \tag{2.58}$$

The subgrid field or the residual field $u'_i(x_i,t)$ that represents the modelled component is defined below as the difference between the non-filtered instantaneous velocity field and the filtered velocity field as:

$$u'_i(x_i,t) \equiv U_i\,(x_i,t) - \overline{U}_i\,(x_i,t)\,. \tag{2.59}$$

The popular filter functions used for LES are the box filter, Gaussian filter and sharp spectral filter.

Consequently, the filtered continuity equation is defined as:

$$\overline{\left(\frac{\partial U_i}{\partial x_i}\right)} = \frac{\partial \overline{U}_i}{\partial x_i} = 0. \tag{2.60}$$

After applying the filtering process to the Navier – Stokes equations, the filter conservation of momentum equation is defined as:

$$\frac{\partial \overline{U}_i}{\partial t} + \frac{\partial \overline{U_i U_j}}{\partial x_j} = -\frac{1}{\rho}\frac{\partial \overline{p}}{\partial x_i} + \nu \frac{\partial}{\partial x_j}\left(\frac{\partial \overline{U}_i}{\partial x_j} + \frac{\partial \overline{U}_j}{\partial x_i}\right), \tag{2.61}$$

where $\overline{p}(x_i,t)$ is the filtered pressure field. The difference between the filtered product $\overline{U_i U_j}$ and the product of the filtered velocities $\overline{U}_i\overline{U}_j$ is the residual-stress tensor τ_{ij}^R which is defined as:

$$\tau_{ij}^R = \overline{U_i U_j} - \overline{U}_i\overline{U}_j. \tag{2.62}$$

As a result, the subgrid kinetic energy is computed as:

$$k_r \equiv \frac{1}{2}\tau_{ii}^{R}. \tag{2.63}$$

The anisotropic residual – stress tensor τ_{ij}^r is expressed as:

$$\tau_{ij}^r \equiv \tau_{ij}^R - \frac{2}{3}k_r\delta_{ij}. \tag{2.64}$$

The modified filtered pressure $\hat{p}$ is defined by including the isotropic subgrid residual stress as:

$$\hat{p} \equiv \overline{p} + \frac{2}{3}k_r. \tag{2.65}$$

By substituting Equations 2.55, 2.56 and 2.58 into Equation 2.54, the modified momentum equation can be redefined as:

$$\frac{\partial \overline{U}_i}{\partial t} + \frac{\partial \overline{U}_i \overline{U}_j}{\partial x_j} = -\frac{1}{\rho}\frac{\partial \hat{p}}{\partial x_i} + \nu \frac{\partial}{\partial x_j}\left(\frac{\partial \overline{U}_i}{\partial x_j} + \frac{\partial \overline{U}_j}{\partial x_i}\right) - \frac{\partial \tau^r_{ij}}{\partial x_j}. \tag{2.66}$$

The three fields $\overline{U_i}(x_i,t)$, $\overline{p}(x_i,t)$ and $\tau^r_{ij}(x_i,t)$ in Equations 2.59 are three – dimensional, random and unsteady even if the simulated flow is statistically stationary. The residual or subgrid (SGS) stress is modelled to close the system of the filtered transport momentum equations, similar to the approach of the Reynolds-averaged Navier-Stokes equations. The modelled stress tensor also depends on the type and width of the filter used. Leonard (1975) introduced the decomposition of the residual-stress tensor into three components: the Leonard stresses L_{ij}, cross stresses C_{ij} and the SGS Reynolds stresses R_{ij}. A Galilean-invariant of the Leonard decomposition proposed by Germano (1986) is defined as:

$$\tau^R_{ij} = L_{ij} + C_{ij} + R_{ij}. \tag{2.67}$$

The Leonard stresses represent the resolved large scale stresses expressed as:

$$L_{ij} = \overline{\overline{U}_i \overline{U}_j} - \overline{\overline{U}}_i \overline{\overline{U}}_j. \tag{2.68}$$

The interaction between the resolved and modelled scales is represented by the cross stresses, which is defined as:

$$C_{ij} = \overline{\overline{U}_i u'_j} + \overline{u'_i \overline{U}_j} - \overline{\overline{U}}_i \overline{u'}_j - \overline{u'}_i \overline{\overline{U}}_j. \tag{2.69}$$

The SGS Reynolds stresses represent the local interactions between the modelled scales and is specified as:

$$R_{ij} = \overline{u'_i u'_j} - \overline{u'}_i \overline{u'}_j. \tag{2.70}$$

The next section describes the numerical SGS methods that model the unresolved stresses.

2.5.2 Subgrid-Scale Modelling

The Boussinesq approximation is used to model the subgrid-scale stress tensor first introduced by Smagorinsky (1963). The approximation is based on the hypothesis that the transfer of energy from the resolved to the subgrid scales is comparable to molecular diffusion. The subgrid-scale eddy viscosity ν_{SGS} relates the mechanism of the residual stresses to the filtered rate of strain $\overline{S}_{ij}$ as:

$$\tau_{ij}^{r} = -2\nu_{\mathrm{SGS}}\overline{S}_{ij}, \tag{2.71}$$

where $\overline{S}_{ij}$ is the filtered rate of strain defined as:

$$\overline{S}_{ij} = \frac{1}{2}\left(\frac{\partial \overline{U}_i}{\partial x_j} + \frac{\partial \overline{U}_j}{\partial x_i}\right). \tag{2.72}$$

Smagorinsky (1963) computes the subgrid-scale eddy viscosity by using the analogy of the mixing length hypothesis. The following sections introduce the Smagorinsky model and two additional models used throughout this project.

Smagorinsky Model

The eddy viscosity model of Smagorinsky (1963) uses global quantities related to the large scales to compute the subgrid-scale viscosity. The eddy viscosity is modelled using the RANS mixing-length model analogy. The characteristic length scale l_S is computed as the product of the filter width Δ and a model coefficient C_S (Smagorinsky constant) as $l_S = \Delta C_S$. The SGS viscosity is computed as:

$$\nu_{\mathrm{SGS}} = l_S^2\sqrt{2\overline{S}_{ij}\overline{S}_{ij}} = (C_S\Delta)^2\sqrt{2\overline{S}_{ij}\overline{S}_{ij}}. \tag{2.73}$$

Near the wall, the Smagorinsky mixing length needs to be modified to take into account the effect of viscous damping and ensure that the residual viscosity and shear stress is zero at the wall. Moin and Kim (1982) proposed the specification of the modified Smagorinsky mixing length using a van Driest damping function for wall-bounded flows as:

$$l_S = C_S\Delta\left[1 - \exp\left(-y^+/A^+\right)\right], \tag{2.74}$$

where A^+ is a model constant and y^+ is the wall-normal distance normalised in viscous units.

The Smagorinsky model has several limitations. The rate of transfer of energy to the residual motions is defined as:

$$P_r \equiv -\tau^r_{ij}\overline{S}_{ij} = 2\nu_r\overline{S}_{ij}\overline{S}_{ij} = \varepsilon_r. \tag{2.75}$$

The transfer of energy between the scales can be decomposed into two directions: forward scatter which account for the local transfer of energy from the resolved motions to the residual field, while backscatter refers to the opposite direction of forward scatter of the transfer to the residual scales. Negative subgrid production P_r or subgrid dissipation accounts for the physical process of backscatter. However, the Smagorinsky model always prescribes the value of the eddy viscosity as greater than zero. Hence, the model does not account for the backscatter energy transfer process from the dissipative scales to the large – scale motions.

Another limitation of the Smagorinsky model is the difficulty in specifying the correct value of the Smagorinsky coefficient C_S. The Smagorinsky coefficient is also very sensitive to the size of the filter width used. Clark et al. (1979) recommends the value of $C_S = 0.2$ for isotropic homogeneous turbulence while Lilly (1992) suggests the value of $C_S = 0.17$. For plane channel flows, Deardorff (1970) specifies an even lower value of $C_S = 0.1$. The value of the Smagorinsky coefficient is not constant but is dependent on the flow.

Furthermore, for laminar flow, the Reynolds stress is zero in the Navier – Stokes equations. The residual stresses are also zero in the modified momentum transport equation for LES. Therefore, the correct value of the residual shear stress is returned if the Smagorinsky coefficient C_S is specified as zero for laminar flows. This characteristic is not realised with the Smagorinsky model as the value of C_S is finite, leading to the incorrect resolution of the filtered fields.

Dynamic Smagorinsky Model

Germano et al. (1991) proposed a model that appropriately prescribes the value of the Smagorinsky coefficient for different flow configurations, solving one of the limitations of the Smagorinsky model. The dynamic model automatically adjusts the coefficient in both space and time. Two filtering operations are established for the dynamic method: the first corresponding to the grid filter width Δ which is proportional to the grid spacing, the second corresponding to the test filter width $\overline{\Delta}$ which is usually taken as twice of Δ that is $\overline{\Delta} = 2\Delta$.

Lilly (1992) determines the dynamic coefficient C_D by using the least-squares method to minimise mean-square errors as:

$$C_D = \frac{M_{ij}L^d_{ij}}{M_{kl}M_{kl}}. \tag{2.76}$$

The subgrid-scale viscosity is computed as:

$$\nu_{\mathrm{SGS}} = (C_D\Delta)^2\sqrt{2\overline{S}_{ij}\overline{S}_{ij}}. \tag{2.77}$$

The variable L_{ij} represents the resolved stress and is derived from the Germano identity (Germano, 1992). The deviatoric part L^d_{ij} of the resolved stress is used in the dynamic Smagorinsky coefficient formula. The resolved stress is defined as:

$$L_{ij} = c_S M_{ij}, \tag{2.78}$$

in which the tensor M_{ij} is defined as:

$$M_{ij} = 2\Delta^2\widetilde{\overline{SS}_{ij}} - 2\overline{\Delta}^2\widetilde{\overline{S}}\widetilde{\overline{S}}_{ij}, \tag{2.79}$$

with $\overline{S} = \left(2\overline{S}_{ij}\overline{S}_{ij}\right)^{1/2}$. The overline $\overline{}$ refers to the grid filtered quantities, while the tilde operator $\widetilde{}$ represents the test filtered quantities.

The computation of the dynamic Smagorinsky coefficient C_D in a channel flow using Equation 2.76 demonstrates considerable fluctuations of the coefficient because of the weak correlation between the stresses and the rate of strain. These large fluctuations lead the LES computations to be unstable. Germano et al. (1991) and Piomelli (1993) solved the problem by averaging the denominator and numerator of Equation 2.76. Consequently, this implementation eliminates the need for special treatments near the wall and give good results for turbulent channel flows and channel flows in transition (Pope, 2000). The dynamic model is also capable of giving accurate computations for laminar flows and permits the possibility of backscatter. The success of the dynamic model reduces if the LES is not well resolved to capture a significant proportion of the turbulent kinetic energy. Also, the dynamic procedure in computing the model coefficient slightly increases the computational costs compared to the standard Smagorinsky model.

One-Equation Model

The one-equation SGS model of Yoshizawa and Horiuti (1985) computes the transport equation for the subgrid-scale turbulent kinetic energy $k_{\mathrm{SGS}} = 1/2\tau_{ii}$. The one-equation model was developed to go beyond the assumption of the local balance of the subgrid-scale production to the dissipation used in the Smagorinsky model. This assumption is not always correct. The subgrid viscosity is computed as:

$$\nu_{\mathrm{SGS}} = C_k \Delta \sqrt{k_{\mathrm{SGS}}}, \tag{2.80}$$

where $C_k = 0.094$ is the model constant. The transport equation for k_{SGS} is defined as:

$$\frac{\partial k_{\mathrm{SGS}}}{\partial t} + \frac{\partial \overline{U}_j k_{\mathrm{SGS}}}{\partial x_j} - \frac{\partial}{\partial x_j}\left[(\nu + \nu_{\mathrm{SGS}})\frac{\partial k_{\mathrm{SGS}}}{\partial x_j}\right] = -\tau_{ij}\overline{S}_{ij} - C_\varepsilon \frac{k_{\mathrm{SGS}}^{3/2}}{\Delta}, \tag{2.81}$$

where $C_\varepsilon = 1.048$ is a constant.

2.5.3 Computational Costs of LES

The computational effort needed to resolve the inner and outer layers of a boundary layer flow is considered in this subsection. The integral length-scales of the wall-bounded flow must be resolved for a good LES. In the outer layer, the large – scale motions scale to the boundary layer thickness δ (and $\delta \sim \mathrm{Re}^{-0.2}$). Assuming the number of cubes or points needed to solve a computational domain is $N_x \times N_y \times N_z$, the number of points needed increases as the Reynolds number rises. In the outer layer, the total number of grid points required to resolve this region is defined as:

$$\left(N_x N_y N_z\right)_{ol} \propto \mathrm{Re}^{0.4}. \tag{2.82}$$

Hence, the number of grid pointed needed in the boundary-layer outer region is weakly dependent on the Reynolds number (Piomelli and Balaras, 2002).

Close to the wall, the size of the energy-carrying eddies is proportional to the viscous length-scale δ_ν in the viscous sublayer. As the viscous length-scale δ_ν is a function of friction velocity, the dependence of the number of grid points in the viscous sublayer vicinity must be relative to wall units. The integral eddies drastically reduce in size in the inner layer compared to the outer layer when the Reynolds number increases. Hence, the separation of length scales between the integral eddies and the dissipative eddies reduces in this region. Chapman (1979) estimated that the number of grid points needed to resolve the inner layer of a boundary layer flow as:

$$\left(N_x N_y N_z\right)_{il} \propto C_f Re^2 \propto \mathrm{Re}^{1.8}, \tag{2.83}$$

where the coefficient of friction $C_f = 2\tau_w/\rho U^2$. The implication of the two estimates indicates that the number of grid points required to resolve the inner layer of a boundary layer flow increases much faster than that of the outer region with increasing Reynolds number. Also, the grid requirements for an LES in the near-wall region is close to that of a DNS. Figure 2.2 shows the CPU time need to compute the LES of a turbulent boundary layer flow by Piomelli (2008) done with different CFD packages. At moderate Reynolds numbers, about 50% of the computational resources are needed to resolve the inner layer, which only makes up 10% of the boundary layer. As the Reynolds number grows, the computational effort required to resolve the inner layer becomes prohibitively high and represents over 90% of the computation time. As expected, the computational time necessary for the outer layer is almost independent of the Reynolds number. The estimates of computational effort for boundary layer flows differ from channel flows or other wall-bounded flows. However, the concept remains the same; the inner layer of wall-bounded flows makes up most of the computational costs of a high Reynolds turbulent flow despite constituting a minuscule part of the boundary layer.

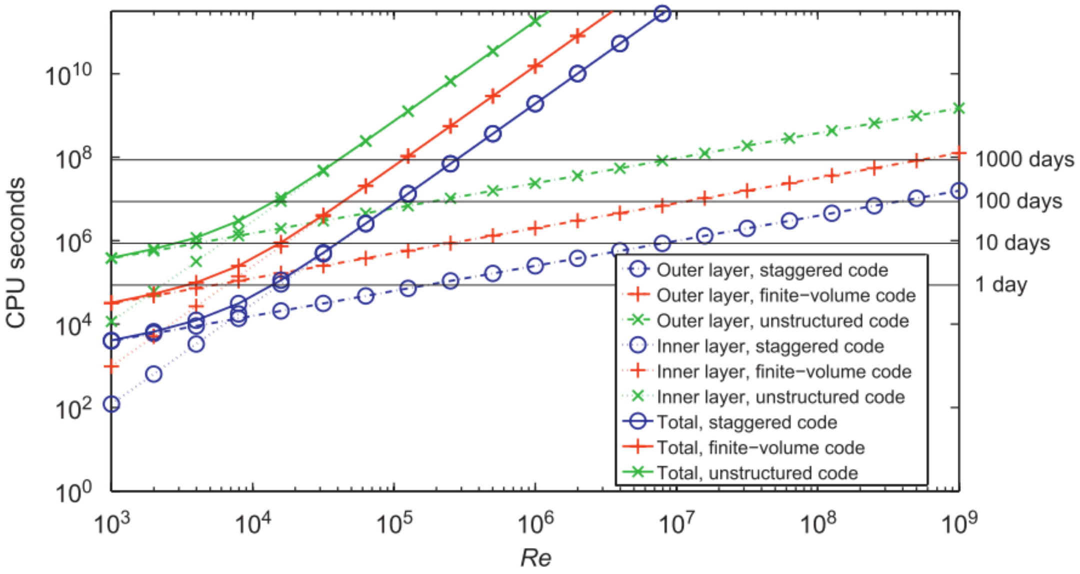

Fig. 2.2 The computed cost in CPU seconds of LES of a flat – plate boundary layer flow (Piomelli, 2008)

2.6 Near – Wall Turbulence

Most turbulent flows of engineering importance are bounded by solid surfaces such as internal flows through pipes or external flows over wind turbines. The presence of solid surfaces alters the behaviour of turbulent quantities near the wall. Consequently, turbulence models that are calibrated for homogeneous flows are adapted near walls.

As the wall is approached, the turbulent Reynolds number $Re_t = \frac{k^2}{\varepsilon\nu}$ tends to zero and molecular viscous effects become dominant. At the wall, viscous friction is imparted on the fluid, which leads to a no-slip condition where the velocity component parallel to the wall is zero at the wall. This viscous friction impacts on mean velocity and turbulent intensity within the vicinity of the wall resulting in high wall-normal gradients of the quantities in this region. Consequently, the strong wall-normal gradient of the parallel component of velocity leads to the high production of turbulent kinetic energy in the near-wall region.

The velocity component normal to the wall is zero at the solid boundary. This feature is known as the impermeability condition; the impermeability condition has a wall – blocking effect that damps the fluctuations of the velocity component normal to the wall. This damping results in the increased anisotropy of turbulence as the wall-normal fluctuations are reduced by two orders of magnitude above that of the wall-parallel fluctuations, leading to the alteration of the shape and size of turbulence structures close to the wall.

Furthermore, the size of the large – scale motions of flow reduces as the viscous effects become dominant close to the wall. The reduction of the size of the large eddies is so drastic that the clear separation of scales between the large and dissipative eddies as introduced in Section 2.2 is no longer easily distinguishable in the near-wall region. This feature leads to the dissipation-rate tensor becoming anisotropic.

The depiction of low-Reynolds effects, wall turbulence damping and anisotropy enhancement makes the prediction and modelling of the near-wall region of a turbulent flow a considerable challenge. The next two sections describe the flow features a simple wall-bounded turbulent flow.

2.6.1 Channel Flow

A plane channel flow is a fluid flow through two long parallel plates of height $h = 2\delta$. The flow has a very large aspect ratio which enables the flow to be statistically independent in the spanwise direction (for clarity, this section refers the streamwise, cross-stream and spanwise directions as representing x, y and z respectively in the nomenclature). The flow is driven by a constant pressure gradient which balances the wall friction. Hence, the mean flow is in the streamwise direction U and is independent of the streamwise direction; the mean spanwise and cross-stream components of velocity are zero. The cross-stream and streamwise Reynolds – Averaged Navier-Stokes momentum equations reduce to:

$$0 = -\frac{1}{\rho}\frac{\partial\langle P\rangle}{\partial y} - \frac{\partial\left\langle v'^2\right\rangle}{\partial y}, \tag{2.84}$$

$$0 = -\frac{1}{\rho}\frac{\partial\langle P\rangle}{\partial x} - \frac{\partial\langle u'v'\rangle}{\partial y} + \nu\frac{\partial^2\langle U\rangle}{\partial y^2}. \tag{2.85}$$

Differentiating the cross-stream momentum equation with respect to the x-axis leads to:

$$\frac{\partial^2 \langle P\rangle}{\partial x \partial y} = \frac{\partial^2 \langle P\rangle}{\partial y \partial x} = \frac{\partial^2 \rho \left\langle v'^2 \right\rangle}{\partial x \partial y}. \tag{2.86}$$

Since $\left\langle v'^2 \right\rangle$ is independent of the streamwise direction, it can be deduced that the streamwise pressure gradient $\partial \langle P\rangle / \partial x$ is independent of the y and is uniform across the flow. This deduction also means that the streamwise pressure gradient is equivalent to the wall pressure gradient $\partial \langle P\rangle / \partial x = \partial \langle P\rangle_w / \partial x$.

The total shear stress τ is defined as:

$$\tau = \mu \frac{\partial \langle U\rangle}{\partial y} - \rho \left\langle u'v' \right\rangle, \tag{2.87}$$

where the two terms on the right-hand side of the equation represent the viscous stress and the Reynolds shear stress, respectively. At the wall, the total stress becomes $\tau_w = \mu \frac{\partial \langle U\rangle}{\partial y}_w = \rho \nu \frac{\partial \langle U\rangle}{\partial y}_w$. At the symmetry plane $y = \delta$, the total shear stress becomes $\tau(\delta) = 0$. Applying these boundary conditions into Equation 2.85 leads to the following two expressions:

$$\frac{\tau_w}{\delta} = -\frac{dp_w}{dx}, \tag{2.88}$$

$$\tau(y) = \tau_w \left(1 - \frac{y}{\delta}\right). \tag{2.89}$$

This formulation illustrates the balance of the streamwise pressure gradient and the wall shear stress. Besides, the shear stress goes to zero at the channel half-height δ. Since the Reynolds shear stress is zero at the wall; the wall shear stress can be defined as:

$$\tau_w = \rho \nu \left(\frac{d\langle U\rangle}{dy}\right)_{y=0}. \tag{2.90}$$

The viscous stress dominates at the wall but becomes negligible in comparison to the Reynolds stresses for most of the channel. The near-wall region where the viscous stress is dominant becomes smaller as the Reynolds number is increased. Hence, the relevant parameters near the wall are the wall shear stress τ_w and the viscosity ν. These parameters lead to the definition of important wall units in the near-wall vicinity. The viscous velocity scale or friction velocity is defined as:

$$u_\tau = \sqrt{\frac{\tau_w}{\rho}} = \sqrt{\nu \left(\frac{d\langle U\rangle}{dy}\right)_{y=0}}. \tag{2.91}$$

The viscous length-scale δ_ν is defined as:

$$\delta_\nu = \nu\sqrt{\frac{\rho}{\tau_w}} = \frac{\nu}{u_\tau}. \tag{2.92}$$

The two length scales, which a wall-bounded turbulent flow motion depends on, are the viscous length scale and the channel half-height δ . The friction Reynolds number Re_τ is defined as:

$$Re_\tau = \frac{u_\tau \delta}{\nu} = \frac{\delta}{\delta_\nu}. \tag{2.93}$$

The distance from the wall can be normalised with the viscous length scale, and it is defined as:

$$y^+ = \frac{y}{\delta_\nu} = \frac{u_\tau y}{\nu}. \tag{2.94}$$

It can be seen that the friction Reynolds number is the y^+ at the channel half-height δ. It is also an important parameter to distinguish the different regions in the channel flow where the viscous stress or the Reynolds stresses dominate the flow.

The Different Regions of Channel Flow

Equation 2.89 can be rewritten as:

$$\nu\frac{d\langle U\rangle}{dy} - \left\langle u'v'\right\rangle = u_\tau^2\left(1 - \frac{y}{\delta}\right). \tag{2.95}$$

Equation 2.95 can be non-dimensionalised into two new equations. Using the velocity scale u_τ and the inner region lengthscale δ_ν, Equation 2.95 is rewritten as:

$$\frac{d\langle U\rangle^+}{dy^+} - \left\langle u'v'\right\rangle^+ = \left(1 - \frac{y^+}{Re_\tau}\right), \tag{2.96}$$

where the normalised velocity is $\langle U\rangle^+ = \langle U\rangle/u_\tau$ and the normalised shear stress is $\langle u'v'\rangle^+ = \langle u'v'\rangle/u_\tau^2$. Non-dimensionalising Equation 2.95 with the velocity scale u_τ and the outer region lengthscale δ leads to:

$$\frac{1}{Re_\tau}\frac{d\langle U\rangle^+}{d\eta} - \left\langle u'v'\right\rangle^+ = (1 - \eta), \tag{2.97}$$

where $\eta = y/\delta$. Integrating Equation 2.96 and using the near-wall asymptotic state for the shear stress $\langle u'v' \rangle^+ = O(y^{+3})$ leads to:

$$\langle U \rangle^+ = y^+ - \frac{1}{2}\frac{y^{+2}}{Re_\tau} + O(y^{+4}), \tag{2.98}$$

According to Pope (2000), the viscous sublayer is defined as the region next to the wall $(y^+ < 8)$ where $U^+ \approx y^+$. The Reynolds stresses are negligible compared to the viscous stress in this region. The linear correlation between the normalised velocity and wall distance breaks down beyond the viscous sublayer $(y^+ > 8)$.

Further away from the wall $(y \gg \delta_v)$, the effect of molecular viscosity reduces. Hence, the flow scales do not depend on the viscous length-scale. Also, this region is far from the channel centreline $(y \ll \delta)$, and hence, the flow scales in this region do not depend on the boundary layer scale δ. Equation 2.96 can be written as:

$$\langle U \rangle^+ = \frac{1}{\kappa}\ln y^+ + B, \tag{2.99}$$

where B is a constant usually given the value of 5.2 and κ is the von Karman constant given the value of 0.41. Equation 2.99 is famously known as the logarithmic law of the wall equation which was proposed by von Kármán (1930). The region where the logarithmic law of the wall applies is called the log – law region. The log – law describes the logarithm profile in the near-wall region between $y^+ > 30$ and $y/\delta > 0.3$. Additionally, there is a region between the viscous sublayer and the log – law region $(8 < y^+ < 30)$ where the logarithmic law of the wall or the linear correlation $U^+ \approx y^+$ do not apply. This region is known as the buffer region (Pope, 2000).

Finally, in the region in the outer part of the flow $y/\delta > 0.3$, where the logarithmic law of the wall does not hold, the size of the turbulent motions scales with the channel half-height δ, and the mixing length becomes constant. This region is known as the defect layer (Pope, 2000). A correlation can be derived from Equation 2.97 for the difference between the velocity and the maximum velocity at the channel centreline, also known as the velocity-defect. This correlation is termed the velocity-defect law and is defined as:

$$\frac{\langle U \rangle - \langle U \rangle_{\max}}{u_\tau} = \frac{2}{0.6\kappa}\left(1 - \frac{y}{\delta}\right)^{3/2}. \tag{2.100}$$

The different regions in a channel flow can be seen in the inflexion points of the velocity profile in Figure 2.3b. The regions can also be distinguished by observing the extrema of the plot of $y^+ \frac{d\langle U \rangle^+}{dy^+}$ in Figure 2.3a. There is a balance of the production of turbulent kinetic energy and the rate of dissipation of the energy $P = \varepsilon$ in the log – layer region.

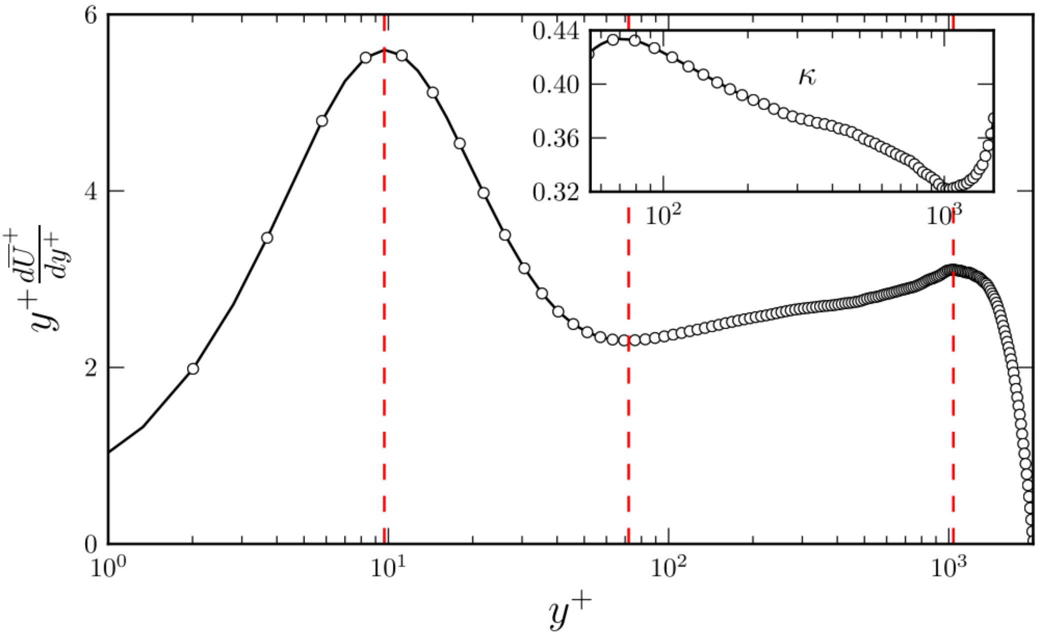

(a) Distribution of $y^+\frac{d\langle U\rangle^+}{dy^+}$

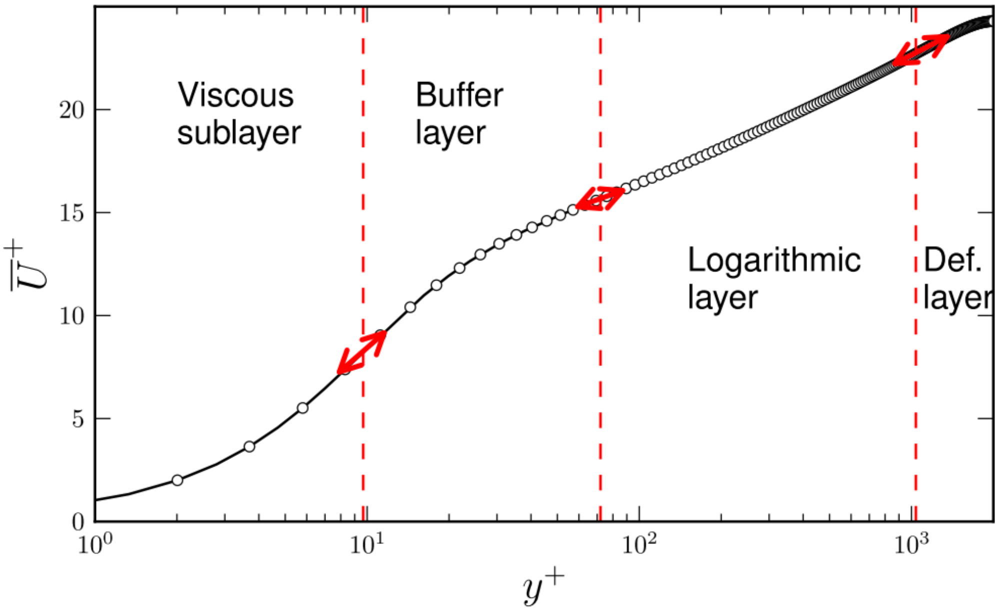

(b) Distribution of U^+

Fig. 2.3 Profiles of $y^+\frac{d\langle U\rangle^+}{dy^+}$ and U^+ for a $Re_\tau = 2000$ channel flow case using Jiménez and Hoyas (2008) DNS data. Figure taken from Billard (2011).

Thereafter, the production reduces and vanishes at the centreline as shear stress and the mean streamwise velocity gradient become zero.

In addition, the peak production of turbulent kinetic energy and the fluctuating components of velocity occurs close to the wall in the viscous region approximately at $y^+ < 20$. Peak turbulent kinetic energy produced close to the walls is moved to the outer region via turbulent transport. For the streamwise, cross-stream and spanwise components of the fluctuating velocity u'^2, v'^2 and w'^2 respectively (also known as Reynolds stresses), the no-slip condition and the impermeability condition result to a two-component limit, where the turbulent motions in the flow become strongly anisotropic in the wall parallel direction. Consequently, the cross-stream Reynolds stress v'^2 is heavily damped compared to the wall parallel components of fluctuating velocity.

2.6.2 High Reynolds Number Flows

In the past, the numerical and experimental investigations of turbulent flows have mostly focused on low friction Reynolds numbers below 1000. From these studies at relatively low Reynolds numbers, it was established that most of the peak production of turbulence occurs in the region where molecular viscous forces are dominant. Also, the turbulent structures in the inner region have a great impact on the large-scale motions in the outer region. Hence, the traditional opinion is that a turbulence method that focuses on modelling the viscous sublayer and buffer region replaces the two areas where most of the critical activities are happening in the turbulent flow. There has been too much reliance on DNS data at very moderate Reynolds numbers, where the separation of scales for the viscous sublayer and inertial range is yet to be established. This reliance has led to the assumption that the modelling of the near-wall region could lead to inaccuracies (Marusic et al., 2010).

The reasoning has been challenged recently with new experimental studies of high Reynolds number channel, pipe and boundary-layer flows. Figure 2.4a shows the profiles of the production of the turbulent kinetic energy for a range of Reynolds numbers. Figure 2.4b shows the bulk production (where the local production is multiplied by the wall-normal distance) to indicate the integral contribution of the production for each equal area under the semi-logarithmic profile. While the peak production of turbulence still occurs at $y^+ = 12$, at high Reynolds numbers, the major contribution to bulk turbulence shifts to the log region as seen in Figure 2.4b. Figure 2.4 clearly shows that the bulk contribution of turbulence comes in the near-wall region for a low Reynolds number flow. However, if the near-wall region is taken as $y^+ \leq 30$, when the friction Reynolds number is increased to 4200, the contribution of bulk production from the logarithmic region equals that from the near-wall region (Smits et al., 2011). Hence,

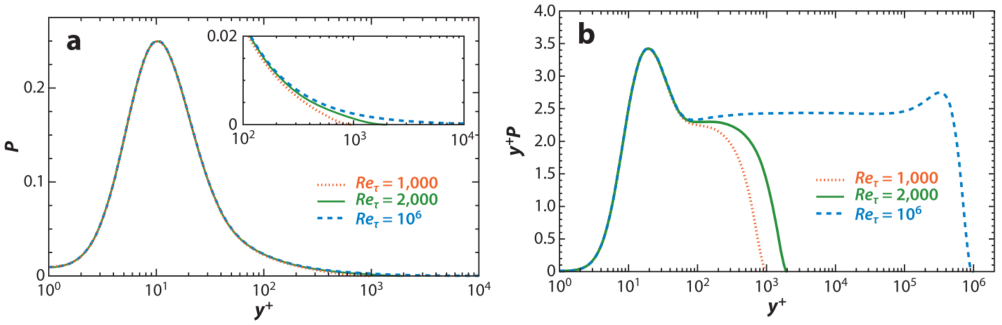

(a) Distribution of local production in semi-logarithmic scale.

(b) Distribution of bulk production (Production multiplied by y^+).

Fig. 2.4 Production of turbulent kinetic energy for a range of Reynolds numbers. Figure taken from Smits et al. (2011).

since the viscous sublayer progressively becomes thinner as the Reynolds number increases, the significance of that region also reduces compared to the outer region. This trend means that turbulence methods that model the inner region of a wall-bounded flow could be more accurate for high Reynolds number flows.

Furthermore, a high Reynolds number flow is characterised by a distinct separation of scales of turbulent motions and a long logarithmic velocity profile. Debates have centred on where the log-layer begins. It has been traditionally accepted that the buffer layer does not extend beyond $y^+ = 50$. Studies by Zagarola and Smits (1998) and Nagib et al. (2007) have shown that viscous effects permeate deeper into the flow at higher Reynolds numbers. Therefore, Zagarola and Smits (1998) note that for a $Re = 35 \times 10^6$ turbulent pipe flow, the logarithmic profile commences at $y^+ \geq 600$. The review done by Smits et al. (2011) indicates that the range of the logarithmic distribution of velocity widens as the Reynolds number is increased. Hence, the log-layer is well established for high Reynolds number flows while it is barely noticeable for low Reynolds number flows.

Also, the log-law is an important equation for standard wall function formulations for RANS and LES methods. The von Karman constant κ has often been taken as 0.41. Though, the review of Smits et al. (2011) notes that the constant rather depends on the type of flow. McKeon et al. (2004) take κ as 0.421 for turbulent pipe flow while Nagib and Chauhan (2008) observe that the constant is 0.384 for boundary layer flows and also differed for channel flow. The differences of the von Karman constant for different flow types at high Reynolds numbers indicate that the constant is not universal. While the small variations do not have a profound impact on the velocity profiles, the non-universality of the von Karman constant affects turbulence models or applications that require the accurate prediction of skin friction at high Reynolds numbers.

Finally, large-scale motions or superstructures scale with the boundary-layer thickness of a turbulent flow. These immense structures appear to exist in the log-layer or the outer layer of the flow. Balakumar and Adrian (2007) discovered that superstructures contribute significantly to the production of turbulent kinetic energy and Reynolds stresses. Hence, when there is a clear separation of scales of motions, the motions in the log-layer and outer layer significantly impact the behaviour of near-wall turbulence. This trend further reinforces the viability of methods that model the near-wall region for high Reynolds number flows.

2.7 Standard Approaches of Wall Functions in RANS

The region near the wall contains complex viscous and turbulent interactions. The steep gradients of relevant turbulence and flow quantities require the need of a very fine computational grid to resolve the quantities, even for a RANS approach. Therefore, wall functions were developed to eliminate the need to resolve the viscous sublayer and part of the log – layer, thereby considerably reducing the computational cost. Wall functions work by using an approach to calculate wall fluxes (momentum, heat transfer or/and mass transfer), which then act as a boundary condition at the first node at the wall, hence, allowing for a reduction in the near-wall mesh requirements (Hanjalic and Launder, 2011). Wall functions provide an approximate expression for the mean velocity distribution in the inner region of the flow.

Standard wall function approaches for the momentum equation use the law of the wall of Equation 2.99 to modify the discretised transport equations for momentum, kinetic energy and rate of dissipation in the near-wall cell. For near cell node P located in the log – layer, as seen in Figure 2.5, the law of the wall equation can be modified to describe the logarithm velocity distribution in the log-layer as:

$$\frac{c_\mu^{1/4} k^{1/2} \langle U \rangle}{\tau_w/\rho} = \frac{1}{\kappa} \ln \left(\frac{E c_\mu^{1/4} k^{1/2} y}{\nu} \right), \tag{2.101}$$

where the normalising velocity scale is taken as $c_\mu^{1/4} k^{1/2}$. This velocity scale is employed rather than the standard viscous velocity scale $\sqrt{\tau_w/\rho}$ to account for non-equilibrium situations where there was no connection between the wall shear stress and turbulent quantities.

Equation 2.101 can be rearranged to define the wall shear stress as:

$$\tau_w = \frac{\rho \kappa c_\mu^{1/4} k^{1/2} \langle U \rangle}{\ln E c_\mu^{1/4} k^{1/2} y/\nu}. \tag{2.102}$$

The turbulent kinetic energy must be known to evaluate the wall shear stress. The turbulent kinetic energy is obtained by solving a transport equation. However, the production P_k and dissipation rate ε rapidly change near the wall, which leads to using

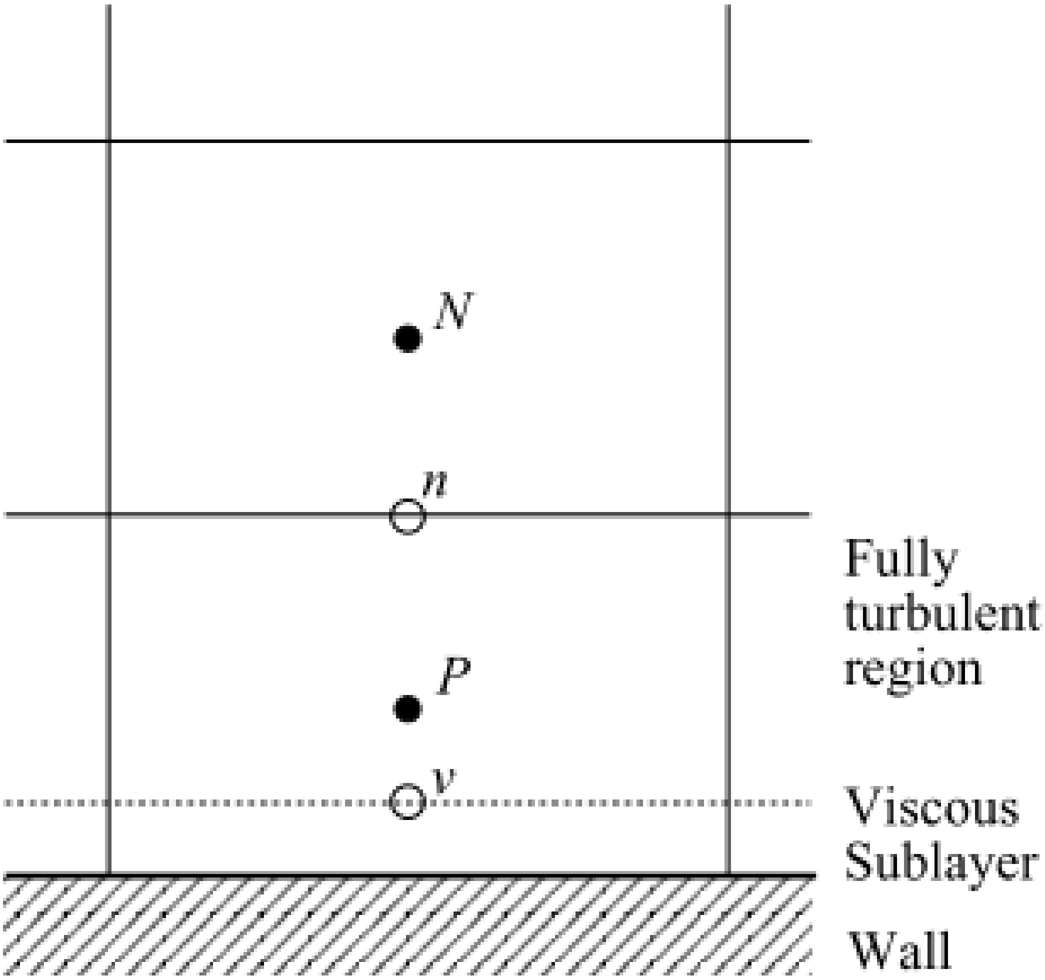

Fig. 2.5 Cell notation used by standard wall functions. Figure obtained from Gant (2002).

their cell centred values at node P as a poor choice. Instead, the cell averaged values of the rate of production $\overline{P_k}$ and dissipation rate $\overline{\varepsilon}$ are used to consider changes in turbulence quantities in the near-wall cell. The methods to calculate $\overline{P_k}$ and $\overline{\varepsilon}$ differ depending on the wall function approach.

Launder and Spalding (1974) assumed that the shear stress $\langle u'v'\rangle$ is constant across the fully turbulent region, but zero in the viscous sublayer. Hence, the average production of turbulent kinetic energy due to shear stress is defined as:

$$\overline{P}_{k_{u'v'}} = \frac{1}{y_n}\int_0^{y_n} -\rho\left\langle u'v'\right\rangle \frac{\partial\langle U\rangle}{\partial y}\mathrm{d}y = \tau_w\frac{\langle U_P\rangle}{y_P}, \tag{2.103}$$

with the Reynolds shear stress assumed being equal to the wall shear stress:

$$-\rho\left\langle u'v'\right\rangle = \rho\tau_w = \mu_t\frac{\partial\langle U\rangle}{\partial y}, \tag{2.104}$$

and the velocity gradient at node P taken as the linear variation of the velocity at node P to the wall-normal distance, which leads to:

$$\frac{\tau_w}{\rho} = c_\mu\frac{k^2}{\varepsilon}\frac{\langle U_P\rangle}{y_P}. \tag{2.105}$$

The cell averaged dissipation rate is obtained as:

$$\overline{\varepsilon} = \frac{c_\mu^{3/4}k_P^{3/2}\langle U_p^+\rangle}{y_P}, \tag{2.106}$$

where $\langle U_p^+\rangle$ is defined as $\rho c_\mu^{1/4}k_p^{1/2}U/\tau_w$.

Chieng and Launder (1980) evaluated the cell average production of turbulent kinetic energy by assuming that Reynolds shear stress is equal to the wall shear stress in the fully turbulent region but zero in the viscous sublayer. Also, the velocity gradient $\partial\bar{U}/\partial y$ is obtained by differentiating the law of the wall equation. Hence, $\overline{P}_{k_{uv}}$ is defined as:

$$\overline{P}_{k_{u'v'}} = \frac{1}{y_n}\int_{y_v}^{y_n}\tau_w\frac{\tau_w}{\rho\kappa c_\mu^{1/4}k^{1/2}y}\mathrm{d}y = \frac{\tau_w^2}{\rho\kappa c_\mu^{1/4}k^{1/2}y_n}\ln\frac{y_n}{y_v}, \tag{2.107}$$

where y_v is the sublayer thickness which is determined by assuming a constant sublayer Reynolds number of 20 ($Re_v = k_P^{1/2}y_v/\nu = 20$).

However, the dissipation rate is not zero in the viscous sublayer, unlike the production. The cell – averaged dissipation rate is assumed to be uniform across the viscous sublayer and is given the value of the dissipation rate at the wall. In the turbulent region, the dissipation rate is computed from $k^{3/2}/\varepsilon = c_l y$. The cell – averaged dissipation rate is thus calculated as:

$$\overline{\varepsilon} = \frac{1}{y_n}\left(\int_0^{y_v}\frac{2\nu k_p}{y_v^2}dy + \int_{y_v}^{y_n}\frac{k_p^{3/2}}{c_l y}\mathrm{d}y\right) = \frac{1}{y_n}\left[\frac{2k_p^{3/2}}{k_p^{3/2}y_v/\nu} + \frac{k_p^{3/2}}{c_l}\ln\frac{y_n}{y_v}\right]. \tag{2.108}$$

For the temperature transport equation, the log law is used to define the temperature equation as:

$$\langle T^+\rangle = \frac{1}{\kappa_h}\ln y^+ + c_h, \tag{2.109}$$

where κ_h is the thermal von Karman constant usually taken 0.38, the constant c_h depends on the molecular Prandtl number, T^+ is the dimensionless temperature defined as $\langle T^+\rangle = (\langle T\rangle - \langle T_w\rangle)/T_\tau$, and the friction temperature T_τ is defined as $T_\tau = q''_w/\rho c_p U_\tau$ (q''_w is the wall heat flux and c_p is the specific heat).

The temperature log law can be rewritten as:

$$\langle T^+\rangle = \sigma_t\left(\langle U^+\rangle + P\right), \tag{2.110}$$

where P is the Jayatilleke function which depends on the ratio of the molecular to turbulent Prandtl numbers and σ_t is the turbulent Prandtl number.

Either the wall temperature or the wall heat flux can be obtained to be used for the discretised transport equation of temperature. If the semi-logarithmic velocity and temperature profiles are assumed to apply in the fully turbulent region, then the wall temperature Tw is defined as:

$$\langle T_w\rangle = \langle T_P\rangle + \frac{q''_w\sigma_t\left(\langle U^+\rangle + P\right)}{\rho c_p c_\mu^{1/4} k_P^{1/2}}. \tag{2.111}$$

The wall heat flux q''_w is defined as:

$$q''_w = \frac{\rho c_p c_\mu^{1/4} k_P^{1/2}\left(\langle T_P\rangle - \langle T_w\rangle\right)}{\sigma_t\left(\langle U^+\rangle + P\right)}. \tag{2.112}$$

The usage of standard wall functions assumes that the turbulent flow follows a semi-logarithmic velocity and temperature distribution near the wall. Another assumption is that the Reynolds shear stress is equal to the wall shear stress. Finally, standard wall functions work with the premise that the turbulent kinetic energy is in local equilibrium which ensures that production balances the dissipation rate.

These assumptions are valid for simple flows that experience constant pressure gradients or do not experience acceleration/deceleration. The performance of standard wall functions has been well validated for channel flows and pipe flows with DNS data. However, for complex flows typically encountered in engineering or even simple geometries with curved wall surfaces, the assumptions do not hold, and the performance of standard wall functions degrades. The University of Manchester developed two new wall function schemes that handle complex turbulent flows that depart far from local equilibrium. The two novel schemes are the analytical wall function of Craft et al. (2002) and the numerical wall function (NWF) of Craft et al. (2004). Only an overview of the numerical wall function scheme will be provided as elements of this approach are incorporated in this research project.

2.7.1 The Numerical Wall Function for RANS

The numerical wall function scheme was developed by Craft et al. (2004) to handle flows where local turbulence deviates far from local equilibrium near the wall. In this approach, there are two computational grids: the main grid and the subgrid (Figure 2.6). The main grid resolves the flow except at the wall where the first cell covers the viscous sublayer and part of the log layer. The subgrid is embedded into the first cell of the main grid and is divided into numerous slices. The numerical wall function is developed for information to be exchanged between the two grids.

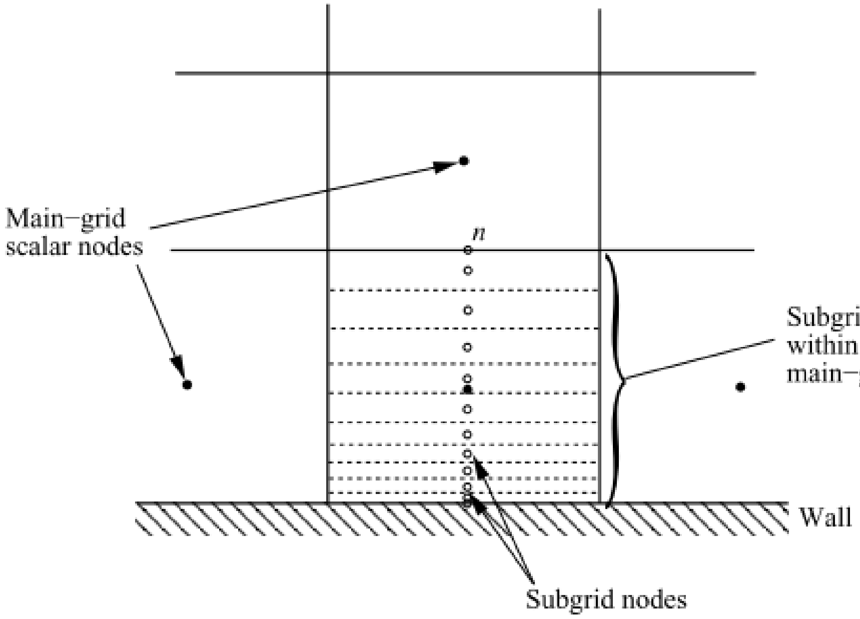

Fig. 2.6 Subgrid embedded in the first cell of the main grid. Figure obtained from Gant (2002).

The subgrid obtains the streamwise pressure gradient $(P_e - P_w)/\Delta x$ from the main grid, as seen in Figure 2.7. The pressure gradient is assumed to be uniform across the subgrid cells. Wall parallel momentum equations are solved in addition to equations of turbulence quantities and scalars. Since the pressure gradient is already known, there is no need for complex pressure – velocity coupling, thereby reducing computational costs.

The main grid supplies the streamwise velocity, turbulent kinetic energy, dissipation and other needed turbulence quantities at position *n* (see Figure 2.7) as boundary conditions to the subgrid domain. Furthermore, the wall-normal velocity *V* can be obtained from the continuity equation. Ultimately, the subgrid domain computes the wall-fluxes of momentum and heat transfer. The information of these wall-fluxes is fed into the main grid as source terms of the transport equations of the main computation. Two-way coupling of information occurs between the primary grid and the subgrid until the important quantities in the main grid satisfy the convergence criteria.

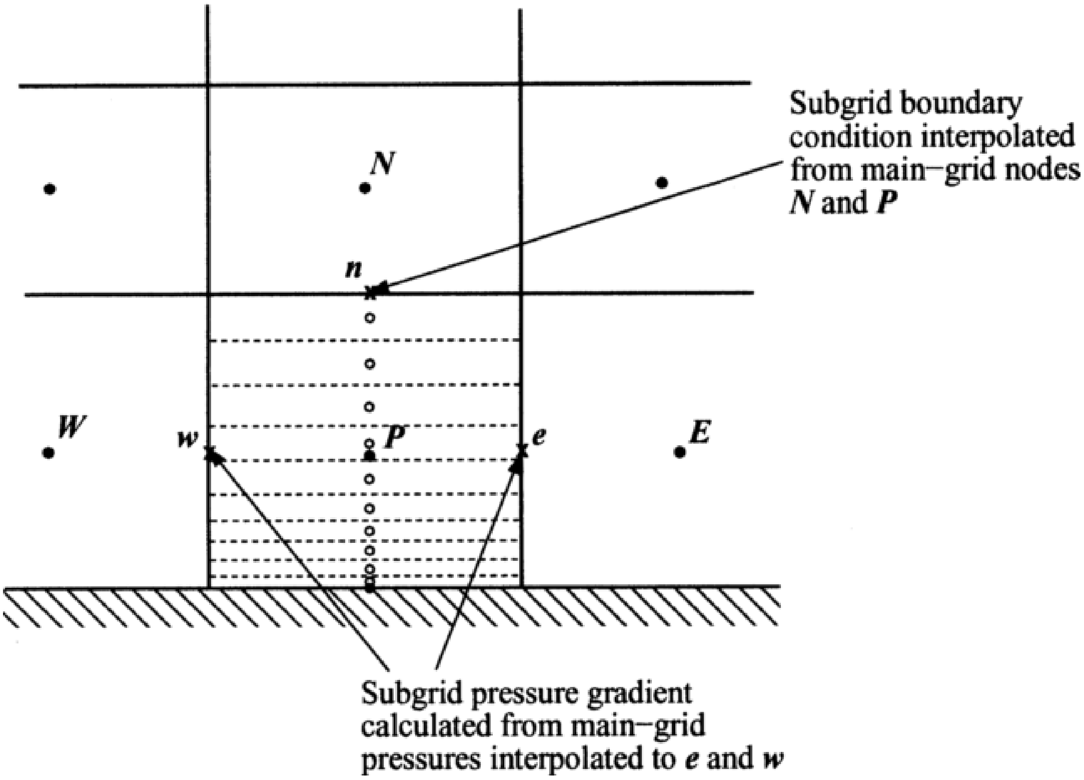

Fig. 2.7 Schematic illustrating the exchange of quantities between the two grids. Figure obtained from Craft et al. (2004).

The numerical wall function has the advantage of working with any turbulence model and has been applied with success to flows where standard wall functions fail. The normal impingement of an axisymmetric jet onto a heated plane was simulated by Craft et al. (2004). Linear turbulent – viscosity models have failed in predicting the parameters of the flow; hence, a cubic turbulent – viscosity model was incorporated with the numerical wall function. The numerical results utilising the wall function was in good agreement with the experimental data. Moreover, the simulated results matched those produced by another simulation done with the low – Reynolds - number cubic turbulent – viscosity model. The distribution of Nusselt number data was not sensitive to the change of the size of the first cell in the primary grid, which is a significant problem faced by standard wall function approaches. Craft et al. (2004) reported a large increase of the computational time for the numerical wall function compared to the standard wall function. However, the numerical wall function still achieved 90% time saving against the low – Reynolds number model.

2.8 Hybrid RANS/LES Methods

The mesh requirements in the inner region of a wall-bounded flow for LES is almost the same as those for DNS. This grid requirement has meant that LES is also unfeasible for high Reynolds number flows. This problem has led to various researches on how to reduce the computational cost of LES. One of the results of the research is the development of hybrid RANS/LES methods. Often these methods involve solving unsteady RANS next to the wall where the Reynolds stresses are highly anisotropic and then solving LES far away from the wall where the grid requirements are almost independent of Reynolds number. This approach takes advantage of the structural similarity of the momentum transport equations of LES and RANS. Both momentum transport equations have stresses that need to be closed. A detailed review of hybrid RANS/LES methods will not be discussed here as the method is not the focus of this project (Extensive reviews can be found in Fröhlich and von Terzi (2008) and Piomelli (2008)). However, some key useful aspects of the hybrid RANS/LES method and its development will be highlighted.

Solving the RANS and LES simultaneously on the same grid often means that there is an interface in the domain between RANS and LES. At the interface, there is a sudden switch between the RANS computation to LES. Hence, the problem of coupling the statistically averaged RANS velocity field and filtered LES velocity field at the interface arises. Also, the LES stresses are quantities representative of the filtered grid while the RANS stresses are physical properties of the flow. This leads to a difference of stresses between the LES and the RANS at the interface, causing the major challenge of insufficient resolved-eddies in that region. These issues result in a mismatch of the logarithm velocity profiles between the LES and RANS regions. This problem known as the log-layer mismatch (LLM) has been the subject of many studies for hybrid RANS/LES methods Piomelli (2008). Efforts at reducing the LLM include adding forcing terms that artificially increases the number of resolved eddies at the interface.

Uribe et al. (2010) attempted to solve the LLM problem by proposing an overlap of the RANS and LES fields. The SGS stress tensor can be decomposed into a locally-isotropic part and an inhomogeneous part, which is derived from ideas by Schumann

(1975). The decomposition of the stress tensor is defined as:

$$\tau_{ij}^{r} - \frac{2}{3}\tau_{kk}\delta_{ij} = \underbrace{-2\nu_r f_b\left(\overline{S}_{ij} - \langle\overline{S}_{ij}\rangle\right)}_{\text{locally isotropic}} - \underbrace{2\left(1-f_b\right)\nu_a\langle\overline{S}_{ij}\rangle}_{\text{inhomogenous}}, \tag{2.113}$$

where the viscosities ν_r and ν_a are based on fluctuating and mean strains, respectively. The viscosity ν_r is computed using an SGS model, while ν_a is evaluated with a RANS model. The isotropic part, which determines the dissipation rate, is proportional to the fluctuating strain, while the inhomogeneous part controls the shear stress and mean velocity profile. A long-time average of the two components leads to the isotropic part being zero and the inhomogeneous part becoming the standard RANS formulation of turbulent viscosity. The term f_b is a blending function. The blending function is tuned to zero in the region near the wall where the shear stress $\langle u'v'\rangle$ is under-resolved and $f_b \to 1$ in the LES region where the shear stress is well resolved. In this formulation, the velocity field is partially time-averaged over an averaging window of 10 times the eddy turnover time. The blending function is designed to give a smooth transition between the RANS region and the LES region. The blending function is defined as:

$$f_b = \tanh\left(C_l\frac{L_t}{\Delta}\right)^n, \tag{2.114}$$

where the empirical constants C_l and n are 1 and 1.5 respectively, and L_t is the turbulent length-scale. The proposed model gives good results when simulating channel flow and trailing-edge flow. The log-layer mismatch problem is not detected in the simulations.

Xiao and Jenny (2012) developed a novel hybrid RANS/LES formulation where the need to specify an interface between the RANS and LES computations is eliminated. Instead, two meshes with the same outer dimensions for the turbulent flow case are used. The LES computations are on one mesh, while RANS computations are done on a separate grid. The LES mesh is not refined near the wall, but the near-wall refinement is done for the RANS mesh. Drift terms are added to the RANS and LES momentum equations to ensure that the mean quantities of the RANS and LES grids are consistent with one another. Hence, near the wall, where the LES is under-resolved, the mean filtered velocity field is relaxed towards the RANS velocity filter through the drift term. In the near-wall region, the RANS is expected to be more accurate than the LES since the LES grid is coarse in this region. In the regions where the LES is well resolved and expected to perform better than the RANS, the RANS velocity field is relaxed towards the exponentially weighted-averaged filtered velocity field. The momentum transport equation for LES and RANS is defined as:

$$\frac{\partial U_i^*}{\partial t} + \frac{\partial U_i^* U_j^*}{\partial x_j} = -\frac{1}{\rho}\frac{\partial p^*}{\partial x_i} + \nu\frac{\partial^2 U_i^*}{\partial x_i \partial x_j} - \frac{\partial \tau_{ij}^*}{\partial x_j} + Q_i^*. \tag{2.115}$$

The pressure equation is defined as:

$$\frac{1}{\rho}\frac{\partial^2 p^*}{\partial x_i \partial x_j} = -\frac{\partial^2}{\partial x_i \partial x_j}\left(U_i^* U_j^* + \tau_{ij}^*\right) - \frac{\partial Q_i^*}{\partial x_i}. \tag{2.116}$$

The variable Q_i^* is the momentum drift term, which ensures that the RANS and LES mean velocity and total Reynolds stress fields gradually become consistent with one another. For the LES momentum equation, the filtered terms in Equations 2.115 and 2.116 are defined as: $U_i^* = \overline{U}_i$, $p^* = \bar{p}$, $\tau_{ij}^* = \tau_{ij}^r$ and $Q_i^* = Q_i^L$. The terms for the RANS equations are replaced as: $U_i^* = \langle U_i \rangle$, $p^* = \langle p \rangle$,$\tau_{ij}^* = \langle u_i' u_j' \rangle$ and $Q_i^* = Q_i^R$.

To compute the drift terms, the partial time average of the filtered velocity, stress and dissipation fields is computed. The partial time average is computed employing the exponentially weighted average (EWA). The exponentially weighted average of a time-dependent quantity $\emptyset$ is defined as:

$$\langle \emptyset \rangle^{\mathrm{EWA}} = \int_{-\infty}^{t} \frac{1}{T} \emptyset\left(t'\right) \exp^{-(t-t')/T} dt', \tag{2.117}$$

where T is the time-scale for the exponential weighted averaging operation. Hence, the exponential weighted averaged velocity is assumed to be equivalent to the Reynolds average velocity $\langle \overline{U}_i \rangle^{\mathrm{EWA}} = \langle U_i \rangle$. The individual stress components of the LES should be consistent with the Reynolds stresses which are defined as $\langle {\tau_{ij}}^{\mathrm{EWA}} \rangle = \langle u'_i u'_j \rangle$. The stresses of the LES field is defined as the composition of the product of resolved fluctuations and modelled fluctuations about the filtered EWA velocity which is defined as $\tau_{ij} = u_i' u_j' + \tau_{ij}^r$.

To enforce the consistency requirements, the drift term for the LES momentum equation is defined as:

$$Q_i^L = \begin{cases} \frac{U_i - \langle {\overline{U}_i}^{\mathrm{EWA}} \rangle}{\tau_l} + \frac{G_{ij}\left(\langle {\overline{U}_j}^{\mathrm{EWA}} \rangle - \overline{U}_j\right)}{\tau_g} & \textit{in} \text{ RANS region} \\ 0 & \textit{in} \text{ LES region} \end{cases}. \tag{2.118}$$

Xiao and Jenny (2012) referred to the *RANS region* as the area of the LES grid that is deemed to have low resolution, while the *LES region* is the area of the LES grid that is expected to resolved flow quantities. Therefore, the drift term Q_i^L in Equation 2.118 is only active in the area of the LES grid that is poorly resolved. The coefficients τ_l and τ_g are the relaxation time-scales that determine how quickly consistency is achieved. G_{ij} is the normalised difference between the partial time-averaged LES stresses and the Reynolds stresses which is defined as:

$$G_{ij} = \frac{\langle {\tau_{ij}}^{\mathrm{EWA}} \rangle - \langle u'_i u'_j \rangle}{\langle {\tau_{kk}}^{\mathrm{EWA}} \rangle + \langle u'_k u'_k \rangle}. \tag{2.119}$$

The left term of the LES drift force in Equation 2.118 forces the average filtered velocity field towards the RANS velocity where the LES grid is under-resolved. Also, the right term with the variable G_{ij} in Equation 2.118 ensures that the LES resolved fluctuations are relaxed towards the Reynolds stresses.

For the RANS grid, the drift force Q_i^R in the RANS momentum equation is defined as:

$$Q_i^R = \begin{cases} \left(\langle \overline{U}_i^{\text{EWA}} \rangle - \langle U_i \rangle\right)/\tau_r & \textit{in}\ \text{LES region} \\ 0 & \textit{in}\ \text{RANS region} \end{cases}, \tag{2.120}$$

where τ_r is the relaxation time-scale. The RANS drift term is only active in the far-wall region of the RANS grid, where the LES is expected to perform better. This drift term Q_i^R ensures that RANS velocity is relaxed towards the EWA velocity of the LES domain.

The dual-mesh hybrid RANS/LES approach is applied to plane channel flow simulation, where the LES grid is very coarse, and channel flow computation with periodic hills. Xiao and Jenny (2012) observe good agreement with DNS data for the two simulations. There are noticeable problems with the implementation of Xiao and Jenny (2012) dual mesh hybrid RANS/LES method. First, the region where the LES grid is under-resolved is not automatically determined. This region is prescribed before the computations commence. This prescription means that it is difficult to use the dual-mesh approach for more complicated geometries. Second, the timescales T, τ_r, τ_l and τ_g are also specified. The reasoning behind the specification of the time-scales are not made clear by the proposers of the method, plus the time scales used for the channel flow simulation differ from that of the periodic hills simulation. Tunstall et al. (2017) remedied the first problem by assuming the LES grid is well resolved at a local distance where the turbulent Reynolds number is greater than 200. The turbulent Reynolds number is defined as $Re_y = \sqrt{k}y/\nu$. Hence, a blending function is defined which automatically switches on or off the computation of drift terms for the LES and RANS fields. Furthermore, the relaxation time-scales are made a function of the turbulent time-scale k/ε obtained from the RANS field. This ensures that the relaxation time-scales are automatically computed in various regions of the computational domain. Ideas of the dual-mesh hybrid RANS/LES form the basis of the subdomain wall function developed by this project. Details of the subdomain wall function are found in Paper I.

Chapter 3

Review of Wall Modelling Approaches in Large Eddy Simulation

LES requires excessive computational effort to compute high Reynolds number wall-bounded flows. Despite the exponentially improving performance of computing technology, access to high-performance computing facilities is still restricted. These problems motivated researchers to develop methodologies to reduce the computational requirements of LES. The focus has been placed on modelling the inner layer of the turbulent flow. The review will put more emphasis on the evolution of the modelling of wall treatments for LES. The current implementation of different frameworks of wall – layered models or wall function for LES will be critically assessed in this chapter.

3.1 Problem Description

As noted in Chapter 2, RANS methods are commonly used in industry as they require the least amount of computational effort compared to LES and DNS approaches. However, the significant effect of boundary conditions of the flow geometry on the integral scales of the flows makes creating a universal RANS model difficult. Hence, the performance of RANS models widely varies for different flow configurations, unless the RANS coefficients are properly tuned. LES and DNS approaches are used in academic research because of the unparalleled level of detail and accuracy of the two methods.

In the inner layer of a turbulent flow, the integral eddies scale with the viscous length scale $\delta_\nu = \nu/u_\tau$. The implication is that the separation of scales between the integral and dissipative eddies is no longer distinct in the inner layer. Hence, for the LES approach, where only the small – scale motions are modelled, a computational grid approaching the requirements of DNS must be employed for the inner layer of the flow where viscous forces are dominant. In LES, the recommended wall-normal distance for the first grid point is $y^+ \approx 1$. While the recommended spacing of the first grid point for the streamwise and spanwise directions are $\Delta x^+ \approx 30-100$ and $\Delta z^+ \approx 15-40$ respectively (Larsson et al., 2016).

Flows typically encountered in engineering are at a very high Reynolds number where the size of the inner layer is almost insignificant in comparison to the flow domain. Consequently, this leads to the motivation of modelling the inner layer to enable the use of LES in engineering design or academic research of high Reynolds number flows. Typical wall function approaches for LES resolve the large energetic motions in the outer layer without making any modifications in this area. Rather, the dynamic processes in the inner layer are represented by a wall shear stress to reduce the required grid size in this location, and hence, lowering the computational costs. This modelling removes the process of peak production of turbulence in the inner layer. The truncating of the inner-wall dynamic processes does not stop the generation of turbulence in the outer region of a boundary layer. As identified in Section 2.6.2, the Reynolds stresses are still produced and dissipated in the outer layer of the flow for high-Reynolds number flows. The next section focuses on methods that algebraically compute the wall shear stress that represent the turbulent processes in the near-wall region.

3.2 Equilibrium Wall Functions (Approximate Boundary Condition)

The implementation of the equilibrium wall functions (also known as the approximate boundary condition) is similar to the standard wall functions that are used in RANS modelling. The first cell at the wall of the domain bypasses the layer where molecular friction is dominant. Similar assumptions to standard wall functions are made such as flow acceleration and pressure gradient are negligible in the first cell, and that the shear stress is assumed constant across the first cell. Hence, the shear stress can implicitly be solved from the law of the wall equation defined as:

$$U^+ = \frac{1}{\kappa} \ln y^+ + B. \tag{3.1}$$

Deardorff (1970) was the first to implement wall functions for LES. The author argued that solving the law of the wall for the wall shear stress only worked when the flow quantities were averaged. The following equations are defined to calculate boundary conditions to feed the momentum transport equation as source term at each time step:

$$\frac{\partial^2 \overline{U}}{\partial y^2} = \frac{1}{\kappa Y^2} + \frac{\partial^2 \overline{U}}{\partial z^2}, \tag{3.2}$$

$$\frac{\partial^2 \overline{W}}{\partial y^2} = \frac{\partial^2 \overline{W}}{\partial x^2}, \tag{3.3}$$

where Y is the location of the first grid point at the wall and $\overline{V} = 0$. The numerical results obtained by Deardorff (1970) poorly agree with the channel flow data of Laufer (1948). The poor results are attributed to the outer layer of the channel flow being under-resolved (Piomelli and Balaras, 2002).

Schumann (1975) first showed success in modelling the boundary layer for LES computations. The author related the calculation of the instantaneous wall shear stress with the velocity components at the first wall cell; the fluctuations of the wall shear stress is ensured to be in phase with the streamwise velocity. The components of wall shear stress are defined as:

$$\tau_{xy,w}(x,z) = \frac{\langle \tau_w \rangle}{\langle \overline{U}(x,Y,z) \rangle} \overline{U}(x,Y,z), \tag{3.4}$$

$$\tau_{yz,w}(x,z) = \nu \frac{\overline{W}(x,Y,z)}{Y}, \tag{3.5}$$

where $\langle\ \rangle$ represents a time-averaged quantity, and $\tau_{xy,w}$ and $\tau_{yz,w}$ are the streamwise and spanwise components of wall shear stress respectively and where Y is the location of the first grid point at the wall. The mean streamwise velocity $\langle \overline{U}(x,Y,z) \rangle$ is obtained from the law of the wall. The time-averaged wall shear stress is given a - priori by computing the value based on the specified pressure gradient of the plane channel. This approach of computing the mean wall shear stress is not feasible for more complex flows. The instantaneous streamwise shear stress fluctuates around the mean value. The computed mean velocity for turbulent channel flow is in good agreement with experimental data. It should be noted that Schumann (1975) used a higher mesh resolution for the channel flow computation than Deardorff (1970), and an improved subgrid turbulence model is also used.

Piomelli et al. (1989) noted from work by Rajagopalan and Antonia (1979) that the inclined elongated turbulent structures near the wall affect the correlation between the wall shear stress and velocity in the first cell. The instantaneous velocity at the first cell is not always connected or affected by the skin friction of the wall directly beneath the cell. Instead, there is a time delay between the velocity at the first cell and the wall shear stress some lateral distance away due to the inclination of the elongated integral eddies. Hence, Piomelli et al. (1989) modified the computation of the instantaneous streamwise and spanwise velocity by introducing a displacement distance Δ in the wall parallel directions in Equations 3.4 and 3.5 to account for the time delay of the correlation between the first cell velocity and skin friction. The modified equations are defined as:

$$\tau_{xy,w}(x,z) = \frac{\langle \tau_w \rangle}{\langle \overline{U}\left(x,Y,z\right) \rangle} \overline{U}\left(x+\Delta_S,Y,z\right), \tag{3.6}$$

$$\tau_{yz,w}(x,z) = \frac{\langle \tau_w \rangle}{\langle \overline{U}\left(x,Y,z\right) \rangle} \overline{W}\left(x+\Delta_S,Y,z\right), \tag{3.7}$$

where the average wall shear stress $\langle \tau_w \rangle$ is closed by solving the law of the wall equation iteratively. Channel flow numerical and experimental data were studied to determine the downstream displacement between the skin friction and first cell velocity. The authors estimate the displacement as $\Delta_S = Y \cot 8^\circ$ for $30 < Y^+ < 50$ and $\Delta_S = Y \cot 13^\circ$ for larger distances away from the wall. Good prediction of the mean velocity profile is reported for the channel flow results, and the mean turbulent quantities are in good agreement with experimental data.

Marusic et al. (2001) argued that for higher Reynolds numbers, the models by Piomelli et al. (1989) and Schumann (1975) give inaccurate results for the components of wall shear stress. In their channel flow experiments and numerical computations, it is observed that the energy of the fluctuating components of wall shear stress is not adequately estimated for the two above models. Secondly, when the spectra of the wall shear stress are calculated by varying the position of the first cell at the wall, the spectra of the different positions do not match, as shown in Figure 3.1. Hence, the authors proposed a new model to ensure that the spectra of the modelled wall shear stress at different wall-normal positions in the log – layer will match each other. The instantaneous wall shear stress is decomposed into its mean wall shear stress and fluctuating components. The fluctuating part is multiplied by a constant to return the correct level of energy. The new model is defined as:

$$\tau_{xy,w}\left(x,z,t\right) = \langle \tau_w \rangle - \alpha_\tau U_\tau \left[\overline{U}\left(x+\Delta_S, y_{o1}, z, t\right) - \langle U_{o1} \rangle \right], \tag{3.8}$$

where α_τ is a characteristic constant which is dependent on the pressure gradient (For a zero – pressure gradient flow, α_τ is given a value of 0.10). The improved results for a turbulent boundary layer flow ($Re_\theta = 3500$) are shown in Figure 3.2.

A limitation of the model is that the characteristic constant varies. The authors argue that the matching of the wall shear stress spectra at different locations is dependent on the pressure gradient. However, a functional form of the characteristic constant can be determined with little dependence on the flow geometry. Another limitation is that the mean wall shear stress has to be known apriori.

Radhakrishnan and Piomelli (2008) applied the models developed by Marusic et al. (2001) (identified as MKP) and Piomelli et al. (1989) (identified as standard) to simulate

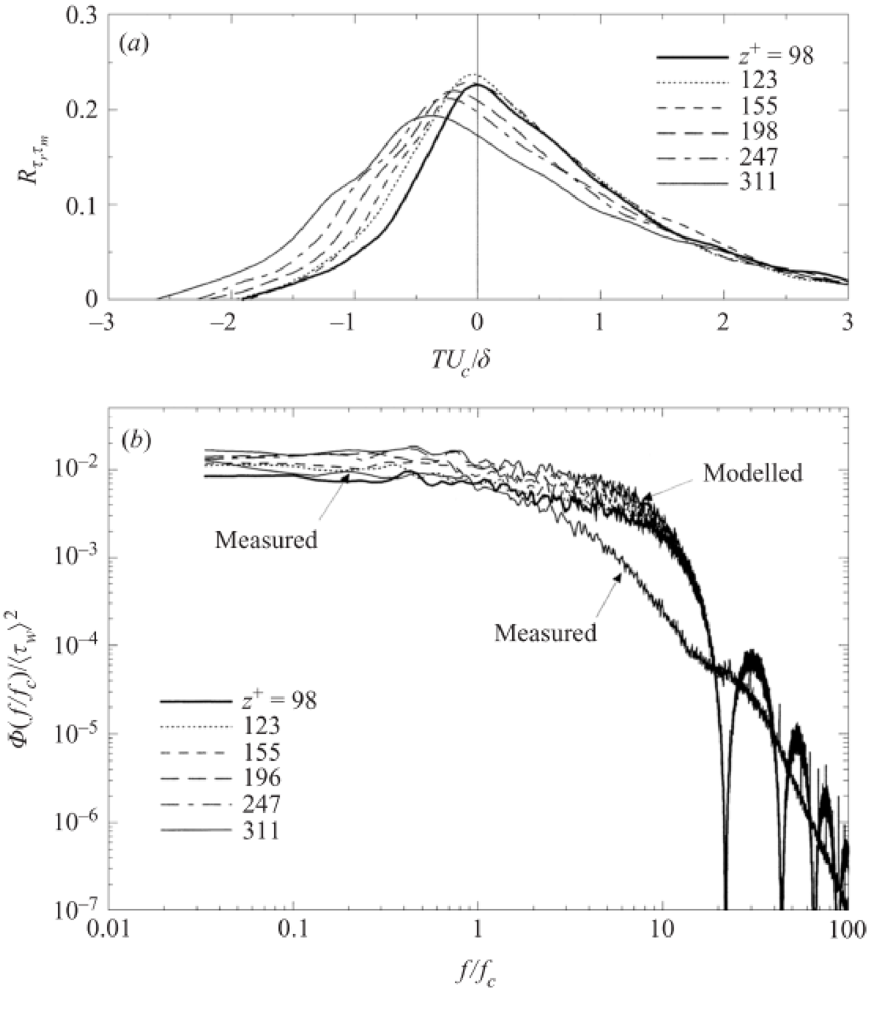

Fig. 3.1 Comparison of the wall shear stress calculated by Piomelli et al. (1989) and measured by experiment. (a) The correlation coefficient between calculated and measured wall shear stress at different first grid point positions, (b) Spectra of calculated and measured wall shear stress. Figures obtained from Marusic et al. (2001).

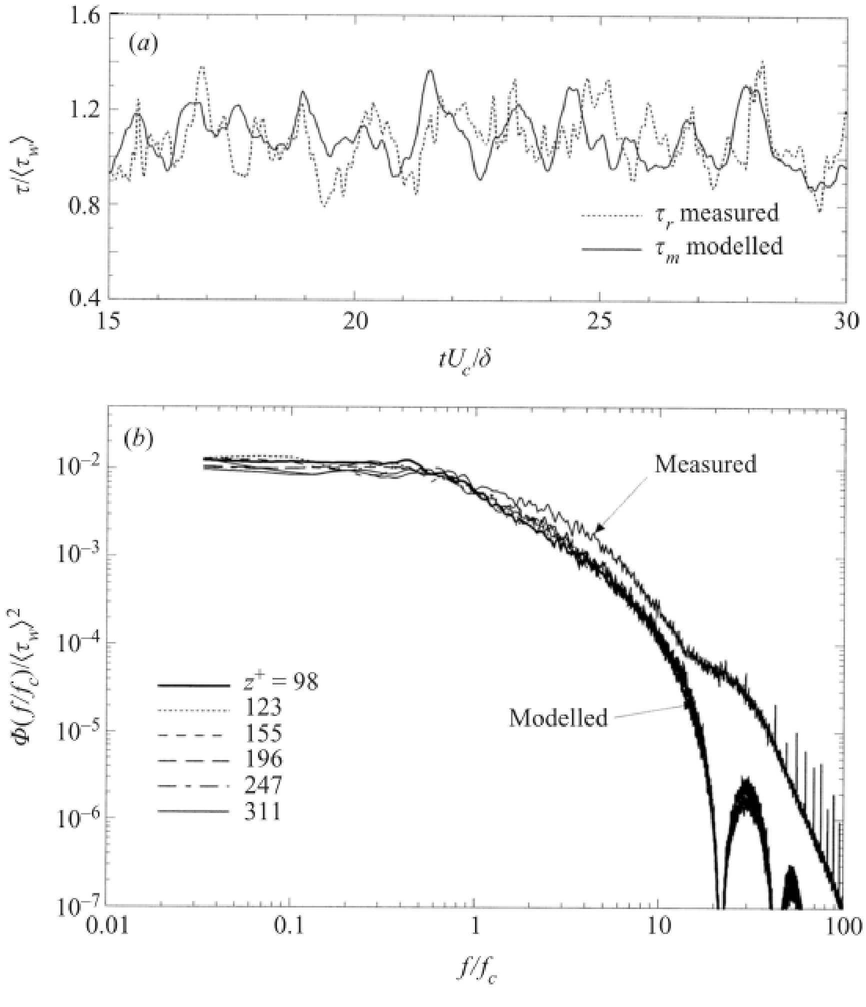

Fig. 3.2 Comparison of the wall shear stress modelled by Marusic et al. (2001) and measured by experiment for a zero - pressure gradient boundary layer flow ($Re_\theta = 3500$). (a) Sample of filtered wall shear stress at y+ = 98, (b) Spectra of calculated and measured wall shear stress. Figures obtained from Marusic et al. (2001) ($Re_\theta = 3500$).

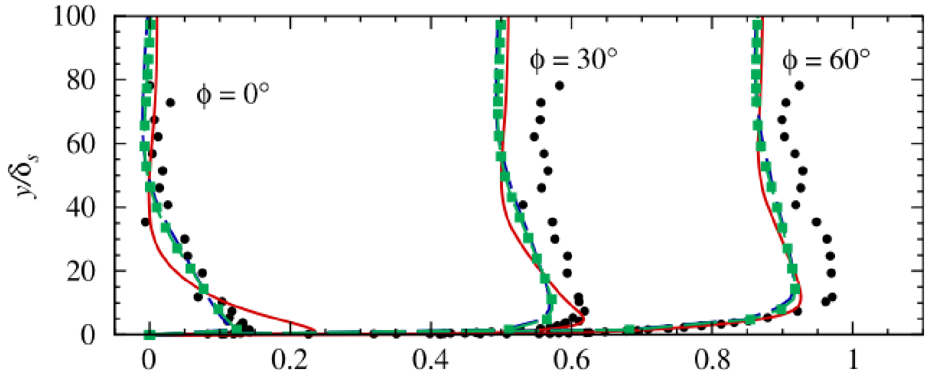

(a) $\phi = 0°, 30°, 60°$.

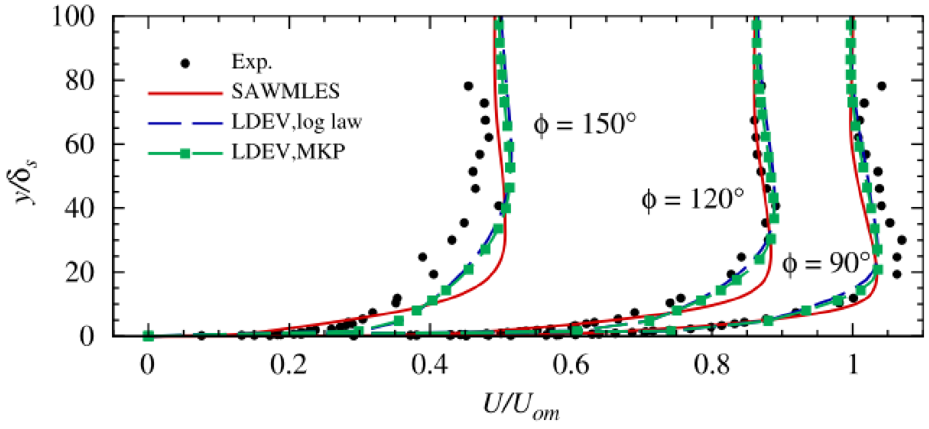

(b) $\phi = 90°, 120°, 150°$.

Fig. 3.3 Profiles of mean velocity at different phase angles. Figures obtained from Piomelli (2008).

a boundary layer flow subjected to sinusoidal oscillation $U_\infty = U_{om} \sin \omega t$, where U_{om} is the freestream velocity oscillation amplitude. The results of a hybrid RANS/LES method are also compared. The predicted wall shear stress distribution by the MKP and standard methods are in good agreement with the experimental data, although the standard method slightly over-predicts the peak values and under-predicts the lowest values of wall shear stress. The velocity profiles by the two methods match the shape of the experimental data at different phases of the flow, as seen in Figure 3.3. However, for a flow that differed from a simple turbulent channel flow, there are obvious deviations from the experimental data.

3.2.1 Appraisal of Equilibrium Wall Functions

The equilibrium wall function method started as a simple correlation between the wall shear stress and the streamwise velocity of the first node at the wall using the law of the wall equation. Added formulations ensured that the computation of the instantaneous components of the wall shear stress was in phase with the streamwise velocity. Equilibrium wall function methods were tested with success for simple flow geometries like the turbulent channel flow. However, the farther the flow departed from local equilibrium, the worse the results became. For instance, the rotating turbulent channel flow was computed by Balaras et al. (1996) using the method by Piomelli et al. (1989). The wall shear stress was under-predicted on the unstable side of the channel and over-predicted on the stable side of the channel flow. The order of magnitude of error for a case with low rotation was about 10%; the error in predicting the wall shear stress increased as the rotation speed was increased. Additionally, when the log-law methods were used to simulate flow over an aerofoil, the flow was predicted accurately in the regions of zero – pressure gradient and favourable pressure gradient. When the flow was in the area of adverse pressure gradient, the equilibrium wall function model did not accurately compute the flow field (Wang and Moin, 2000). Consequently, the application of approximate boundary condition methods to complex engineering flows is limited.

It should be noted that Wu and Squires (1998) accurately predicted the three - dimensional turbulent boundary layer flow over a swept bump using methods developed by Schumann (1975), despite the presence of adverse and favourable pressure gradients in the flow. In this case, the mean wall shear stress was not computed from the log-law equation but was obtained separately from RANS computations and experimental data. This idea illustrates that there is an opportunity to test these methods if a scheme to calculate the wall shear stress under non – equilibrium conditions are developed.

Furthermore, Piomelli et al. (1989) and Marusic et al. (2001) noted the occurrence of time and space delay of the correlation between the instantaneous velocity and the wall shear stress. A – priori studies of DNS turbulent channel flow data is needed to accurately model the delay to ensure that the wall shear stress is correctly imposed in the LES.

3.3 Two-Layer Modelling (Wall-Modelled LES)

The two-layer approach, also known as wall-modelled LES (hereinafter known as TLM or WMLES) is similar to the implementation of the RANS numerical wall function. Two grids solve different sets of equations. The first grid is the main domain of the flow, which solves the LES transport equations. The grid resolution near the wall is coarsened; therefore, the first grid point bypasses the region where molecular viscosity is dominant. The second grid often has the height of the first cell of the main domain. The second grid receives information of the instantaneous filtered velocity and the instantaneous filtered temperature from the main LES grid at the interface between the two domains. RANS transport equations are solved in the second grid, which leads to the computation of wall fluxes of momentum, heat transfer or mass transfer. These wall fluxes are then supplied to the first grid as source terms to the LES momentum

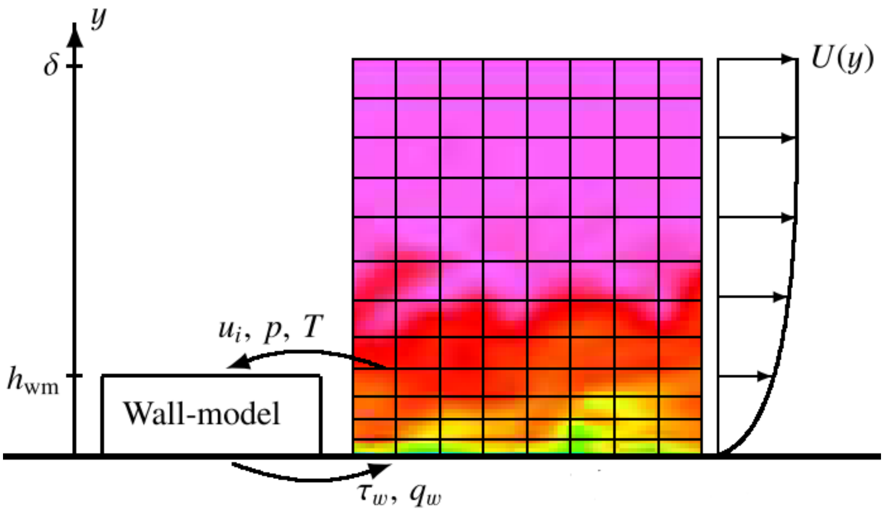

Fig. 3.4 Schematic showing the two grids used for the wall-modelled LES method. Figure obtained from Larsson et al. (2015).

and heat transfer transport equations. The illustration of the two-layer scheme and how information is exchanged is shown in Figure 3.4.

Balaras et al. (1996) were the first to propose this approach. Computations are done for the turbulent plane channel, square duct and rotating channel flows, and the results are compared to those produced by the approximate boundary condition method of Piomelli et al. (1989).

In the second grid of the wall-modelled LES, boundary layer assumptions are made for the RANS momentum equations. Thus, the momentum transport equation for the velocity component normal to the plane is not solved, and diffusion only in the normal direction is considered. The cross – stream velocity is obtained from the continuity equation. The boundary layer equations are defined as:

$$\frac{\partial \langle U_i \rangle}{\partial t} + \frac{\partial \langle U_n \rangle \langle U_i \rangle}{\partial x_i} + \frac{1}{\rho}\frac{\partial \langle P \rangle}{\partial x_i} = \frac{\partial}{\partial x_n}\left[(\nu + \nu_t)\frac{\partial \langle U_i \rangle}{\partial x_n}\right], \tag{3.9}$$

where $i = 1, 3$ represents the wall-parallel components of the momentum equation that are solved and n indicates the normal direction. The pressure gradient is obtained from the first point of the main grid. The wall-normal velocity is calculated as:

$$\langle U_n \rangle = -\int_0^y \left(\frac{\partial \langle U_1 \rangle}{\partial x_1} + \frac{\partial \langle U_3 \rangle}{\partial x_3}\right) \mathrm{d}y. \tag{3.10}$$

The turbulent viscosity ν_t in the RANS grid is closed using the mixing – length turbulence model since the flow configuration is relatively straightforward. The turbulent viscosity is chosen to represent all the scales of motion that are under - resolved in the first cell of the main grid. The mixing length model used by the authors is defined as:

$$\nu_t = (\kappa y)^2 D(y) \left| S \right|, \tag{3.11}$$

where $|S|$ is the magnitude of the rate of strain in the RANS grid and D is a damping function defined as:

$$D(y) = \left[1 - \exp\left(-\left(y^+/A^+\right)^3\right)\right], \tag{3.12}$$

where $A^+ = 25$.

For the square duct flow, secondary flow occurs at the corners or in the transverse plane; hence, the departure from standard velocity logarithm profile in those regions. The friction Reynolds number of the case is 1125. The approximate boundary condition method fails to predict the skin friction at the corners, although the wall-modelled LES does better (Figure 3.6). Away from the corners, the skin friction predicted by the WMLES deviates a little from experimental data. In the mid-plane of the duct, the mean velocity profiles are accurately predicted, as seen in Figure 3.5. However, the two methods deviated from the reference data in predicting the Reynolds stresses, especially close to the wall.

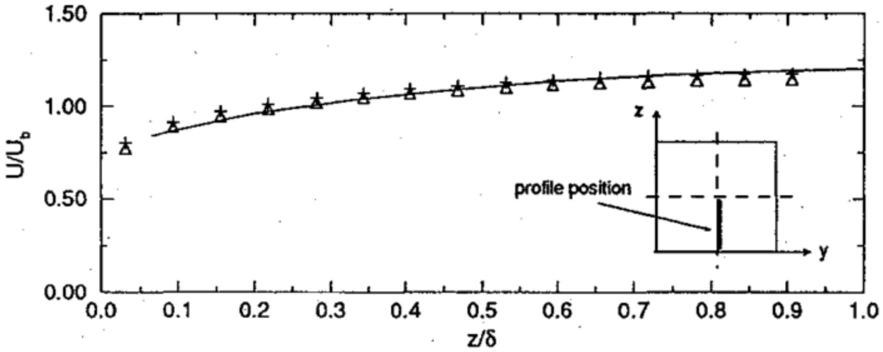

Fig. 3.5 Mean streamwise velocity profile along the mid-plane for square duct flow. Legend: WMLES (+ + +), Approximate boundary condition (Δ Δ Δ), Experimental Data 1 (—), Experimental Data 2 (- - -). Figure obtained from Balaras et al. (1996).

Wall-modelled LES demonstrates its superiority in simulating the rotating channel flow case. The friction Reynolds number of the flow is 200, and the rotation rate is varied between 0.069 to 0.210. The approximate boundary condition failed in predicting the skin friction as noted in Section 3.2.1, while the WMLES is in reasonable agreement with the experimental and the fully resolved LES data. While the prediction of mean velocity and Reynolds stresses is in fairly good agreement for the WMLES for all rotation cases, the results worsened in the region of the stable side of the rotation as the rate of rotation increased.

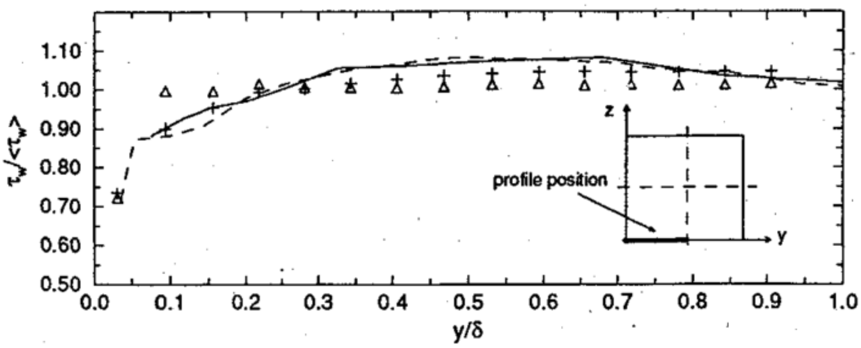

Fig. 3.6 Normalised wall shear stress along the lower wall for square duct flow. Legend is the same as Figure 3.5. Figure obtained from Balaras et al. (1996).

Wall-modelled LES demonstrates its superiority in simulating the rotating channel flow case. The friction Reynolds number of the flow is 200, and the rotation rate is varied between 0.069 to 0.210. The approximate boundary condition failed in predicting the skin friction as noted in Section 3.2.1, while the WMLES is in reasonable agreement with the experimental and the fully resolved LES data. While the prediction of mean velocity and Reynolds stresses is in fairly good agreement for the WMLES for all rotation cases, the results worsened in the region of the stable side of the rotation as the rate of rotation increased.

Cabot (1996) and Diurno et al. (2001) extended the application of the new method to simulate a turbulent flow behind a backwards-facing step of Reynolds number $Re_h = 28,000$ (based on step height and inlet velocity) and with a 4:5 expansion ratio (geometry shown in Figure 3.7)) . Cabot (1996) modified the von Karman constant κ in the mixing – length turbulent equation by creating a model to damp the value of the constant κ dynamically. The paper argued that since Reynolds stresses are already contained in the advection term of the RANS boundary layer equations, the value of the turbulent viscosity will be overpredicted. The approximate boundary condition method is tested as well. Cabot (1996) reported that the approximate boundary condition underpredicts the wall shear stress while the wall-modelled LES without the damping of κ overpredicts the wall shear stress due to excessive turbulent viscosity. Skin friction is moderately overpredicted in the separated region when the WMLES with the dynamically damped von Karman constant is used. All the models did not detect the corner recirculation that is typical of turbulent flow behind a backwards step and produced a bigger backflow than the experiment in the main recirculation zone.

Diurno et al. (2001) argued that for a backwards-facing step flow that is far from local equilibrium, a more advanced turbulence model than the mixing length model should be used in the secondary RANS grid. The one – equation model of Spalart – Allmaras (SA) is chosen, which needs an additional boundary condition at the interface of the secondary grid for the RANS eddy viscosity. The SGS viscosity of the LES

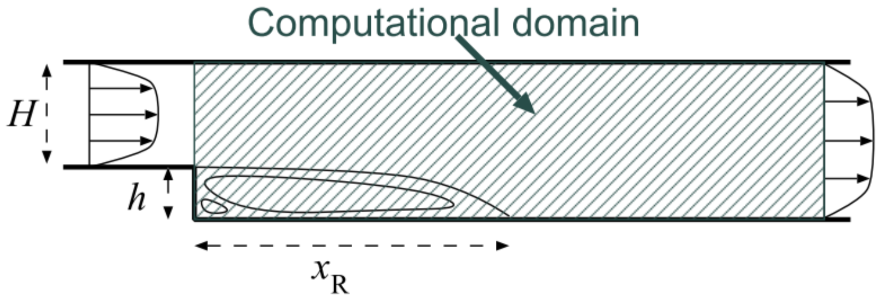

Fig. 3.7 Schematic of the backwards-facing step with the locations of the main and corner recirculations shown. Figure obtained from Diurno et al. (2001).

grid is matched with the RANS turbulent viscosity at the interface. The mixing-length turbulence model is also tested (named algebraic for the case). The reattachment point is reported to be reasonably predicted by the WMLES with the two turbulence models. The other smaller separation bubble is also observed, but this was because the LES mesh is refined in the streamwise and cross-stream directions in the region of the corner recirculation. The WMLES - SA shows slight overprediction of the skin friction after the recirculation zone, while the WMLES – algebraic underpredicted skin friction in the recirculation zone, as seen in Figure 3.8. Furthermore, the two WMLES simulations are in agreement with the streamwise velocity predictions. However, there are discrepancies between the velocity results and the reference data near the wall in the separation bubble. Overall, the WMLES with the Spalart – Allmaras model in the RANS domain has a better agreement with reference data than the WMLES with the mixing-length turbulence model, with just a 10% increase in computational time.

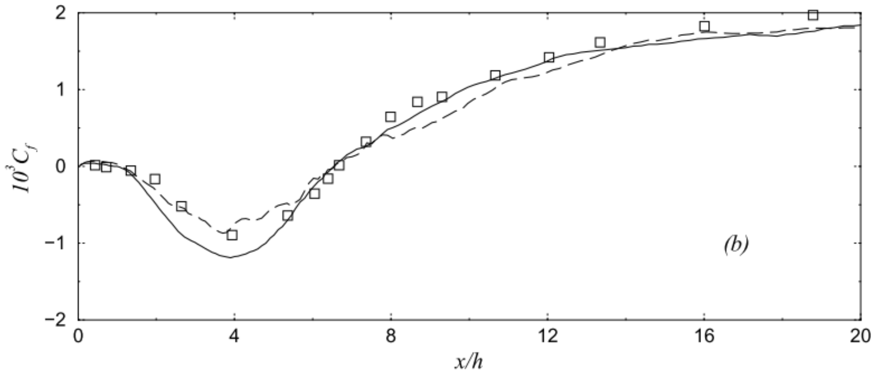

Fig. 3.8 Plot showing results for skin - friction coefficient for backwards-facing step flow. Legend: experiment (□ □ □ □), WMLES – SA (- - - -), WMLES – Algebraic (——). Figure obtained from Diurno et al. (2001).

Wang and Moin (2002) revisited the study of flow over an aerofoil with the WMLES. A different mixing-length model from Balaras et al. (1996) is used, which is defined as:

$$\frac{\nu_t}{\nu} = \kappa y^+ \left[1 - \exp\left(-\left(y^+/A\right)\right)\right]^2, \tag{3.13}$$

where $A = 19$ and $\kappa = 0.4$. The paper used three options for the boundary layer equations in the RANS grid. The normal velocity is set to zero at the wall of the LES grid, while the wall parallel components of velocity are imposed in terms of the streamwise and spanwise wall shear stress $\tau_{w,i}\ (i = 1,3)$. The boundary layer momentum equations to determine the wall shear stress from the RANS domain are defined as:

$$\frac{\partial}{\partial x_n}\left[(\nu + \nu_t)\frac{\partial \langle U_i \rangle}{\partial x_n}\right] = F_i, \quad i = 1,3 \tag{3.14}$$

where

$$F_i = \frac{1}{\rho}\frac{\partial P}{\partial x_i} + \frac{\partial \langle U_i \rangle}{\partial t} + \frac{\partial \langle U_i \rangle \langle U_j \rangle}{\partial x_j}. \tag{3.15}$$

The first option solves the pressure gradient and convection terms, as seen in Equation 3.15. This form returns the original boundary layer formulation of Equation 3.9. Two simpler forms are defined where the convection terms are dropped as $F_i = \frac{1}{\rho}\frac{\partial P}{\partial x_i}$, and the other form where the convection and pressure gradient terms are assumed to be in balance and eliminated as $F_i = 0$. The third form, where there is only the diffusion term in the boundary layer transport equation, is named the equilibrium equation, which is an ordinary differential equation that is straightforward to solve numerically. As seen in Figure 3.9, the wall shear stress is well predicted along the lower side of the aerofoil by the WMLES for $F_i = 0$ and $F_i = \frac{1}{\rho}\frac{\partial P}{\partial x_i}$. The reference data is a wall-resolved LES of the aerofoil blade. Along the upper side, where the flow transitions due to the presence of an adverse pressure gradient, the performance of the two models reduces. This poor performance is not surprising as the equilibrium version of the WMLES did not include the effect of the pressure gradient, while the second model which dropped the convections terms ensured that the momentum equation is not balanced (although the authors suggested that the convection terms are not important after observing the performance).

Simulations are done with all the terms included in the boundary layer equations for WMLES, and the results are shown in Figure 3.10. The von Karman constant κ is set as 0.4, and the WMLES overpredicts and underpredicts the skin friction along the upper and lower surfaces of the aerofoil respectively. The paper argued that since the non-linear convection term in the RANS momentum equations contained Reynolds stresses, the value of skin friction predicted by the WMLES is going to be wrong. Hence, the value of the turbulent eddy viscosity has to be reduced to account for only the unresolved part of the Reynolds stresses. The turbulent viscosity of the RANS grid is matched with the LES SGS viscosity at the interface of the two grids $\langle \nu_t \rangle = \langle \nu_{SGS} \rangle$, while the turbulent viscosity in the internal region of the RANS grid is reduced by dynamically damping the von Karman constant κ. The constant κ is modelled as:

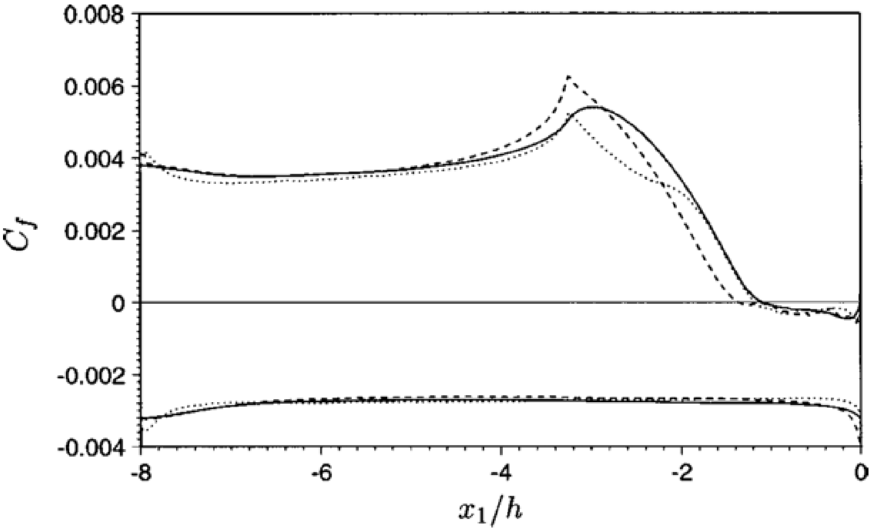

Fig. 3.9 Plot showing the distribution of mean skin friction. Legend: Full LES (·····), WMLES $\left(F_i = \frac{1}{\rho}\frac{\partial P}{\partial x_i}\right)$ (- - - -), WMLES $(F_i = 0)$ (——). Figure obtained from Wang and Moin (2002).

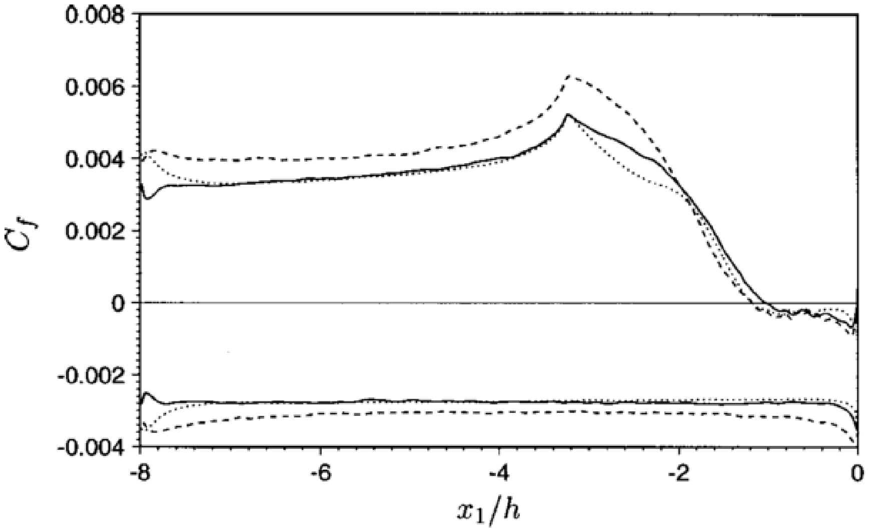

Fig. 3.10 Plot showing the distribution of mean skin friction. Legend: Full LES (·····), WMLES - κ = 0.4 (- - - -), : WMLES - dynamic κ (——). Figure obtained from Wang and Moin (2002).

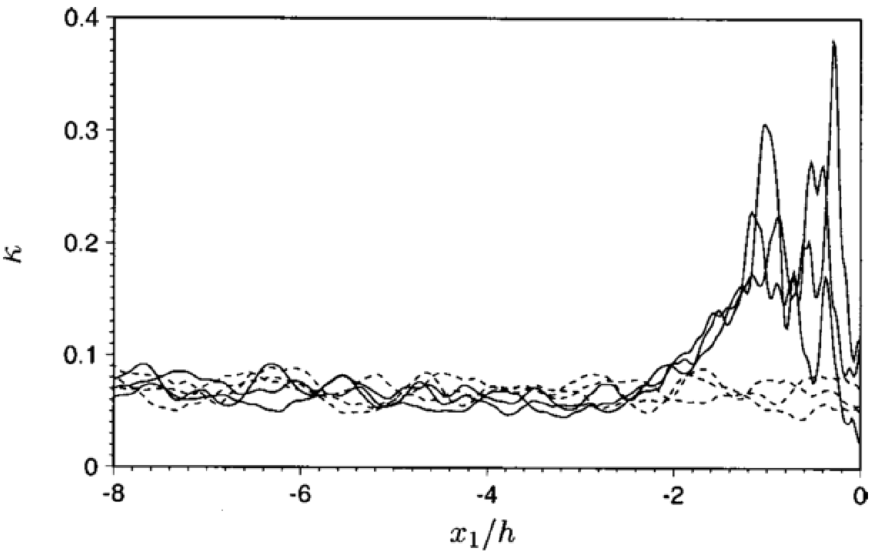

Fig. 3.11 Plot showing the modelled dynamic constant κ for the mixing-length turbulent viscosity at three time instants. Legend: lower side (——), upper side (- - - -). Figure obtained Wang and Moin (2002).

$$\kappa = \langle \nu_{\mathrm{SGS}} \rangle / \left\langle y_w^+ \left(1 - exp\left(-y_w^+/A\right)\right)^2 \right\rangle, \tag{3.16}$$

where the averaging is done in the spanwise direction over the previous 150 time-steps. This formulation forces the drastic reduction of the constant κ in most of the flow region, as seen in Figure 3.11. Although, this formulation means that κ does not change in the wall-normal direction. The dynamic model for the WMLES performs better in predicting the skin friction, as presented in Figure 3.10, although there were still discrepancies between the results and the reference data at the leading edge of the aerofoil.

Kawai and Larsson (2013) used the dynamic approach a simulate a high Reynolds number shock/boundary layer flow ($Re_\delta = 6.1 \times 10^5$). The dynamic damping of the von Karman constant approach developed by Wang and Moin (2002) is also tested. As with Wang and Moin (2002), the authors argued that at the boundary interface between the LES grid and the RANS grid, the value of the RANS turbulent viscosity should be equated with the SGS viscosity at that position. This matching of the viscosities ensures that the velocity gradients for the LES and WMLES at that position would be the same. For the high Reynolds flow, the dynamic method of Wang and Moin (2002) grossly underpredicts the skin friction and consequently, also overestimates the streamwise velocity when scaled with friction velocity. The dynamic method of Wang and Moin (2002) forces the eddy viscosity in the RANS grid to be too low throughout much of the domain of the secondary RANS grid, as shown in Figure 3.12a.

Kawai and Larsson (2013) proposed another dynamic model for the constant κ for the mixing-length turbulence model, which is dependent on the distance from the wall

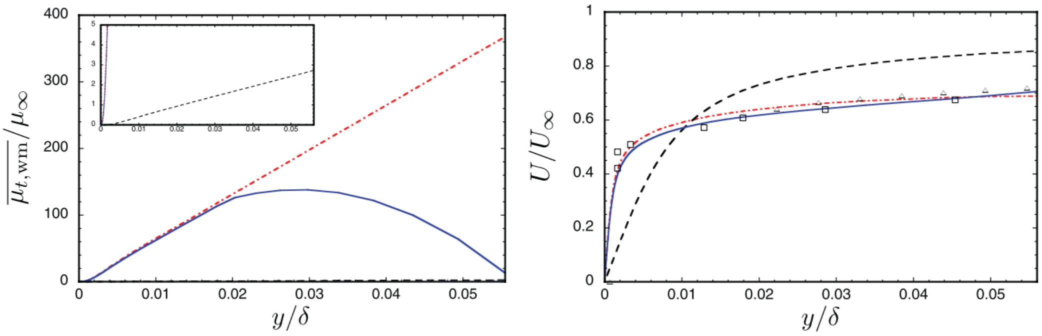

(a) Eddy viscosity of the RANS grid.

(b) Mean streamwise velocity of LES.

Fig. 3.12 Plots showing the computed turbulent viscosity in the RANS grid and the mean streamwise velocity profile in the LES. Legend: WMLES - κ = 0.4 (-·-), WMLES - dynamic κ by Kawai and Larsson (2013)) (—), WMLES - dynamic κ by Wang and Moin (2002) (- - -). The inset in the turbulent viscosity plot is the result predicted by Wang and Moin (2002) because the eddy viscosity predicted is too low. Figures obtained from Kawai and Larsson (2013).

and grid spacing. It is argued that the non – linear spacing of the mesh used for the RANS grid means that the proportion of the resolved and unresolved stresses changes drastically with the wall-normal direction. At the wall, the length of the wall parallel integral scale $L_\uparrow = C_\uparrow y$ (where $C_\uparrow$ is determined by the solver used) is under – resolved, while further from the wall, as the size of the integral length-scale increases, some of the stresses should be resolved. If the ratio of the integral length scale and parallel grid spacing $L_\uparrow/\Delta_\uparrow$ (where $\Delta_\uparrow = \max(\Delta_x, \Delta_z)$) is less than a new constant α (defined as the number of grid points per wavelength), the resolved stress is determined to be negligible. Hence, the dynamic model for the constant κ is defined as:

$$\kappa = 0.41K + \widetilde{\kappa}(1-K)\,, \tag{3.17}$$

where K is defined as:

$$K = \min\left\{\frac{L_{\uparrow,\mathrm{top}}/\Delta_\uparrow - L_\uparrow/\Delta_\uparrow}{L_{\uparrow,\mathrm{top}}/\Delta_\uparrow - \alpha}, 1\right\} = \min\left\{\frac{h-y}{h-y_{\mathrm{crit}}}, 1\right\}, \tag{3.18}$$

$$y_{\mathrm{crit}} = \frac{\alpha}{C_\uparrow}\Delta_\uparrow = \alpha'\Delta_\uparrow, \tag{3.19}$$

where y_{crit} is the position from which the constant κ gets damped, h is the height of the RANS grid or the interface, $\alpha' = 0.48$, and $L_{\uparrow,\mathrm{top}} = C_\uparrow h$ is the integral length-scale at the interface. As seen in Figure 3.12a close to the wall, where the resolved turbulent stresses are expected to be negligible, the turbulent viscosity predicted by Kawai and Larsson (2013) is not damped. As the interface is approached, damping of the constant κ is introduced. Hence, the prediction of the streamwise velocity improves with the new

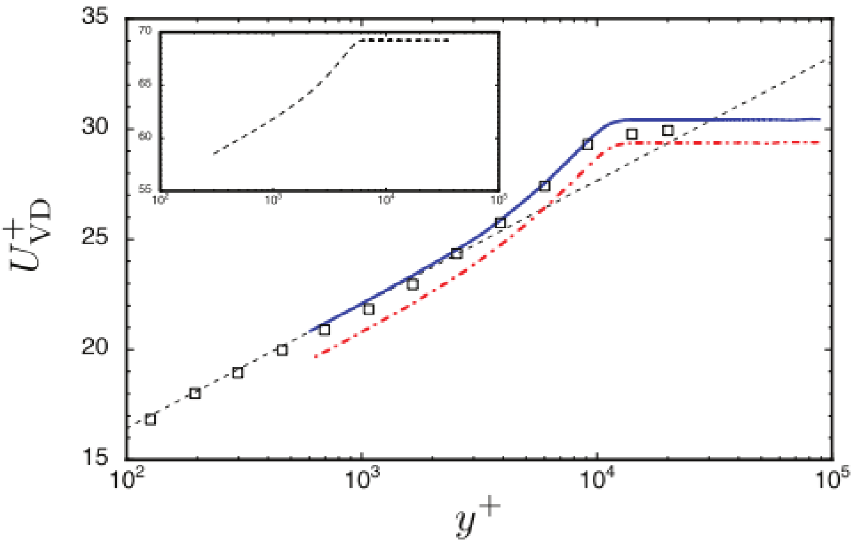

Fig. 3.13 Plot of Streamwise velocity normalised by friction velocity. Legend is the same as Figure 3.12. Figure obtained from Kawai and Larsson (2013).

dynamic modelling method, as seen in Figures 3.12b and 3.13. The log-layer intercept for the WMLES method ($\kappa = 0.41$) of Balaras et al. (1996) is lower, and therefore the velocity profile is slightly underpredicted, while the dynamic κ method of Wang and Moin (2002) greatly overpredicts the reference data.

It is worth noting that for the two dynamic approaches of modelling the mixing-length turbulent model, proper validation of the turbulent viscosity in the RANS grid is not done. Hence, a dynamic approach to modelling the constant κ for a particular flow may fail for another type of flow.

Catalano et al. (2003) computed the flow around a cylinder at three supercritical Reynolds numbers ($Re_D = 5 \times 10^5$, 1×10^6 and 5×10^6). The WMLES is simplified by eliminating the convective terms in the equation, while the turbulent – viscosity in the RANS is obtained using the mixing-length turbulent equation. The distribution of pressure is in good agreement with the experimental data. However, the drag coefficient in the areas that undergo relaminarisation is poorly overpredicted. Skin friction in the front of the cylinder, where there is strong acceleration is also wrongly predicted. The performance of the simplified WMLES gets worse as the Reynolds number is increased. The WMLES is unable to predict the transition of the flow from turbulence to a laminar regime as the wall model always assumes fully developed turbulence.

The poor performance in predicting skin friction in regions where the turbulent fluid undergoes a transition to laminar flow is due to the overprediction of turbulent viscosity by the wall model. The mixing-length model popularly used by researchers in the RANS grid always computes a turbulent viscosity and predicts a boundary layer around the cylinder. Also, the simplification of the boundary layer equations in the

RANS grid done by Catalano et al. (2003) to the WMLES is wrong because eliminating the convection terms ensures that the momentum transport equation is not in balance.

Bodart and Larsson (2012) proposed a solution of correctly predicting the skin friction when a flow underwent transition by incorporating a sensor in the formulation. If the sensor detects relaminarisation, the mixing-length turbulent model is switched off. Quantities at the interface between the RANS grid and the LES grid is examined as it is assumed that the interface will always lie in the log – layer (or away from the viscous sublayer). Consequently, the sensor s_w is defined as:

$$s_w\left(x_w,t\right)=\left(\frac{\left\langle\sqrt{u_i^{\prime}u_i^{\prime}/2}\right\rangle}{\left\langle U_\tau\right\rangle}\right)^2=\frac{\left\langle\rho_w\right\rangle(t)\;k(t)}{\left\langle\tau_w\right\rangle(t)}, \tag{3.20}$$

where the turbulent kinetic energy and friction velocity are exponentially time-averaged. The time-scale $T\left(t\right)$ for the exponential averaging operation is defined from the strain – rate at the interface of the RANS grid as:

$$T\left(t\right)=\left(S_{ij}S_{ij}\right)^{-1/2}, \tag{3.21}$$

and the exponentially weighted averaging of the quantity is defined as:

$$\frac{\mathrm{d}\left\langle f\right\rangle(t)}{\mathrm{d}t}=\frac{f\left(t\right)-\left\langle f\right\rangle(t)}{T}. \tag{3.22}$$

Hence, the value of the sensor s_{tl} should be zero in laminar regions. The authors deduced that there should be a threshold for the sensor s_{lim} where the boundary layer is assumed to be locally laminar. A-priori studies of plane channel flow are done to determine the threshold of the sensor. It is deduced that the turbulent kinetic energy, when normalised by the viscous length scale, is mostly in the range of $2.5\leq s_w\leq 4.0$ for $20\leq y^+\leq 0.2\delta^+$. Hence, the threshold is set as $s_{lim}<2.5$. The approach is tested by simulating a boundary layer flow over a flat plate where transition is induced by localised blowing and suction. The new approach well predicts the point of transition and skin friction. A disadvantage of the approach, observed by Park and Moin (2014), is that the grid region where the transition occurs needs to be refined to predict the wall shear stress accurately.

Duprat et al. (2011) and Chen et al. (2014) simplified the WMLES by eliminating the convection terms in the momentum transport equations. Hence, this enables closed analytical solutions of the wall shear stress to be derived. Since the convection and pressure – gradient terms in the momentum equation are no longer in balance, further modifications have to be made to account for the unphysical process in the boundary layer. Duprat et al. (2011) made changes to the mixing – length turbulent model. While good results are obtained for a plane channel flow and periodic hills simulation with properly tuned coefficients, it is unlikely that the success will be replicated in other flow geometries due to the inconsistency of the convection – pressure balance.

Hickel et al. (2012) did an a-priori study of an adverse pressure gradient boundary layer using several modifications of the momentum equation and the model developed by Duprat et al. (2011). The changes made are the elimination of the convection terms and pressure gradient, hence assuming equilibrium, and another of eliminating just the convection term. All the models underpredict the skin friction, but the performance of the models that eliminates only the convection terms is the worse.

Finally, Larsson et al. (2015) considered a multi-physics problem by validating the wall-modelled LES for flow in a HyShot II scramjet combustor. The ramjet is used for propulsion of aircrafts at Mach numbers over 5. Hence, the supersonic combustion process with an adverse pressure gradient, separation and oblique shock-train propagations poses a challenging case to simulate. Additional transport equations are solved for nine chemical species. The source and scalar variance terms of the transport equations for the chemical species are modelled as zero-flux in the WMLES since there is no prior knowledge of how the terms are to be represented. Also, the convection and pressure gradient terms are dropped from the transport equation of the wall model. For such a complicated process, the trends of pressure and heat flux distributions are adequately predicted, although there are noticeable differences between the numerical results and experimental data for heat transfer. The positive results show the ability to use wall functions in LES for multi-physics problems, though modelling of the extra terms in the additional transport equations remains a challenge.

One common feature that is observed in the wall function for LES in all the papers reviewed apart from Kawai and Larsson (2013) and Larsson et al. (2015) is that the RANS grid is embedded in the first cell of the main LES grid. Consequently, the velocity and the SGS viscosity that are prescribed for the interface boundary of the RANS grid are obtained from the first cell of the LES. While this is acceptable for the numerical wall function approach in RANS calculations, this practice leads to additional errors in the LES method. Since, the first cell of the primary LES grid bypasses the region where viscous forces are dominant, the velocity in the cell is expected to be grossly under-resolved and hence inaccurate. As a result, these errors feed into the wall model computation. This problem leads to the need to either shift the interface of the RANS grid deeper into the outer layer of the LES grid or refine the mesh of the main LES grid close to the wall. This change will provide more accurate information to the interface boundary of the RANS domain, although with slightly increased computation cost.

3.3.1 Velocity Mismatch Problem

A common problem encountered in the development of wall function models for LES or the creation of hybrid RANS/LES methods is the occurrence of the log – layer mismatch (LLM) error. The log – layer mismatch happens when the velocity profile, when scaled by the friction velocity, shifts upwards or downwards of the log – law line. This mismatch of the velocity profile and the log layer leads to errors in predicting the skin friction. It was observed that the nature of the mismatch seemed to have depended on the CFD solver used. Simulation of incompressible flow using a staggered grid seems to produce a downwards shift of the velocity profile, while simulations that are done using a collocated grid produced an upwards shift of the velocity profile (Larsson et al., 2016).

Kawai and Larsson (2011) proposed a solution to eliminating the log-layer mismatch problem for wall function models in LES. If the LES grid below the interface is refined by adding at least 2 points in the wall-normal direction, the normalised velocity profile of the WMLES converges to the log-law profile. For a boundary layer flow with thickness δ, the height h of the RANS grid for the wall function model is assumed at $h \approx 0.2\delta$. In the log-layer, if the length of the integral scale can be defined in each direction as $L_i = C_i y$, the required grid spacing needed to resolve the integral eddies of size L_i is $\Delta x_i \leq L_i/N$, where N is the number of grid points per integral scale. Going by the Nyquist criterion, the number of grid points should be $N \geq 2$. Hence, the LES feeds the RANS grid incorrect information if the number of grid points for the LES grid in the region below the interface is just one. To eliminate the log-layer mismatch problem, the grid spacing for the main LES domain is defined as:

$$\Delta x \leq \frac{C_1}{N}h, \qquad \Delta y \leq \frac{C_2}{N}h, \qquad \Delta z \leq \frac{C_3}{N}h. \tag{3.23}$$

While this condition is already achieved in the wall parallel directions, refining the grid in the wall-normal direction leads to a convergence of the WMLES distribution of velocity to the log-law profile. The authors found that refining the number of points of the LES grid to 2 – 4 below the interface of the two grids is sufficient for wall-modelled LES.

3.3.2 Appraisal of Two-Layer Modelling

The two-layer modelling approach was developed to overcome the limitations of the approximate – boundary condition model in simulating flows with strong pressure gradients or very far from local equilibrium in LES. The TLM or WMLES involves solving boundary layer equations on a separate RANS grid that overlaps the near-wall region of the LES domain. The LES grid supplies instantaneous filtered velocity to the interface between the RANS grid and main LES mesh; it also supplies the wall parallel pressure gradient as a source term to RANS equations. In return, the RANS grid calculates the wall flux of momentum and heat transfer. These wall fluxes are mapped to the wall of the LES domain and act as a source term in the LES transport equations of momentum and heat transport.

A common trend by previous researchers is the embedding of the RANS grid in the first cell of the LES grid. Since the first cell at the wall of the LES is too coarse to resolve any scales of turbulent motion, the underlying subgrid-scale model of the LES cannot accurately compute the velocity at the first grid point. This leads to the LES grid supplying poor information to the interface of the RANS grid. This problem can be solved by either shifting the height of the RANS grid deeper into the LES computational domain where the interface of the RANS grid receives better information or refining the LES mesh below the interface.

Another major issue of the WMLES is the modelling of the turbulent eddy viscosity in the RANS momentum equations. The mixing-length model is the most popular approach in closing the turbulent eddy viscosity for WMLES. It has been argued that the turbulent viscosity of the RANS grid needs to be set equal to the SGS viscosity of the LES to ensure that the velocity gradients of the RANS grid and the main mesh at the interface are consistent. Besides, the turbulent viscosity in the RANS grid must be further damped to account for the resolved component of stresses contained in the convection term of the RANS momentum equation. Unfortunately, the various modifications to the mixing-length turbulent model have not been adequately validated to determine what the actual distribution of the turbulent viscosity in the RANS grid is supposed to be for a given flow configuration.

Some researchers tried to bypass the problem of modifying the mixing length model in the RANS by assuming the convection and pressure gradient are in balance beyond the viscous sublayer of the flow. Hence, the two identified terms are eliminated in the RANS momentum equation with only the diffusion term being solved numerically. While the assumption of the balance of the convection and pressure gradient in the log-layer is valid for flows in local equilibrium, this assumption breaks down for flows with strong pressure gradients, flows with considerable secondary motions or other flows with complex phenomena. Such flows need for all the terms in the boundary layer momentum equations to be solved.

Surprisingly, more advanced turbulent models than the mixing length model for the RANS grid have not been adequately tested in the past. A review of literature shows that only one paper has used a turbulence model other than the mixing length model. Diurno et al. (2001) successfully used the Spalart – Allmaras turbulence model to compute flow behind a backwards-facing step. The Spalart – Allmaras turbulence model solves a transport equation of the eddy viscosity. Diurno et al. (2001) equated the turbulent viscosity of the subgrid to SGS viscosity at the interface of the RANS and LES grids. There is a need to research the applicability of other turbulence models for wall functions in LES. There is an immediate problem of how to prescribe boundary conditions for the turbulent kinetic energy, dissipation rate, Reynolds stress tensor and other turbulent quantities at the interface of the RANS grid. This issue needs to be handled delicately.

Researchers matched the instantaneous filtered velocity of the LES grid to the Reynolds averaged velocity at the interface of the RANS grids. Also, some methods have equated the LES SGS viscosity to the RANS turbulent viscosity. This approach is clearly unphysical as the LES equations solve instantaneous quantities while the RANS grid solves time or ensembled-averaged variables. This unphysical matching has led to the corrections of the computed wall shear stress by the RANS grid via the modification of the mixing length model.

Furthermore, the ideas of Piomelli et al. (1989) are not further tested in two-layer models. At a distance away from the wall, the velocity is not always correlated to the wall shear stress directly below because of the inclination of the eddies close to the wall. Consequently, since the point of the first cell of the LES is mostly beyond the viscous sublayer, there is a need to correctly specify the wall shear stress that will be applied to the LES through means of relaxation of terms or by applying damping functions. This approach could correct the problem of the skin friction been overpredicted as observed in literature.

Finally, all the wall function approaches reviewed applied the computed wall shear stress at the wall of the LES grid. This method means that the wall function corrects only the first cell at the wall of the LES grid. However, to enable the computation of high Reynolds number flows, the resolution of the near-wall grid is reduced. This reduction ensures that the first few cells normal to the wall, not just the first grid point, are under-resolved and need correction. This project explores the idea of modifying the application of the wall function beyond the first node at the wall, which is demonstrated in Paper I.

3.4 New Approaches to Wall Modelling

The two-layer modelling approach for LES requires the need for a second grid to calculate wall fluxes. Since the boundary layer equations of the RANS grid are partial differential equations (PDE), the PDEs require a full grid with neighbour connectivity in the RANS grid to be solved. This requirement adds an extra computational cost that also includes resolving the LES grid. Also, while it is easy to use an additional mesh for an academic test case, this implementation becomes more challenging for unstructured – grid codes (Hickel et al., 2012). Hence, there has been some research to remove the non – linear terms in the boundary layer equations. The typical approach has been to exclude the convection and pressure gradient terms, which reduces the boundary layer equations to an ordinary differential equation. Another method has been to eliminate the convection term and prescribed the pressure gradient from the main LES grid. However, these approaches have obvious limitations, as seen in the previous sections.

Hickel et al. (2012) proposed parametrising the convection term to avoid the need to solve transport equations for the streamwise and spanwise velocity terms in the RANS grid. It is argued that since convection is balanced by the pressure gradient in a boundary layer flow, except in the region of the viscous sublayer, the convection term could be approximated as:

$$\frac{U_j \partial U_i}{\partial x_j} \approx \frac{1}{\rho} \left. \frac{\partial p}{\partial x} \right|_h \times \begin{cases} y/y_{pg} & y < y_{pg} \\ 1 & y \geq y_{pg} \end{cases}, \tag{3.24}$$

where y_{pg} is the position where the streamwise convection starts getting damped by the viscous forces. Below y_{pg}, the convection term decreases linearly to the wall. This approach means that the term y_{pg} has to be prescribed. Another approach proposed by the authors is to fit a shape function to the streamwise convection term. It is assumed that the streamwise convection term is dominant in an unsteady type of boundary layer flow, hence the vertical shape of the derivative $\partial U/\partial x$ could be modelled by the velocity profile. Unfortunately, the two approaches do not give good results in the simulation of an adverse pressure-gradient boundary layer flow.

Yang et al. (2015) also followed the above method of defining a shape function for the velocity profile in the RANS grid. This enabled the inclusion of the non-linear convection term in the boundary layer equations, and the RANS momentum equation is analytically integrated in the wall-normal direction. Various parameters are used in defining the velocity profile at each time step and include the effect of surface roughness. The method is tested with a pseudo-spectral code and a finite-difference code for a plane channel flow. Good results of the distribution of velocity are obtained at a much reduced computational cost compared to standard wall-modelled LES approaches.

Bose and Moin (2014) took a different approach to model the inner layer for the LES. The authors removed the need for a second RANS grid to calculate the wall shear to supply the main LES grid. Instead, the authors use a differential filter to compute slip velocities that act as the boundary condition at the wall for the LES domain. The slip velocities correct the under-resolved near-wall grid of the LES domain and are dynamically computed. The wall boundary condition smoothly reverts to no-slip when the LES grid is refined enough ($\Delta \to 0$) to resolve the flow in the near-wall region adequately or when there is flow separation. The approach is tested for a plane channel flow with various Reynolds numbers and flow around an aerofoil with acceptable results.

Chapter 4

Preliminary Tests in the Development of Wall Function Approaches for Large Eddy Simulation

4.1 Rationale behind the Development of the Numerical Wall Function

The subdomain wall function for large eddy simulation is the main objective of this project. However, before the implementation of the subdomain wall function, the numerical wall function was created in the CFD code OpenFOAM. The development of this method aimed to establish the base code structure upon which the subdomain wall function would be built on. Hence, the numerical wall function is a simpler version of the subdomain wall function. The numerical wall function is similar to the wall-modelled LES with how the computed wall shear stress is specified at the wall of the coarse LES grid to correct the under-resolved first cell at the wall. However, the numerical wall function for LES (NWF), tackles two problems encountered with the two-layer modelling approach of LES. The first challenge is specifying boundary conditions at the interface of the RANS grid. The RANS grid is hereinafter referred to as the subdomain. Previous researchers have coupled the instantaneous quantities of the LES grid to the mean quantities of the RANS subdomain, which is an inconsistent approach. Another challenge that the numerical wall function for LES solves is the specification of more advanced turbulence models than the mixing length model traditionally used in WMLES. Linear eddy viscosity turbulence models solve transport quantities for at least the turbulent kinetic energy and the dissipation rate. These quantities also need their boundary conditions to be specified at the interface of the subdomain. The numerical wall function uses the realizable $k-\varepsilon$ model and the elliptic blending $k-\varepsilon$ model in the RANS subdomain. The solutions developed to tackle the two aforementioned challenges are also adopted by subdomain wall function. Although, the correction of the near-wall LES region using a volumetric source term as done for the subdomain wall function is not implemented for the numerical wall function as the code structure for this function is an elaborate task.

Initial tests of the numerical wall function for LES are done using the mixing length turbulence model in the RANS subdomain with success. The success of the numerical wall function reduces when advanced turbulence models are used. The reduction in performance is due to how the computed wall shear stress is applied to the LES domain in a CFD code. OpenFOAM, which is an open-source unstructured finite volume toolbox, generates too much numerical noise in the first cell of the coarse near-wall LES grid, which leads to the resolved turbulent kinetic energy being overpredicted in the LES grid. The overprediction of the resolved turbulent kinetic energy leads to the LES domain supplying a higher, but incorrect, value of the total turbulent kinetic energy to the interface of the RANS subdomain, thereby inducing errors in the RANS computations. The numerical noise reduces as the near-wall LES grid is refined, but this approach goes against the objective of this project. It is recommended for future work that the numerical wall function is implemented in a different open-source code to investigate whether the effects of the generation of artificial noise is eliminated. Conversely, this problem of numerical noise at the first cell of the coarse LES grid is not encountered with the subdomain wall function, where the application of the wall function is spread over several cells.

Overview of the numerical wall function for LES method with results in a plane channel flow and flow through a 90° pipe bend is provided in Paper III, which is published in the proceedings of the 2018 MACE PGR Conference and appended to this thesis. The following chapter illustrates the complete setup and the initial tests done for the numerical wall function. Several of the strategies implemented by the numerical wall function are adopted by the subdomain wall function.

4.2 Methodology of the Numerical Wall Function

The numerical wall function is similar in approach to the two-layer model for LES. Two regions are solved simultaneously, as shown in Figure 4.1. The main region covers the entire flow domain as the LES grid. The LES domain is purposely designed to be coarse near the wall as not to resolve the turbulent motions. The rest of the LES grid is well refined to resolve the dynamic motions. The RANS grid, also known as the subdomain, overlaps the coarse inner region of the LES grid. The grid resolution of the subdomain is refined in the wall-normal direction to represent the Reynolds-averaged velocity in the RANS domain adequately. The grid refinement in the subdomain enables the RANS grid to compute the wall fluxes of momentum and heat transfer to correct the first cell of the LES grid as is done for the wall-modelled LES. The computed wall fluxes of the RANS subdomain are supplied to the LES grid and act as source terms to the LES momentum transport equations. The RANS subdomain solves the full Reynolds-averaged Navier-Stokes equations, unlike the WMLES that solves the simplified boundary layer equations. Hence, the pressure gradient from the LES is not prescribed in the RANS momentum equations; instead, the pressure gradient term is solved. The top boundary of the RANS subdomain receives information from the LES grid at the same matching location. The consistent exchange of information between the LES and RANS grids at the interface is a focus of the numerical wall function method. Furthermore, the numerical wall function uses suggestions of Kawai and Larsson (2012) to shift the top boundary of the RANS domain to bypass at least the first three cells of the LES grid as seen in Figure 4.1. This design ensures that the top boundary of the subdomain receives better-resolved information from the LES grid unlike when the subdomain is embedded in the first cell at the wall of the LES grid as done for traditional WMLES approaches.

This project tackles the problem of consistently coupling variables at the interface of the RANS and LES grids by performing a partial time average which is inspired by the work of Xiao and Jenny (2012). The partial time average of LES fields of interest is achieved utilising the exponentially weighted time average (EWA). Hence, the exponentially weighted time average is assumed to be equivalent to the Reynolds time average. The exponentially weighted time average of an LES variable φ is computed as:

$$\langle\varphi\rangle^{\mathrm{EWA}} = \int_{-\infty}^{t} \frac{1}{T}\varphi\left(t'\right)\exp^{-(t-t')/T}\,\mathrm{d}t', \tag{4.1}$$

where T is the period of the exponentially weighted average. Using Leibniz' rule for differentiation under an integral, Equation 4.1 is a solution of the following differential

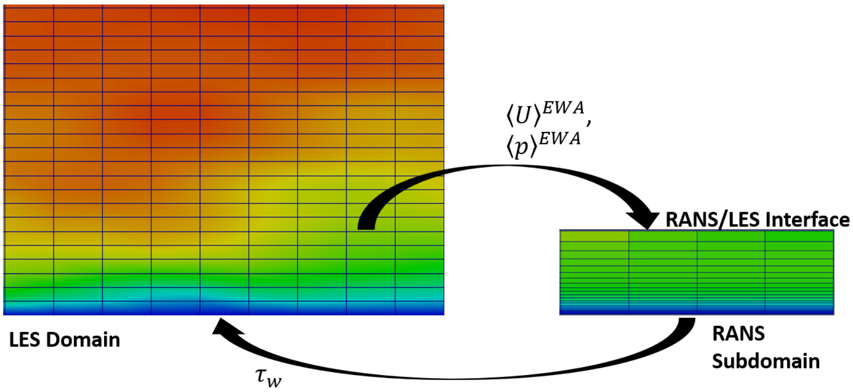

Fig. 4.1 Schematic showing the setup of the numerical wall function for LES and the quantities exchanged between the LES and RANS regions.

equation defined as:

$$\frac{\mathrm{d}\left<\varphi\right>^{\mathrm{EWA}}}{\mathrm{d}t} = \frac{1}{T}\left(\varphi - \left<\varphi\right>^{\mathrm{EWA}}\right). \tag{4.2}$$

The differential equation of Equation (4.2) permits the exponentially weighted time average to be approximated to first order as:

$$\left<\varphi\right>^{\mathrm{EWA}}\Big|_{t_n} = (1-\alpha)\,\varphi|_{t_n} + \alpha\left<\varphi\right>^{\mathrm{EWA}}\Big|_{t_{n-1}}, \tag{4.3}$$

where n is the timestep and $\alpha = 1/(1+\Delta t/T)$. The exponentially weighted time average reduces the required period to initialise the averaging operation compared to the traditional-time average. In addition, the EWA prioritises recent events during a simulation (Tunstall et al., 2017). The computation of the fluctuating velocity with respect to the partial mean filtered velocity results to $u_i'' = \overline{U}_i - \left<\overline{U}_i\right>^{\mathrm{EWA}}$. Correspondingly, the total LES stress tensor is defined as the summation of the resolved fluctuations and the modelled fluctuations as:

$$\tau_{ij} = u_i'' u_j'' + \tau_{ij}^{\mathrm{SGS}}. \tag{4.4}$$

The period T of the EWA is ensured to be sufficiently long enough to enable the assumption that the exponentially weighted average of the filtered velocity field of the LES is approximately equivalent to the Reynolds-averaged velocity field:

$$\left<\overline{U}_i\right>^{\mathrm{EWA}} \approx \left<U_i\right>. \tag{4.5}$$

The total stress tensor $\left<\tau_{ij}\right>^{\mathrm{EWA}}$ of the LES domain is also assumed to be approximately equivalent to the Reynolds stress tensor:

$$\left<\tau_{ij}\right>^{\mathrm{EWA}} \approx \left<u'_i u'_j\right>. \tag{4.6}$$

4.2.1 LES Domain

The filtered momentum transport equations for the LES domain is defined as:

$$\frac{\partial \overline{U}_i}{\partial t} + \frac{\partial \overline{U}_i \overline{U}_j}{\partial x_j} = -\frac{\partial \overline{P}}{\partial x_i} + \nu \frac{\partial}{\partial x_j}\left(\frac{\partial \overline{U}_i}{\partial x_j} + \frac{\partial \overline{U}_j}{\partial x_i}\right) - \frac{\partial \tau_{ij}^r}{\partial x_i} - \frac{\partial}{\partial x_j}\left(\left<\tau_w\right>\right), \tag{4.7}$$

where τ_w is the wall shear stress computed from the RANS subdomain to correct the under-resolved first cell at the wall of the coarse LES grid. The wall shear stress from the RANS is added as a source term to the LES momentum transport equations. The wall shear stress field is finite only at the wall with the rest of the field being zero; hence, the wall shear stress only modifies the velocity field in the first cell at the wall. The diffusive flux at the wall of the LES grid is set to zero to enable the addition of the source term. The SGS stress tensor τ^r_{ij} in Equation 4.7 is computed as:

$$\tau^r_{ij} - \frac{1}{3}\tau_{kk}\delta_{ij} = -2\nu_{\mathrm{SGS}}\overline{S}_{ij}, \tag{4.8}$$

where ν_{SGS} is the subgrid-scale viscosity. Three turbulence models are used for this project: the wall adapting local eddy viscosity model of Nicoud and Ducros (1999), the one-equation eddy viscosity model of Yoshizawa (1986) and the dynamic one-equation eddy viscosity model of Kim and Menon (1995). The SGS turbulence models are represented with the symbols WALE, kEqn and dynamicKEqn, respectively in this project.

4.2.2 RANS Subdomain

The Reynolds-averaged Navier Stokes equation is used in the RANS subdomain, which is defined as:

$$\frac{\partial \langle U_i \rangle}{\partial t} + \frac{\partial \langle U_i \rangle \langle U_j \rangle}{\partial x_j} = -\frac{1}{\rho}\frac{\partial \langle p \rangle}{\partial x_i} + \nu \frac{\partial^2 \langle U_i \rangle}{\partial x_i \partial x_j} - \frac{\partial \langle u'_i u'_j \rangle}{\partial x_j}. \tag{4.9}$$

The subdomain solves the full momentum transport equations, including performing the pressure – velocity coupling of Issa (1986). The subdomain needs quantities of the velocity and pressure fields at the interface to be specified to complete the boundary conditions. This work feeds the exponentially weighted averaged filtered velocity and pressure fields of the LES to the interface of the RANS subdomain.

$$\langle U_i \rangle^{\mathrm{RANS}} = \langle \overline{U}_i \rangle^{\mathrm{EWA}}. \tag{4.10}$$

$$\langle p \rangle^{\mathrm{RANS}} = \langle \overline{p} \rangle^{\mathrm{EWA}}. \tag{4.11}$$

Feeding the exponentially weighted averaged fields to the interface ensures a consistent coupling between the LES and the RANS grids. This approach is the first new element in respect to the traditional wall function methods for LES. Hence, corrections to the turbulent viscosity predicted by the RANS turbulence model is eliminated. Furthermore, the height of the top boundary or interface of the RANS subdomain is designed to bypass at least the first three cells of the coarse near-wall LES grid. This feature ensures that the interface of the RANS subdomain receives better resolved information from the LES domain at this specified height compared to when the RANS subdomain bypasses only the first cell of the LES grid.

This numerical wall function for LES is first tested with the usage of the traditional mixing length in the RANS subdomain. The mixing length turbulence model used is defined as:

$$\nu_t = \kappa y \sqrt{\frac{\tau_w}{\rho}} D, \tag{4.12}$$

with

$$D = \left[1 - \exp\left(-\left(y^+/A\right)\right)\right]^2, \tag{4.13}$$

where $y^+ = y u_\tau / \nu$ is the wall distance in viscous units and $u_\tau = \sqrt{\tau_w/\rho}$ is the friction velocity. The constant A is taken as 17. The following section shows the testing of the numerical method for LES for turbulent flow through plane channels. As the RANS grid is refined in the viscous sublayer of the flow, the wall shear stress is computed linearly as:

$$\tau_w = \nu \frac{\langle U_P \rangle}{y_P}, \tag{4.14}$$

where $\langle U_P \rangle$ and y_P are the cell centred velocity and wall-normal distance at the first cell of the subdomain. In OpenFOAM, Equation 4.14 is evaluated as:

$$\tau_w = 2\nu S_{ij,w} n_{i,w}, \tag{4.15}$$

where $S_{ij,w}$ is the rate of strain tensor at the wall and $n_{i,w}$ is the wall-normal unit vector. The wall shear stress that is computed by the RANS subdomain is mapped to the wall of the LES grid to be the source term in the LES momentum transport equation.

4.3 Testing of Numerical Wall Function for LES in a Plane Channel Flow (RANS Turbulence Model: Mixing Length Model)

The numerical wall function for LES is tested for a plane channel flow. The plane channel is a classic case used to validate numerical models. Two parallel plates bound the plane channel in the cross-stream direction. The channel is assumed to have a huge aspect ratio, and hence, periodic boundary conditions are applied in the spanwise direction. Periodic boundary conditions are also applied in the streamwise direction of the flow as it is assumed that the geometry is long.

Three friction Reynolds numbers are tested for the new methods: Re_τ = 395, 1000 and 5200. The LES domain has the physical dimensions of $2\pi\delta \times 2\delta \times \pi\delta$, where

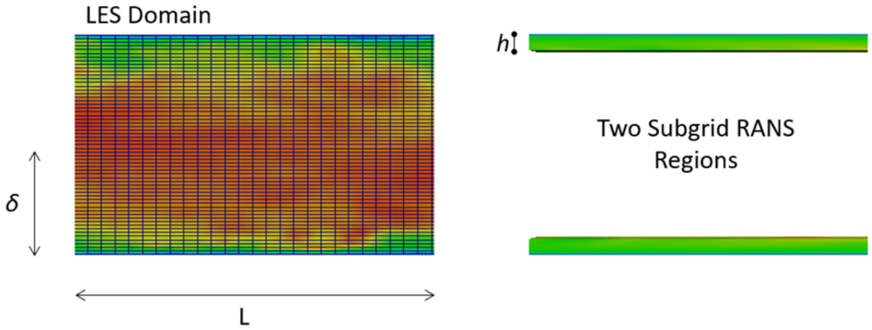

Fig. 4.2 Schematic showing the case setup for the LES for a plane channel flow.

δ is the half channel height. All the LES domains for the test cases employ uniform grids, as seen in Figure 4.2, with the first cell at the wall bypassing the viscous sublayer. The LES grid represents the subgrid-scale turbulence in the domain using the WALE, one-equation and the dynamic one-equation models.

As the channel has two parallel walls in the LES domain, there are two near-wall regions in the LES grid that are under-resolved. Consequently, there are two RANS subdomains for the plane channel flow case with each RANS grid corresponding to a wall of the LES grid. Also, the height of the interface of the RANS subdomains is designed to overlap at least the first three grid points at the wall of the LES domain. The turbulence model used in the RANS subdomain is the mixing length model.

An additional pressure gradient is added to the momentum transport equation of the LES domain to drive the flow in the channel. The same pressure gradient source term is also applied to the momentum transport equations of the two subdomains. The applied pressure gradient matches the friction Reynolds number of the test case. The pressure gradient is defined as:

$$-\frac{dp}{dx} = \frac{\rho Re_\tau^2 \nu^2}{\delta}. \tag{4.16}$$

4.3.1 Results of the $Re_\tau = 395$ Plane Channel Flow

The results of the numerical wall function for LES for the $Re_\tau = 395$ plane channel flow case are compared with the DNS dataset of Moser et al. (1999). The LES grid has $50 \times 60 \times 30$ points with constant spacing in all directions, and the near-wall region being deliberately under-resolved. The RANS subdomain has the dimensions of $2\pi\delta \times 0.141\delta \times \pi\delta$ ensuring that the height of the RANS subdomain is $h = 0.141\delta$. Each of the RANS grids has $50 \times 30 \times 30$ points with the grid biased towards the wall in the wall-normal direction. The RANS grid maintains constant spacing in the streamwise and spanwise directions. Four test cases are done. Three of the test cases use the numerical wall function for LES with either the WALE, one-equation or the dynamic one-equation models in the LES domain, while the RANS grids use the mixing length

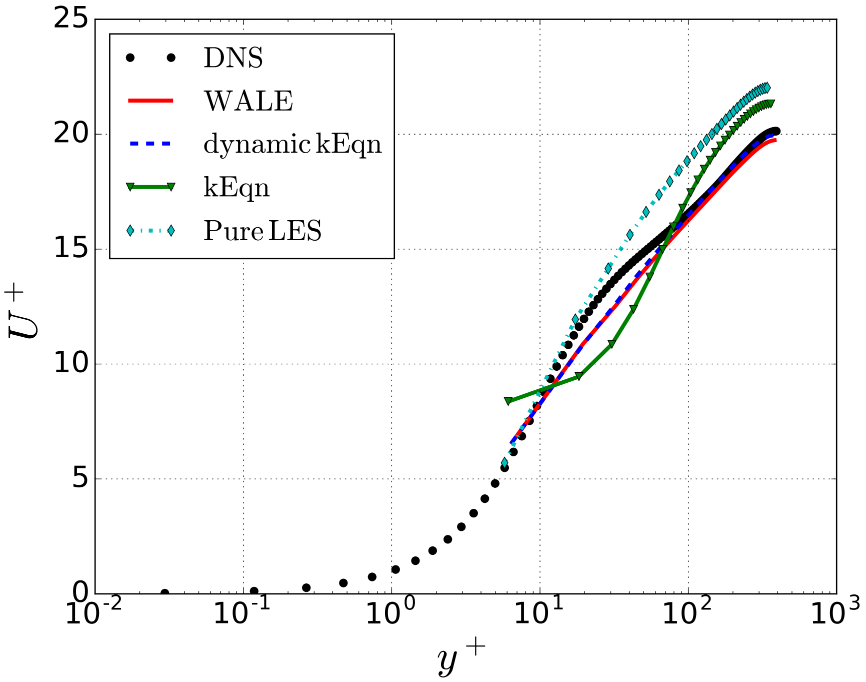

Fig. 4.3 Plot of the mean streamwise velocity in semi-logarithm scale in the LES domain for the $Re_\tau = 395$ plane channel. Legend for the NWF cases represents the SGS turbulence models used in the coarse LES.

turbulence model. The fourth test case is a pure LES done on the same coarse LES grid using the WALE SGS model without the aid of a wall function.

Figure 4.3 shows the profiles of the mean streamwise velocity in the LES domain predicted by the test cases. The cases that use the numerical function with the WALE and the dynamic one-equation models in the LES domain are in good agreement with the reference DNS data. Although, there is a little discrepancy between the two cases and the reference data in the buffer region, which is likely due to the LES grid still being coarse in this area. However, the pure LES case done on the coarse LES grid underpredicts the wall shear stress as the viscous sublayer is not resolved. Thus, the mean velocity profile is overpredicted when scaled with friction velocity. The overprediction of the streamwise velocity illustrates the need for the numerical wall function to supply an accurate wall shear stress to the LES domain to correct the under-resolved near-wall region of the LES grid. Curiously, the numerical wall function fails when the one-equation model (kEqn) is used in the LES domain. This failure may be as a result of the subgrid k in the SGS transport equation not been altered when the wall function is applied, leading to a wrong prediction of the subgrid-scale viscosity. In the subdomain wall function approach, the production of the subgrid k is modified in the one-equation model when the wall function is applied.

The next section shows the performance of the numerical wall function for a higher Reynolds number $Re_\tau = 1000$. The test cases use the same LES grids as the $Re_\tau = 395$

channel flow cases to demonstrate the success of the numerical wall function when the grid resolution of the outer region of the boundary layer is held constant.

4.3.2 Results of the $Re_\tau = 1000$ Plane Channel Flow

The results of the numerical wall function for LES for the $Re_\tau = 1000$ plane channel flow case are compared with the DNS dataset of Lee and Moser (2015). The test cases of the $Re_\tau = 1000$ simulations match those of the $Re_\tau = 395$ cases with the same LES grid of $50 \times 60 \times 30$ points used. Figure 4.4 shows the profiles of the streamwise velocity in the LES domain predicted by the test cases, while Figure 4.5 shows the plot of the streamwise velocity in the RANS subdomains. The streamwise velocity of the wall function cases is normalised by friction velocity produced by the RANS subdomain, while friction velocity of the LES grid is used to normalise the velocity of the pure LES case (there is no RANS subdomain for the pure LES case). As with the lower Reynolds number cases, the numerical wall function cases that used the WALE and dynamic one-equation SGS models accurately predict the mean streamwise velocity. There is a small discrepancy in the velocity-defect region of the channel flow due to the low resolution of the grid in that area. The numerical wall function matches the mean velocity of the LES grid to the RANS grid at the interface, as seen in Figure 4.5. This consistent matching enables the RANS subdomain to accurately compute the RANS profiles and supply the right wall shear stress to the LES grid. The numerical wall function case that uses the one-equation SGS model feeds the wrong velocity information to the interface of the RANS subdomain. Hence, the wall shear stress is inaccurately predicted in the RANS subdomain leading to more errors in the LES domain for the kEqn case. The pure LES case predicts a lower wall shear stress, and consequently a lower friction velocity, for the $Re_\tau = 1000$ case than the $Re_\tau = 395$ case when the same grid is used since the near-wall grid is more poorly under-resolved. Hence, the streamwise velocity profile for the $Re_\tau = 1000$ pure LES case is worse than the $Re_\tau = 395$. Note that the normalised streamwise velocity of the pure LES case appears greatly overpredicted because of the division of the velocity by a much lower value of the friction velocity. This failure for the pure LES cases shows the strength of the numerical wall function in predicting profiles for coarse LES grids.

Figure 4.6 shows the plots of the mean turbulence kinetic energy, the streamwise Reynolds stress, the Reynolds shear stress and the non-normalised Reynolds shear stress. The square of the friction velocity normalises the profiles. The shear stress predicted by the numerical wall function is in excellent agreement with the DNS data excluding the kEqn case. The correct wall shear stress, obtained from the RANS grid, leads to a proper adjustment of the LES shear stress. This trend can clearly be seen in Figure 4.6d, where the shear stress is underpredicted for the pure LES case that has

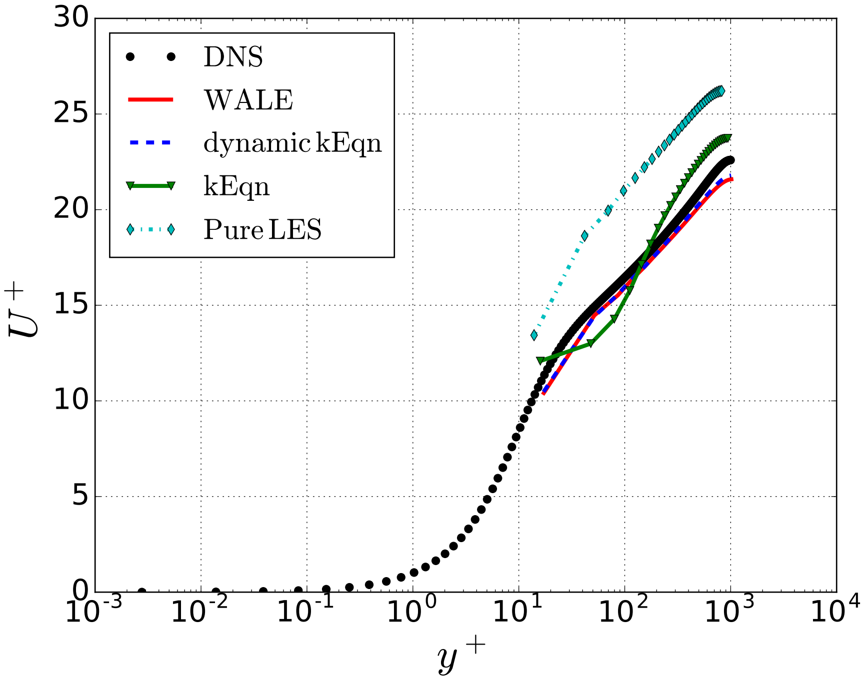

Fig. 4.4 Plot of the mean streamwise velocity in semi-logarithm scale in the LES domain for the $Re_\tau = 1000$ plane channel.

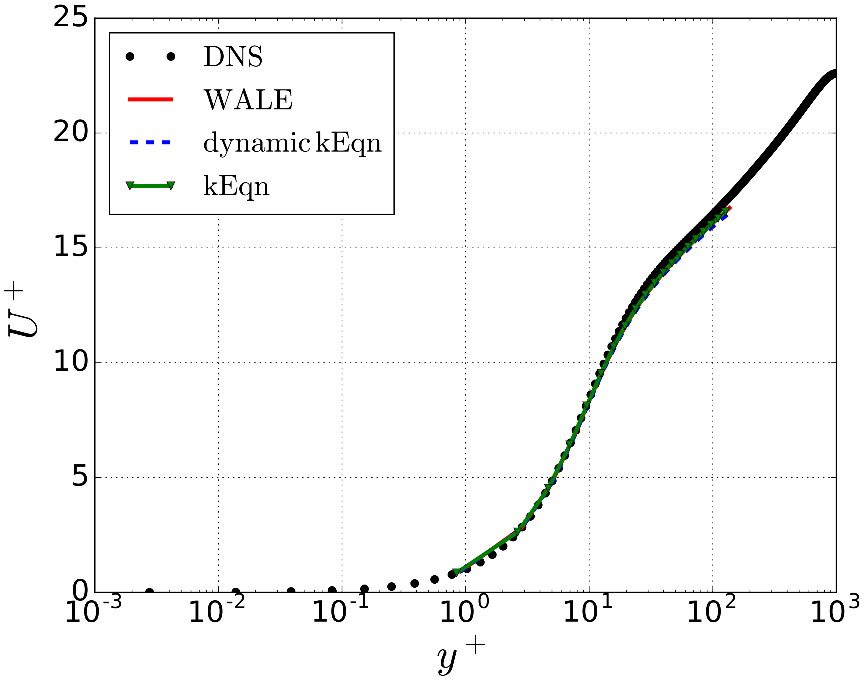

Fig. 4.5 Plot of the mean streamwise velocity in the RANS subdomain for the $Re_\tau = 1000$ plane channel. Legend is the same as Figure 4.4.

no wall shear stress correction. There are wiggles of the shear stress profiles in the near-wall region due to the low resolution of the LES grid. It should be noted that the pure LES case underpredicts the computed wall shear stress. Hence, when the low value mean shear stress of the pure LES case is normalised by the wall shear stress, the resulting normalised mean shear stress is increased and appears to wrongly match the reference data.

The mean turbulent kinetic energy predicted by the numerical wall function exhibit different trends in the near-wall region and the outer-wall region. When the wall distance is less than 100 wall units, the turbulent kinetic energy is over-predicted. The same trend is observed for the pure LES case. This problem is first attributed to the streamwise Reynolds stress being overpredicted near the wall. Small scales dominate the pressure-velocity correlation or the pressure rate of strain in the Reynolds stress transport equation. The pressure-velocity correlation acts to redistribute energy from the streamwise fluctuations to the other components of the Reynolds stress. As these small-scale motions are not captured in the coarse near-wall LES grid (and SGS models are not advanced enough to represent the pressure-rate of strain process), the streamwise Reynolds stress remains too high. This feature leads to the underprediction of the cross-stream Reynolds stress. Furthermore, the OpenFOAM code induces numerical noise for coarse LES grids. This trend can be seen in the overprediction of the turbulent kinetic energy for the pure LES case. The numerical noise leads to the inaccurate overprediction of the resolved turbulent kinetic energy since the near-wall LES grid is too coarse to resolve the flow. The numerical noise is further amplified when the wall function is applied to the wall of the LES grid as a source term in the LES momentum equation, with the wall shear stress source term being active only on the first cell. The failure of the numerical wall function in overpredicting the resolved turbulent kinetic energy in the near-wall LES grid with the application of the wall function in the first cell led to a shift in focus in developing the main objective of this project, which is the subdomain wall function. The subdomain wall function applies a correction to the near-wall LES fields beyond the first cell at the wall. This feature is the innovation of this work, and it leads to the potential generation of numerical noise being spread over several cells, rather than focused on the first cell, like the numerical wall function approach, to reduce the inducement of errors in the wall function application. Details of the subdomain wall function are demonstrated in Paper I. As the interface of the RANS subdomains only receives information of the mean velocity, the overprediction of the near-wall LES turbulent kinetic energy does not affect the RANS computations. Away from the near-wall region, the turbulent kinetic energy predicted by the DNS is well captured by all the LES cases that use the numerical wall function.

Results for the predicted friction Reynolds number are given in Table 4.1. The friction Reynolds number for the numerical wall function cases is calculated from the

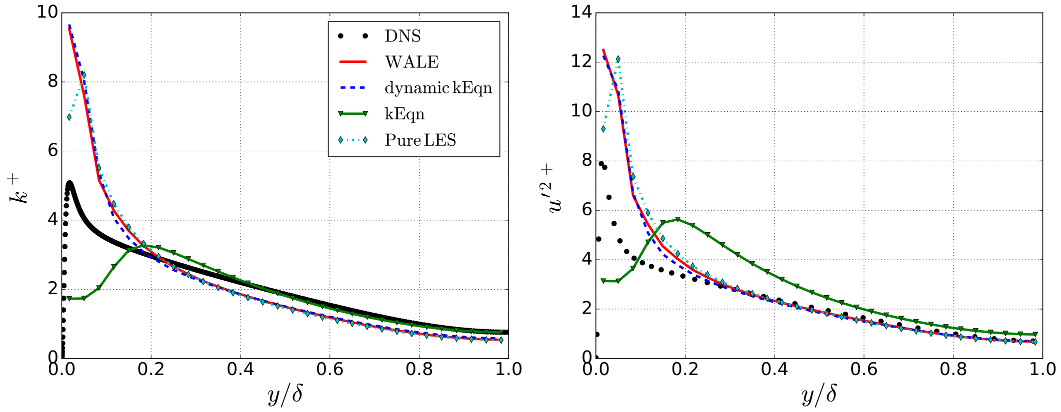

(a) Mean turbulent kinetic energy

(b) Mean streamwise Reynolds stress

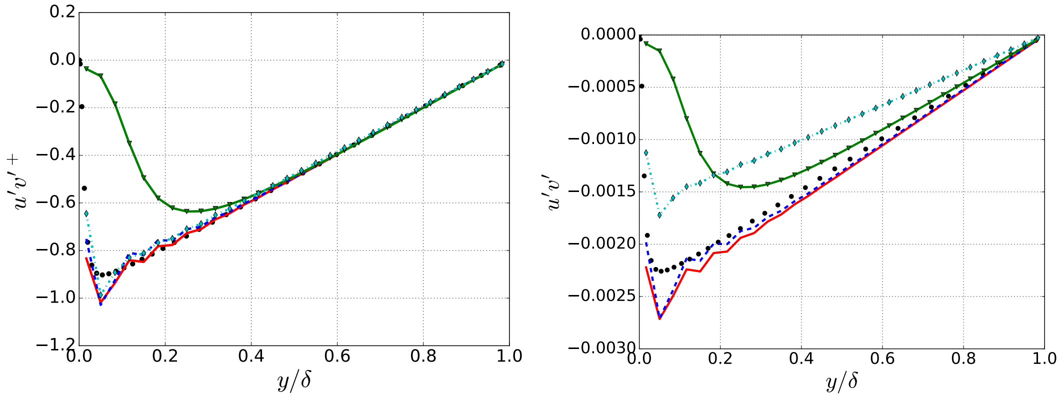

(c) Mean shear stress

(d) Mean shear stress (Non - normalised)

Fig. 4.6 Plots of the mean turbulent kinetic energy and the Reynolds stress components in the LES subdomain for the $Re_\tau = 1000$ plane channel.

Table 4.1 Comparison of Re_τ predictions from the numerical wall function for LES. DNS data from Lee and Moser (2015)

Solution	**Re$_\tau$**
Nominal	1000.00
DNS	1000.51
Numerical wall function (LES-WALE)	1032.61
Numerical wall function (LES-dynamic one-equation) - dynamicKEqn	1027.01
Numerical wall function (LES-one-equation) - kEqn	956.56
Pure LES	832.68

wall shear stress value of the RANS subdomain, while the pure LES case uses the wall shear stress computed from the LES grid. The friction Reynolds number is calculated using the wall shear stress supplied by the RANS subdomain for the numerical wall function cases, while the pure LES case computes the friction Reynolds number value from the wall shear stress obtained from the LES domain. The friction Reynolds number predicted by the numerical wall function for LES cases using the WALE or the dynamic one-equation SGS models (except for the kEqn case) is in better agreement with the

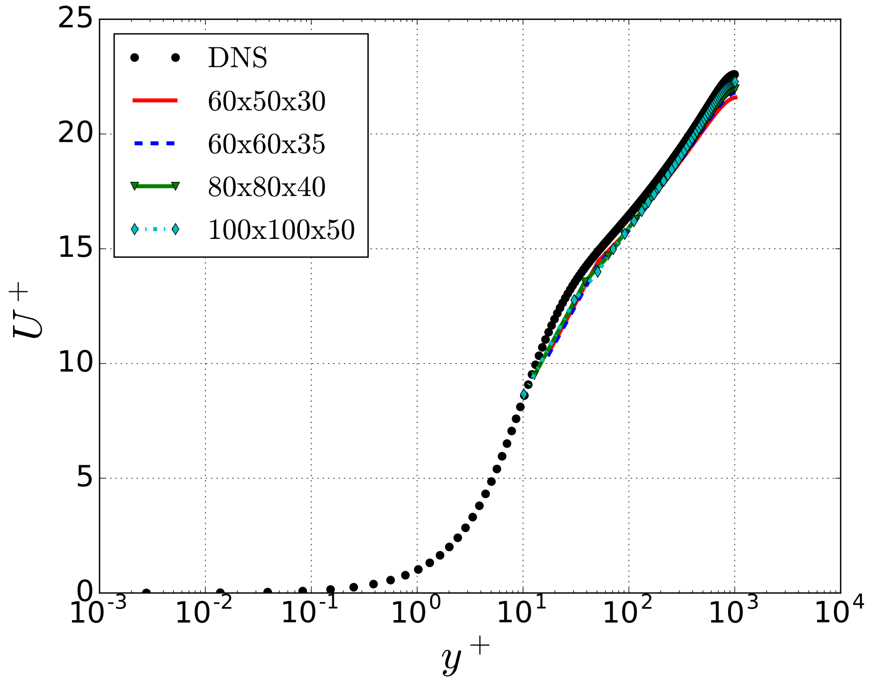

Fig. 4.7 Plot of the mean streamwise velocity in semi-logarithm scale in the LES domain for the different LES grid refinements for the $Re_\tau = 1000$ plane channel.

reference DNS data than the pure LES case for the same grids. The prediction by the numerical wall function is within 3% of the reference value.

4.3.3 Testing the Numerical Wall Function for Different LES Grid Resolutions for the $Re_\tau = 1000$ Plane Channel Flow

The LES grid for the aforementioned test cases used 90,000 points. This section assesses the performance of the numerical wall function when the LES grid is refined in all three spatial directions. Details of the grid points used for the four test cases are shown in Table 4.2. The WALE SGS model models the subgrid-scale turbulence for the four test cases, while the grid resolution for the RANS subdomains remains the same as those of the previous sections.

Table 4.2 Details of the grid refinement for the numerical wall function for LES cases.

Case	Grid	Number of points	Re$_\tau$
1	DNS: $2304 \times 512 \times 2048$	2.4×10^9	1000.51
2	$50 \times 60 \times 30$	90,000	1032.61
3	$60 \times 60 \times 35$	126,000	1028.96
4	$80 \times 80 \times 40$	256,000	1023.68
5	$100 \times 100 \times 50$	500,000	1018.97

Figure 4.7 shows the prediction of the mean streamwise velocity by the different LES grids. All grids are in excellent agreement with the DNS data. However, the finer grids predict the velocity-defect region of the flow than the coarse grids. This agreement demonstrates the ability to use the numerical wall function for much higher Reynolds numbers without significantly increasing the grid resolution.

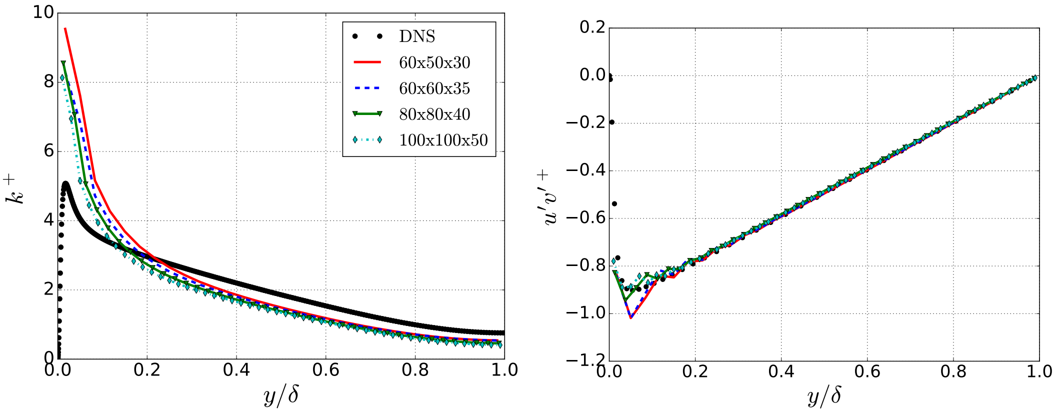

(a) Mean turbulent kinetic energy (b) Mean shear stress

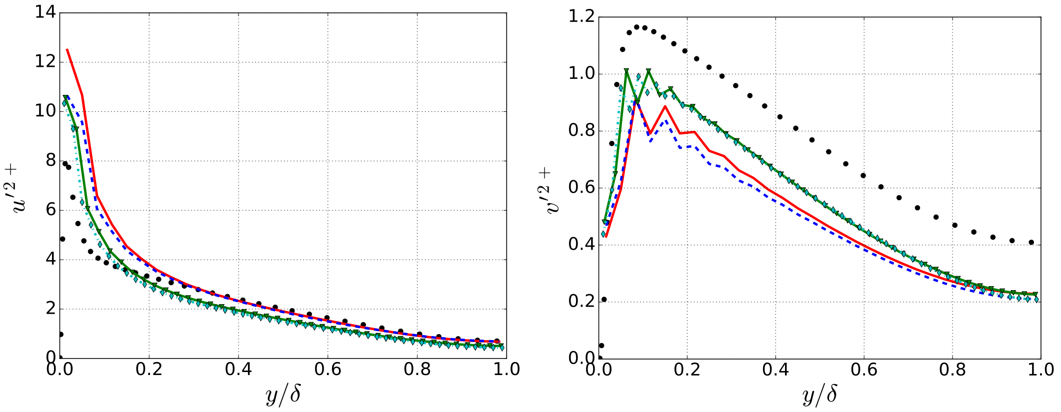

(c) Mean streamwise Reynolds stress (d) Mean cross-stream Reynolds stress

Fig. 4.8 Plots of the mean turbulent kinetic energy and the Reynolds stress components in the LES subdomain for the different LES grid refinements for the $Re_\tau = 1000$ plane channel.

Figure 4.8 shows the graphs of the turbulent kinetic energy and components of the Reynolds stress tensor for the different LES grid sizes. The shear stress predicted by the LES cases compares favourably with the DNS data. The wiggles in the shear stress profiles reduce as the grid is refined in the near-wall region. The overprediction of the turbulent kinetic energy and the streamwise Reynolds stress in the near-wall region by the LES grids is still prominent. However, the overprediction reduces as the near-wall LES grid is refined, indicating the transport of energy from the streamwise Reynolds stress to the other stress components, via the pressure strain term, is becoming more active. However, numerical noise, when the wall function is applied at the wall for the OpenFOAM code, is still dominant. The overprediction of the turbulent kinetic energy in the near-wall region of the LES grid by the numerical wall function wall will become a problem when more advanced turbulence models are used in the RANS subdomain.

4.3.4 Testing the Numerical Wall Function for Different Heights of the Subdomain for the $Re_\tau = 5200$ Plane Channel Flow

The sensitivity of the performance of the numerical wall function for LES to adjusting the height of the subdomain interface is tested. The second aim is to determine the minimum location of the subdomain interface. One of the major points of this project has been to ensure that the subdomain is not embedded in the first cell of the coarse LES grid. This decision is because the first cell at the wall of the LES grid is too coarse to resolve filtered quantities. Hence, information fed to the interface of the subdomain will most likely be incorrect.

The sensitivity study is done for a $Re_\tau = 5200$ plane channel flow case and the results are compared with the DNS data of Lee and Moser (2015). The WALE SGS model is used in the LES domain. The LES grid has $70 \times 60 \times 35$ points with constant spacing in all spatial directions. This uniform spacing means that the wall-normal height of the first cell of the LES grid is 0.0167δ. The heights of the subdomains tested range from 0.0167δ to 0.0833δ, which correspond to the RANS subdomain overlapping 1 LES grid cell to 5 grid cells. Details of the different RANS subdomains tested are shown in Table 4.3.

Table 4.3 Details of setup on the RANS subdomain for the $Re_\tau = 5200$ plane channel flow. This information is for each of the two subdomain grids used for the plane channel flow.

S/N	Subdomain Case	No. of Points	Height	Wall-Normal LES Cells Overlapped
0	DNS	-	N/A	N/A
1	ML1	$70 \times 15 \times 35$	0.0167	1
2	ML2	$70 \times 20 \times 35$	0.0333	2
3	ML3	$70 \times 20 \times 35$	0.05	3
4	ML4	$70 \times 25 \times 35$	0.0667	4
5	ML5	$70 \times 25 \times 35$	0.0833	5

Profiles of the mean streamwise velocity predicted in the LES domain for the different RANS subdomains are shown in Figure 4.9. The velocity profiles for the cases where the RANS subdomain overlap at least the first three cells of the LES grid (ML3, ML4 and ML5) converge and are in good agreement with the DNS data. However, the performance of the numerical wall function reduces when the subdomain overlaps either

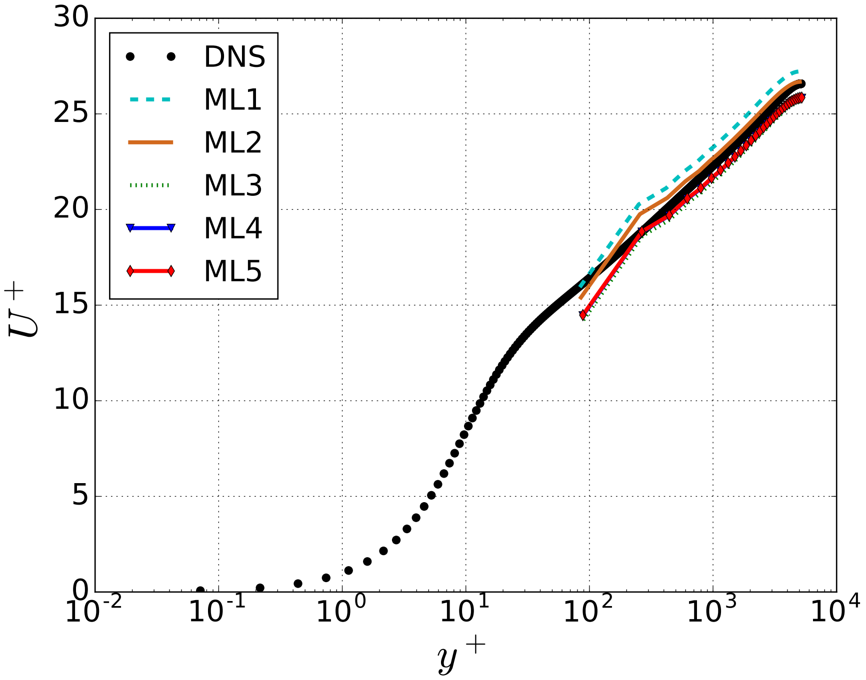

Fig. 4.9 Plot of the mean streamwise velocity in semi-logarithm scale in the LES domain for the different RANS subdomains for the $Re_\tau = 5200$ plane channel.

the first cell or the first two cells. For the ML1 case, the gradient of the velocity profile in the log-layer is different from that reported by the DNS data. This difference illustrates the presence of the log-layer mismatch of the velocity profile when the subdomain is embedded in the first cell of the LES. This problem arises as the filtered velocity of the first cell of the coarse LES grid is incorrect. However, the performance of the LES with the numerical wall function improves when the height of the subdomain is located at the second cell of the LES. Although, the results of ML2 do not converge with ML3, ML4 and ML5. These results demonstrate two critical points. First, the LES grid in the outer region should still be fine enough to resolve the turbulent motions despite using a wall function. Second, the interface between the RANS subdomain and the LES domain should be located in a region where the LES resolves most of the turbulence.

It should be noted that the comparison for the ML3, ML4 and ML5 cases with the DNS data reduces for the first two points around the buffer area. The second point of the coarse LES grid still suffers poor resolution, which suggests the need for a wall function to correct the under-resolved area beyond the first cell at the wall.

In all the test cases done in this section, the algebraic mixing length model is used to compute the turbulent eddy viscosity in the RANS subdomains. This approach is in line with practice by researchers in literature. The next section addresses the challenge of using more advanced turbulence models in the subdomain. The challenge of specifying boundary conditions at the interface for the turbulent kinetic energy, the rate of dissipation and other turbulent quantities are discussed.

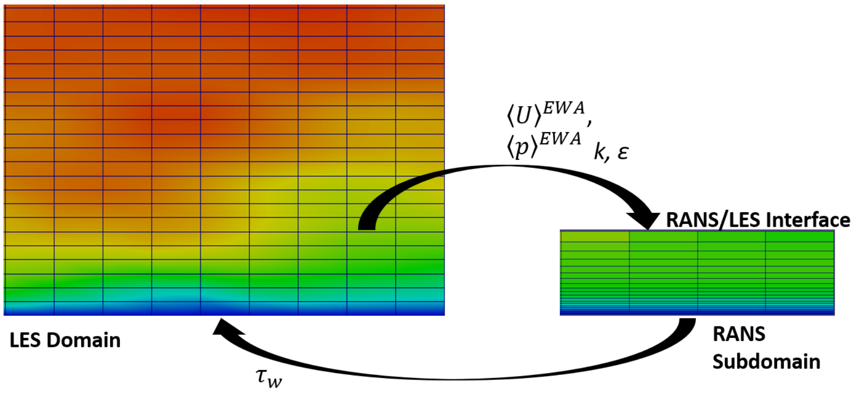

Fig. 4.10 Schematic showing the setup of the numerical wall function for LES and the quantities exchanged the LES and RANS regions for $k-\varepsilon$ models in the subdomain.

4.4 Testing of Numerical Wall Function for LES in a Plane Channel Flow using the $k-\varepsilon$ Model in the RANS Subdomain

In literature, the mixing length turbulence model has been used predominantly for the RANS subdomain for wall-modelled LES. While this is suitable for simple flows, the model becomes limited when complex applications need to be simulated, such as separated flows and flows with secondary motion. One of the challenges of using more advanced turbulence models is the specification of boundary conditions for turbulence quantities at the interface of the subdomain to enable the computation of the transport equations in the RANS subdomain. This project uses the elliptic blending $k-\varepsilon$ model of Billard and Laurence (2012) and the realizable $k-\varepsilon$ model of Shih et al. (1995). The elliptic blending $k-\varepsilon$ model integrates all transported quantities down to the wall without the need for a wall function, while the realizable $k-\varepsilon$ model is implemented as a high-Reynolds number model in OpenFOAM. The proposed boundary conditions at the interface of the RANS subdomain for the turbulent kinetic energy, dissipation rate and other quantities are discussed in subsequent subsections. These boundary conditions, hereinafter referred to as the interface boundary conditions, will be tested in a $Re_\tau = 1000$ plane channel flow case.

4.4.1 Interface Boundary Conditions for Turbulent Kinetic Energy Based Turbulence Models

The $k-\varepsilon$ turbulence model solves transport equations for the turbulent kinetic energy k and the dissipation rate of the turbulent kinetic energy ε. These turbulence models were developed to improve on the features of the mixing length model. The length-scale and velocity-scale are not algebraically calculated or prescribed, which is a useful attribute for more complex turbulent flows. The transport equation for the turbulent kinetic energy can be defined as:

$$\frac{\partial k}{\partial t}+\frac{\partial\left(\langle U_j\rangle k\right)}{\partial x_j}=P-\varepsilon+\frac{\partial}{\partial x_j}\left[\left(\nu+\frac{\nu_t}{\sigma_k}\right)\frac{\partial k}{\partial x_j}\right]. \tag{4.17}$$

The problem of using more advanced turbulence models in the RANS subdomain arises from how to specify the values of the turbulent kinetic energy and the dissipation rate at the interface of the subdomain. As the interface is mostly located in the log-layer region of the flow, the assumption is made that convection of the turbulent kinetic energy is negligible in that region, and the production of turbulence and dissipation terms are in balance. Hence, Equation 4.17 reduces to:

$$\frac{\partial}{\partial x_j}\left[\left(\nu+\frac{\nu_t}{\sigma_k}\right)\frac{\partial k}{\partial x_j}\right]=0. \tag{4.18}$$

An option for specifying the interface boundary condition for the turbulent kinetic energy is by specifying a Neumann condition as:

$$\frac{\mathrm{d}k}{\mathrm{d}n}=0. \tag{4.19}$$

However, specifying the Neumann boundary condition means that the subdomain interface does not receive any information regarding k from the LES region. This problem is remedied by feeding the exponentially weighted time average of the LES stress tensor to the interface of the RANS subdomain to enable stronger coupling of the LES domain and the RANS domain. Hence, the resolved turbulent kinetic energy of the LES domain is obtained by computing the trace of the LES stress tensor. This process establishes a consistent coupling between the turbulent kinetic energy of the RANS and LES grids and becomes the main interface boundary condition for the turbulent kinetic energy for the RANS subdomain. This work defines the interface boundary condition for the turbulent kinetic energy obtained from the LES domain as:

$$\langle k\rangle^{\mathrm{RANS}}=\frac{1}{2}\langle\tau_{ii}\rangle^{\mathrm{EWA}}. \tag{4.20}$$

The interface boundary condition for the dissipation rate is handled differently. If the turbulent eddy viscosity is defined as:

$$\nu_t=C_\mu\frac{k^2}{\varepsilon}=C_\mu^{1/4}k^{1/2}l_m, \tag{4.21}$$

with $u_\tau = C_\mu^{1/4} k^{1/2}$ and $l_m = \kappa y$, then the interface boundary condition for the dissipation rate obtained in the RANS subdomain is defined as:

$$\varepsilon = \frac{u_\tau^3}{\kappa y}. \tag{4.22}$$

As with the original turbulent kinetic energy interface boundary condition, the Dirichlet boundary condition for the dissipation rate of Equation 4.22 is not coupled to the LES region. Stronger coupling between the LES and RANS domains at the interface is obtained by computing the partial mean dissipation rate in the LES grid. The total dissipation rate from the LES region can be decomposed into the sum of the resolved dissipation rate linked with the large eddies of the flow ε_r and the modelled dissipation rate associated with the subgrid scales ε_{SGS}. This decomposition of ε in the LES domain can be written as:

$$\langle\varepsilon\rangle = \langle\varepsilon_r\rangle + \langle\varepsilon_{\text{SGS}}\rangle = 2\nu \left\langle \overline{S}_{ij} \right\rangle \left\langle \overline{S}_{ij} \right\rangle - \left\langle \tau_{ij}^{\text{SGS}} \right\rangle \left\langle \overline{S}_{ij} \right\rangle. \tag{4.23}$$

The value of the total dissipation rate from the LES region is exponentially weighted time-averaged and also mapped to the interface of the subdomain. This procedure forms the second Dirichlet method of specifying the dissipation rate at the subdomain interface.

The elliptic blending $k-\varepsilon$ model solves two additional equations. The additional quantities that are solved are the ratio of the normal Reynolds stress to the turbulent kinetic energy (φ) and the elliptic blending parameter (α). The initial specification of the interface boundary condition is to stipulate the boundary-normal gradient of the two quantities as zero.

$$\frac{\mathrm{d}\varphi}{\mathrm{d}n} = \frac{\mathrm{d}\alpha}{\mathrm{d}n} = 0. \tag{4.24}$$

This condition is initially tested. Although postprocessing of a channel flow DNS database indicates that the assumption that the normal gradient of φ and α in the log-layer is zero is not accurate, this formulation forms the first test for using more advanced turbulence models in the RANS subdomain.

Finally, the elliptic blending does not solve the transport equation for the dissipation rate but the homogeneous dissipation rate ε_h. When the value of the dissipation rate ε is established at the interface either with Equations 4.22 or 4.23, the homogeneous dissipation rate is defined as:

$$\varepsilon_h = \langle\varepsilon\rangle^{\text{EWA}} - \frac{1}{2}\frac{\mathrm{d}^2 k}{\mathrm{d}x_j^2}. \tag{4.25}$$

Initial simulations using Equation 4.25 as the interface boundary condition produced negative values at the interface of the RANS boundary. Hence, the stability of the numerical wall function computations was reduced. This project adopted another approach. Away from the viscous sublayer that is dominated by molecular viscosity, the dissipation rate profile converges to the homogeneous dissipation rate. As the interface of the RANS subdomain is designed to bypass the viscous sublayer of the turbulent flow, the interface boundary for the homogeneous dissipation rate is defined as:

$$\varepsilon_h = \varepsilon^{\mathrm{EWA}}. \tag{4.26}$$

Equation 4.26 is applicable when the subdomain interface location satisfies the condition $y^+ \geq 20$.

Three test cases are done using the $k-\varepsilon$ model in the RANS subdomain for a $Re_\tau = 1000$ plane channel flow. All cases use the strong coupling of the turbulent kinetic energy between the LES and RANS grids by feeding the trace of the LES stress tensor to the interface of the RANS subdomain. Two of the test cases use the elliptic blending $k-\varepsilon$ model in the subdomain. The first elliptic blending $k-\varepsilon$ model NWF case strongly couples the dissipation rate between the two domains, while the second case computes the dissipation rate at the interface from RANS quantities. The third numerical wall function case uses the realizable $k-\varepsilon$ model in the RANS subdomain; the realizable $k-\varepsilon$ model is a high Reynolds number model. The interface of the RANS subdomain needs information of the total turbulent kinetic energy from the LES grid, which is the summation of the resolved and subgrid turbulent kinetic energy. Hence, all three cases use the dynamic one-equation SGS model to represent subgrid-scale stress in the LES grid. The use of the dynamic one-equation model has already been established to produce good results in Section 4.3.2. Details of the test cases are found in Table 4.4.

Figure 4.11 shows the plot of the mean streamwise velocity in the LES and RANS grids. The cases that use the elliptic blending $k-\varepsilon$ model in the subdomain perform the best in predicting the mean streamwise velocity of the DNS. The EB-$k\varepsilon$ (LES: ε) case performs slightly better than the EB-$k\varepsilon$ (RANS: ε) because the LES grid feeds the interface with information of the dissipation rate to the subdomain interface achieving a strong coupling between the RANS and LES simulations.

The case that used the realizable $k-\varepsilon$ model in the RANS subdomain underperforms. This poor performance is a result of the realizable $k-\varepsilon$ model also needing wall functions to be specified for k and ε in the RANS subdomain as it is a high Reynolds number model. Whereas, the elliptic blending $k-\varepsilon$ model integrates all transported quantities down the wall. Also, RANS models use the dissipation rate to generate a length scale to compute the turbulent eddy viscosity. For the realizable $k-\varepsilon$ model, the

Table 4.4 Details of case setups using the two-equation turbulence models in the subdomain.

S/N	Subdomain Turbulence Model	SGS Turbulence Model	Case Name	Epsilon Interface Boundary Type	Friction Reynolds Number
1	Elliptic Blending $k-\varepsilon$	Dynamic one-equation	EB-$k\varepsilon$ (LES: ε)	LES dissipation	1051
2	Elliptic Blending $k-\varepsilon$	Dynamic one-equation	EB-$k\varepsilon$ (RANS: ε)	RANS dissipation	1072
3	Realizable $k-\varepsilon$	Dynamic one-equation	real-$k\varepsilon$ (LES: ε)	LES dissipation	1453

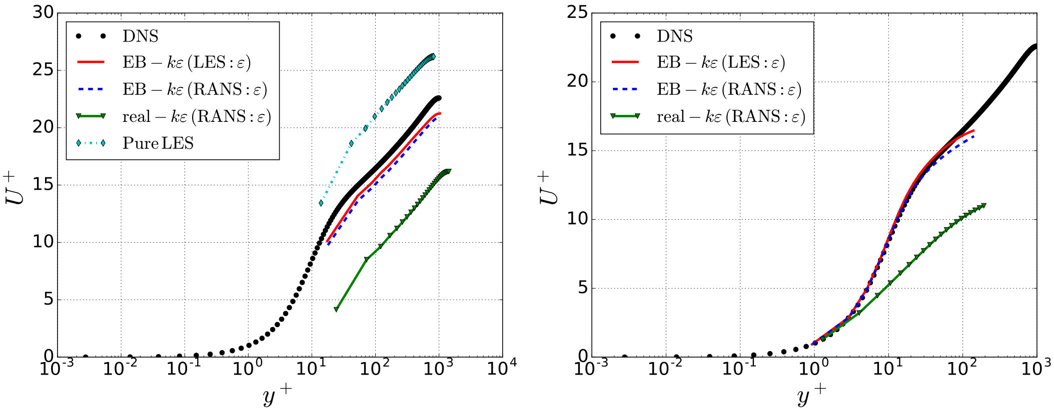

(a) LES domain

(b) RANS domain

Fig. 4.11 Plots of the mean streamwise velocity in viscous units and semi-logarithm scale in the LES and RANS domains for the $Re_\tau = 1000$ plane channel (Incorrect interface boundary specification for v'^2/k and α).

mismatch between the empirical model ε and the DNS ε could have led to additional errors in the RANS subdomain. The difference in results between cases that use the elliptic blending $k-\varepsilon$ model or the realizable $k-\varepsilon$ model in the subdomain illustrates the need for the wall function method to use a low-Reynolds model in the RANS subdomain.

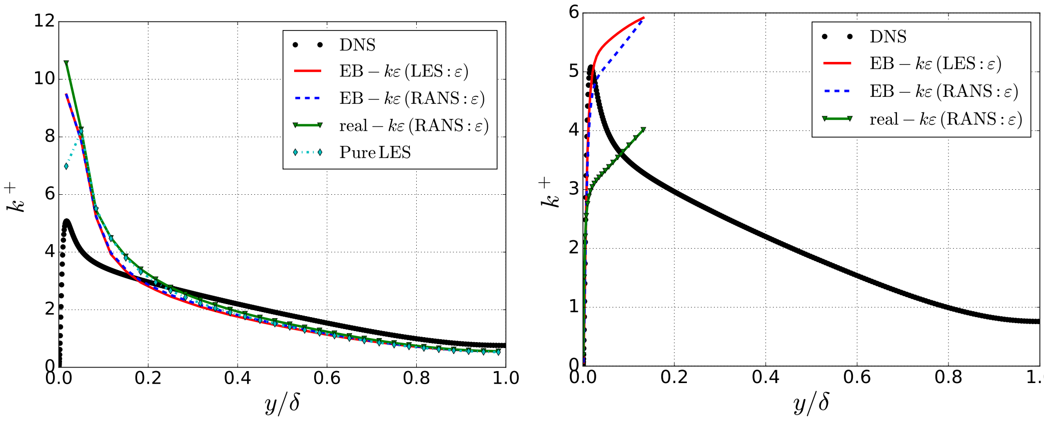

(a) LES domain

(b) RANS domain

Fig. 4.12 Plots of the mean turbulent kinetic energy in viscous units in the LES and RANS domains for the $Re_\tau = 1000$ plane channel (Incorrect interface boundary specification for v'^2/k and α).

Curiously, the overprediction of the turbulent kinetic energy in the near-wall region of the LES grid does not affect the results when coupled to k in the RANS subdomain. Figure 4.12 shows the plots of the mean turbulent kinetic energy in the RANS and LES grids. The interface of the RANS grids receives the overprediction of the turbulent kinetic energy from the LES domain. However, the value of k is rapidly damped away from the interface. This damping leads to the correct prediction of the wall shear stress by the RANS subdomain. The damping of the turbulent kinetic energy is due to the underprediction of the profiles of the ratio of the normal Reynolds stress to k and the elliptic blending parameter α in the RANS subdomain as seen in Figure 4.13. There is a massive difference between φ predicted in the numerical wall function models and the DNS data away from the wall. Also, in the outer layer where the effect of viscous forces is minimal, the elliptic blending parameter converges to the value of one as the dissipation rate tends towards its homogenous value. This trend is not noticed at the interface for the elliptic blending parameter as $\alpha < 1$. The discrepancies in predicting φ and α in the RANS subdomain are due to the wrong prescription of the interface boundary conditions for the two quantities. The wrong prescription of the interface boundary condition for $\varphi = v'^2/k$ and α leads to the inaccurate damping of the turbulent kinetic energy in the RANS subdomain, and consequently the appropriate computation of the wall shear stress. The correct specification of the boundary conditions for v'^2/k and α is addressed in the next section.

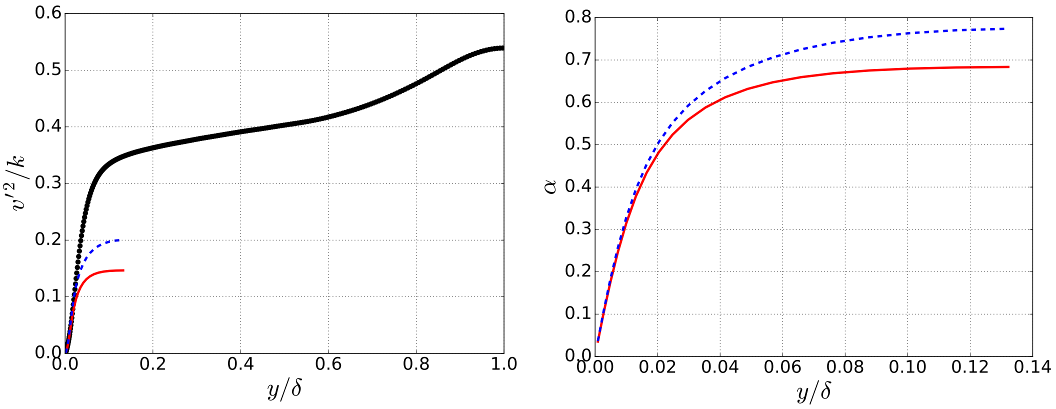

(a) $\varphi = v'^2/k$ (b) α

Fig. 4.13 Plots of the ratio of the normal stress to turbulent kinetic energy and the elliptic blending parameter in the RANS subdomain for the $Re_\tau = 1000$ plane channel (Incorrect interface boundary specification for v'^2/k and α). Legend the same as Figure 4.12.

4.4.2 Interface Boundary Conditions for the Elliptic Blending Parameter and the Ratio of the Normal Reynolds Stress to Turbulent Kinetic Energy

This project makes use of ideas from research by Billard et al. (2015). Adaptive wall functions are developed for all the transported terms and the elliptic term for the elliptic blending $k-\varepsilon$ model. The algebraic correlations developed for v'^2/k and α for the first cell at the wall are adapted to be used at the interface. The ratio of normal Reynolds stress to the turbulent kinetic energy is defined algebraically as:

$$\varphi\left(y^+\right) = \min\left[2/3,\ 0.3077\ln\left(y^+\right)/\ln(10) - 0.2775\right]. \tag{4.27}$$

Equation 4.27 is applicable when the height of the subdomain satisfies the condition $y^+ \geq 30$. There is an upper bound of 2/3 in the algebraic formulation of v'^2/k at the interface to guarantee realizability for φ. The elliptic blending parameter ranges from 0 to 1, and the parameter is computed at the subdomain interface as:

$$\alpha\left(y^+\right) = \left(1 + \left(17/y^+\right)^4/3\right)^{-1}. \tag{4.28}$$

This formulation applies when the interface location satisfies $y^+ \geq 17$.

The correct specification of the interface boundary condition of v'^2/k and α is tested for the EB-$k\varepsilon$ (LES: ε) case in the previous section. Figure 4.14 shows the mean streamwise velocity for the wrong (Wrong interface α and φ) and correct (Correct interface α and φ) specification of v'^2/k and α interface boundary conditions at the subdomain interface, while Figure 4.15 shows mean the plots of the mean turbulent kinetic energy. As expected, the correct specification of the interface boundary conditions ensures that

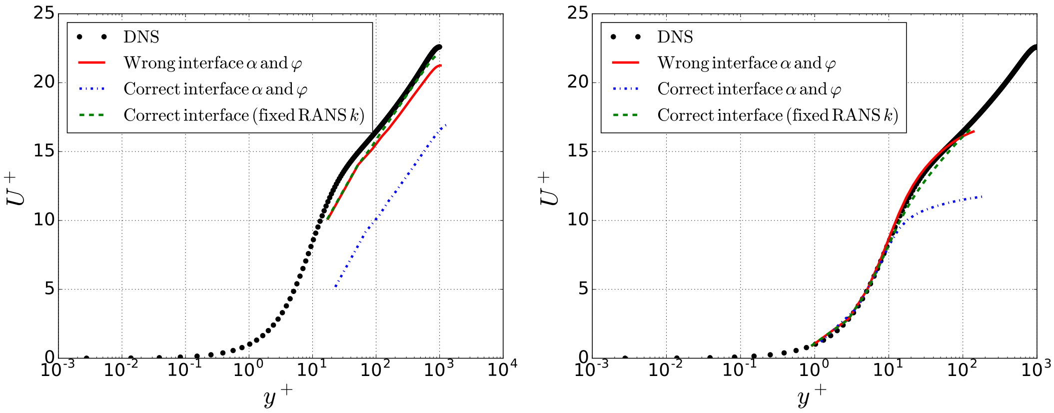

(a) LES domain

(b) RANS domain

Fig. 4.14 Plots of the mean streamwise velocity in viscous units and semi-logarithm scale in the LES and RANS domains for the $Re_\tau = 1000$ plane channel (Correct interface boundary specification for v'^2/k and α).

the overpredicted turbulent kinetic energy in the near-wall region of the LES grid leads to the computation of a much larger wall shear stress in the RANS subdomain. The higher value of the wall shear stress leads to the inaccurate resolution of the velocity profile in the LES grid as seen in Figure 4.14.

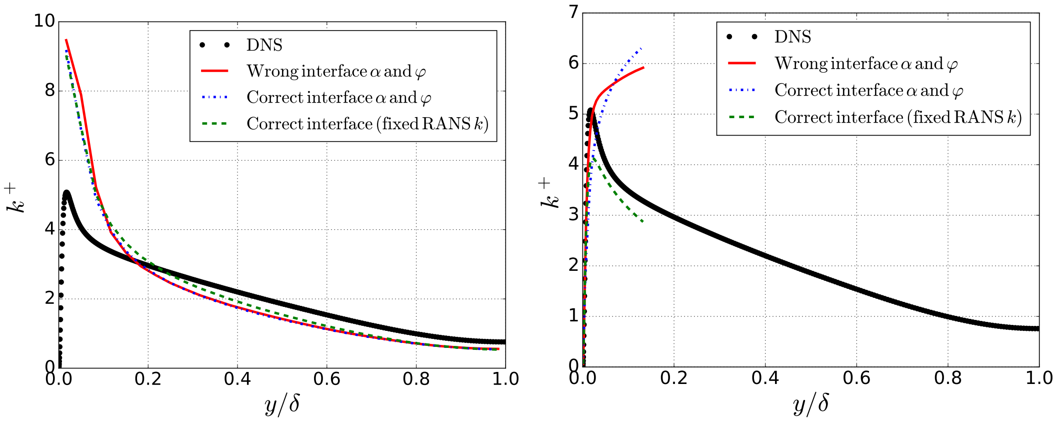

(a) LES domain

(b) RANS domain

Fig. 4.15 Plots of the mean turbulent kinetic energy in viscous units in the LES and RANS domains for the $Re_\tau = 1000$ plane channel (Correct interface boundary specification for v'^2/k and α).

The better specification of the interface boundary conditions for v'^2/k and α leads to a much higher value of the ratio of the normal Reynolds stress to the turbulent kinetic energy at the interface, as shown in Figure 4.16a. However, since the algebraic correlation for v'^2/k is dependent on the wall distance units (which is also dependent on the higher value of the friction velocity), v'^2/k is overpredicted at the interface. The elliptic blending parameter is closer to the value of 1.0, as expected, compared

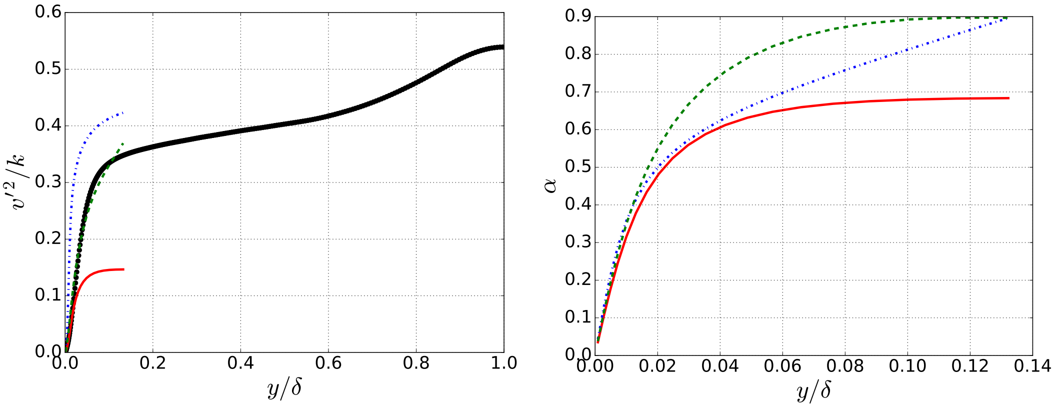

(a) $\varphi = v'^2/k$ (b) α

Fig. 4.16 Plots of the ratio of the normal stress to turbulent kinetic energy and the elliptic blending parameter in the RANS subdomain for the $Re_\tau = 1000$ plane channel (Correct interface boundary specification for v'^2/k and α). Legend the same as Figure 4.12.

to when the interface boundary condition for α is a boundary normal gradient of 0 (Figure 4.16b).

A third case is done (Correct interface (fixed RANS k)), where the value of the turbulent kinetic energy is fixed at the interface of the two RANS subdomains. The value of the turbulent kinetic energy at the interface is determined by a separate RANS precursor simulation of the overall channel domain. Hence, the LES domain does not supply information of the turbulent kinetic energy to the RANS subdomains; the LES domain only supplies information of the partial time-averaged velocity and dissipation fields to the interface. Therefore the performance of the interface boundary conditions for v'^2/k and α using suggestions by Billard et al. (2015) can be investigated when a more accurate value of the turbulent kinetic energy feeds the interface of the RANS subdomains. Figure 4.14 shows that the third case has the best agreement with the DNS profile of the mean streamwise velocity compared to the other two cases. This good agreement is a result of the RANS subdomains mapping an accurate value of the wall shear stress to the LES grid. The LES total turbulent kinetic energy is still overpredicted as seen in Figure 4.15a. However, this overprediction of the LES k does not affect the results as the value of the turbulent kinetic energy at the interface of the RANS grid is fixed. Consequently, the RANS turbulent kinetic energy follows the DNS profile for the third case as seen in Figure 4.15b. Crucially, the third case predicts the correct profile of v'^2/k using Equation 4.27 to determine the value v'^2/k at the interface (Figure 4.16a). Also, the value of the elliptic blending parameter approaches its limit of 1.0 quicker than the other two cases (Figure 4.16b). The correct specification of the turbulent kinetic energy at the subdomain interface leads to the interface boundary conditions defined for the ratio of the normal Reynolds stress to the turbulent kinetic energy and the elliptic blending parameter behaving optimally. Therefore, the subdomain wall function adopts the algebraic correlations of v'^2/k and α as suggested by Billard et al. (2015) as the interface boundary conditions of the two quantities, since the subdomain wall function does not suffer the problem of the generation of numerical noise in the LES grid.

Overprediction of the turbulent kinetic energy in the near-wall region of the LES grid due to numerical noise in the OpenFOAM remains a challenge in the adoption of the numerical wall function for LES in OpenFOAM for more advanced turbulence models in the RANS subdomain. This problem of the numerical noise arising from the application of the computed wall shear stress to the coarse LES grid could probably be solved with the use of another CFD software with a different numerical setup from OpenFOAM to implement the numerical wall function. As earlier noted, the subdomain wall function for LES does not suffer from the problem of excess numerical noise when the wall function is applied, and the approach is covered in Paper I. Crucially, the development of the code structure for the numerical wall function in OpenFOAM was vital in finalising the implementation of the subdomain wall function, which is the main focus of this project, in the open-source code.

The next section tests the numerical wall function for LES for turbulent flow through a 90° pipe bend. The pipe bend is a challenging case as it features the presence of centrifugal force, counter-rotating flow vortices and separation.

4.5 Testing of Numerical Wall Function for LES for a 90° Pipe Bend Geometry

The numerical wall function for large eddy simulation is tested for the pipe bend geometry to investigate how the model predicts the development of counter-rotating vortices due to the imbalance of the radial pressure gradient and centrifugal forces. The ratio of the radius of curvature of the pipe bend to the pipe diameter is $R_c/D = 1.58$. The lower the ratio, the sharper the pipe bend and vice versa. A ratio corresponding to 1.58 corresponds to a sharp bend. The pipe bend geometry is a challenging case as several additional forces are acting on the flow compared to a straight pipe flow. At the entrance of the bend, there is a strong favourable streamwise pressure gradient acting along the inner wall. This streamwise pressure gradient acts to accelerate the fluid near the inner wall at the bend entrance. As the flow moves deeper into the bend, centrifugal forces act to move the core of the high-velocity fluid towards the outer wall. There is a development of a radial pressure gradient to balance the presence of the outward centrifugal forces. This radial pressure gradient moves low momentum fluid near the sides of the pipe wall to the inner wall of the bend. Hence, there is a strong development of secondary motion in the radial direction. The movement of the high and low momentum fluid due to additional forces lead to the formation of counter-rotating vortices, famously known as Dean vortices. These Dean vortices become weak downstream of the bend exit as the flow recovers its earlier axis-symmetric features.

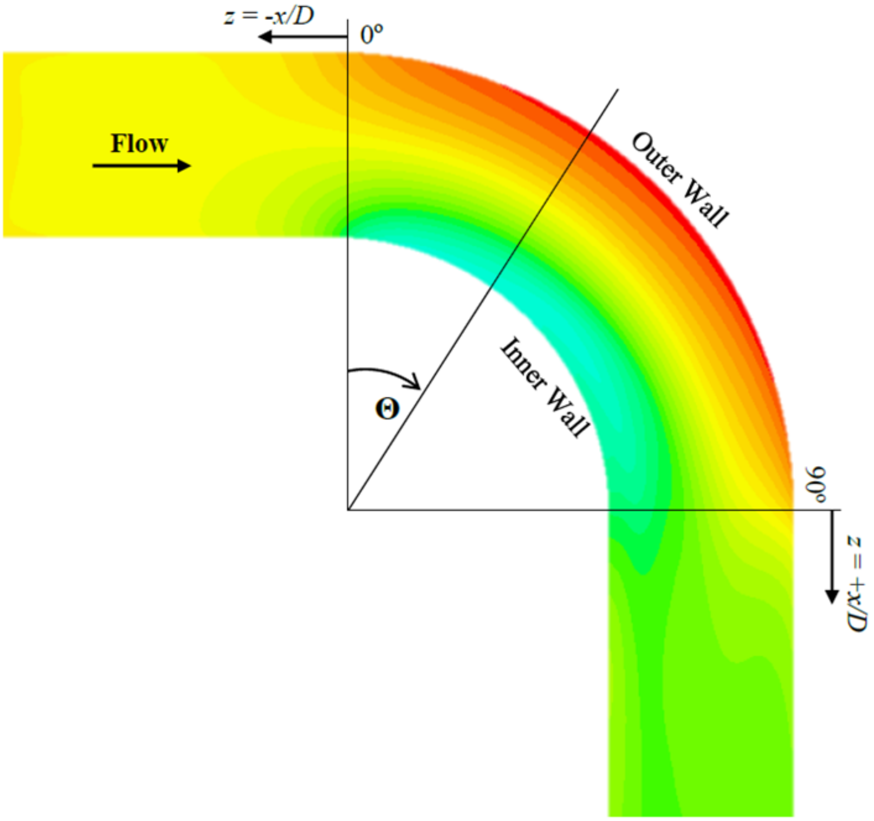

Fig. 4.17 Schematic showing the cross-section of the pipe bend geometry. Features of the pipe are shown.

The complex physics of the pipe bend flow makes the geometry a difficult case to simulate. Typically RANS models fail to capture the flow details along the inner wall of the flow when the Dean vortices become dominant (Iyamabo, 2015). Hence, the pipe bend is a challenging case to test the numerical wall function for LES. Results are validated with the wall-resolved LES of Holgate (2018) and the experimental data of Kalpakli and Örlü (2013). The wall-resolved LES used 19 million grid points.

4.5.1 Case Details for the Pipe Bend Geometry

The bulk Reynolds number based on the pipe diameter of all the cases is 34,000. The LES grid is coarse in the near-wall region, as shown in Figure 4.18. Hence, the LES grid for the numerical wall function cases does not resolve the viscous sublayer. The number of points used in the LES grid is 540,125, which represents 5% of the grid points used in the wall-resolved LES case. A cross-sectional face has 3625 nodes with the length of the pipe split into 149 identical cross-section planes.

The RANS subdomain, as shown in Figure 4.19, is refined in the near-wall region to resolve the viscous sublayer of the flow. The height of the interface of the subdomain

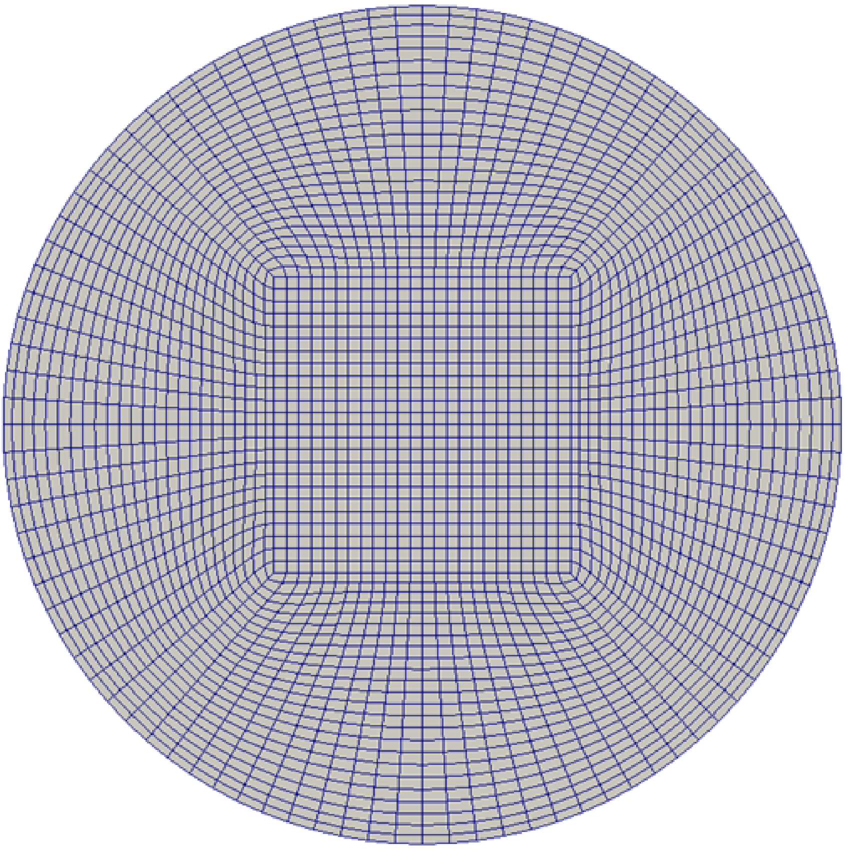

Fig. 4.18 Cross-section of the computation grid used in the LES domain.

is set to 0.05D to ensure that the subdomain bypasses at least the first three nodes of the LES grid. The RANS grid uses 131,274 points with 1,326 points in the cross-sectional plane. The RANS grid is split into 99 grid planes along the streamwise direction of the pipe.

The LES domain for the numerical wall function cases uses the dynamic one-equation SGS model to represent the subgrid-scale turbulence. A separate precursor simulation is run to generate mean inlet boundary conditions for the straight pipe. The precursor simulation is done on a straight pipe with the same diameter as the pipe bend. Periodic boundary conditions are prescribed in the streamwise direction, and the elliptic blending $k-\varepsilon$ model computes the eddy-viscosity in the straight pipe. The precursor simulation generates fully developed profiles of the velocity vector, the isotropic Reynolds stress and the rate of dissipation. The synthetic eddy method of Skillen et al. (2016) utilises the mean profiles to instigate a fluctuating instantaneous velocity at the inlet of the LES grid.

The fully developed profiles from the precursor simulation are also mapped to the inlet boundary of the subdomain. The subdomain uses the elliptic blending $k-\varepsilon$ model and the mixing length turbulence models to compute the RANS equations. The case that used the elliptic blending $k-\varepsilon$ model in the subdomain prescribes the improved

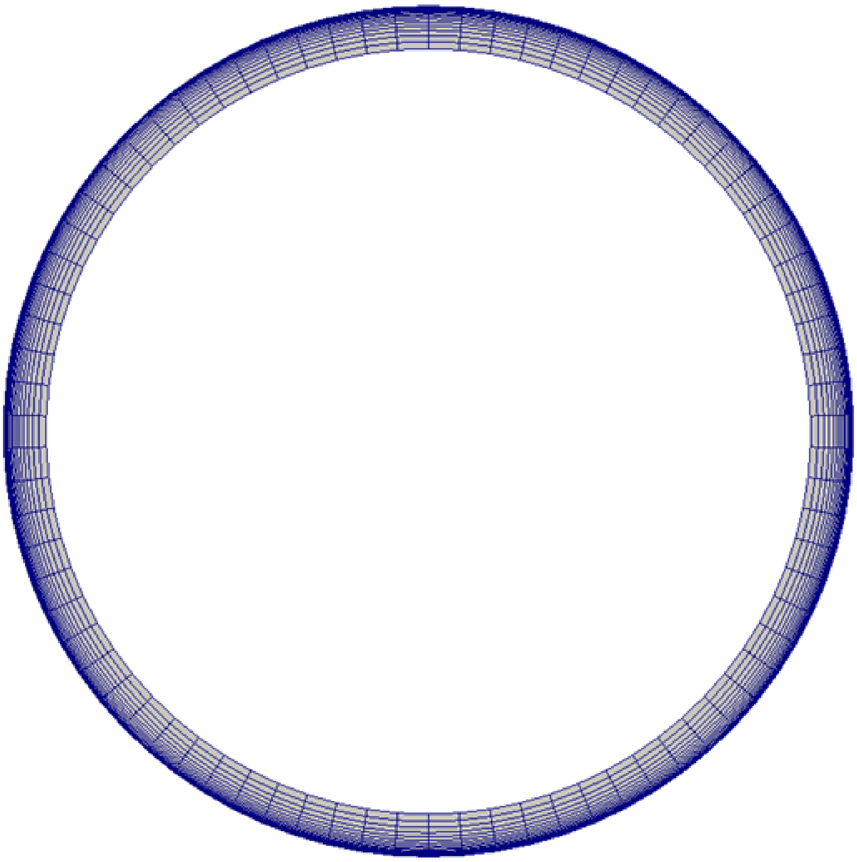

Fig. 4.19 Cross-section of the computation grid used in the LES domain.

interface boundary conditions for v'^2/k and the elliptic blending parameter α. The usage of the improved boundary conditions for v'^2/k and α ensures that the computed wall shear stress by the RANS subdomain is not artificiality suppressed as is done with the zero-gradient implementation of the two quantities. The interface boundary conditions for k and ε are obtained from the equivalent partial mean LES quantities.

An additional case is studied using the detached eddy simulation (DES) for the same geometry. The aim is to compare the performance of the numerical wall function with the most popular hybrid RANS/LES method in industry. The variant of DES used for the study is the improved delayed detached eddy simulation with $k-\omega$ SST turbulence model (IDDES) of Gritskevich et al. (2011). The IDDES case uses 1.2 million grid points with the near-wall region refined to resolve the viscous sublayer. Details of the test cases are shown in Table 4.5.

Figure 4.20 shows the plot of the mean streamwise velocity along the symmetry line between the inner and outer walls immediately downstream of the bend exit at $z = 0.67D$. Position -1.0 is taken as the inner wall, while position 1.0 indicates the outer wall on all plots. Figure 4.20 also compares the results with the experimental data. At $z = 0.67D$, the numerical wall function and the IDDES results are in good agreement with the reference experimental and numerical data. However, the plot of the numerical

Table 4.5 Details of test cases for flow through a 90° pipe bend.

S/N	Subdomain Turbulence Model	SGS Turbulence Model	Case Name	Total Cells LES
1	N/A	Dynamic Smagorinsky	Wall-Resolved LES	19,000,000
2	Mixing Length	Dynamic one-equation	NWF-Mixing Length	540,125
3	Elliptic Blending $k-\varepsilon$	Dynamic one-equation	NWF-EB $k-\varepsilon$	540,125
4	N/A	IDDES: $k-\omega$ - SST	IDDES: $k-\omega$ - SST	1,200,000

wall function with the mixing length does not capture the shift of the high momentum fluid towards the outer wall.

Figure 4.21 shows the evolution of the mean streamwise velocity through the pipe bend, while Figure 4.22 shows the evolution of the cross-stream velocity. Upstream of the bend entrance, the streamwise velocity profile is symmetric; the cross-stream velocity is negligible, and the results from the numerical simulations perform well in predicting the reference data. At the bend entrance of $\Theta = 0°$, there is a strong favourable streamwise pressure gradient that accelerates the fluid near the inner wall. The acceleration of the flow leads to the deceleration of the cross-stream velocity due to continuity. All models capture these trends.

From the bend middle plane ($\Theta = 45°$), secondary flow begins to appear, which act to move high momentum fluid towards the plane-centre of the flow. On the outer wall, there is very good agreement of the velocity gradient between all the models. This agreement continues throughout the bend along the outer wall.

Along the inner wall, the IDDES (blue) produces a much too thick and slower boundary layer. On the contrary, the numerical wall function with the elliptic blending $k-\varepsilon$ (red) predicts higher velocities at $\Theta = 45°$ but is still in excellent agreement with the reference data. The overprediction of the wall shear stress at the inner wall is more pronounced for the NWF-Mixing Length case (green) than the NWF-EB $k-\varepsilon$ case. The numerical wall function case with the elliptic blending $k-\varepsilon$ model in the subdomain predicts the cross-stream velocity well at $\Theta = 45°$ favourably; the IDDES case overpredicts the cross-stream velocity at the inner wall for this location. Hence, the high momentum fluid moves deeper into the core of the flow than the wall-resolved LES for the IDDES case.

At the plane position $\Theta = 67.5°$, the counter-rotating vortices become more dominant, and the cross-stream velocity increases near the inner wall. The NWF-EB $k-\varepsilon$ is in good agreement with the reference cross-stream velocity profile, while the IDDES

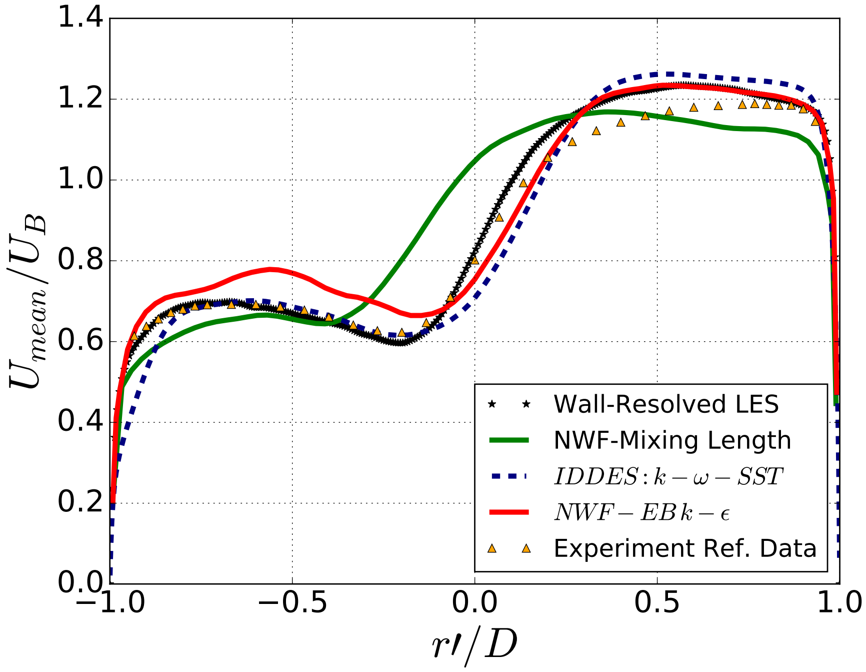

Fig. 4.20 Plot of the mean streamwise velocity at $z = 0.67D$ along the symmetry line between the inner and outer walls.

and the NWF-Mixing Length overpredict and underpredict the secondary velocity near the inner wall respectively. Therefore, the NWF-EB $k-\varepsilon$ case captures the trend of the streamwise velocity around the inner wall while the other two test cases deviate markedly from the reference data.

At the bend exit $\Theta = 90°$, the performance of the IDDES and NWF-Mixing Length reduces further, while the NWF-EB $k-\varepsilon$ still captures the streamwise and cross-stream velocity profiles. The boundary layer around the inner wall for the IDDES case slows down to the point that flow reversal is observed at the bend exit. Although the NWF-Mixing Length case mostly yields similar near-wall gradients as the reference data, the case largely underestimates the asymmetry of the streamwise velocities in the core, due to underprediction of the secondary motion. Downstream of the bend exit, as the effect of the counter-rotating vortices reduces, the underperforming test cases recover the profiles of the streamwise velocity.

The numerical wall function with elliptic blending $k-\varepsilon$ model in the RANS subdomain performs well for most of the flow in predicting the velocity profiles. This good performance is due to the utilisation of a more advanced turbulence model in the RANS subdomain than the mixing length model to predict the wall shear stress for the complex pipe bend flow.

Figure 4.23 shows the plots of the mean turbulent kinetic energy at different sections of the pipe between the inner and outer walls. As earlier identified from the channel flow cases, numerical noise in the OpenFOAM code when the wall function is applied

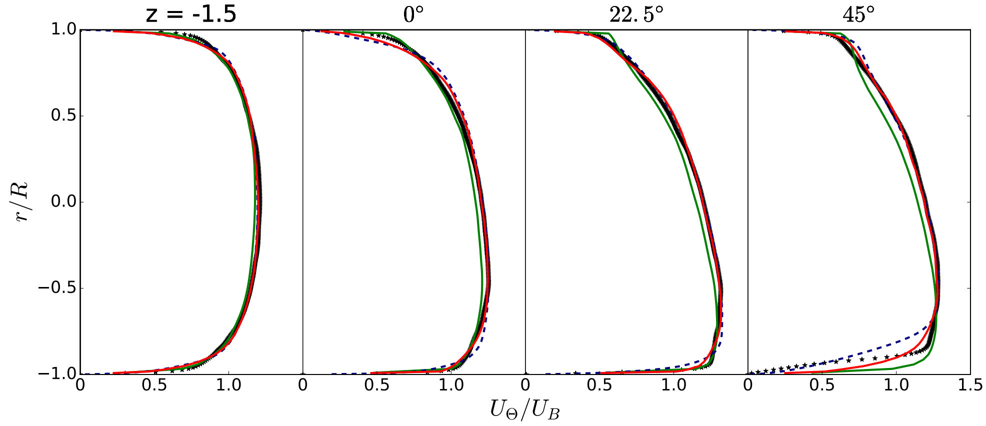

(a) $z = -1.5x/D$, 0°, 22.5° and 45°

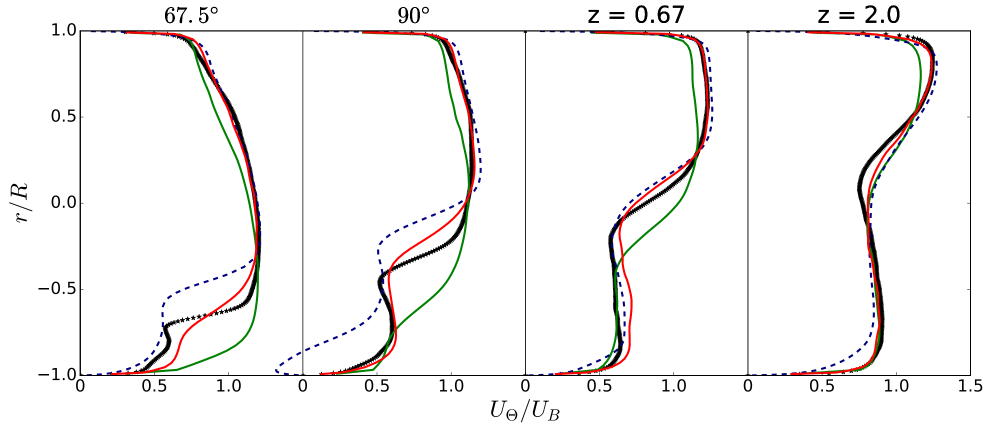

(b) 67.5°, 90°, $z = 0.67x/D$ and $z = 2.0x/D$

Fig. 4.21 Plots of the mean streamwise velocity through the pipe along the symmetry line between the inner and outer walls. Profiles are from different sections through the pipe. Legend is the same as Figure 4.20.

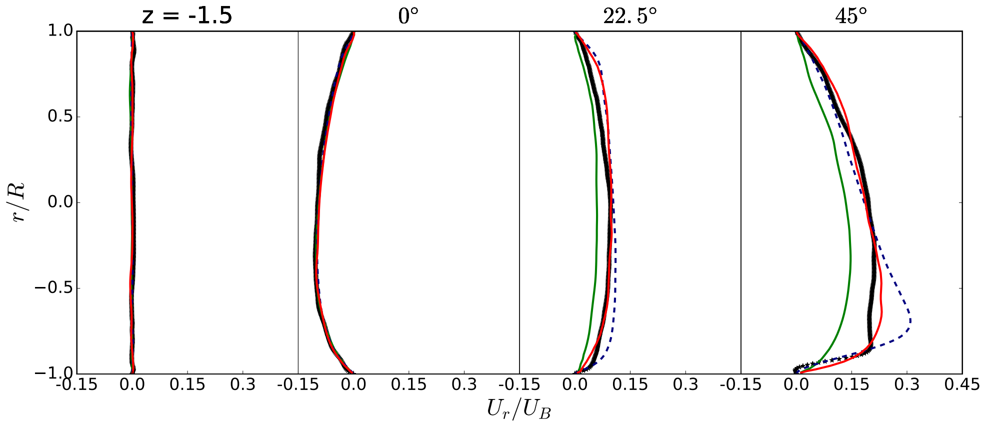

(a) $z = -1.5x/D$, 0°, 22.5° and 45°

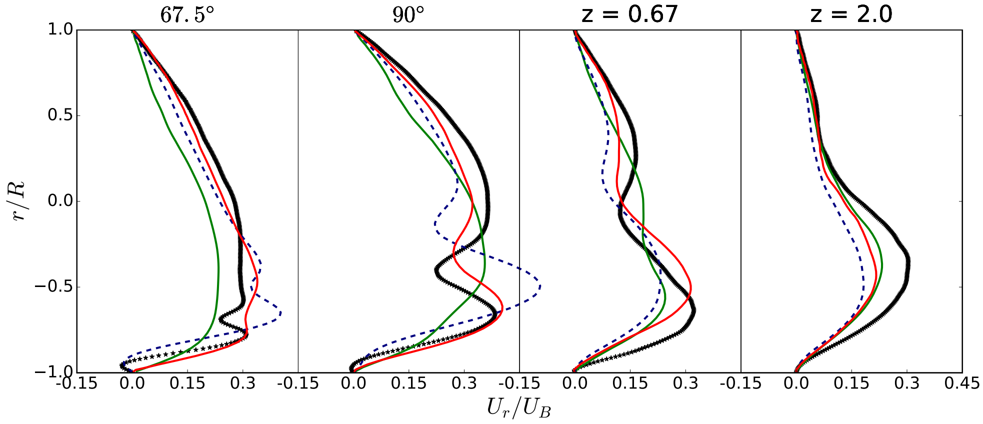

(b) 67.5°, 90°, $z = 0.67x/D$ and $z = 2.0x/D$

Fig. 4.22 Plots of the mean cross-stream velocity through the pipe along the symmetry line between the inner and outer walls. Profiles are from different sections through the pipe. Legend is the same as Figure 4.20.

leads to the overprediction of the turbulent kinetic energy near the wall for the numerical wall function cases. This overprediction has the effect of increasing the wall shear stress computed by the RANS subdomain for the NWF-EB $k-\varepsilon$ case. However, the turbulent kinetic energy decayed at the matching location of the interface of the RANS subdomain for most of the pipe bend. Thereby the negative effect of the overprediction of the turbulent kinetic energy is reduced for the NWF-EB $k-\varepsilon$ case.

4.5.2 Case Details for the Pipe Bend Geometry

Approaches of wall modelled LES have made the assumption that the pressure gradient balances the convection term in the Navier-Stokes equations, and hence, the two terms can be removed when solving the RANS boundary layer momentum equations. Only the diffusion term is solved in the RANS subdomain to supply the wall shear stress to correct the under-resolved near-wall LES grid. Figure 4.24 shows the balance of the convection and the pressure gradient through the pipe bend. The balance between the

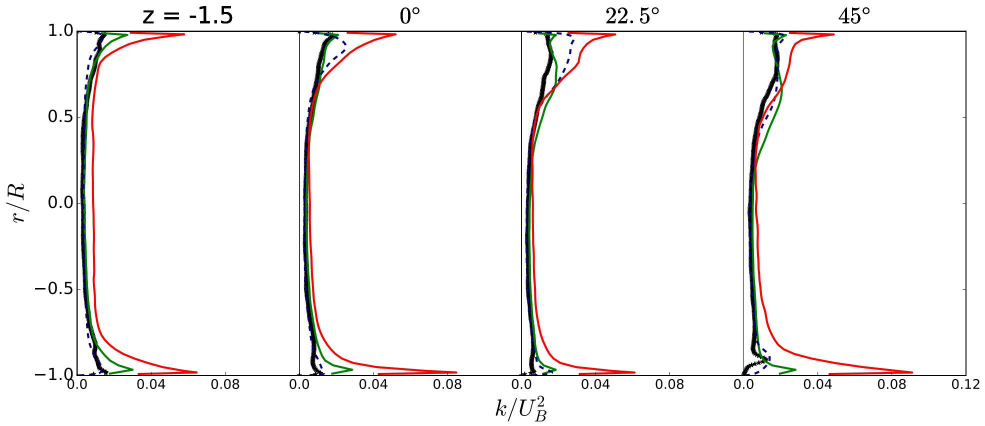

(a) $z = -1.5x/D$, 0°, 22.5° and 45°

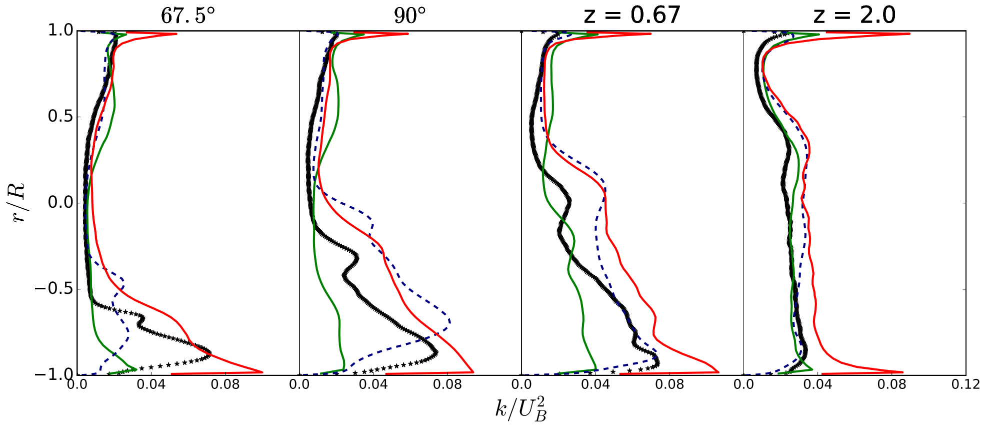

(b) 67.5°, 90°, $z = 0.67x/D$ and $z = 2.0x/D$

Fig. 4.23 Plots of the mean turbulent kinetic energy through the pipe along the symmetry line between the inner and outer walls. Legend is the same as Figure 4.20.

two terms is zero for much of the flow domain. However, when the counter-rotating vortices become dominant in the second half of the bend, the convection term becomes much higher than the pressure gradient term. Hence, the assumption of solving only the diffusion term in the RANS subdomain fails for the pipe bend case.

4.6 Appraisal of the Numerical Wall Function for LES

The numerical wall function for LES made improvements over the classic wall-modelled LES. Both approaches use the RANS subdomain to compute a wall shear stress to correct the under-resolved coarse near-wall LES grid. Essentially, the numerical wall function establishes a consistent coupling of quantities at the interface between the LES and RANS grids through the exponentially weighted time average. This consistent coupling enables the computation of the full Reynolds-averaged Navier-Stokes equation in the subdomain without the need of introducing corrections. Also, the exponentially weighted time average enables the calculation of the turbulent kinetic energy and the

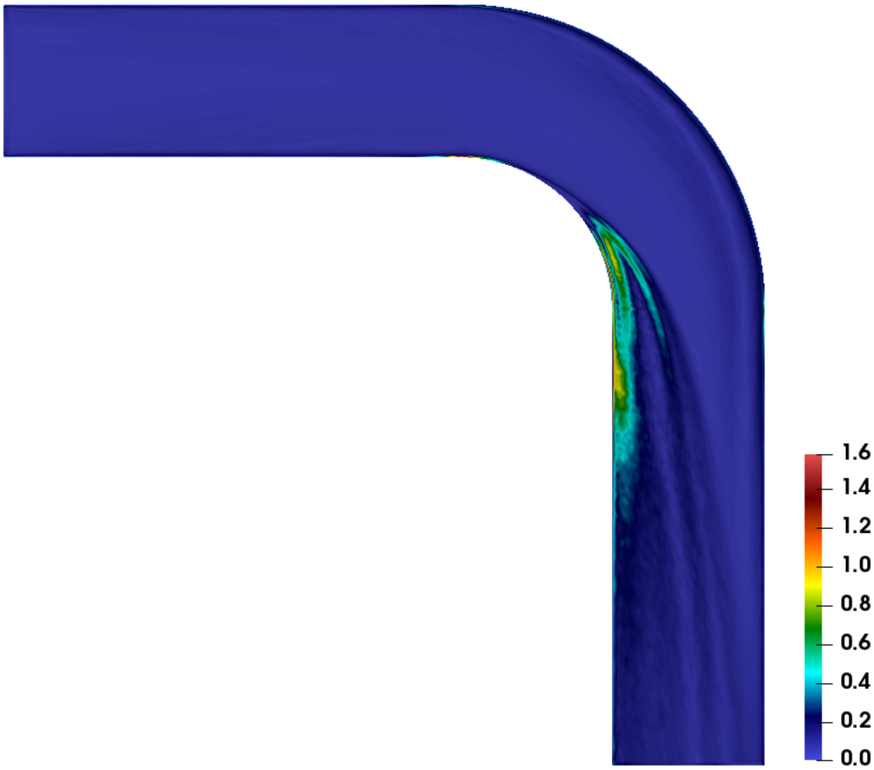

Fig. 4.24 Contour showing the magnitude of the summation of the convection and the pressure gradient terms in the momentum transport equation.

dissipation rate in the LES domain; these two terms are fed to the interface to enable the use of more advanced turbulence models in the RANS subdomain. These strategies have also been adopted by the main wall function approach of this project. The use of the elliptic blending $k-\varepsilon$ model in the subdomain of the pipe bend case has proven to be a success.

However, the application of the wall shear stress in the first cell of the coarse LES grid leads to the generation of numerical noise in the OpenFOAM code, which appears as additional resolved turbulence. This additional resolved turbulence leads to the overprediction of the turbulent kinetic energy in the near-wall region of the LES grid. When the higher than expected k is fed to the interface, it also leads to the overprediction of the wall shear stress computed in the RANS subdomain. The overpredicted wall shear stress wrongly decreases the velocity gradient at the wall of the LES domain. The problem of the numerical noise reduces as the coarse near-wall grid is refined, which defeats the purpose of using a wall function. The artificial noise generated by the numerical wall function can be eliminated if the method is implemented in a different code. It is recommended for future work that the numerical wall function is implemented and tested in another open-source CFD code with a different numerical setup from OpenFOAM.

Chapter 7 gives an overview of the successful development and implementation of the main wall function method by this project in the open-source code OpenFOAM. Rather than applying the correction at the wall, the wall function is applied as a weak source term over the first few cells at the wall of the LES grid to drive the under-resolved near-wall LES fields towards the equivalent fields in the RANS domain. This new approach utilises ideas from the hybrid RANS/LES dual mesh method of Xiao and Jenny (2012) while incorporating the improvements made for the numerical wall function. The excessive numerical noise encountered in the first cell of the coarse LES grid for the numerical wall function method is not witnessed for the new implementation as the noise is spread across several wall-normal cells. This new approach, known as the subdomain wall function, is fully demonstrated in Paper I.

Chapter 5

Contributions to the Field

The primary focus of the PhD has been the development of wall functions for large eddy simulation. This project presents detailed results of the research conducted throughout the PhD in the form of two journal papers and a conference paper. These papers are appended to this thesis. This chapter summarises the significant contributions of each paper with respect to the three principal objectives of this project.

(I) **Utilisation of advanced turbulence models in the RANS subdomain of the wall function approaches**: Assessment of the current literature of wall function approaches for LES and the implementation of two and four-equation RANS models in the subdomain. (**Papers I & III**)

(II) **Development of a novel wall function for LES**: Implementation and evaluation of new wall function approaches for LES to enable high Reynolds number scale-resolving simulations. (**Papers I & III**)

(III) **Investigation of thermo-hydraulic properties of flow through a pipe bend**: Application of a wall-resolved LES to study the evolution of flow and thermal physics through a 90° pipe bend. (**Paper II**)

5.1 Utilisation of Advanced Turbulence Models in the RANS Subdomain of the Wall Function

The usage of more advanced turbulence models than the mixing length model in the RANS subdomain is reported in Papers I and III. The purpose of this implementation is to enable the RANS subdomain to better support the under-resolved LES grid for challenging industrial applications as generally at such high Re numbers, the viscous and buffer near-wall layers must be modelled, rather than being resolved by a quasi-DNS mesh refinement. The framework is developed to allow the use of any RANS models. This work uses two and four-equation transport eddy viscosity models in the RANS subdomains to evaluate the wall function approaches.

As explained in Papers I and III, proper coupling between the LES and RANS grids is established to enable the use of more advanced turbulence models in the RANS subdomain. Current wall function approaches in literature feed the instantaneous filtered LES velocity and pressure fields to the top boundary of the RANS subdomain. The coupling of the instantaneous field of the LES domain to the Reynolds-averaged fields of the RANS domain at the interface is inconsistent. This inconsistent coupling has led to the simplification of the RANS momentum equation to just solving the diffusion term or the introduction of corrections to the RANS mixing length turbulence model. This work solves this problem by computing the partial time average of the filtered velocity and pressure fields in the LES grid. The period of the partial time average of quantities of interest is long enough to ensure that the partial mean LES quantities are equivalent to the corresponding Reynolds averaged quantities. The partial time average is done by means of the exponentially weighted time average. The exponentially weighted time average reduces the required period to initialise the averaging operation compared to the traditional-time average, and the recent events of the simulation are prioritised. The partial time average of filtered variables ensures that the LES grid supplies consistent quantities to the interface of the RANS subdomain. Hence, paper III demonstrates the computation of the full RANS equations in the subdomain without the need for corrections when a consistent coupling at the interface is established.

Papers I and III overcome the problem of prescribing boundary conditions at the interface of the RANS subdomain for the turbulent kinetic energy and the dissipation rate by computing the instantaneous total Reynolds stress tensor and the dissipation rate in the LES domain. These two quantities are exponentially weighted averaged and transferred to the interface to enable the use of advanced turbulence models in the RANS subdomain. The four-equation elliptic blending $k-\varepsilon$ model is used in the two identified papers. The turbulence model solves the additional transport equation for $\overline{v^2}/k$ and the elliptic equation for the blending parameter α. Algebraic correlations are done to specify the interface boundary conditions for the two additional quantities for all the test cases in Paper I and the pipe bend case in paper III. However, a boundary normal gradient of zero is incorrectly specified at the interface for the two additional quantities for the channel flow case in paper III.

In summary, a consistent coupling of fields at the interface of the LES and RANS grids has been accomplished by computing the exponentially weighted time average of LES filtered fields of interest. The consistent coupling enables the utilisation of any advanced turbulence model in the RANS subdomain. Hence, the RANS grid is able to support the coarse LES domain for more demanding test cases in the region of the LES grid that is expected to be weak.

5.2 Development of a Novel Wall Function for LES

Paper I demonstrates the implementation of the subdomain wall function for large eddy simulation. This new method is the main focus of the project in the development of a novel wall function. Paper III shows the implementation of the numerical wall function in the open-source toolbox OpenFOAM. The code of the numerical wall function was developed to form the backbone of the later implementation of the subdomain wall function for LES.

The grid resolution in the near-wall region of the LES domain is deliberately reduced to enable the use of LES for high Reynolds number flows. The setup of the wall functions used in this project is similar to the wall-modelled LES approach first developed by Balaras et al. (1996) where a smaller RANS domain overlaps the first cell at the wall of the LES grid. The RANS domain computes a wall shear stress which is supplied to the LES momentum transport equation to correct the first cell at the wall of the coarse near-wall LES grid. In return, the top boundary of the RANS domain, which meets with the top face of the first grid point of the LES grid, receives instantaneous filtered information to complete the boundary conditions. Simplified boundary layer momentum transport equations are solved in the RANS domain. Some researchers such as Kawai and Larsson (2013) made corrections to the boundary layer equations to reduce the stress computed by the RANS domain. Other researchers simplified the boundary layer equations by solving only the diffusion term without needing modifications to the RANS momentum equations. The algebraic mixing-length turbulence model was the typical approach used to represent turbulence in the RANS domain.

Paper III implements the numerical wall model for LES where the RANS domain computes the wall shear stress to correct the under-resolved first cell of the LES grid akin to the wall-modelled LES approach. However, the numerical wall function made several improvements over the standard wall-modelled LES method. First, the height of the RANS domain is increased to bypass at least the first three cells of the LES grid. This modification is done to ensure that the top boundary of the RANS domain receives better resolved filtered information from the LES grid compared to when the RANS grid is embedded in the first node of the LES domain. Furthermore, the numerical wall function utilises the progress achieved in the first objective of the PhD by establishing a consistent coupling of fields between the LES and RANS regions by the exponentially weighted averaging of LES fields of interest. This strategy ensures that the full Navier-Stokes equations in the RANS domain are solved. Also, the major challenge of using any turbulence model in the RANS domain is overcome. The numerical wall function in Paper III used the elliptic blending $k-\varepsilon$ model in the RANS to enable the computation of the wall shear stress. This enabled the numerical wall function for LES to be used for challenging test cases.

Application of the numerical wall function for LES demonstrates good performance for plane channel flow simulations in comparison to reference DNS data. The error of the friction Reynolds number predicted is less than 4%. The performance of the coarse LES grid degrades when the numerical wall function is not used. The new method is applied for a flow through a 90° pipe bend and is in good agreement with the reference data. The numerical wall function case used about 3% grid points of the reference wall-resolved LES case for the pipe bend case. Results predicted by the improved delayed detached eddy simulation (IDDES) method is also compared. The IDDES case struggles to predict the flow features when the counter-rotating vortices become dominant in the latter part of the pipe bend. The streamwise and secondary velocity profiles are well predicted by the numerical wall function at the pipe bend exit despite using a significant fraction of the computational cost.

Paper I presents the implementation of a novel wall function approach, known as the subdomain wall function for LES. The setup of the subdomain wall function is the same as the numerical wall function where a RANS domain, labelled the subdomain, overlaps the near-wall region of the coarse LES grid. The RANS subdomain receives mean information from the LES at the interface to complete the boundary conditions of the grid and compute the RANS equations. However, rather than compute a wall shear stress to correct the first grid point at the wall of the LES grid, the RANS subdomain supplies velocity, turbulent kinetic energy and dissipation rate fields to the LES domain to form the new wall function.

The reduction of the grid resolution in the inner region of the LES grid to support high Reynolds number scale-resolving computations ensures that the near-wall grid is under-resolved beyond the first cell at the wall of the LES domain. However, the numerical wall function and other wall function approaches correct just the first cell at the wall with a computed wall shear stress, while the subsequent unrefined grid points are left uncorrected. The significant achievement of the subdomain wall function is to correct the under-resolved near-wall LES grid beyond the first node at the wall. The subdomain wall function makes use of ideas of the innovative dual mesh hybrid RANS/LES method by Xiao and Jenny (2012) and Tunstall et al. (2017). A weak volumetric source term, known as the drift term, is added to the momentum transport equation of the LES domain. The drift term acts to force the partial mean LES velocity field towards the RANS velocity and rescale the trace of the mean total LES Reynolds stress tensor towards the RANS turbulent kinetic energy. Hence, the RANS subdomain supports the near-wall region of the LES grid that is expected to underperform. The method computes relaxation timescales, based on the RANS turbulent timescales, to determine how quickly the wall function makes the LES velocity and Reynolds stress fields consistent with the equivalent RANS fields. Furthermore, the areas of the LES grid that are under-resolved are automatically determined by the subdomain wall function method. This automation eliminates the need to specify the areas of the LES grid that is under-resolved before the start of the simulation.

The subdomain wall function demonstrates excellent performance for a plane channel flow. The overprediction of the turbulent kinetic energy in the near-wall region, as seen for the numerical wall function case, is not observed. Paper I investigate the effect of varying the height of the interface for the same LES grid. The velocity profiles show a log-layer mismatch when the subdomain covers either the first one or two cells at the wall of the LES grid. The mismatch disappears when the subdomain overlaps at least the first three cells of the LES grid.

The performance of the subdomain wall function is tested for the challenging periodic hills and asymmetric diffuser cases, which features flow separation and reattachment. A pure LES case using the same LES grid as the subdomain wall function cases, but without the support of a wall function, is also studied for the simulations. The subdomain wall function predicts the separation bubble in the periodic hills and asymmetric diffuser accurately, while the pure LES fails to predict the flow features as the resolution of the near-wall LES grids is too low. The difference between the wall function case and the pure LES case in predicting the reference data highlights the importance of the subdomain wall function method improving the performance of LES with coarse near-wall grids.

5.3 Investigation of Thermo – Hydraulic Properties of Flow through a Pipe Bend

The thermal properties of flow through a 90° pipe bend was investigated with a wall-resolved LES demonstrated in paper II. Hydrodynamic properties of flows through pipe bends have been extensively investigated with numerical and experimental studies. However, there have been very few investigations for heat transfer through pipe bends. Baughn et al. (1987) conducted a heat transfer experiment, while Cvetkovski et al. (2015) performed a thermal detached eddy simulation for flow through a U-Bend pipe. Iyamabo (2015) did RANS investigations on heat transfer through a 90° pipe bend. Paper II compares the heat transfer results of the LES with the mass transfer experimental data of Mazhar et al. (2013) using the well-known correlation between heat and mass transfer to validate the numerical results. Mazhar et al. (2013) measured the mass transfer coefficient of a 90° pipe bend using a dissolvable wall technique in their experiment. The bulk Reynolds number of the flow based on pipe diameter is 40,000, and the ratio of the radius of curvature of the bend to the pipe diameter is $R_c = 1.5D$. A section of the flow results are also validated with the wall-resolve LES data of Holgate (2018) and the experiment data of Kalpakli and Örlü (2013), whose bulk Reynolds number and the ratio of the curvature radius to the pipe diameter are 34,000 and $R_c = 1.58D$ respectively. The Cartesian coordinate system of the velocity field is converted to an intrinsic coordinate system. Hence, the study generated the streamwise, cross-stream and spanwise velocity components through the bend. This led to the production of an extensive dataset of thermal and flow properties through the bend.

The fluid accelerates around the inner wall at the entrance of the bend. This flow acceleration had a negligible effect on the temperature profiles, which remained symmetric and unchanged at the bend entrance. The flow acceleration led to an increase of skin friction along the inner wall immediately downstream of the bend entrance. By the middle of the bend, a strong streamwise adverse pressure gradient appears along the inner wall leading to the flow to separate. Also, counter-rotating vortices, known as the Dean vortices, become prominent from the middle of the bend and transport high momentum fluid from the inner wall towards the outer wall, while low momentum fluid from the sides of the bend is moved towards the inner wall. The Dean vortices have an effect on the temperature field, which behave like the velocity field. Consequently, in the second half of the bend where the Dean vortices are dominant, there are high gradients of velocity and temperature fields along the outer walls. The Reynolds stress tensor becomes highly anisotropic with the spanwise component becoming the largest stress close to the inner wall.

When the heat transfer results are compared with the mass transfer experimental data, the heat transfer along the outer wall follows the increasing trend of the mass transfer as expected. However, along the inner wall, a remarkable discovery is made; the correlation between heat and mass transfer breaks down. The mass transfer data is strongly correlated with skin friction along the inner wall, while the heat transfer results scale more closely with turbulent intensity and are greatly influenced by the secondary flow. The disparity in the trend of the heat and mass transfer profiles along the inner wall is due to the difference in the evolution of the thermal and flow fields through the bend.

Chapter 6

Summary and Future Work

This PhD project has focussed on the development of wall functions for large eddy simulation to enable the computation of the scale-resolving method for high Reynolds number flows found in industrial applications. The PhD has made contributions to large eddy simulation applications at high Reynolds by developing the subdomain wall function for LES; the subdomain wall function was the main objective at the conception of the project. A second wall function was created, namely the numerical wall function, by this project; the development of the numerical wall function was used to aid the code implementation of the subdomain wall function in an open-source toolbox. These wall function approaches were implemented in the OpenFOAM package and have been validated with standard and demanding test cases. The wall function methods have a separate RANS grid that overlaps the near-wall region of the LES. The top boundary of the RANS grid, or the subdomain, that interfaces with the LES grid receives mean information from the LES grid to complete the boundary conditions of the subdomain. This coupling enabled the utilisation of advanced turbulence models in the RANS subdomain. Consequently, the RANS subdomain of the numerical wall function computes a wall shear stress to correct the under-resolved first cell at the wall of the coarse LES grid. On the other hand, the RANS grid of the recommended subdomain wall function sends information of the RANS velocity and turbulent kinetic energy to the main domain to support the correction of the coarse near-wall region of the LES grid beyond the first cell at the wall.

Furthermore, the PhD project conducted an extensive study of turbulent heat transfer through a 90° pipe bend. The results of the heat transfer coefficient were compared with an experimental mass transfer dataset. The heat transfer results along the outer wall of the bend compared favourably with the mass transfer experimental data. However, the correlation between numerical heat and experimental mass transfer broke down along the inner wall.

This thesis presented an overview of methods used to model or represent turbulence in CFD study. A comprehensive review of traditional wall function approaches to LES and the development of the numerical wall function was detailed with explanations of the failure of the implementation of the approach in open-source code OpenFOAM. Finally, the results of this PhD project were presented in the form of 2 journal papers, which are currently under review, and a published conference paper.

> **Paper I** reports on the development and implementation of the subdomain wall function for large eddy simulation. This method is the novel approach of this project in computing large eddy simulation for high Reynolds number flow. A source term is added to the momentum transport equation of the main LES domain, which acts to readjust the mean velocity and the resolved and subgrid-scale turbulence fields of the LES grid towards the equivalent fields of the RANS subdomain. Hence the RANS subdomain supports the near-wall LES domain where the LES grid is expected to underperform. The correction of the under-resolved near-wall LES grid is done beyond the first cell at the wall. In return, the LES grid forces the quantities at the interface of the RANS and LES grids, by supplying mean filtered information to the top boundary of the RANS subdomain. This supply of mean information from the LES grid enables all the boundary conditions of the RANS grid to be complete. The areas of the under-resolved LES grid are also automatically determined by the new wall function approach without the need to prescribe the zones prior to the start of a simulation. The subdomain wall function achieves success in using any advanced turbulence model in the RANS grid. The subdomain wall function accurately predicts the DNS profiles of the $Re_\tau = 395, 1000$ and 5200 plane channel flow cases. Testing of the method is done for the more demanding periodic hills case that experiences flow separation and reattachment. Results of the subdomain wall function are compared with the data of a wall-resolved LES of Breuer et al. (2009). The results of the novel wall function approach are in excellent agreement with the reference data while using a significant fraction of grid points in the main domain compared to the wall-resolved LES grid size. Validation of the subdomain wall function method is also extended to the asymmetric plane diffuser case. Results of the subdomain wall function are compared with the data of the experiment of Buice and Eaton (2000). The subdomain wall function shows massive improvement in predicting the experimental data with a coarse LES grid compared to when a pure LES is run without the aid of a wall function on the same grid.
>
> **Paper II** investigates the heat transfer properties of turbulent flow through a 90° pipe bend using the wall-resolved LES method. A synthetic eddy method is used to generate the fluctuating instantaneous velocity field at the inlet, which instigated the development of the fluctuating instantaneous temperature field

in the inlet straight pipe upstream of the bend entrance. The bulk Reynolds number based on the pipe diameter is 40,000 while the ratio of the radius of curvature of the bend to the pipe diameter is $R_c = 1.5D$. The heat transfer results of the simulation are compared with the mass transfer experimental data of Mazhar et al. (2013) due to the absence of a heat transfer experimental dataset for 90° pipe bends. The heat transfer coefficient along the outer wall of the bend compares favourably with the mass transfer data. However, the heat transfer results along the inner wall completely fail in predicting the mass transfer data in that section of the bend. Mass transfer along the inner wall of the bend scales better with skin friction, while heat transfer correlates with the peak turbulence intensity near the inner wall. The breakdown in the correlation between heat and mass transfer is due to the difference in the evolution of the flow and thermal fields around the bend.

Immediately downstream of the bend entrance, there is a strong favourable pressure gradient along the inner wall, which acts to accelerate the flow near that location, thereby increasing skin friction. However, the temperature profile remains unaffected. Counter-rotating vortices due to the imbalance of centrifugal forces and the radial pressure gradient, in the second half of the bend, transports high momentum fluid towards the outer wall, while low momentum fluid at the side walls is moved towards the inner wall. The temperature fields also become affected by the counter-rotating vortices and now follow the same trend of the flow field, leading to an increase of heat flux along the outer wall. Turbulent transport via secondary flow in the pipe bend also accounts for the spanwise component of the highly anisotropic Reynolds stress being the most dominant component in the turbulent kinetic energy in the second half of the bend. An extensive dataset of the velocity field decomposed into its streamwise, cross-stream and spanwise components, the Reynolds stress tensor, wall shear stress vector and heat flux vector is produced by this publication.

Paper III demonstrates the implementation of the numerical wall function for large eddy simulation. This method is similar to the wall-modelled LES, where a separate grid overlaps the near-wall region of the coarse LES grid. The separate grid computes a wall shear stress to correct the first cell at the wall of the coarse LES grid. On the other hand, the partial time average of the filtered velocity and pressure fields plus the Reynolds stress and dissipation rate of the LES domain are calculated using the exponentially weighted average operator. These partial mean quantities are mapped to the top boundary of the separate grid to enable the computation of the full Reynolds-averaged Navier Stokes equation in the secondary grid. The numerical wall function has been tested for the $Re_\tau = 1000$

plane channel flow. The method successfully predicted the flow parameters of a 90° pipe bend flow at a significant fraction of the computational costs.

6.1 Future work

6.1.1 Elliptic Blending Lag Model in RANS Subdomain

The subdomain wall function approach requires the RANS grid to support the LES predictions in the near-wall coarse LES grid. This requirement implies that it is desirable to use a RANS turbulence model that accurately predicts the near-wall features of a turbulent flow. The recently developed elliptic blending lag model has been designed by Lardeau and Billard (2016) to provide predictions similar to the Reynolds stress transport models in a linear eddy-viscosity framework by accounting for the overall degree of stress-strain misalignment in a flow. The elliptic blending lag model predicts both the near-wall peak in the turbulent kinetic energy and its profile throughout the logarithm-region in channel flows better than the elliptic blending $k-\varepsilon$ model used in the two new wall functions methods. This model can be further investigated to determine whether it can improve predictions of the subdomain wall function for large eddy simulation.

6.1.2 Reduction of MPI Costs

The subdomain and numerical wall functions have demonstrated success in predicting turbulent flows with scale-resolving methods on grids that are too coarse for wall-resolved LES. However, this success is achieved with a computational overhead of about 35% higher than pure LES when the same grid is used. There is a need to lessen this increased cost. Separate simulations for the pure RANS and the pure LES are done in OpenFOAM for the wall function approaches. The pure LES and RANS simulations exchange information as the computation progresses. This exchange of information between domains becomes challenging when the simulations are decomposed on parallel processors. OpenFOAM has several decomposition libraries that optimise the distribution of cells on the respective domains between the processors to **reduce the associated MPI costs**. However, these libraries have not been optimised for multi-domain decomposition, thereby leading to an increase in MPI overhead for exchange of information between the separate LES and RANS grids. The increase in MPI costs is particularly severe at the top boundary of the RANS domain that interfaces with the LES grid. Further work is required to develop a new library to reduce MPI costs associated with the exchange of information between two grids to maximise the savings in computational costs for the new wall function approaches.

6.1.3 Eliminating the Spurious Coarse LES Turbulent Kinetic Energy

A significant problem of the implementation of the numerical wall function for large eddy simulation in OpenFOAM was the generation of numerical noise when the near-wall grid resolution was reduced. This noise artificially increased the resolved turbulence in the LES grid; therefore, the turbulent kinetic energy supplied to the interface of the RANS grid from the LES was overpredicted. There is a need for further investigations to determine the root cause of the numerical noise in OpenFOAM. Also, it is recommended that the numerical wall function is implemented in a different open-source CFD package, which uses another type of numerics that differs from OpenFOAM.

6.1.4 Other Work

This present work has made significant progress in the development of wall function approaches for large eddy simulation. The subdomain wall function can be extended to solve the energy equation for thermal industrial applications. When this is complete, the subdomain wall function can be assessed for more complex test cases such as pipe bends that are found in the thermal-hydraulic systems in power plants.

References

Balakumar, B. and Adrian, R. (2007). Large- and very-large-scale motions in channel and boundary-layer flows. *Philosophical Transactions of the Royal Society A: Mathematical, Physical and Engineering Sciences*, 365(1852):665–681.

Balaras, E., Benocci, C., and Piomelli, U. (1996). Two-layer approximate boundary conditions for large-eddy simulations. *AIAA Journal*, 34(6):1111–1119.

Baldwin, B. and Barth, T. (1991). A one-equation turbulence transport model for high Reynolds number wall-bounded flows. In *29th Aerospace Sciences Meeting*. American Institute of Aeronautics and Astronautics.

Baughn, J. W., Iacovides, H., Jackson, D. C., and Launder, B. E. (1987). Local heat transfer measurements in turbulent flow around a 180-deg pipe bend. *Journal of Heat Transfer*, 109(1):43–48.

Billard, F. (2011). *Development of a robust elliptic-blending turbulence model for near-wall, seperated and buoyant flows*. PhD thesis, The University of Mancherster.

Billard, F. and Laurence, D. (2012). A robust $k-\varepsilon-\overline{v^2}/k$ elliptic blending turbulence model applied to near-wall, separated and buoyant flows. *International Journal of Heat and Fluid Flow*, 33(1):45 – 58.

Billard, F., Laurence, D., and Osman, K. (2015). Adaptive wall functions for an elliptic blending eddy viscosity model applicable to any mesh topology. *Flow, Turbulence and Combustion*, 94(4):817–842.

Bodart, J. and Larsson, J. (2012). Sensor-based computation of transitional flows using wall-modeled large eddy simulation. In *Annual Research Briefs*. Center for Turbulence Research.

Bose, S. T. and Moin, P. (2014). A dynamic slip boundary condition for wall-modeled large-eddy simulation. *Physics of Fluids*, 26(1):015104.

Boussinesq, M. J. (1868). Mémoire sur l'influence des frottements dans les mouvements réguliers des fluides. *Journal de mathématiques pures et appliquées*, 13:377–424.

Breuer, M., Peller, N., Rapp, C., and Manhart, M. (2009). Flow over periodic hills – numerical and experimental study in a wide range of Reynolds numbers. *Computers & Fluids*, 38(2):433 – 457.

Buice, C. U. and Eaton, J. K. (2000). Experimental investigation of flow through an asymmetric plane diffuser. *Journal of Fluids Engineering*, 122(2):433–435.

Cabot, W. (1996). Near-wall models in large eddy simulations of flow behind a backward-facing step. In *Annual Research Briefs*. Center for Turbulence Research.

Catalano, P., Wang, M., Iaccarino, G., and Moin, P. (2003). Numerical simulation of the flow around a circular cylinder at high Reynolds numbers. *International Journal of Heat and Fluid Flow*, 24(4):463 – 469. Selected Papers from the Fifth International Conference on Engineering Turbulence Modelling and Measurements.

Chapman, D. R. (1979). Computational aerodynamics development and outlook. *AIAA Journal*, 17(12):1293–1313.

Chen, Z. L., Hickel, S., Devesa, A., Berland, J., and Adams, N. A. (2014). Wall modeling for implicit large-eddy simulation and immersed-interface methods. *Theoretical and Computational Fluid Dynamics*, 28(1):1–21.

Chieng, C. C. and Launder, B. E. (1980). On the calculation of turbulent heat transport downstream from an abrupt pipe expansion. *Numerical Heat Transfer*, 3(2):189–207.

Clark, R. A., Ferziger, J. H., and Reynolds, W. C. (1979). Evaluation of subgrid-scale models using an accurately simulated turbulent flow. *Journal of Fluid Mechanics*, 91(01):1.

Craft, T., Gerasimov, A., Iacovides, H., and Launder, B. (2002). Progress in the generalization of wall-function treatments. *International Journal of Heat and Fluid Flow*, 23(2):148 – 160.

Craft, T. J., Gant, S. E., Iacovides, H., and Launder, B. E. (2004). A new wall function strategy for complex turbulent flows. *Numerical Heat Transfer, Part B: Fundamentals*, 45(4):301–318.

Cvetkovski, C. G., Reitsma, S., Bolisetti, T., and Ting, D. S. (2015). Heat transfer in a u-bend pipe: Dean number versus Reynolds number. *Sustainable Energy Technologies and Assessments*, 11:148 – 158.

Daly, B. J. and Harlow, F. H. (1970). Transport equations in turbulence. *The Physics of Fluids*, 13(11):2634–2649.

Deardorff, J. W. (1970). A numerical study of three-dimensional turbulent channel flow at large Reynolds numbers. *Journal of Fluid Mechanics*, 41(2):453–480.

Diurno, V. G., Balaras, E., and Piomelli, U. (2001). Wall-layer models for LES of separated flows. In Geurts, B., editor, *Modern simulation strategies for turbulent flows*, pages 207–222.

Duprat, C., Balarac, G., Métais, O., Congedo, P. M., and Brugière, O. (2011). A wall-layer model for large-eddy simulations of turbulent flows with/out pressure gradient. *Physics of Fluids*, 23(1):015101.

Durbin, P. A. (1991). Near-wall turbulence closure modeling without "damping functions". *Theoretical and Computational Fluid Dynamics*, 3(1):1–13.

Ferziger, J. H. and Perić, M. (2002). *Computational Methods for Fluid Dynamics*. Springer Berlin Heidelberg.

Fröhlich, J. and von Terzi, D. (2008). Hybrid LES/RANS methods for the simulation of turbulent flows. *Progress in Aerospace Sciences*, 44(5):349 – 377.

Gant, S. (2002). *Development and application of a new wall function for complex turbulent flows*. PhD thesis, The University of Manchester.

Germano, M. (1986). A proposal for a redefinition of the turbulent stresses in the filtered Navier–Stokes equations. *The Physics of Fluids*, 29(7):2323–2324.

Germano, M. (1992). Turbulence: the filtering approach. *Journal of Fluid Mechanics*, 238:325–336.

Germano, M., Piomelli, U., Moin, P., and Cabot, W. H. (1991). A dynamic subgrid-scale eddy viscosity model. *Physics of Fluids A: Fluid Dynamics*, 3(7):1760–1765.

Gritskevich, M. S., Garbaruk, A. V., Schütze, J., and Menter, F. R. (2011). Development of DDES and IDDES formulations for the k-ω shear stress transport model. *Flow, Turbulence and Combustion*, 88(3):431–449.

Hanjalic, K. and Launder, B. (2011). *Modelling Turbulence in Engineering and the Environment*. Cambridge University Press.

Hickel, S., Touber, E., Bodart, J., and Larsson, J. (2012). A parametrized non-equilibrium wall-model for large-eddy simulations. In *Proceedings of the Summer Program 2012*, pages 127–136. Center for Turbulence Research.

Holgate, J. W. (2018). *Development and Application of Embedded Large Eddy Simulation for Internal Fluid Flows in Industrial Computational Fluid Dynamics*. PhD thesis, The University of Manchester.

Issa, R. (1986). Solution of the implicitly discretised fluid flow equations by operator-splitting. *Journal of Computational Physics*, 62(1):40 – 65.

Iyamabo, B. E. O. (2015). Numerical investigation of turbulent heat transfer through a circular 90-deg pipe bend. Dissertation, The University of Manchester.

Jiménez, J. and Hoyas, S. (2008). Turbulent fluctuations above the buffer layer of wall-bounded flows. *Journal of Fluid Mechanics*, 611:215–236.

Jones, W. and Launder, B. (1972). The prediction of laminarization with a two-equation model of turbulence. *International Journal of Heat and Mass Transfer*, 15(2):301–314.

Kalpakli, A. and Örlü, R. (2013). Turbulent pipe flow downstream a 90° pipe bend with and without superimposed swirl. *International Journal of Heat and Fluid Flow*, 41:103 – 111. ETMM9.

Kawai, S. and Larsson, J. (2011). Wall modeling in large-eddy simulation: predicting accurate skin friction at very high Reynolds number. In *49th AIAA Aerospace Sciences Meeting including the New Horizons Forum and Aerospace Exposition*, pages 1–20. American Institute of Aeronautics and Astronautics, Inc.

Kawai, S. and Larsson, J. (2012). Wall-modeling in large eddy simulation: Length scales, grid resolution, and accuracy. *Physics of Fluids*, 24(1):015105.

Kawai, S. and Larsson, J. (2013). Dynamic non-equilibrium wall-modeling for large eddy simulation at high Reynolds numbers. *Physics of Fluids*, 25(1):015105.

Kim, W.-W. and Menon, S. (1995). A new dynamic one-equation subgrid-scale model for large eddy simulations. In *33rd Aerospace Sciences Meeting and Exhibit*. American Institute of Aeronautics and Astronautics.

Kolmogorov, A. (1941). The Local Structure of Turbulence in Incompressible Viscous Fluid for Very Large Reynolds' Numbers. *Akademiia Nauk SSSR Doklady*, 30:301–305.

Lardeau, S. and Billard, F. (2016). Development of an elliptic-blending lag model for industrial applications. In *54th AIAA Aerospace Sciences Meeting*. American Institute of Aeronautics and Astronautics.

Larsson, J., Kawai, S., Bodart, J., and Bermejo-Moreno, I. (2016). Large eddy simulation with modeled wall-stress: recent progress and future directions. *Mechanical Engineering Reviews*, 3(1):15–00418–15–00418.

Larsson, J., Laurence, S., Bermejo-Moreno, I., Bodart, J., Karl, S., and Vicquelin, R. (2015). Incipient thermal choking and stable shock-train formation in the heat-release region of a scramjet combustor. Part II: Large eddy simulations. *Combustion and Flame*, 162(4):907 – 920.

Laufer, J. (1948). *Investigation of turbulent flow in a two-dimensional channel*. PhD thesis, California Institute of Technology.

Launder, B. and Sharma, B. (1974). Application of the energy-dissipation model of turbulence to the calculation of flow near a spinning disc. *Letters in Heat and Mass Transfer*, 1(2):131 – 137.

Launder, B. and Spalding, D. (1974). The numerical computation of turbulent flows. *Computer Methods in Applied Mechanics and Engineering*, 3(2):269 – 289.

Lee, M. and Moser, R. D. (2015). Direct numerical simulation of turbulent channel flow up to $Re_\tau \approx 5200$. *Journal of Fluid Mechanics*, 774:395–415.

Leonard, A. (1975). Energy cascade in large-eddy simulations of turbulent fluid flows. In Frenkiel, F. and Munn, R., editors, *Turbulent Diffusion in Environmental Pollution*, volume 18 of *Advances in Geophysics*, pages 237 – 248. Elsevier.

Lilly, D. K. (1992). A proposed modification of the Germano subgrid-scale closure method. *Physics of Fluids A: Fluid Dynamics*, 4(3):633–635.

Manceau, R. and Hanjalić, K. (2002). Elliptic blending model: A new near-wall Reynolds-stress turbulence closure. *Physics of Fluids*, 14(2):744–754.

Marusic, I., Kunkel, G. J., and Porté-Agel, F. (2001). Experimental study of wall boundary conditions for large-eddy simulation. *Journal of Fluid Mechanics*, 446:309–320.

Marusic, I., Mathis, R., and Hutchins, N. (2010). High Reynolds number effects in wall turbulence. *International Journal of Heat and Fluid Flow*, 31(3):418 – 428. Sixth International Symposium on Turbulence and Shear Flow Phenomena.

Mazhar, H., Ewing, D., Cotton, J., and Ching, C. (2013). Experimental investigation of mass transfer in 90° pipe bends using a dissolvable wall technique. *International Journal of Heat and Mass Transfer*, 65:280 – 288.

McKeon, B. J., Li, J., Jiang, W., Morrison, J. F., and Smits, A. J. (2004). Further observations on the mean velocity distribution in fully developed pipe flow. *Journal of Fluid Mechanics*, 501:135–147.

Moin, P. and Kim, J. (1982). Numerical investigation of turbulent channel flow. *Journal of Fluid Mechanics*, 118:341–377.

Moser, R. D., Kim, J., and Mansour, N. N. (1999). Direct numerical simulation of turbulent channel flow up to Re_{τ}=590. *Physics of Fluids*, 11(4):943–945.

Nagib, H. M. and Chauhan, K. A. (2008). Variations of von Kármán coefficient in canonical flows. *Physics of Fluids*, 20(10):101518.

Nagib, H. M., Chauhan, K. A., and Monkewitz, P. A. (2007). Approach to an asymptotic state for zero pressure gradient turbulent boundary layers. *Philosophical Transactions of the Royal Society A: Mathematical, Physical and Engineering Sciences*, 365(1852):755–770.

Nicoud, F. and Ducros, F. (1999). Subgrid-scale stress modelling based on the square of the velocity gradient tensor. *Flow, Turbulence and Combustion*, 62(3):183–200.

Park, G. I. and Moin, P. (2014). An improved dynamic non-equilibrium wall-model for large eddy simulation. *Physics of Fluids*, 26(1):015108.

Piomelli, U. (1993). High Reynolds number calculations using the dynamic subgrid-scale stress model. *Physics of Fluids A: Fluid Dynamics*, 5(6):1484–1490.

Piomelli, U. (2008). Wall-layer models for large-eddy simulations. *Progress in Aerospace Sciences*, 44(6):437 – 446. Large Eddy Simulation - Current Capabilities and Areas of Needed Research.

Piomelli, U. and Balaras, E. (2002). Wall-layer models for large-eddy simulations. *Annual Review of Fluid Mechanics*, 34(1):349–374.

Piomelli, U., Ferziger, J., Moin, P., and Kim, J. (1989). New approximate boundary conditions for large eddy simulations of wall-bounded flows. *Physics of Fluids A: Fluid Dynamics*, 1(6):1061–1068.

Pope, S. B. (2000). *Turbulent Flows*. Cambridge University Press.

Prandtl, L. (1945). Über ein neues formelsystem für die ausgebildete turbulenz. Nachrichten der Akademie der Wissenschaften. In *Göttingen, Mathematisch-Physikalische Klasse*, volume 1, pages 6–19.

Radhakrishnan, S. and Piomelli, U. (2008). Large-eddy simulation of oscillating boundary layers: Model comparison and validation. *Journal of Geophysical Research: Oceans*, 113(C2).

Rajagopalan, S. and Antonia, R. A. (1979). Some properties of the large structure in a fully developed turbulent duct flow. *The Physics of Fluids*, 22(4):614–622.

Reynolds, O. (1883). Xxix. an experimental investigation of the circumstances which determine whether the motion of water shall be direct or sinuous, and of the law of resistance in parallel channels. *Philosophical Transactions of the Royal Society of London*, 174:935–982.

Richardson, L. F. (1922). *Weather Prediction by Numerical Process*. Cambridge University Press.

Schumann, U. (1975). Subgrid scale model for finite difference simulations of turbulent flows in plane channels and annuli. *Journal of Computational Physics*, 18(4):376 – 404.

Shih, T.-H., Liou, W. W., Shabbir, A., Yang, Z., and Zhu, J. (1995). A new k-ε eddy viscosity model for high Reynolds number turbulent flows. *Computers & Fluids*, 24(3):227 – 238.

Skillen, A., Revell, A., and Craft, T. (2016). Accuracy and efficiency improvements in synthetic eddy methods. *International Journal of Heat and Fluid Flow*, 62:386 – 394.

Smagorinsky, J. (1963). General Circulation Experiments with the Primitive Equations. *Monthly Weather Review*, 91(3):99.

Smits, A. J., McKeon, B. J., and Marusic, I. (2011). High–Reynolds number wall turbulence. *Annual Review of Fluid Mechanics*, 43(1):353–375.

Spalart, P. and Allmaras, S. (1992). A one-equation turbulence model for aerodynamic flows. In *30th Aerospace Sciences Meeting and Exhibit*. American Institute of Aeronautics and Astronautics.

Speziale, C. G., Sarkar, S., and Gatski, T. B. (1991). Modelling the pressure–strain correlation of turbulence: An invariant dynamical systems approach. *Journal of Fluid Mechanics*, 227:245–272.

Tennekes, H. and Lumley, J. L. (1972). *A First Course in Turbulence.* M.I.T. Press, Cambridge, Massachusetts and London, England.

Tunstall, R., Laurence, D., Prosser, R., and Skillen, A. (2017). Towards a generalised dual-mesh hybrid LES/RANS framework with improved consistency. *Computers & Fluids*, 157:73 – 83.

Uribe, J. C., Jarrin, N., Prosser, R., and Laurence, D. (2010). Development of a two-velocities hybrid RANS-LES model and its application to a trailing edge flow. *Flow, Turbulence and Combustion*, 85(2):181–197.

van Driest, E. R. (1956). On Turbulent Flow Near a Wall. *Journal of the Aeronautical Sciences (Institute of the Aeronautical Sciences)*, 23(11):1007–1011.

von Kármán, T. (1930). Mechanische Ähnlichkeit und Turbulenz. In *Third International Congress of Applied Mechanics*, pages 85–105, Stockholm.

Wang, M. and Moin, P. (2000). Computation of trailing-edge flow and noise using large-eddy simulation. *AIAA Journal*, 38(12):2201–2209.

Wang, M. and Moin, P. (2002). Dynamic wall modeling for large-eddy simulation of complex turbulent flows. *Physics of Fluids*, 14(7):2043–2051.

Weller, H. G., Tabor, G., Jasak, H., and Fureby, C. (1998). A tensorial approach to computational continuum mechanics using object-oriented techniques. *Computers in Physics*, 12(6):620.

Wilcox, D. (2006). *Turbulence Modeling for CFD*. Number v. 1 in Turbulence Modeling for CFD. DCW Industries.

Wolfshtein, M. (1969). The velocity and temperature distribution in one-dimensional flow with turbulence augmentation and pressure gradient. *International Journal of Heat and Mass Transfer*, 12(3):301 – 318.

Wu, X. and Squires, K. D. (1998). Numerical investigation of the turbulent boundary layer over a bump. *Journal of Fluid Mechanics*, 362:229–271.

Xiao, H. and Jenny, P. (2012). A consistent dual-mesh framework for hybrid LES/RANS modeling. *Journal of Computational Physics*, 231(4):1848 – 1865.

Yang, X. I. A., Sadique, J., Mittal, R., and Meneveau, C. (2015). Integral wall model for large eddy simulations of wall-bounded turbulent flows. *Physics of Fluids*, 27(2):025112.

Yoshizawa, A. (1986). Statistical theory for compressible turbulent shear flows, with the application to subgrid modeling. *Physics of Fluids*, 29(7):2152–2164.

Yoshizawa, A. and Horiuti, K. (1985). A statistically-derived subgrid-scale kinetic energy model for the large-eddy simulation of turbulent flows. *Journal of the Physical Society of Japan*, 54(8):2834–2839.

Zagarola, M. V. and Smits, A. J. (1998). Mean-flow scaling of turbulent pipe flow. *Journal of Fluid Mechanics*, 373:33–79.

Appendix A

Turbulence Models Employed

The following appendix describes the turbulence models used in the current thesis that have not been covered in Chapter 2. The following subgrid-scale models for LES and RANS models are demonstrated.

LES subgrid-scale models:

- Wall-adapting local eddy-viscosity SGS model
- Dynamic one-equation SGS model

RANS models:

- Realisable $k-\varepsilon$ model

A.1 Large Eddy Simulation

A.1.1 Wall-Adapting Local Eddy-Viscosity Model

The wall-adapting local eddy-viscosity model (WALE) of Nicoud and Ducros (1999) is an algebraic eddy viscosity model, which is akin to the 0-equation approach of the Smagorinsky SGS model. However, the WALE model differs from the Smagorinsky model as it is designed to return the correct wall asymptotic behaviour; hence, no damping functions are needed in the near-wall region. The computation of the subgrid-scale viscosity accounts for the rate of strain as well as the rate of rotation tensor to enable the representation of turbulence structures relevant for the subgrid-scale dissipation rate. The WALE model can handle the laminar to turbulent transition process. The SGS viscosity is computed as:

$$\nu_{\mathrm{SGS}} = C_k \Delta \sqrt{k_{\mathrm{SGS}}}, \tag{A.1}$$

where C_k is a model coefficient and k_{SGS} is the subgrid-scale turbulent kinetic energy. The subgrid-scale turbulent kinetic energy is defined as:

$$k_{\mathrm{SGS}} = \left(\frac{C_w^2 \Delta}{C_k}\right)^2 \frac{\left(S_{ij}^d S_{ij}^d\right)^3}{\left(\left(\overline{S}_{ij}\overline{S}_{ij}\right)^{5/2} + \left(S_{ij}^d S_{ij}^d\right)^{5/4}\right)^2}, \tag{A.2}$$

where S_{ij}^d is the traceless symmetric part of the square of the velocity gradient, which is defined as:

$$S_{ij}^d = \frac{1}{2}\left(\frac{\partial \overline{U}_k}{\partial x_i}\frac{\partial \overline{U}_j}{\partial x_k} + \frac{\partial \overline{U}_k}{\partial x_j}\frac{\partial \overline{U}_i}{\partial x_k}\right) - \frac{1}{3}\delta_{ij}\frac{\partial \overline{U}_k}{\partial x_l}\frac{\partial \overline{U}_l}{\partial x_k}, \tag{A.3}$$

and the filtered rate of strain tensor is defined as:

$$\overline{S}_{ij} = \frac{1}{2}\left(\frac{\partial \overline{U}_i}{\partial x_j} + \frac{\partial \overline{U}_j}{\partial x_i}\right). \tag{A.4}$$

The SGS viscosity can be redefined by substituting Equation A.2 into Equation A.1 as:

$$\nu_{\mathrm{SGS}} = (C_w \Delta)^2 \frac{\left(S_{ij}^d S_{ij}^d\right)^{3/2}}{\left(\overline{S}_{ij}\overline{S}_{ij}\right)^{5/2} + \left(S_{ij}^d S_{ij}^d\right)^{5/4}}, \tag{A.5}$$

where C_w is the constant of the model. The WALE model suffers the same limitations as the Smagorinsky SGS model because its model constant C_w is not universal. However, the constant C_w is not as sensitive to the type of flow regime as the Smagorinsky SGS model, and a single value for the constant can be used for a variety of flows.

A.1.2 Dynamic One-Equation Subgrid-Scale Model

This project makes use of the dynamic one-equation SGS model of Kim and Menon (1995), where a transport equation for the subgrid-scale turbulent kinetic energy k_{SGS} is solved. The computation of k_{SGS} enables the phenomenon of the reverse cascade of energy from the subgrid scales to the resolved scales to be captured by the model. Coarse grids employed for high Reynolds number flow leads to a significant proportion of the total turbulence being unresolved which traditional Smagorinsky methods struggle to model. The dynamic one-equation model is designed to represent the full range of the subgrid scales when a coarse grid is used for the LES. The model coefficients are automatically determined to eliminate the problem of the variation of the constants in different flow regimes. The SGS viscosity is computed as:

$$\nu_{\mathrm{SGS}} = C_k \Delta \sqrt{k_{\mathrm{SGS}}}. \tag{A.6}$$

The transport equation for the subgrid turbulent kinetic energy is defined as:

$$\frac{\partial k_{\mathrm{SGS}}}{\partial t} + \frac{\partial \overline{U}_j k_{\mathrm{SGS}}}{\partial x_j} - \frac{\partial}{\partial x_j}\left[(\nu + \nu_{\mathrm{SGS}})\frac{\partial k_{\mathrm{SGS}}}{\partial x_j}\right] = -\tau_{ij}\overline{S}_{ij} - C_\varepsilon \frac{k_{\mathrm{SGS}}^{3/2}}{\Delta}. \tag{A.7}$$

The two model constants C_k and C_ε are dynamically determined. The constant C_k is calculated as:

$$C_k = \frac{M_{ij} L_{ij}^d}{M_{kl} M_{kl}}, \tag{A.8}$$

where the Leonard stress L_{ij} is defined as:

$$L_{ij} = \widetilde{\overline{U}_i \overline{U}_i} - \widetilde{\overline{U}}_i \widetilde{\overline{U}}_i. \tag{A.9}$$

The tensor M_{ij} is defined as:

$$M_{ij} = 2\Delta^2 \widetilde{\overline{S}\,\overline{S_{ij}}} - 2\overline{\Delta}^2 \widetilde{\overline{S}}\,\widetilde{\overline{S_{ij}}}, \tag{A.10}$$

with$\overline{S} = \left(2\overline{S_{ij}}\,\overline{S_{ij}}\right)^{1/2}$. The overline $\bar{}$ refers to the grid filtered quantities, while the tilde operator $\widetilde{}$ represents the test filtered quantities.

The constant C_ε is defined as:

$$C_\varepsilon = (\nu + \nu_{\mathrm{SGS}}) \left(\widetilde{\frac{\partial \overline{U}_i}{\partial x_j} \frac{\partial \overline{U}_i}{\partial x_j}} - \frac{\partial \widetilde{\overline{U}}_i}{\partial x_j} \frac{\partial \widetilde{\overline{U}}_i}{\partial x_j} \right) \div \Delta \left(\frac{1}{2} \left(\widetilde{\overline{U}_i \overline{U}_i} - \widetilde{\overline{U}}_i \widetilde{\overline{U}}_i \right) \right)^{3/2}. \tag{A.11}$$

The constant C_ε is devised to prevent the value from unphysically vanishing at high Reynolds numbers as the effective viscosity is used in its formulation. The dynamic one-equation model is used extensively as the SGS model of the numerical wall function for LES.

A.2 Reynolds-Averaged Navier-Stokes Equations

A.2.1 Realisable $k - \varepsilon$ Turbulence Model

The realisable $k - \varepsilon$ model is a high Reynolds number model that was devised by Shih et al. (1995). Hence, the model requires wall functions to model the near-wall turbulence. The model is created to meet the physical realisability constraints on the Reynolds stress tensor. The normal Reynolds stresses must be positive, while the Schwarz' inequality is imposed on the Reynolds shear stresses ($\left\langle u'_i u'_j \right\rangle^2 \leq \langle u'^2_i u'^2_j \rangle$ - with no summation of indices). The eddy-viscosity is computed as:

$$\nu_t = C_\mu \frac{k^2}{\varepsilon}. \tag{A.12}$$

The coefficient C_μ is a constant in the standard $k-\varepsilon$ model, which leads to the realizability criteria not being satisfied for flows experiencing high strain rates. Shih et al. (1995) proposed a new formulation for C_μ as:

$$C_\mu = \frac{1}{A_0 A_s U^{(*)} \frac{k}{\varepsilon}}, \tag{A.13}$$

where $U^{(*)}$ is defined as:

$$U^{(*)} = \sqrt{\langle S_{ij} \rangle \langle S_{ij} \rangle - \langle W_{ij} \rangle \langle W_{ij} \rangle}, \tag{A.14}$$

and the mean rate of rotation tensor $\langle W_{ij} \rangle$ is defined as:

$$\langle W_{ij} \rangle = \frac{1}{2} \left(\frac{\partial \langle U_i \rangle}{\partial x_j} - \frac{\partial \langle U_j \rangle}{\partial x_i} \right). \tag{A.15}$$

The transport equation for the turbulent kinetic energy is solved as:

$$\frac{\partial k}{\partial t} + \langle U_j \rangle \frac{\partial k}{\partial x_j} = -\langle u'_i u'_j \rangle \frac{\partial \langle U_i \rangle}{\partial x_j} + \frac{\partial}{\partial x_j} \left[\left(\nu + \frac{\nu_t}{\sigma_k} \right) \frac{\partial k}{\partial x_j} \right] - \varepsilon. \tag{A.16}$$

The transport equation for the dissipation rate is based on the dynamic equation of the mean-square vorticity fluctuations for large Reynolds numbers. The transport equation for ε is defined as:

$$\frac{\partial \varepsilon}{\partial t} + \langle U_j \rangle \frac{\partial \varepsilon}{\partial x_j} = C_{\varepsilon_1} S \varepsilon - C_{\varepsilon_2} \varepsilon \frac{\varepsilon}{k + \sqrt{\nu \varepsilon}} + \frac{\partial}{\partial x_j} \left[\left(\nu + \frac{\nu_t}{\sigma_\varepsilon} \right) \frac{\partial \varepsilon}{\partial x_j} \right], \tag{A.17}$$

where the modulus of the mean strain rate tensor S is defined as:

$$S = \left| \langle S_{ij} \rangle \right| = \sqrt{2 \langle S_{ij} \rangle \langle S_{ij} \rangle}. \tag{A.18}$$

The model coefficients are shown in Table A.1.

Table A.1 Coefficients of the realisable $k-\varepsilon$ model

C_{ε_1}	C_{ε_2}	σ_k	σ_ε	C_μ
$\max\left(0.43, \frac{\eta}{5+\eta}\right)$	1.9	1.0	1.2	Eqn. A.14

η	A_0	A_s	ϕ	W
$\frac{Sk}{\varepsilon}$	4.0	$\sqrt{6}\cos(\phi)$	$\frac{1}{3}\cos^{-1}\left(\sqrt{6}W\right)$	$\frac{\langle S_{ij}\rangle\langle S_{jk}\rangle\langle S_{ki}\rangle}{S^3}$

Chapter 7

Paper I: *The Subdomain Wall Function for Large Eddy Simulation*

This paper was submitted to the International Journal of Heat and Fluid Flow on 16/03/2020.

The subdomain wall function for large eddy simulation

Brendan Ehimen Omozopia Iyamabo[a,b,*], Dominique Laurence[a], Alistair Revell[a], Imran Afgan[c,a]

[a] *Department of Mechanical, Aerospace and Civil Engineering, The University of Manchester, Oxford Road, Manchester, M13 9PL, UK*
[b] *EDF Energy R&D UK Centre, Modelling and Simulation Centre, The University of Manchester, Manchester, UK*
[c] *Khalifa University, Department of Mechanical Engineering, P. O. Box 127788, Abu Dhabi, United Arab Emirates*

Abstract

This paper presents the methodology of a new wall function for large eddy simulation (LES). The new wall function, named the subdomain wall function for LES, simulates two regions of the flow domain simultaneously, akin to the wall-modelled LES approach. The first region covers the entire flow domain and solves LES transport equations. The LES grid is deliberately made coarse in the near-wall region to reduce computational costs. The second region is much smaller and overlaps the near-wall area of the LES grid. The second region solves transient Reynolds Averaged Navier Stokes (RANS) transport equations and supplies the LES grid with information to derive drift volumetric-source terms. The subdomain wall function for LES is a simplification of the dual-mesh hybrid RANS/LES method, where the information of a much smaller RANS grid is used to correct the under-resolved inner region of the LES domain using the drift source terms. In return, the top interface of the truncated RANS gird receives partially time-average quantities from the LES grid to complete the boundary conditions of the RANS grid and to enable the use of more advanced turbulence models in the RANS subdomain. This paper presents results of testing the new method in a plane channel flow, periodic hills and an asymmetric plane diffuser.

Keywords: Wall function, Large eddy simulation, Periodic hills,

---

[*] Corresponding author

Email address: `brendan.iyamabo@manchester.ac.uk` (Brendan Ehimen Omozopia Iyamabo)

RANS/LES coupling, Embedded RANS, Asymmetric diffuser

1. Introduction

Large eddy simulation (LES) directly resolves the large energetic scales of turbulent flows while the smaller subgrid-scales are modelled. However, in wall-bounded flows, the integral length scale of the energy-carrying eddies decreases as the flow approaches the wall with a limit scaled by molecular viscosity or inverse Reynolds number, Re. Hence a much finer numerical grid is required to resolve the flow at practical Re numbers. Chapman (1979) estimated that the LES grid size needed to characterise all the large-scale processes in the inner layer of a turbulent boundary flow increased significantly in proportion to $Re^{1.8}$. In contrast, the grid size required to resolve the large-scale motions in the outer region grew moderately as $Re^{0.4}$. These approximations were revisited by Choi and Moin (2012), who estimated that the number of grid points required for a wall-resolving LES scales with $Re^{1.86}$, while the number required for a wall-modelled LES is proportional to Re. Hence, the motivation for wall functions to model the inner region of the wall-bounded turbulent flow statistically.

Several approaches have been developed in literature to model the inner region of a turbulent flow, thereby enabling the utilisation of a coarse grid in the near-wall area for LES. An equilibrium wall function approach was implemented by Deardorff (1970) and Schumann (1975), where a simple algebraic correlation between the wall shear stress and velocity in the first cell at the wall was established. This approach is akin to the standard wall function used in the Reynolds-averaged Navier-Stokes (RANS) method. The equilibrium wall function utilises the assumption of the law of the wall. This assumption limits the use of equilibrium wall functions to relatively simple geometries and flows with fully developed, steady mean-flow state and non-separating boundary layers.

Balaras et al. (1996) developed a wall-layered model, also known as the wall-modelled LES (WMLES), where a separate RANS subdomain is embedded in the first cell of the coarse LES grid. The RANS subdomain solves a simplified boundary-layer momentum transport equation where the pressure gradient is supplied from the first cell of the LES grid. The algebraic mixing length equation is typically the eddy-viscosity model used in the RANS subdomain. The top boundary or interface of the RANS subdomain receives instantaneous filtered velocity information from the LES grid. On the other hand, the LES domain receives wall shear stress information from the RANS subdomain, which acts to correct the under-resolved velocity of the first cell of the coarse LES grid. The implementation of the numerical wall function for RANS computations by Craft et al. (2004) whereby a fine viscous layer resolving 1D grid is embedded in the first near-wall cell is similar to that of the wall-layer LES approach. Further developments or investigations of the wall-modelled LES are conducted by Cabot and Moin (2000), Wang and Moin (2002), Kawai and Larsson (2011), Kawai and Larsson (2013) and Park and Moin (2014). Reviews of the implementation of the wall-layered LES approach can be found in Piomelli and Balaras (2002), Piomelli (2008) and Larsson et al. (2015).

Approaches with a similar LES/RANS grid setup to the wall modelled LES are classified as zonal models. The LES and RANS domains have different numerical integration techniques, which many zonal models seek to harmonise Yang et al. (2015). Consequently, a user has to decide on the number of grid points and the level of grid distribution in the near-wall region of the LES and RANS zones. Also, the user determines the areas of the LES grid that is under-resolved for zonal approaches, which becomes challenging for complex geometries. Yang et al. (2015) implemented a zonal method, termed the integral wall model for LES, where the velocity profile in the RANS zone is approximated by a parametric shape function; the RANS momentum equation is analytically integrated in the wall-normal direction. There are many equations required to define the shape function of the RANS velocity and other parameters, which would become an enormous task if the integral model is extended to buoyancy, heat transfer and rotation cases.

This work develops a new wall function method using the same grid setup as the wall-modelled LES. A consistent coupling between the instantaneous filtered fields of the LES domain and the Reynolds time-averaged fields of the RANS subdomain is established to incorporate more advanced turbulence models in the RANS subdomain, which enables the usage of coarse LES grid in complex geometries. The interface where the RANS grid receives information from the LES domain is moved beyond the first cell of the LES grid as suggested by Kawai and Larsson (2012) to ensure that the interface receives better resolved filtered information. Most importantly, the correction of the coarse LES field is extended beyond the first cell at the wall of the LES domain, with the RANS model smoothly supporting the under-resolved near-wall LES grid through a volumetric-source term in the LES momentum equation. The RANS model automatically informs on the grid quality of the LES, and the novel method determines the extent of the LES grid be corrected without user input. This present proposal termed “subdomain wall function for large eddy simulation (LES-SWF or SWF)” is a simplification of the dual-mesh hybrid RANS/LES method, first proposed by Xiao and Jenny (2012), to ensure the near-wall mean velocity and resolved stress fields of the LES domain are rescaled towards the equivalent fields in the RANS subdomain.

2. The Subdomain Wall Function Framework

The subdomain wall function for LES solves two domains independently but at the same time, as shown in Figure 1. The model is implemented in the open-source code OpenFOAM. The coarse LES grid extends to but does not need to fully resolve the viscous sublayer of the flow to ensure continuity of large eddies travelling across the interface. The RANS subdomain is generated and solved separately. The RANS grid density is biased towards the wall to ensure that the wall distance of the first cell normalised by viscous units is less than one. The RANS subdomain computes quantities that are needed by the near-wall region of the LES domain. On the other hand, the interface of the RANS grid receives information from the LES domain to complete the boundary conditions of the subdomain. The RANS grid is designed to overlap the inner region of the LES domain; the height of the RANS subdomain is constructed to bypass at least the first three wall-normal cells of the LES grid. This height ensures that the interface receives better resolved information at that matching location than from the first cell of the coarse LES grid.

This work computes the exponentially time-weighted average (EWA) of LES fields during a simulation. The EWA of the LES fields of interest is a partial time-average and is assumed to be equivalent to Reynolds averaging. The EWA of an LES field φ is defined as:

$$\langle\varphi\rangle^{EWA} = \int_{-\infty}^{t} \left(\frac{1}{T}\varphi(t')e^{-(t-t')/T}\mathrm{d}t' \right), \qquad (1)$$

where T is the time-scale of the exponentially weighted average. Equation 1 is a solution of the following differential equation using the Leibniz’ rule for

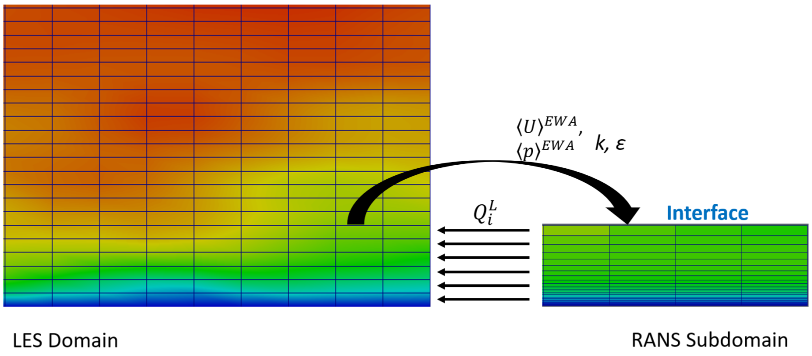

Figure 1: Schematic showing the setup of the subdomain wall function for LES.

differentiation under an integral:

$$\frac{\mathrm{d}\left\langle \varphi \right\rangle^{EWA}}{\mathrm{d}t} = \frac{1}{T}\left(\varphi - \left\langle \varphi \right\rangle^{EWA}\right). \tag{2}$$

Hence, Equation 2 can be approximated to first order as:

$$\left\langle \varphi \right\rangle^{EWA}\Big|_{t_n} = \left(1-\alpha\right)\varphi|_{t_n} + \alpha\left\langle \varphi \right\rangle^{EWA}\Big|_{t_{n-1}}, \tag{3}$$

where n relates to the time step and $\alpha = 1/(1+\Delta t/T)$. The use of the exponentially weighted average prioritizes recent events in the LES simulations and reduces the time length for the average to initialise compared to a standard time average (Tunstall et al., 2017). The averaging time T is ensured to be long enough for the EWA fields to be sufficiently smooth for the use of unsteady RANS models. The EWA of the filtered velocity of the LES domain $\overline{U_i}$ is assumed to be equivalent to the Reynolds-average velocity $\langle U_i \rangle$ as:

$$\left\langle \overline{U_i} \right\rangle^{EWA} \approx \left\langle U_i \right\rangle. \tag{4}$$

The resolved fluctuation about the filtered velocity is defined as:

$$u_i'' = \overline{U_i} - \left\langle \overline{U_i} \right\rangle^{EWA}. \tag{5}$$

Hence the LES stress tensor is defined as:

$$\tau_{ij} = u_i'' u_j'' + \tau_{ij}^{SGS}, \tag{6}$$

where τ_{ij}^{SGS} is the modelled subgrid-scale (SGS) stress tensor and $u_i'' u_j''$ is the resolved stress tensor about the EWA of the filtered velocity field.

2.1. RANS Subdomain

The momentum transport equation for the RANS subdomain is defined as:

$$\frac{\partial \langle U_i \rangle}{\partial t} + \frac{\partial \langle U_i \rangle \langle U_j \rangle}{\partial x_j} = -\frac{1}{\rho}\frac{\partial \langle p \rangle}{\partial x_i} + v\frac{\partial^2 \langle U_i \rangle}{\partial x_i \partial x_j} - \frac{\partial \langle u_i u_j \rangle}{\partial x_j}, \tag{7}$$

where the angle brackets $\langle\ \rangle$ is the Reynolds averaging operator. No modifications are made to the transport equations in the RANS subdomain. However, quantities of the solved variables of the transport equation need to be specified at the interface of the subdomain to complete the boundary conditions. This work maps the partially time-averaged quantities of filtered velocity and pressure from the LES domain to the interface of the RANS grid.

$$\langle U_i \rangle^{\text{RANS}} = \langle \overline{U_i} \rangle^{\text{EWA}}. \tag{8}$$

$$\langle p \rangle^{\text{RANS}} = \langle \overline{p} \rangle^{\text{EWA}}. \tag{9}$$

The use of the partially time-averaged fields ensures a consistent coupling between the two regions at the interface. Furthermore, quantities for turbulence transport equations such as the Reynolds stress tensor, the turbulent kinetic energy and the dissipation rate need to be specified at the interface of the RANS grid. This work maps the computed LES stress tensor of Equation 6 to the interface of the RANS grid. The interface boundary condition of the turbulent kinetic energy k^{RANS} is found by taking the trace of the LES stress tensor as:

$$k^{\text{RANS}} = \frac{1}{2}\left\langle \tau_{ii}^{\text{LES}} \right\rangle^{\text{EWA}}. \tag{10}$$

This work calculates the dissipation rate of the LES domain ε^{LES} by summing the molecular dissipation of the large eddy scales of the flow (not negligible for lower Re numbers) and the subgrid-scale dissipation rate defined as:

$$\varepsilon^{\text{LES}} = 2\nu \overline{S}_{ij}\overline{S}_{ij} - \tau_{ij}^{\text{SGS}}\overline{S}_{ij}, \tag{11}$$

where $\overline{S}_{ij}$ is the filtered rate of train tensor defined as:

$$\overline{S}_{ij} = \frac{1}{2}\left(\frac{\partial \overline{U_i}}{\partial x_j} + \frac{\partial \overline{U_j}}{\partial x_i}\right). \tag{12}$$

The interface boundary condition for the dissipation rate $\varepsilon^{\mathrm{RANS}}$ is obtained by computing the partial time average of the LES dissipation rate at the matching location.

The elliptic blending $k-\varepsilon$ model (EB $k-\varepsilon$) of Billard and Laurence (2012) is used to model turbulence in the RANS subdomain. The two models solve additional quantities. The elliptic blending $k-\varepsilon$ model solves the elliptic blending parameter and the transport equation for the ratio of the normal Reynolds stress to the turbulent kinetic energy. This work prescribes the interface boundary condition for the two additional parameters by making use of ideas by Billard et al. (2015) for coarse-grid high Re applications or embedded local down to the wall resolution. The elliptic blending parameter β is computed algebraically at the interface, which is defined as:

$$\beta\left(y^{+}\right)=\left(1+\left(17/y^{+}\right)^{4}/3\right)^{-1}, \tag{13}$$

where y^{+} is the wall-normal distance normalized by viscous units. The value prescribed for the ratio of the normal Reynolds stress to the turbulent kinetic energy $\Phi = v'^{2}/k$ at the interface of the RANS subdomain is defined as:

$$\Phi\left(y^{+}\right)=min\left[2/3;0.3077\ln\left(y^{+}\right)/\ln\left(10\right)-0.2775\right], \tag{14}$$

where $2/3$ is the upper bound for Φ to guarantee realizability. At high Re with coarse grid LES, $\beta=1$ and $\Phi=2/3$ conditions are sufficient while the above refined conditions are only needed for intermediate Re numbers (for which direct numerical simulation DNS validation data is only available). Reintroducing the wall distance y and friction velocity may seem unfortunate as the elliptic blending $k-\varepsilon$ model was devised to alleviate such doubtful practice, but Billard et al. (2015) provides a correlation for extracting y^{+} from only RANS model results where alpha is an indirect measure of wall proximity.

2.2. LES Domain

The momentum and pressure transport equations for the LES domain are defined as:

$$\frac{\partial\overline{U_i}}{\partial t}+\frac{\partial\overline{U_i}\,\overline{U_j}}{\partial x_j}=-\frac{1}{\rho}\frac{\partial\overline{p}}{\partial x_i}+v\frac{\partial^2\overline{U_i}}{\partial x_i\partial x_j}-\frac{\partial\tau_{ij}^{\mathrm{SGS}}}{\partial x_j}+Q_i, \tag{15}$$

$$\frac{1}{\rho}\frac{\partial^2\overline{p}}{\partial x_i\partial x_i}=-\frac{\partial^2}{\partial x_i\partial x_j}\left(\overline{U_i}\,\overline{U_j}+\tau_{ij}^{\mathrm{SGS}}\right)+\frac{\partial Q_i}{\partial x_i}, \tag{16}$$

where $\overline{\quad}$ is the LES filtering operator and Q_i is a momentum called “drift term” by analogy with two-phase flow modelling where similar source terms force the lighter fluid phase motion to relax towards the denser high-inertia fluid phase values over a characteristic timescale. The drift term is a weak volumetric-source term that corrects the under-resolved near-wall fields of the coarse LES. The term is derived from novel ideas of the hybrid RANS/LES approach of Xiao and Jenny (2012). Quantities from the RANS subdomain are required to compute the drift term. These RANS quantities are interpolated onto the LES grid. The drift term relaxes the solution of the filtered fields of the LES grid in the near-wall region towards the solution of the equivalent Reynolds averaged. This forcing ensures consistency between the mean fields of the two grids where the drift term is active. The drift term is defined as:

$$Q_i = \left(1-\sigma^L\right)\left[\frac{\langle U_i\rangle - \left\langle\overline{U_i}\right\rangle^{\text{EWA}}}{\gamma_{l_1}} + \frac{G_i}{\gamma_{l_2}}\right], \tag{17}$$

where γ_{l_1} and γ_{l_2} are relaxation timescales which determine how quickly the near-wall LES fields become consistent with the RANS subdomain fields. The zoning parameter σ^L varies between 0 and 1 to distinguish the near-wall regions of the LES grid that are under-resolved from the well resolved inner regions. The value of $\sigma^L = 0$ indicates that the region of the LES grid is under-resolved, and hence, the drift term is active in that area. Conversely, the drift term is deactivated in areas of the LES grid where $\sigma^L = 1$.

The first term in Q_i acts to drive the partially time-average LES filtered velocity towards the Reynolds-averaged velocity of the RANS subdomain (the high inertia and viscosity phase in the two-phase flow model analogy). In the second term in Q_i, the resolved and modelled subgrid fluctuations about EWA of the filtered velocity are rescaled to ensure consistency between the LES stress tensor of the main domain and the Reynolds stresses of the RANS subdomain. Since eddy-viscosity models are more popular than Reynolds stress models, the trace of the LES stress tensor is adjusted towards the turbulent kinetic energy field of the RANS subdomain. Consequently, this work uses the ideas of Tunstall et al. (2017) to define the term G_i as:

$$G_i = \left(1-\frac{k_{\text{sgs}}^{\text{EWA}}}{k^{\text{EWA}}}\right)\frac{k^{\text{RANS}}-k^{\text{EWA}}}{k^{\text{RANS}}+k^{\text{EWA}}}\left(\overline{U_i}-\left\langle\overline{U_i}\right\rangle^{\text{EWA}}\right), \tag{18}$$

where $k_{\text{sgs}}^{\text{EWA}}$ is the EWA subgrid turbulent kinetic energy equivalent to the trace of the subgrid stress tensor $k_{\text{sgs}}^{\text{EWA}} = \left\langle \tau_{ii}^{\text{SGS}} \right\rangle^{\text{EWA}}/2$, and k^{EWA} is the partial time-averaged resolved turbulent energy that is equivalent to the trace of the LES stress tensor $k^{\text{EWA}} = \langle \tau_{ii} \rangle^{\text{EWA}}/2$. To ensure that consistency is achieved between the LES turbulent kinetic energy and the RANS subdomain turbulent energy, the resolved and modelled fluctuations in the LES are adjusted according to their relative contributions to the total EWA turbulent kinetic energy of the LES. The adjustment of the modelled fluctuations is accomplished by modifying the production of the subgrid turbulent kinetic energy. This work uses the one-equation subgrid-scale model of Yoshizawa (1986) to compute the modelled turbulent kinetic energy. The term for the production modelled k of the subgrid-scale model is defined as:

$$P_{k_{\text{sgs}}} = P_{k_{\text{sgs}}}^{\text{model}} + \left(1 - \sigma^L\right) \frac{k_{\text{sgs}}^{\text{EWA}}}{k^{\text{EWA}}} \frac{k^{\text{RANS}} - k^{\text{EWA}}}{\gamma_{l_2}}, \tag{19}$$

where $P_{k_{\text{sgs}}}^{\text{model}}$ is the original formulation of the subgrid turbulent kinetic energy production term and the second term represents the additional production of subgrid turbulent kinetic energy needed to ensure that the EWA turbulent kinetic energy of the LES is consistent with the RANS turbulent kinetic energy. The production term returns to the original formulation if the proportion of the subgrid fluctuations to the EWA of the LES turbulent kinetic energy is zero. Note that the RANS model must be selected among those that yield realistic near-wall profiles of k, unlike e.g. the k-omega SST.

The relaxation timescales γ_{l_1} and γ_{l_2} used in the drift terms are not constants but are computed automatically during the simulation. The relaxation timescales are defined as:

$$\gamma_{l_1} = \max\left(C_{\gamma_1} \frac{k^{\text{RANS}}}{\varepsilon^{\text{RANS}}}, \mathrm{d}t\right), \tag{20}$$

$$\gamma_{l_2} = \max\left(C_{\gamma_2} \frac{k^{\text{RANS}}}{\varepsilon^{\text{RANS}}}, \mathrm{d}t\right), \tag{21}$$

where $C_{\gamma_1} = 0.1$ and $C_{\gamma_2} = 0.01$. The relaxation timescales in the LES grid are computed using mapped RANS quantities.

The zoning parameter determines the areas of the LES grid where the volumetric drift term in the LES momentum transport equation is active. The RANS subdomain will guide the LES solution in viscous affected areas where the coarse LES grid saves computational costs but is expected to underperform. The zoning parameter uses the turbulent Reynolds number based on local wall distance to distinguish between the viscous affected and fully turbulent regions. The turbulent Reynolds number Re_y is defined as:

$$Re_y = \frac{\sqrt{k^{\mathrm{RANS}}}y}{\nu}, \tag{22}$$

where $Re_y < 200$ specifies a viscous affected region and $Re_y > 200$ specifies a fully turbulent region. The zoning parameter σ^L is formulated as a blending function which is defined as:

$$\sigma^L = \max \begin{cases} \frac{1}{2}\left(1 + \tanh\left(\frac{Re_y - Re_y^*}{A}\right)\right) & y < h \\ 1 & y \geq h \end{cases} \tag{23}$$

where Re_y^* is the critical turbulent Reynolds number that determines the activation of the drift term and h is the wall-normal height of the RANS subdomain. The areas of the LES grid that are above the interface of the RANS subdomain are automatically deemed to be well resolved. This work uses the recommended constants by Tunstall et al. (2017) of $Re_y^* = 200$ and $A = 10$, which determines the sharpness of the switching in the blending function.

2.3. Implementation in OpenFOAM

The subdomain wall function has been implemented in the open-source code OpenFOAM versions 5 and 6 of Weller et al. (1998). A multi-region solver is implemented in OpenFOAM which solves the RANS and LES domains separately and their respective transport equations. The multi-region solver uses the pressure implicit with splitting of operations (PISO) scheme of Issa (1986) to couple the momentum and pressure transport equations of the LES domain and the RANS subdomain. This work utilises the mesh-to-mesh interpolation library of OpenFOAM to map fields between the RANS and LES grids.

The elliptic blending $k-\varepsilon$ model is used to model turbulence in the RANS subdomain. The elliptic blending $k - \varepsilon$ model is an advanced eddy-viscosity model that accounts for the wall-normal stress anisotropy, thereby better predicting the near-wall turbulence and input values for Equations 18 and 19. For the same reasons, the LES domain uses the one-equation SGS model with a transport equation for the subgrid-scale turbulent kinetic energy. Van

Driest damping is applied to the computation near-wall LES grid length scales.

At the wall of the LES domain, a no slip boundary condition is specified for the velocity field. A Dirichlet boundary condition of zero is prescribed for the subgrid-scale turbulent kinetic energy and zoning parameter fields, with a Neumann boundary condition of zero assigned for pressure and the two relaxation timescales. The drift term is a vector field with the vector components designated the value of zero at the wall.

All transport equations for the two regions are discretised using second-order schemes. A second-order backwards temporal scheme is also used. A new simulation commences with only the LES domain active, and the solvers of the RANS subdomain turned off for at least the first $2T$ of runtime. This feature enables the EWA filtered fields of the LES to develop and allow for a more stable coupling between the main domain and the subdomain when the RANS solvers are turned on.

3. Results for a Plane Channel Flow

The performance of the subdomain wall function is assessed by performing an LES for a fully developed flow through a plane channel of half-height δ. The half-height used for the simulations is 1m. The friction Reynolds number of the flow is 1000, and the results are compared to the DNS dataset of Lee and Moser (2015). The size of the domain of the LES region is $2\pi\delta \times 2\delta \times \pi\delta$ with periodic boundary conditions specified on the streamwise and spanwise boundaries. The channel flow case uses two RANS subdomains corresponding to the two walls of the channel. The LES grid uses $80 \times 60 \times 80$ points with constant spacing in the three spatial directions. The distance of the first cell of the LES grid is $y^+ \approx 17$, with uniform spacing ensuring that the first cell of the LES grid is clearly bypassing the viscous sublayer but straddling the buffer layer which is more challenging than starting from the equilibrium log-layer. The size of each of the RANS subdomain is $2\pi\delta \times 0.2\delta \times \pi\delta$ with periodic boundary conditions on the streamwise and spanwise boundaries. The RANS subdomains use $20 \times 50 \times 10$ points with the wall-normal grid spacing biased towards the wall ensuring the wall distance of $y^+ \leq 1$ for the first cell. A pressure gradient is prescribed to drive the flow in the LES grid and the RANS subdomains. The period used for the exponentially weighted time average is defined as $44\delta/U_B$ where U_B is the bulk velocity of the simulation. A simulation with the subdomain wall function is done with the elliptic blending $k - \varepsilon$ model of Billard and Laurence (2012) used in the RANS subdomains. A second case is done of a pure LES on the coarse grid without the support of a wall function.

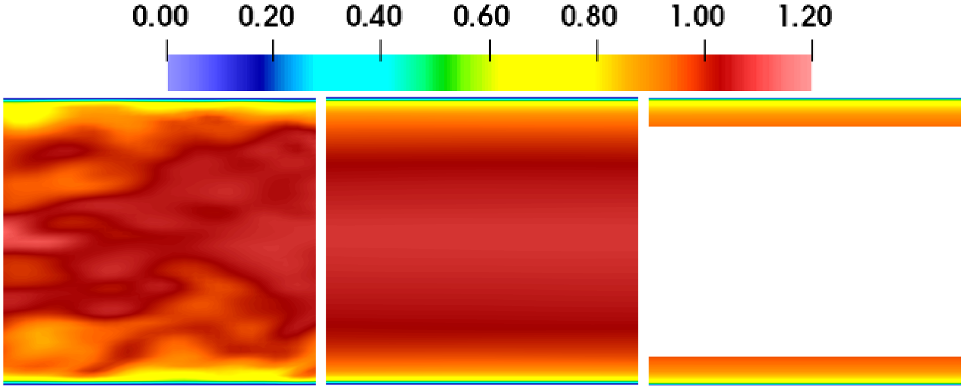

(a) Instantaneous streamwise velocity of the LES grid
(b) Partial mean streamwise velocity of the LES grid
(c) Streamwise velocity of the RANS subdomain

Figure 2: Contours showing the velocity profiles in the LES and RANS domains.

Figure 2 shows the contour plots of velocity in the LES domain and the RANS subdomain. The subdomain wall function drives the partial mean velocity of the LES domain in the near-wall region towards the RANS solution when Figure 2b and Figure 2c are compared. The source term in the LES momentum equation ensures the mean filtered velocity of the LES domain is consistent with the Reynold averaged velocity of the RANS subdomain. The instantaneous filtered velocity of Figure 2a of the LES domain is incompatible with the Reynolds-averaged nature of the RANS subdomain of Figure 2c. Forcing the instantaneous filtered velocity to the interface will introduce too many instabilities in the RANS subdomain. This observation justifies the need for matching the partial mean filtered velocity of the LES grid to the interface of the RANS subdomain.

Figure 3 shows the quantitative plot of the zoning parameter in the wall-normal direction of the LES grid predicted by the subdomain wall function. The height of the interface of the two subdomains is 0.2 m. Hence, the LES grid is automatically set to be fully resolved beyond this height, and the wall function is turned off. Furthermore, the blending function in Equation 23 switches off the drift source term when the turbulent Reynolds number is greater than 200. For the subdomain wall function case, this switch-off happens around the wall-normal height of 0.1 m, where the zoning parameter

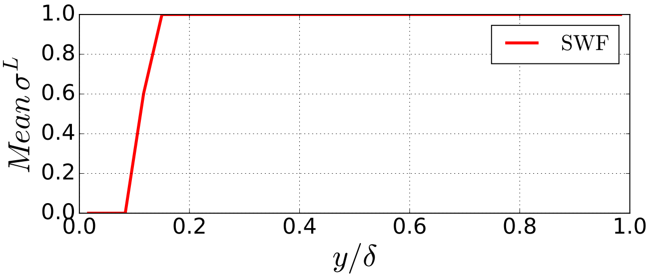

Figure 3: Plot of the mean zoning parameter σ^L predicted in the LES grid by the subdomain wall function. A value of $\sigma^L = 0$ represents the wall function source term being active, the value of $\sigma^L = 1$ represents a well resolved LES grid area and the drift term being turned off.

becomes 1.0. The region of the LES grid where the subdomain wall function is activated is where the zoning parameter is set to 0.0. The switchover between 0 and 1 occurs rapidly.

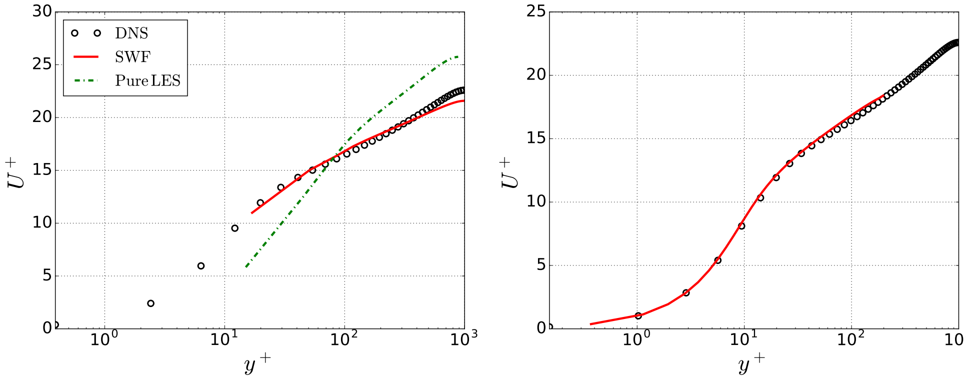

(a) LES Domain

(b) RANS Subdomain

Figure 4: Plots of mean streamwise velocity predicted by the subdomain wall function (—), the case that solves a pure LES on a coarse grid (-·-) and the reference DNS data of Lee and Moser (2015) (∘ ∘ ∘).

The plots of the mean streamwise velocity produced by the LES domain and the RANS subdomains are shown in Figure 4. The results of a pure LES done with the same coarse grid used for the wall function case are also analysed. The results of the plot are normalised by viscous units. The LES case that used the subdomain wall function is in excellent agreement with the reference DNS data, as shown in Figure 4a. The pure LES case predicts the reference data poorly with the coarse near-wall grid straddling the buffer layer. Figure 4b shows results of the RANS regions in excellent agreement with the reference data when fed accurate information at the interface. In return, the subdomain wall function relaxes the mean filtered velocity of the near-wall LES region towards the solution of the RANS subdomains. The drift source term ensures that the mean velocity fields of the LES domain and RANS subdomain are consistent.

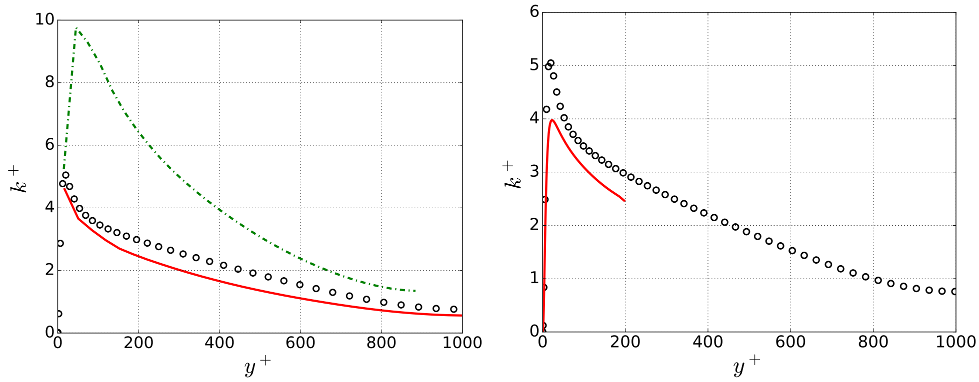

(a) LES Domain

(b) RANS Subdomain

Figure 5: Plots of the mean turbulent kinetic energy in the LES and RANS grids. Legend is the same as Figure 4.

Figure 5 shows the plots of mean turbulent kinetic energy in the LES domain and the RANS subdomains. The results are also normalised by viscous units. The mean turbulent kinetic energy plotted in the LES domain is the summation of the trace of the resolved fluctuations and the modelled turbulent kinetic energy. The turbulent kinetic energy predicted by the subdomain wall function case is in very close agreement with the reference data as shown in Figure 5a. The subdomain wall function modifies the resolved and modelled components of the turbulent kinetic energy in the near-wall region of the LES grid. However, the normalised turbulent kinetic energy of the pure LES case done on the coarse grid is over-predicted due to the low resolution of the near-wall grid, which leads to a high streamwise component of the Reynolds stress but low cross-stream Reynolds stress and shear stress, resulting from poor mixing of momentum. Figure 5b also shows that the results in the RANS subdomains are also in good agreement with the reference DNS data. The peak of the turbulent kinetic energy is somewhat underpredicted by the subdomain wall function in the LES domain. This underprediction is inherent to eddy viscosity models (Billard and Laurence, 2012). Since the peak turbulent kinetic energy occurs near the wall, the subdomain wall function forces the LES case that uses the elliptic blending $k-\varepsilon$ model in the RANS grid also to underpredict the peak turbulent kinetic energy.

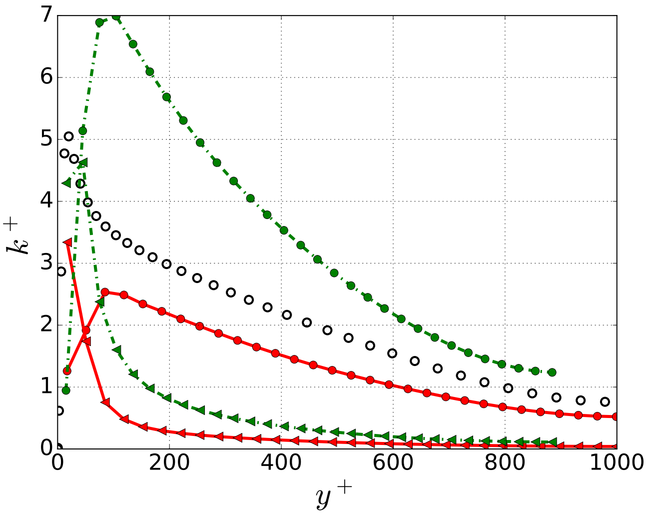

Figure 6: Plot of the resolved and modelled components of the LES total turbulent kinetic energy predicted by the subdomain wall function (—), the case that solves a pure LES on a coarse grid (-·-·) and the reference DNS data of Lee and Moser (2015) (○ ○ ○). Filled circle markers (● ● ●) indicate the resolved component while triangle markers (◄ ◄ ◄)represent the modelled component of the LES total turbulent kinetic energy.

Figure 6 shows the breakdown of the mean turbulent kinetic energy in the LES domain into the resolved and modelled components. The resolved turbulent kinetic energy for the pure LES case is too high in the low-resolution near-wall region, which is unphysical. The source term for the subdomain wall function acts to boost the production of the subgrid-scale turbulent kinetic energy in the near-wall region, consequently reducing the resolved turbulent kinetic energy for the subdomain wall function case. Hence, the EWA of the total turbulent kinetic energy of the LES domain gets rescaled towards the RANS solution in the near-wall region.

3.1. Variation of the Height of the Interface of the RANS Subdomain

We investigate the effect of varying the height h of the interface of the RANS domain as well as the position of the interface height, i.e. the matching location where the LES grid feeds information to the RANS subdomain changes. In the previous section, the height of the RANS subdomain was 0.2δ; the RANS subdomain covering the first 6 grid cells of the $80 \times 60 \times 80$-point LES domain. We investigate the performance where the subdomain covers just the first cell of the LES grid or 2, 3, 4 and 8 cells of the LES grid as in Table 1. The grid resolution in the wall-parallel directions stays the same for all the test cases; the resolution in the wall-normal direction changes as the height of the interface is varied. The nominal friction Reynolds number of the investigation is 1000.

Table 1: Information about the different subdomains used

Case number	Number of LES nodes overlapped	Height of subdomain interface	Grid Specification
1	1	0.0333δ	$20 \times 15 \times 10$
2	2	0.0667δ	$20 \times 20 \times 10$
3	3	0.1δ	$20 \times 25 \times 10$
4	4	0.1333δ	$20 \times 35 \times 10$
5	8	0.2667δ	$20 \times 60 \times 10$

The results for the mean streamwise velocity and the mean turbulent kinetic energy for the LES domain are shown in Figure 6 for the different RANS subdomains used. There is a mismatch of the velocity profile of the case that overlaps just the first cell of the LES grid. This discrepancy is also noticeable for the mean turbulent kinetic energy profile. The mismatched velocity and turbulent kinetic energy profiles are due to the underprediction of the wall shear stress. This difference reduces substantially as the number of LES grid cells overlapped by the RANS subdomain increases and the profiles converges. The log-layer mismatch is eliminated for the profiles when the RANS subdomain overlaps the LES grid by at least 3 points.

3.2. Variation of the Grid Resolution of the LES Domain

The performance of the novel wall function is investigated for three different grid resolutions in the LES domain. The friction Reynolds number of the

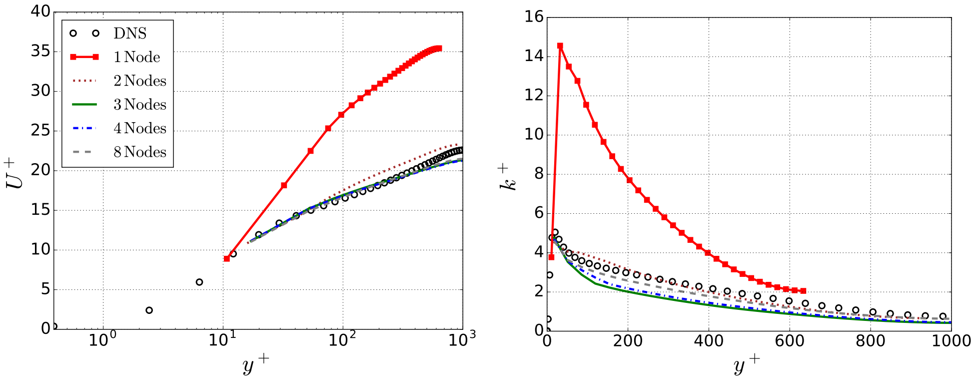

(a) Mean streamwise velocity

(b) Mean turbulent kinetic energy

Figure 7: Plots of the mean streamwise velocity and mean turbulent kinetic energy for LES cases with different subdomain interface heights. The profiles in the plot signify the number of LES grid nodes that are overlapped by the RANS subdomain.

test cases is $\mathrm{Re}_\tau = 1000$. The main LES grid resolution used in this paper contains $80 \times 60 \times 80$ nodes. A finer LES grid and coarser LES grid than the main grid resolution are simulated, and details are provided in Table 2. The three LES grid resolutions used the RANS subdomain configuration. The size of each of the RANS subdomains for all test cases is $2\pi\delta \times 0.2\delta \times \pi\delta$, and the RANS subdomains use $20 \times 50 \times 10$ points with the wall-normal grid spacing biased towards the wall. A pure LES on the $80 \times 60 \times 80$ grid is shown for comparison.

Table 2: Information about the different LES grid resolutions

Case number	Case name	Number of grid points	Grid Specification
1	Coarse	90,000	$60 \times 50 \times 30$
2	Main	384,000	$80 \times 60 \times 80$
3	Medium	720,000	$120 \times 100 \times 60$
4	Fine Medium	1,350,000	$150 \times 120 \times 75$

Figure 8 shows the profiles of the streamwise velocity and the turbulent kinetic energy for different grid resolutions. The plots of the streamwise velocity converge onto the reference DNS data even with the very coarse 90,000-grid. The same trend is witnessed in the turbulent kinetic energy profiles, although the coarse LES grid slightly underpredicts the DNS data. The underprediction of the turbulent kinetic energy by the coarse grid is expected, as there is a reduced number of points to resolve the flow in the outer layer of the plain channel flow. However, the coarse LES grid with the subdomain wall function substantially outperforms the main LES grid simulation done without a wall function. The performance of subdomain wall function for a range of LES grid densities demonstrates the capability of the method to perform scale-resolving simulations accurately at a much-reduced grid resolution. For the Medium and the Fine Medium cases, the LES grid is more refined close to the wall, which can be seen with the additional points near the wall in Figure 8b. Yet the peak total turbulent kinetic energy is slightly underpredicted for the two cases due to the wall function still forcing the LES mean turbulent kinetic energy profile towards the RANS solution in the near-wall region.

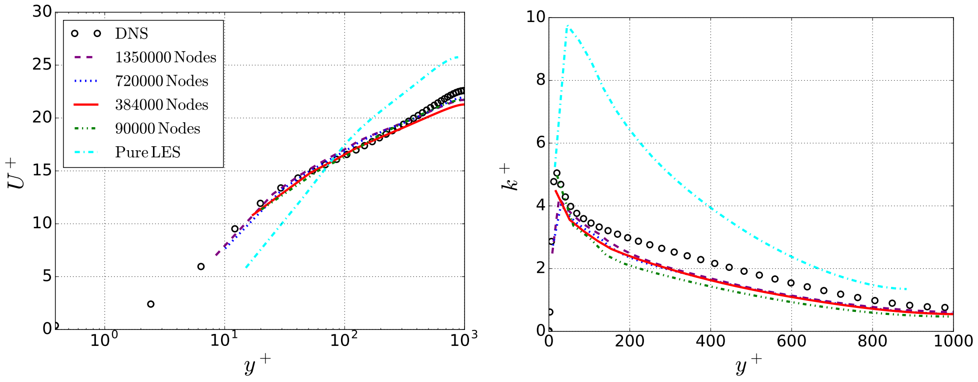

(a) Mean streamwise velocity

(b) Mean turbulent kinetic energy

Figure 8: Plots of the mean streamwise velocity and mean turbulent kinetic energy for LES cases with different grid resolutions in the LES domain.

3.3. Variation of the Friction Reynolds Number

Two different friction Reynolds numbers are examined with the subdomain wall function. The two friction Reynolds numbers are $Re_\tau = 395$ and $Re_\tau = 5200$. The size of the LES domain for the two wall function cases is $2\pi\delta \times 2\delta \times \pi\delta$. For the $Re_\tau = 395$ case, the LES grid is designed to fully resolve the turbulent flow to investigate the performance of the wall function method for a grid with wall - resolved resolution. The LES grid uses

$100 \times 120 \times 50$ with constant spacing in the streamwise and spanwise directions; the LES grid is refined at the wall in the cross-stream direction. The range of the cell spacing in the normal direction normalised by viscous units from the wall to the channel half-height is $0.6 < \Delta y^+ < 24.5$. The wall spacing in the streamwise and spanwise directions is $\Delta x^+ = \Delta z^+ = 24.7$. The two RANS subdomains use a 2D grid to test whether the coupling method of the wall function in the OpenFOAM code is robust for different grid types. The size of each of the RANS subdomain is $2\pi\delta \times 0.2\delta \times \pi\delta$ with $20 \times 50 \times 1$ grid points.

For the much higher Reynolds number case of $Re_\tau = 5200$, a very coarse grid is used in the LES domain. The number of grid points in the LES domain is $100 \times 120 \times 50$ with constant spacing in the three spatial directions. The normalised grid spacings in all directions are $\Delta x^+ \approx 232, \Delta y^+ \approx 130$ and $\Delta z^+ \approx 232$. The height of the RANS subdomain is reduced since the viscous layer is much smaller for the higher friction Reynolds number. The size of the two RANS subdomains is $2\pi\delta \times 0.1\delta \times \pi\delta$ with $20 \times 50 \times 10$ grid points.

Figure 9 shows the plot of the mean streamwise velocity in the LES domain for the $Re_\tau = 395$ and $Re_\tau = 5200$ cases. The results of the $Re_\tau = 395$ case are compared with the DNS data of Moser et al. (1999), while Lee and Moser (2015) provides the reference DNS data for the $Re_\tau = 5200$ case. The mean streamwise velocity of the wall-resolved $Re_\tau = 395$ case is in excellent agreement with the reference DNS data as seen in Figure 9a. This close agreement demonstrates the validity of the subdomain wall function maintaining the accurate mean velocity profile in the highly resolved near-wall region of the LES grid. The left fraction in the square bracket of the drift term in Equation 17 becomes negligible as the partial mean LES velocity of the highly resolved near-wall region is already approximately equivalent to the RANS velocity. Consequently, the influence of the drift source term reduces for the high-resolution region.

On the other hand, the mean velocity of the $Re_\tau = 5200$ case is in good agreement with the DNS data as shown in Figure 9b. A good agreement is established for the high friction Reynolds number despite the very low resolution of the near-wall grid with the drift term being more active in forcing the partial mean LES velocity towards the RANS solution. It should be noted that the viscously affected area of the flow for the $Re_\tau = 5200$ case is thinner than that of the $Re_\tau = 1000$ case. Therefore the size of the RANS subdomain that supports the wall function method can be reduced for higher Reynolds number simulations.

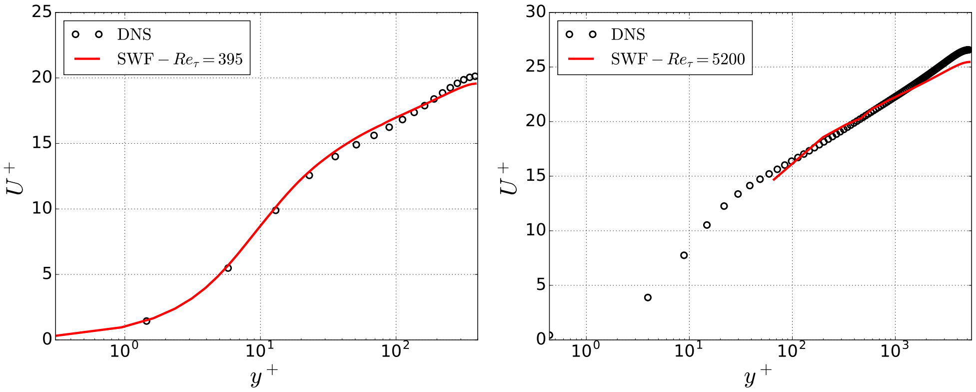

(a) $Re_\tau = 395$

(b) $Re_\tau = 5200$

Figure 9: Plots of the mean streamwise velocity in the LES domain for the two friction Reynolds number cases.

4. Results for a $Re = 10,595$ Flow through Periodic Hills

Flow through periodic hills is further investigated to test the ability of the subdomain wall function method in predicting flow separation and reattachment. This phenomenon has proven challenging for both RANS and wall-modelled LES methods. This case has been studied extensively with a wall-resolved LES by Fröhlich et al. (2005) and Breuer et al. (2009). Tessicini et al. (2005) investigated the case with a hybrid RANS/LES scheme and a wall-modelled LES approach. The wall-modelled LES simplified the momentum equation used in the RANS domain by solving only the diffusion and pressure gradient terms, while the mixing length model was used to model turbulence. Nguyen et al. (2019) also studied this case with a dual-grid hybrid RANS/LES method. The Reynolds number of the test case is $Re = HU_{in}/\nu = 10,595$ where H denotes the height of the hills and U_{in} symbolises the bulk velocity at the hill crest. The size of the computational domain of the LES grid is $9H \times 3.036H \times 4.5H$. In addition, the size of the two RANS subdomains attached to each wall of the LES grid is $9H \times 0.25H \times 4.5H$. Periodic boundary conditions are imposed in the streamwise and spanwise directions for the LES domain and the two RANS subdomains. A pressure gradient, computed from a precursor RANS simulation, is enforced in the streamwise direction in the LES and RANS grids to drive the flow. The results of the test cases are validated by the wall-resolved LES data of Breuer et al. (2009). This reference data used 13.1

million points.

Table 3: Summary of simulations of the periodic hills flow

Case name	Graph name	Main Grid Size	Subdomain Grid Size	Subdomain height
Benchmark data	Reference			
Pure LES	Pure LES	$140 \times 60 \times 70$	N/A	N/A
Subdomain wall function (Equidistance Spacing)	SWF-EQ	$140 \times 60 \times 70$	$100 \times 20 \times 30$	$0.25H$
Subdomain wall function (Refined Spacing)	SWF-Refined	$140 \times 60 \times 70$	$100 \times 20 \times 30$	$0.25H$

Table 3 shows the list of the test cases done for the periodic hills' geometry with the number of grid points specified for each domain. The number of grid points are listed in the streamwise, normal and spanwise directions. The cases are allocated names to be identified on the quantitative plots.

The computational grid of the LES domain for the subdomain wall function case has $140 \times 60 \times 70$ points giving a total of 588,000 nodes. Each of the RANS subdomains has 60,000 grid points. The LES grid is designed not to resolve the viscous sublayer of the flow, while the RANS grids have a wall spacing $y^+ < 1$ for all the first cells. The period used for the exponentially weighted average is defined as $45H/U_{in}$, which was determined to be long enough to average the LES fields. The elliptic blending $k - \varepsilon$ model calculates turbulence in the RANS subdomains. Two LES grids with the same number of nodes are used to test the subdomain wall function case as shown in Figure 10. The first grid is approximately equidistant in the streamwise, spanwise and cross-stream directions. The second grid uses the same total number of cells but is refined in the streamwise direction after the top of the first hill, but equidistant in the spanwise and cross-stream directions. The second grid is designed akin to the grids used in the detached eddy simulation investigation by Mockett et al. (2012).

A pure LES case is run on the same equidistant LES grid used for the subdomain wall function case. The case is done to assess the performance

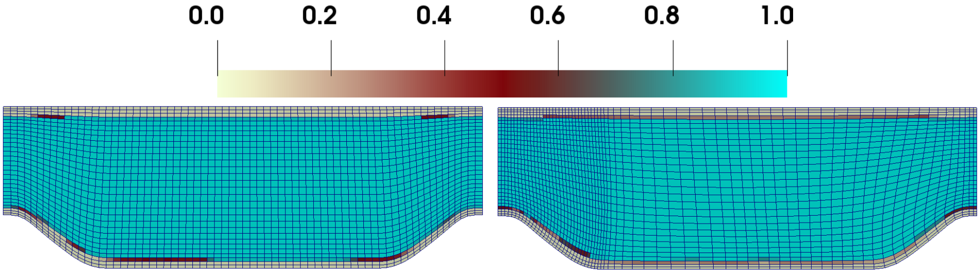

(a) Equidistant grid (SWF-EQ) (b) Streamwise-refined grid (SWF-Refined)

Figure 10: Cross-sectional plane of computational grids (only every 2$^{\mathrm{nd}}$ point shown). Grids are coloured by the zoning parameter.

of the coarse near-wall grid without the aid of the subdomain wall function. The one-equation subgrid-scale model of Yoshizawa (1986) is used to model the subgrid-scale fluctuations.

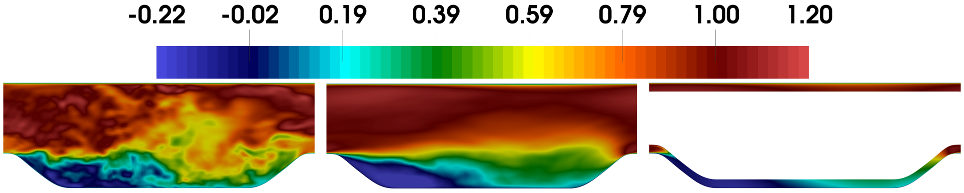

(a) Instantaneous streamwise velocity of the LES grid (b) Partial mean streamwise velocity of the LES grid (c) Streamwise velocity of the RANS subdomain

Figure 11: Contour plots in the LES and RANS domains predicted by the subdomain wall function.

Figure 11 shows the contours plots at a cross-sectional plane of the velocity profiles for the LES and RANS domains. As with the channel flow case, the profile of the instantaneous filtered velocity is not smooth enough to be mapped to the interface of the RANS subdomain. The drift source term uses quantities from the RANS subdomain to correct the near-wall partial mean fields of the LES grids. The source term is applied between the first three to six wall-normal cells of the LES domain as seen in Figure 10, ensuring that the correction of the coarse near-wall LES grid goes beyond the first cell.

Figure 12 shows the profiles of the mean streamwise velocity at different sections of the periodic hills' geometry. The profiles are time- and spatially-averaged in the spanwise direction of the geometry. The subdomain wall function case captures the recirculation bubble. The subdomain wall function

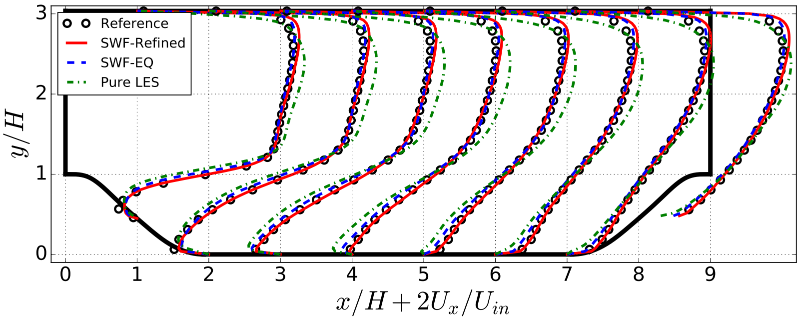

Figure 12: Profiles of the mean streamwise velocity in the LES domain predicted by the subdomain wall function - SWF-Refined (—), by the subdomain wall function - SWF-EQ (- - -) and the coarse LES (-·-·). The black markers (o o o) represent the reference LES data of Breuer et al. (2009).

results are in good agreement with the reference data after the flow reattaches to the wall. On the other hand, the pure LES case under-predicts the velocity throughout the recirculation bubble without the aid of the wall function. The results predicted by the pure LES case recovers when the second hill is reached at $x/H = 8$. When the results of the subdomain wall function predicted by the two grids are compared, the SWF-Refined grid matches the reference data better than the SWF-EQ grid. This better performance of the SWF-Refined domain is due to the refinement of the grid around the point of separation of the flow. Nonetheless, the performance of the SWF-EQ grid is still excellent if one does not have a-priori knowledge of the flow field. Figure 13 shows the profiles of the mean shear stress predicted by the LES domain of the four cases. The subdomain wall function perfectly matches the reference shear stress profiles for most of the flow. There is a discrepancy where the flow separates at $x/H = 1$, which is due to the RANS model not being able to predict the effect of the stress-strain misalignment around the point of separation. The performance of capturing the shear stress profiles degrades for the pure LES case and breaks down for the wall modelled LES case.

Figure 14 shows the prediction of the mean turbulent kinetic energy profiles by the three wall function cases and the pure LES case. There is a significant improvement by the subdomain wall function over the wall modelled LES in predicting the turbulent kinetic energy profiles particularly in the area where local production boosts turbulence between $y/H = 0.5$ and

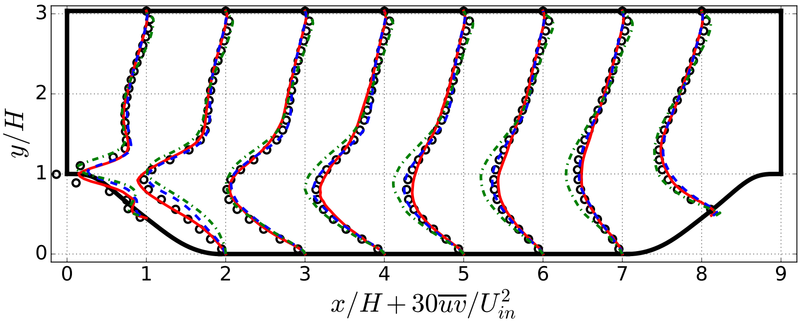

Figure 13: Profiles of the mean shear stress in the LES domain. Legend same as Figure 12.

$y/H = 2$. The peaks of turbulent kinetic energy profiles by the pure LES case are shifted upwards in this region. For the subdomain wall function cases, the SWF-Refined grid performs better than the SWF-EQ grid between $x/H = 1$ to $x/H = 2$, where the grid is refined around the point of separation in the streamwise direction.

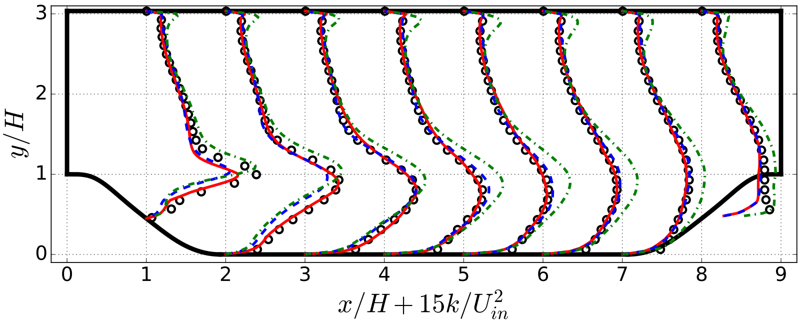

Figure 14: Profiles of the mean turbulent kinetic energy in the LES domain. Legend same as Figure 12.

Figure 15 shows a close-up view around the lower wall for the streamwise velocity and turbulent kinetic energy profiles. The quantitative plots compare the results predicted by the LES domain and the RANS subdomain for the subdomain wall function case using the SWF-Refined grid. The two plots show how the drift term in the momentum equation forces the mean near-wall LES solution towards the RANS subdomain quantities. The RANS region underpredicts the turbulent kinetic energy at $x/H = 8$, and consequently, the drift term rescales the EWA of the total kinetic energy to be underpredicted at that location. This trend illustrates the need for a good RANS model to guide the LES results in the near-wall region where the LES grid is expected to underperform. Furthermore, the consistent matching of the RANS quantities to the equivalent mean LES quantities at the interface is observed in Figure 15.

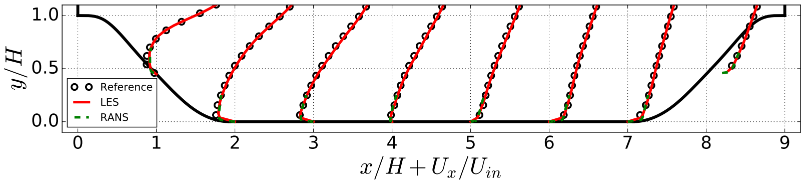

(a) (Mean streamwise velocity profiles

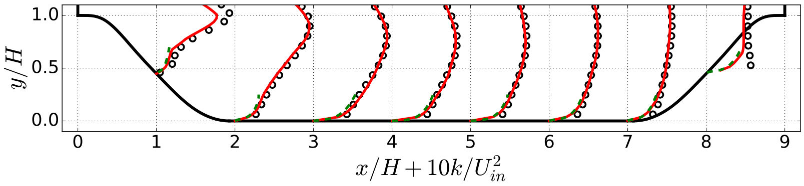

(b) Mean turbulent kinetic energy profiles

Figure 15: Contour plots in the LES and RANS domains predicted by the subdomain wall function.

Table 4: Summary of simulations of the periodic hills flow: separation point($\mathrm{x_s/H}$), reattachment point($\mathrm{x_r/H}$)

Case name	$\mathrm{x_s/H}$	$\mathrm{x_r/H}$
DNS	0.2	4.51
SWF-Refined	0.216	4.197
SWF-EQ	0.159	4.61
Pure LES	0.218	5.559

Figure 16 shows the plot of the mean skin friction along the lower wall of the periodic hills geometry. The results are validated by the DNS data of Krank et al. (2018). The skin friction predicted by the subdomain wall function cases is in good agreement with the reference data. The peak skin friction is underpredicted as the LES grid is too coarse to capture the flow acceleration in that area. The SWF-Refined grid captures the point of separation better than the SWF-EQ grid as seen in Table 4. The pure LES case fails to capture the reference skin friction profile.

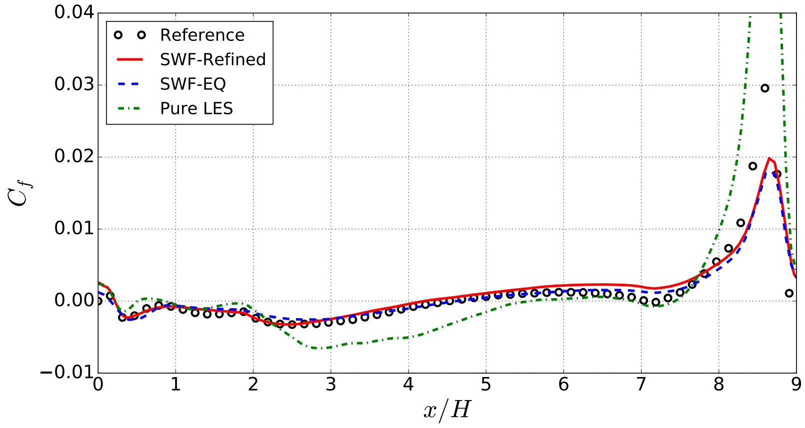

Figure 16: Plot of the skin friction coefficient along the lower wall in the LES domain predicted by the subdomain wall function - SWF-Refined (—), by the subdomain wall function - SWF-EQ (- - -), the wall modelled LES (⋯) and the coarse LES (-·-). The black markers (∘ ∘ ∘) represent the reference DNS data of Krank et al. (2018).

Figure 17 shows the distribution of the mean coefficient of pressure along the bottom wall for different cases. The pressure coefficient is defined as $C_P = \left(\langle P\rangle^{LES} - P_{ref}\right)/0.5\rho U_B^2$, where P_{ref} is the reference pressure. The cases are compared with the DNS data of Krank et al. (2018). The distribution of pressure predicted by the subdomain wall function case using the refined grid is in excellent agreement with the DNS data with changes in the gradient of the pressure profile being well captured. The subdomain wall function case with constant spacing grid underpredicts the pressure coefficient profile but captures the changes in the pressure gradient of the reference data. However, the performance in predicting the pressure coefficient reduces for the pure LES case.

5. Results for a $Re = 18,000$ Flow through an Asymmetric Plane Diffuser

Flow through an asymmetric diffuser is studied with the subdomain wall function. The size of the diffuser investigated matches the specifications of the geometry used in the experiments of Obi et al. (1993a), Obi et al. (1993b)

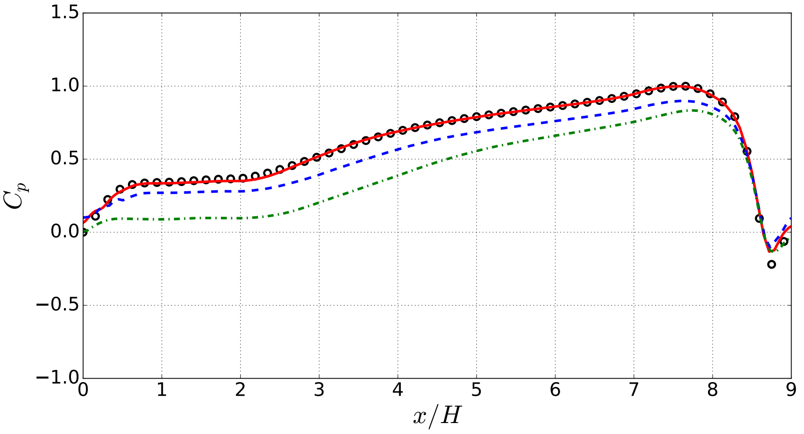

Figure 17: Plot of the coefficient of pressure along the lower wall in the LES domain. Legend same as Figure 16.

and Buice and Eaton (2000). The Reynolds number of the test case is $Re = H_{in}U_{in}/\nu = 18,000$ where H_{in} denotes the height of the inlet channel and U_{in} represents the inlet bulk velocity. The asymmetric diffuser domain consists of a sudden expansion with an angle of 10° with the height of the outlet channel being $4.7H_{in}$. The length and width of the computational domain are $43H_{in}$ and $4H_{in}$ respectively. The size of the two RANS subdomains attached to each wall of the LES domain is $43H_{in} \times 0.2H_{in} \times 4H_{in}$.

Periodic boundary conditions are imposed in the spanwise direction for the LES domain and the two RANS subdomains. A fully developed velocity profile is prescribed at the inlet, while a Neumann boundary condition of zero is prescribed for the pressure and the subgrid-scale turbulent kinetic energy fields. A precursor RANS simulation is done with the plane channel geometry, matching the channel height of the diffuser inlet to generate fully developed profiles for the inlet of the LES domain. The synthetic eddy method (SEM) of Skillen et al. (2016) and Jarrin et al. (2006) is used to instigate the fluctuating velocity field from the specified fully developed velocity profile at the diffuser inlet of the LES domain. Also, the fully developed profiles computed from the RANS precursor simulation are mapped to the inlet of the two RANS subdomains.

The LES domain uses 200 × 50 × 60 points in the computational grid. The total number of grid points in the LES domain is 600,000, which represents a very coarse mesh with the given Reynolds number and length of the computational domain. The grid is biased in the streamwise direction close to the domain inlet as seen in Figure 18. This grid bias leads to the nodes on the right half side of the domain being significantly unrefined. Each of the RANS subdomains has 200 × 30 × 10 grid points resulting in a total of 60,000 nodes. The period used for the exponentially weighted average is $750H_{in}/U_{in}$.

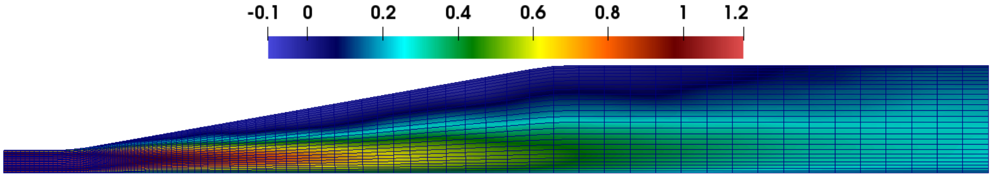

Figure 18: Contour plot of the mean streamwise velocity predicted by the subdomain wall function of the LES domain. The computational grid lines are shown (only every 2$^{\text{nd}}$ point shown.)

A pure LES case is run on the same coarse LES grid used for the subdomain wall function case to study the performance of the help of a wall function. As with the previous cases, the one-equation subgrid-scale model of Yoshizawa (1986) is used to model the subgrid-scale fluctuations. The results of the two cases are validated by the experimental data of Buice and Eaton (2000).

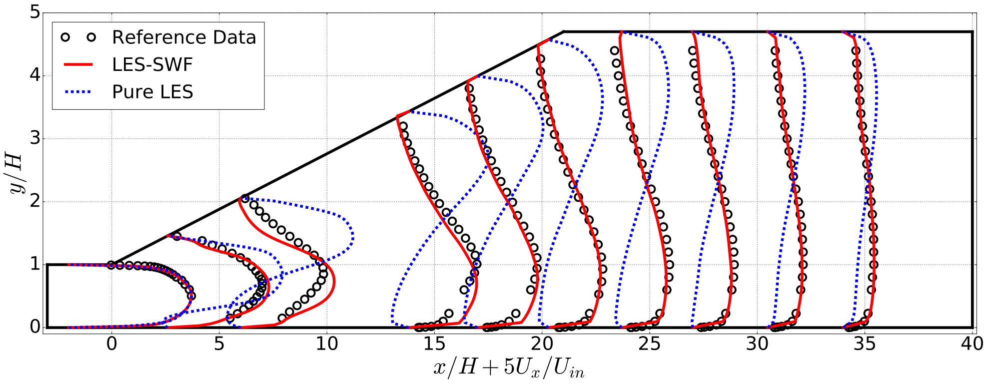

Figure 19: Profiles of the mean streamwise velocity in the LES domain predicted by the subdomain wall function - LES-SWF (—) and the coarse LES (- - -). The black markers (∘ ∘ ∘) represent the reference LES data of Buice and Eaton (2000).

Figure 19 shows the profiles of the mean streamwise velocity at different sections of the asymmetric diffuser domain. The profiles are temporally- and spatially- averaged; the spatial averaging is done in the spanwise direction of the domain. The subdomain wall function case compares favourably with the reference data. The profile in the inlet plane channel is in excellent agreement with the experimental data, which is the expected performance of the subdomain wall function as demonstrated in Section 3. As the domain expands, a recirculation bubble is formed at the upper wall, which is captured by the SWF case. There is a slight discrepancy between the SWF profile and the experimental data around where the flow separates at $x/H = 6$. The recirculation bubble at the upper wall is captured by the SWF case. As identified with the periodic hills case, the discrepancy is due to the supporting RANS subdomain not being able to accurately account for the effect of the stress-strain misalignment around the point of separation. Further down the domain, beyond where the expansion of the geometry stops, the streamwise velocity profiles are favourably predicted despite the extreme coarsening of the LES computational grid.

The pure LES case, which uses the same grid as the subdomain wall function case completely fails in matching the experimental data except at the inlet channel. The pure LES case wrongly predicts the recirculation bubble to be at the lower wall. This inaccurate prediction demonstrates the extremely low resolution of the LES grid to resolve the flow. Despite the low resolution of the LES grid, the RANS subdomains are able to adequately support the near-wall regions of the LES domain to transform the LES calculations to be close to the reference data for the SWF case.

Figure 20 illustrates the plot of the mean friction coefficient along the upper wall of the asymmetric diffuser domain. The results are compared with the experimental data of Buice and Eaton (2000). The profile of the subdomain wall function decently matches the reference profile. The SWF case separates at $x/H = 4.5$ while the experiment recorded the separation at $x/H = 6.0$. The SWF case predicts that the flow reattaches at $x/H = 25$, while the experiment recorded the reattachment point at $x/H = 28.9$. It should be noted that the grid resolution in the streamwise direction for the LES grid is relatively coarse, especially around the point of reattachment. This explains the slight differences in predicting the separation and reattachment points between the SWF case and the experiment. As earlier noted, the pure LES case completely fails in predicting the flow separation/reattachment phenomena along the upper wall.

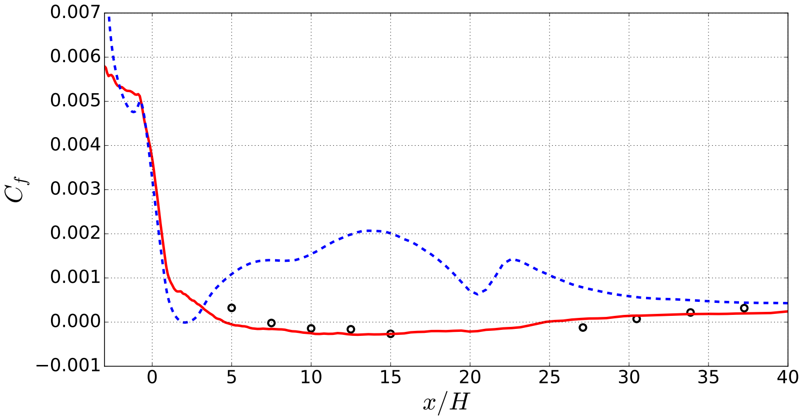

Figure 20: Plot of the skin friction coefficient along the upper wall in the LES domain. Legend same as Figure 19.

6. Conclusions

The subdomain wall function approach for LES has been implemented in OpenFOAM based on the coupling of two regions. The main region covering the flow domain solves LES transport equations, and the grid is deliberately made coarse near the wall. The second region, known as the subdomain, solves RANS transport equations. The subdomain overlaps the under-resolved near-wall region of the LES domain. The RANS subdomain is used to support the under-resolved viscous affected near-wall region of the LES grid.

The RANS subdomain feeds information to the near-wall region of the coarse LES, which leads to the formulation of the volumetric source term. The source term is known as the drift term which corrects the under-resolved region of the LES grid. The source term, which is added to the momentum equation of the LES domain, acts to force the partially time-averaged filtered velocity of the LES grid towards the Reynolds average velocity. This forcing is done in the areas where the LES grid is considered to be under-resolved. Furthermore, the source term adjusts the resolved and modelled fluctuations of the LES domain and rescales the total fluctuations towards the Reynolds stress tensor of the RANS subdomain. This method ensures that the correction of the low-resolution near-wall LES grid is done beyond the first cell of the wall as was previously implemented in traditional wall function approaches.

The LES domain matches partially time-averaged quantities of velocity, pressure and turbulence variables to the interface of the RANS subdomain. This is an improvement on previous approaches that supplied instantaneous filtered velocity to the RANS domain. Hence, a consistent coupling of quantities at the interface between the RANS and LES grids is established. This coupling enables the use of more advanced turbulence models than the mixing length model in the RANS subdomain. The elliptic blending $k-\varepsilon$ model is used in the RANS subdomain.

The subdomain wall function predictions for the $Re_\tau = 1000$ plane channel flow is in excellent agreement with the reference DNS data. The low-resolution near-wall LES grid underperforms without the aid of the wall function. This work investigates the effect of adjusting the height of the interface of the RANS subdomain has on the predictions by the LES grid. There is a log-layer mismatch when the subdomain overlaps either the first one or two cells of the LES grid. The velocity profile predicted by the LES grid collapses to the reference data when the subdomain overlaps at least the first three cells of the LES grid. The subdomain wall function is tested for the $Re_\tau = 395$ plane channel flow and the much higher $Re_\tau = 5200$ plane channel flow with success. The wall function is able to accurately predict the reference DNS streamwise velocity for the $Re_\tau = 5200$ case despite the extremely low grid resolution used in the near-wall region of the LES grid.

The framework is extended to a $Re = 10,595$ flow through periodic hills and a $Re = 18,000$ flow through an asymmetric plane diffuser. A pure LES case is also tested. The predictions by the subdomain wall function are in better agreement with the reference data than the pure LES case.

The subdomain wall function approach has proven successful in utilising low-resolution near-wall LES grids to save computational costs while accurately predicting reference data. This work aims to test the new framework for more demanding test cases. The subdomain wall function approach will be extended to predicting temperature variables in the future.

Acknowledgements

The authors are profoundly grateful for the funding provided by the Department of Mechanical, Aerospace and Civil Engineering of The University of Manchester for this work. The assistance given by the IT Services and the use of the Computational Shared Facility at The University of Manchester are acknowledged. The authors would also like to thank EPSRC for the computational time made available on the UK supercomputing facility ARCHER via the UK Turbulence Consortium (EP/R029326/1).

References

Balaras, E., Benocci, C., Piomelli, U., 1996. Two-layer approximate boundary conditions for large-eddy simulations. AIAA Journal 34, 1111–1119. doi:10.2514/3.13200.

Billard, F., Laurence, D., 2012. A robust $k - \varepsilon - \overline{v^2}/k$ elliptic blending turbulence model applied to near-wall, separated and buoyant flows. International Journal of Heat and Fluid Flow 33, 45 – 58. URL: `http://www.sciencedirect.com/science/article/pii/S0142727X11001512`, doi:https://doi.org/10.1016/j.ijheatfluidflow.2011.11.003.

Billard, F., Laurence, D., Osman, K., 2015. Adaptive wall functions for an elliptic blending eddy viscosity model applicable to any mesh topology. Flow, Turbulence and Combustion 94, 817–842. URL: `https://doi.org/10.1007/s10494-015-9600-x`, doi:10.1007/s10494-015-9600-x.

Breuer, M., Peller, N., Rapp, C., Manhart, M., 2009. Flow over periodic hills – numerical and experimental study in a wide range of Reynolds numbers. Computers & Fluids 38, 433 – 457. URL: `http://www.sciencedirect.com/science/article/pii/S0045793008001126`, doi:https://doi.org/10.1016/j.compfluid.2008.05.002.

Buice, C.U., Eaton, J.K., 2000. Experimental investigation of flow through an asymmetric plane diffuser. Journal of Fluids Engineering 122, 433–435. URL: `https://doi.org/10.1115/1.483278`, doi:10.1115/1.483278.

Cabot, W., Moin, P., 2000. Approximate wall boundary conditions in the large-eddy simulation of high Reynolds number flow. Flow, Turbulence and Combustion 63, 269–291. URL: `https://doi.org/10.1023/a:1009958917113`, doi:10.1023/a:1009958917113.

Chapman, D.R., 1979. Computational aerodynamics development and outlook. AIAA Journal 17, 1293–1313. URL: `https://doi.org/10.2514/3.61311`, doi:10.2514/3.61311.

Choi, H., Moin, P., 2012. Grid-point requirements for large eddy simulation: Chapman's estimates revisited. Physics of Fluids 24, 011702. URL: `https://doi.org/10.1063/1.3676783`, doi:10.1063/1.3676783.

Craft, T.J., Gant, S.E., Iacovides, H., Launder, B.E., 2004. A new wall function strategy for complex turbulent flows. Numerical Heat Transfer, Part B: Fundamentals 45, 301–318. URL: `https://doi.org/10.1080/10407790490277931`, doi:10.1080/10407790490277931, `arXiv:https://doi.org/10.1080/10407790490277931`.

Deardorff, J.W., 1970. A numerical study of three-dimensional turbulent channel flow at large Reynolds numbers. Journal of Fluid Mechanics 41, 453–480. doi:10.1017/S0022112070000691.

Fröhlich, J., Mellen, C.P., Rodi, W., Temmerman, L., Leschziner, M.A., 2005. Highly resolved large-eddy simulation of separated flow in a channel with streamwise periodic constrictions. Journal of Fluid Mechanics 526, 19–66. URL: `https://doi.org/10.1017/s0022112004002812`, doi:10.1017/s0022112004002812.

Issa, R., 1986. Solution of the implicitly discretised fluid flow equations by operator-splitting. Journal of Computational Physics 62, 40 – 65. URL: `http://www.sciencedirect.com/science/article/pii/0021999186900999`, doi:https://doi.org/10.1016/0021-9991(86)90099-9.

Jarrin, N., Benhamadouche, S., Laurence, D., Prosser, R., 2006. A synthetic-eddy-method for generating inflow conditions for large-eddy simulations. International Journal of Heat and Fluid Flow 27, 585–593. URL: `https://doi.org/10.1016/j.ijheatfluidflow.2006.02.006`, doi:10.1016/j.ijheatfluidflow.2006.02.006.

Kawai, S., Larsson, J., 2011. Wall modeling in large-eddy simulation: predicting accurate skin friction at very high Reynolds number, in: 49th AIAA Aerospace Sciences Meeting including the New Horizons Forum and Aerospace Exposition, American Institute of Aeronautics and Astronautics, Inc. pp. 1–20. URL: `http://arc.aiaa.org/doi/pdf/10.2514/6.2011-482`.

Kawai, S., Larsson, J., 2012. Wall-modeling in large eddy simulation: Length scales, grid resolution, and accuracy. Physics of Fluids 24, 015105. URL: `https://doi.org/10.1063/1.3678331`, doi:10.1063/1.3678331.

Kawai, S., Larsson, J., 2013. Dynamic non-equilibrium wall-modeling for large eddy simulation at high Reynolds numbers. Physics of Fluids 25, 015105. URL: `https://doi.org/10.1063/1.4775363`, doi:10.1063/1.4775363, `arXiv:https://doi.org/10.1063/1.4775363`.

Krank, B., Kronbichler, M., Wall, W.A., 2018. Direct numerical simulation of flow over periodic hills up to re_h = 10,595. Flow, Turbulence and Combustion 101, 521–551. URL: `https://doi.org/10.1007/s10494-018-9941-3`, doi:10.1007/s10494-018-9941-3.

Larsson, J., Laurence, S., Bermejo-Moreno, I., Bodart, J., Karl, S., Vicquelin, R., 2015. Incipient thermal choking and stable shock-train formation in the heat-release region of a scramjet combustor. Part II: Large eddy simulations. Combustion and Flame 162, 907 – 920. URL: `http://www.sciencedirect.com/science/article/pii/S0010218014002983`, doi:https://doi.org/10.1016/j.combustflame.2014.09.017.

Lee, M., Moser, R.D., 2015. Direct numerical simulation of turbulent channel flow up to $Re_\tau \approx 5200$. Journal of Fluid Mechanics 774, 395–415. doi:10.1017/jfm.2015.268.

Mockett, C., Fuchs, M., Thiele, F., 2012. Progress in DES for wall-modelled LES of complex internal flows. Computers & Fluids 65, 44–55. URL: `https://doi.org/10.1016/j.compfluid.2012.03.014`, doi:10.1016/j.compfluid.2012.03.014. sixth International Conference on Computational Fluid Dynamics (ICCFD6).

Moser, R.D., Kim, J., Mansour, N.N., 1999. Direct numerical simulation of turbulent channel flow up to $Re_\tau = 590$. Physics of Fluids 11, 943–945. URL: `https://doi.org/10.1063/1.869966`, doi:10.1063/1.869966.

Nguyen, P.T.L., Uribe, J.C., Afgan, I., Laurence, D.R., 2019. A dual-grid hybrid RANS/LES model for under-resolved near-wall regions and its application to heated and separating flows. Flow, Turbulence and Combustion URL: `https://doi.org/10.1007/s10494-019-00070-8`, doi:10.1007/s10494-019-00070-8.

Obi, S., Ohizumi, H., Aoki, K., Masuda, S., 1993a. Experimental and computational study of turbulent separating flow in an asymmetric plane diffuser, in: Ninth Symposium on Turbulent Shear Flows, Kyoto, Japan, p. 305.

Obi, S., Ohizumi, H., Aoki, K., Masuda, S., 1993b. Turbulent separation control in a plane asymmetric diffuser by periodic perturbation, in: RODI, W., MARTELLI, F. (Eds.), Engineering Turbulence Modelling and Experiments. Elsevier, Oxford, pp. 633–642. URL: `https://www.sciencedirect.com/science/article/pii/B9780444898029500642`, doi:https://doi.org/10.1016/B978-0-444-89802-9.50064-2.

Park, G.I., Moin, P., 2014. An improved dynamic non-equilibrium wall-model for large eddy simulation. Physics of Fluids 26, 015108. URL: `https://doi.org/10.1063/1.4861069`, doi:10.1063/1.4861069, `arXiv:https://doi.org/10.1063/1.4861069`.

Piomelli, U., 2008. Wall-layer models for large-eddy simulations. Progress in Aerospace Sciences 44, 437 – 446. URL: `http://www.sciencedirect.com/science/article/pii/S037604210800047X`, doi:https://doi.org/10.1016/j.paerosci.2008.06.001. large Eddy Simulation - Current Capabilities and Areas of Needed Research.

Piomelli, U., Balaras, E., 2002. Wall-layer models for large-eddy simulations. Annual Review of Fluid Mechanics 34, 349–374. URL: `https://doi.org/10.1146/annurev.fluid.34.082901.144919`, doi:10.1146/annurev.fluid.34.082901.144919, `arXiv:https://doi.org/10.1146/annurev.fluid.34.082901.144919`.

Schumann, U., 1975. Subgrid scale model for finite difference simulations of turbulent flows in plane channels and annuli. Journal of Computational Physics 18, 376 – 404. URL: `http://www.sciencedirect.com/science/article/pii/0021999175900935`, doi:https://doi.org/10.1016/0021-9991(75)90093-5.

Skillen, A., Revell, A., Craft, T., 2016. Accuracy and efficiency improvements in synthetic eddy methods. International Journal of Heat and Fluid Flow 62, 386 – 394. URL: `http://www.sciencedirect.com/science/article/pii/S0142727X16305604`, doi:https://doi.org/10.1016/j.ijheatfluidflow.2016.09.008.

Tessicini, F., Temmerman, L., Leschziner, M., 2005. Approximate near-wall treatments based on zonal and hybrid RANS-LES methods for LES at high Reynolds numbers, in: Rodi, W., Mulas, M. (Eds.), Engineering Turbulence Modelling and Experiments 6. Elsevier, pp.

359–368. URL: `https://doi.org/10.1016/b978-008044544-1/50034-0`, doi:10.1016/b978-008044544-1/50034-0.

Tunstall, R., Laurence, D., Prosser, R., Skillen, A., 2017. Towards a generalised dual-mesh hybrid LES/RANS framework with improved consistency. Computers & Fluids 157, 73–83. doi:10.1016/j.compfluid.2017.08.002.

Wang, M., Moin, P., 2002. Dynamic wall modeling for large-eddy simulation of complex turbulent flows. Physics of Fluids 14, 2043–2051. URL: `https://aip.scitation.org/doi/abs/10.1063/1.1476668`, doi:10.1063/1.1476668, `arXiv:https://aip.scitation.org/doi/pdf/10.1063/1.1476668`.

Weller, H.G., Tabor, G., Jasak, H., Fureby, C., 1998. A tensorial approach to computational continuum mechanics using object-oriented techniques. Computers in Physics 12, 620–631. URL: `https://doi.org/10.1063/1.168744`, doi:10.1063/1.168744.

Xiao, H., Jenny, P., 2012. A consistent dual-mesh framework for hybrid LES/RANS modeling. Journal of Computational Physics 231, 1848 – 1865. URL: `http://www.sciencedirect.com/science/article/pii/S0021999111006516`, doi:https://doi.org/10.1016/j.jcp.2011.11.009.

Yang, X.I.A., Sadique, J., Mittal, R., Meneveau, C., 2015. Integral wall model for large eddy simulations of wall-bounded turbulent flows. Physics of Fluids 27, 025112. URL: `https://doi.org/10.1063/1.4908072`, doi:10.1063/1.4908072, `arXiv:https://doi.org/10.1063/1.4908072`.

Yoshizawa, A., 1986. Statistical theory for compressible turbulent shear flows, with the application to subgrid modeling. Physics of Fluids 29, 2152–2164. URL: `https://doi.org/10.1063/1.865552`, doi:10.1063/1.865552.

Chapter 8

Paper II: *Large Eddy Simulation of Turbulent Heat Transfer through a Circular* 90° *Pipe Bend*

This paper was submitted to the International Journal of Heat and Mass Transfer on 10/03/2020.

Large eddy simulation of turbulent heat transfer through a circular 90° pipe bend

Brendan Ehimen Omozopia Iyamabo[a,b,*], Alistair Revell[a,**], Dominique Laurence[a], Imran Afgan[c,a]

[a] *Department of Mechanical, Aerospace and Civil Engineering, The University of Manchester, Oxford Road, Manchester, M13 9PL, UK*
[b] *EDF Energy R&D UK Centre, Modelling and Simulation Centre, The University of Manchester, Manchester, UK*
[c] *Khalifa University, Department of Mechanical Engineering, P. O. Box 127788, Abu Dhabi, United Arab Emirates*

Abstract

This paper presents a large eddy simulation analysis of turbulent heat transfer flow through a 90° circular pipe bend. The ratio of the radius of curvature of the bend to the pipe diameter is 1.5, while the bulk Reynolds number of the simulation based on the pipe diameter is 40,000. Heat transfer augmentation is observed along the outer wall as the development of counter-rotating vortices transports cold fluid towards the outer heated wall. The maximum Nusselt number is 1.85 of the inlet straight pipe value and is located at the outer wall of the bend exit. Heat transfer decreases then increases along the inner wall. The wall heat flux fluctuations are greatly enhanced on the side and outer walls, and also at a thin area along the inner wall. The presence of a pair of counter-rotating vortices leads to the conveyance of peak thermal fluctuations towards the core of the flow where the turbulence fields are strongly anisotropic. With the absence of heat transfer experimental data for 90° pipe bends, this work compares the numerical results with two mass transfer experimental datasets using a dissolvable wall technique. The increasing heat transfer coefficient along the outer wall of the pipe bend compares favourably with the mass transfer data of the Mazhar et al. (2013)

---

[*] Corresponding author
[**] Corresponding author

Email addresses: `brendan.iyamabo@manchester.ac.uk` (Brendan Ehimen Omozopia Iyamabo), `alistair.revell@manchester.ac.uk` (Alistair Revell)

Preprint submitted to International Journal of Heat and Mass Transfer August 3, 2021

experiment. In contrast along the inner wall, the heat transfer profile follows the trend of Ikarashi et al. (2017) experimental data. Heat transfer along the outer wall maintains a correlation with skin friction. However, heat transfer along the inner wall, which is significantly influenced by the development of secondary flow, scales more with turbulent intensity rather than with wall shear stress.

Keywords: Pipe bend, Large eddy simulation, Heat transfer, Mass transfer, Turbulent pipe flow, 90-degrees bend

---

1. Introduction

Turbulent flow in pipe bend configurations is found in many engineering components in thermal power industries, particularly those connected with convective heat transport. A review of industrial applications with curved pipe geometries can be found in Vashisth et al. (2008). Industrial applications such as heat exchangers take advantage of pipe bends enhancing thermal mixing of the fluid. Hence, understanding the physical processes through curved pipe geometries will improve the modelling of the heat and flow phenomena through pipe bends and enable engineers to enhance the performance of the dependent thermal and flow devices.

Thermal flow through pipe bends are considerably more complex than straight pipe flows as the bend redirects various sections of the flow which leads to the generation of a cross-stream pressure field that balances the centrifugal forces acting on the fluid. The imbalance of the cross-stream pressure gradient and centrifugal forces leads to the alteration of the flow and thermal fields, and the establishment of counter-rotating fluid particle motions. These motions, also known as the Dean vortices, act to move the higher inertia core of the fluid towards the outer wall leading to thermal and mechanical fatigue on the pipe walls. In addition to the development of secondary motions, the bend geometry induces temperature and velocity profile inhomogeneity on cross-sectional planes, adverse and favourable pressure gradients in different areas of the pipe and changes due to turbulent heat flux and stresses due to transverse streamline curvature effects. Hydrodynamic turbulent flows in pipe bends have been investigated in several experimental studies such as Enayet et al. (1982), Azzola et al. (1986), Sudo et al. (1998) and Ebara et al. (2010). Sakakibara and Machida (2012), Kalpakli and Örlü (2013), Hellström et al. (2013) and Vester et al. (2015) investigated the swirl switching phenomena experimentally utilising two-dimensional (2D) proper orthogonal decomposition (POD).

The increase in computational power has led to bent pipe flows being studied more in-depth with scale-resolving methods. Flow statistics of turbulent flow through pipe bends have been generated with wall-resolved large eddy simulation (LES) by Röhrig et al. (2015), Holgate (2018), Tunstall et al. (2016), while Iyamabo and Afgan (2018) conducted an LES on a coarse grid using a novel wall function. Investigation of the swirl-switching phenomena was extended using LES by Rütten et al. (2001), Rütten et al. (2005) and Carlsson et al. (2015), while Noorani and Schlatter (2016) were the first to do the swirl-switching analysis with direct numerical simulation (DNS). Further DNS studies have been done by Wang et al. (2018) and Hufnagel et al. (2018). A review of the recent experimental and numerical studies in curved pipe geometries can be found in Vester et al. (2016).

Despite the numerous studies on hydrodynamic flow, relatively few investigations have included heat transfer. Baughn et al. (1987) conducted an experiment and Cvetkovski et al. (2015) performed a detached eddy simulation of heat transfer through a U-Bend pipe, where heat transfer enhancement along the outer wall is observed. Salimpour (2009) conducted experiments to measure the heat transfer coefficient of shell and helically coiled tube heat exchangers, while Acharya et al. (2001), Li et al. (1998) and Lin and Ebadian (1999) performed numerical analysis of heated helically coiled pipes. Kang and Yang (2015) and Di Liberto and Ciofalo (2013) used LES and DNS respectfully to study turbulent heat transfer in toroidal pipes with periodic boundary conditions specified for the inlet and outlet of the pipe; heat transfer rates were discovered to be larger in toroidal pipes than straight pipes. To the best of the authors' knowledge, no work has been published on turbulent heat transfer through a 90° pipe bend except for the Reynolds-averaged Navier Stokes (RANS) study done by Iyamabo (2015).

This present numerical study is aimed at assessing the evolution of thermal and flow properties through the bend. The main purpose is to gain an understanding of turbulent heat transfer as the flow develops through a 90° circular pipe bend. The thermal field data is presented as forced convection due to the secondary velocity and the fluctuating velocity fields greatly determining the level of heat transfer coefficient through the pipe. The heat transfer results are compared with the mass transfer experimental data of Mazhar et al. (2013) and Ikarashi et al. (2017), who measured the mass transfer coefficient of a 90° pipe using a dissolvable wall technique. The experiment of

Mazhar et al. (2013) utilised test sections of cast from gypsum and was done over the range of Reynolds numbers: 40,000 - 130,000. Mazhar et al. (2013) reported that the normalised mass transfer enhancement through the bend is nearly independent of Reynolds number. Ikarashi et al. (2017) did their experiment at the Reynolds number of 50,000 using plaster walls. In the preparation of the plaster walls, Ikarashi et al. (2017) used a vacuum pump to remove air bubbles to reduce the effect of roughness on the plaster surface. The validation of the numerical heat transfer results with the experimental data is inspired by the Chilton-Colburn analogy, which correlates heat and mass transfer(Chilton and Colburn (1934) and Colburn (1964)).

In this study, a large eddy simulation of forced convection turbulent heat transfer through a 90° pipe bend has been performed. The ratio of the radius of curvature of the bend to the pipe diameter is 1.5, and the bulk Reynolds number based on pipe diameter is 40,000. These two specifications match those of the mass transfer experiment of Mazhar et al. (2013), while the curvature of the bend is equivalent to the Ikarashi et al. (2017) experimental setup. An intrinsic coordinate system is defined to ensure that the streamwise component of the velocity is aligned with the tangential path of the flow as the path changes through the bend, while the cross-stream component is normal to the path. The spanwise component of the intrinsic coordinate remains the same as the spanwise component of the Cartesian coordinate. The usage of the intrinsic coordinate system enables the generation of a comprehensive dataset of first and second-order thermal and flow statistics that is not found in previous numerical publications of 90° pipe bends.

2. Numerical Methodology

The Navier-Stokes equations govern the conservation of mass and momentum for an incompressible Newtonian fluid. The transport equations for the filtered mass and momentum are defined as:

$$\frac{\partial \overline{U}_i}{\partial x_i} = 0, \tag{1}$$

$$\frac{\partial \overline{U}_i}{\partial t} + \frac{\partial \overline{U}_i \overline{U}_j}{\partial x_j} = -\frac{1}{\rho}\frac{\partial \overline{p}}{\partial x_i} + \nu \frac{\partial}{\partial x_j}\left(\frac{\partial \overline{U}_i}{\partial x_j} + \frac{\partial \overline{U}_j}{\partial x_i}\right) - \frac{\partial \tau_{ij}^{SGS}}{\partial x_i}, \tag{2}$$

where $\overline{U}_i$ and $\overline{p}$ are the filtered velocity and pressure fields. The term τ_{ij}^{SGS} represent the unresolved stresses which is modelled using the Boussinesq approximation defined as:

$$\tau_{ij}^{SGS} = \frac{1}{3}\delta_{ij}\tau_{kk} - 2\nu_{SGS}\overline{S}_{ij}, \tag{3}$$

where ν_{SGS} is the subgrid viscosity, δ_{ij} is the Kronecker delta and $\overline{S}_{ij}$ is the filtered rate of strain tensor define as:

$$\overline{S}_{ij} = \frac{1}{2}\left(\frac{\partial \overline{U}_i}{\partial x_j} + \frac{\partial \overline{U}_j}{\partial x_i}\right). \tag{4}$$

The isotropic term τ_{kk} in Equation 3 is absorbed in the filtered pressure term in the Navier Stokes equation. The subgrid viscosity ν_{SGS} is computed using the dynamic Smagorinsky model developed by Germano et al. (1991) defined as:

$$\nu_{SGS} = C_D\Delta^2\sqrt{2\overline{S}_{ij}\overline{S}_{ij}}, \tag{5}$$

where Δ is the filter width calculated as the cube root of the grid cell volume and C_D is the coefficient which is dynamically evaluated by the method proposed by Lilly (1992). Negative effective viscosity $\nu + \nu_{SGS}$ values are reset to zero to prevent numerical instabilities (Passalacqua, n.d.).

The temperature variable in the energy transport equation is treated as a passive scalar. Constant wall temperature is specified as the thermal wall boundary condition. The transport equation for temperature using the simple gradient-diffusion hypothesis for the turbulent heat flux term is defined as:

$$\frac{\partial \overline{T}}{\partial t} + \overline{U}_j\frac{\partial \overline{T}}{\partial x_j} = \frac{\partial}{\partial x_j}\left(\frac{\nu}{Pr}\frac{\partial \overline{T}}{\partial x_j} + \frac{\nu_{SGS}}{Pr_t}\frac{\partial \overline{T}}{\partial x_j}\right), \tag{6}$$

where Pr and Pr_t are the Prandtl and turbulent Prandtl numbers respectively. The turbulent Prandtl number relates the subgrid-scale turbulent heat flux to the subgrid-scale turbulent viscosity as $-\overline{u_i'\theta'}_{SGS} = \frac{\nu_{SGS}}{Pr_t}\frac{\partial \overline{T}}{\partial x_j}$.

The three components of the velocity vector $\overline{U}_i$ in Cartesian coordinates, U_x, U_y and U_z are converted to their intrinsic components U_s, U_c and U_z during the simulation as seen in the schematic in Figure 1. The streamwise component of the velocity vector in the intrinsic coordinate system is aligned with the path tangent to the streamline of the pipe bend. Also, the cross-stream component is normal to the path forming a pair of orthogonal vectors

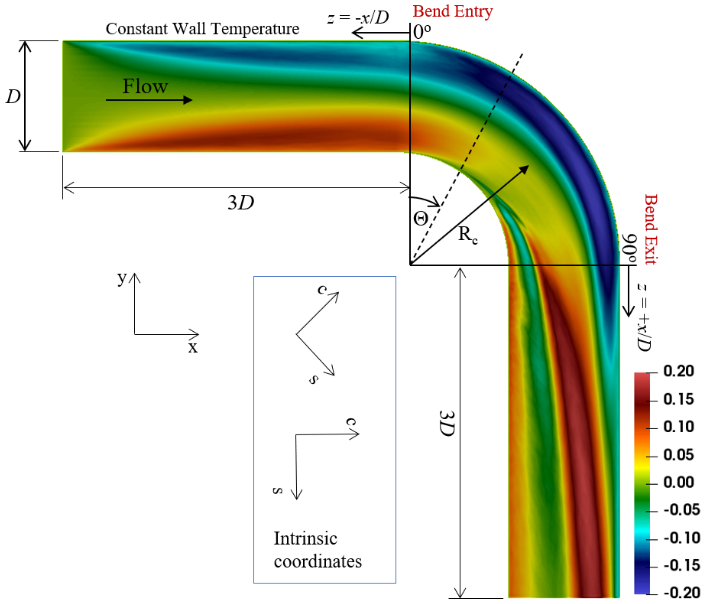

Figure 1: Schematic showing the setup of the computational domain. The contour of wall-normal heat flux is shown. Contour is shown on the symmetry midplane.

with the streamwise velocity. The binormal velocity U_z in the intrinsic coordinates that is normal to both the streamwise and cross-stream velocities is the same as the spanwise velocity in Cartesian coordinates. The streamwise velocity U_s and the cross-stream (curvilinear normal) velocity U_c are defined in three sections of the pipe: the inlet straight pipe, the bend and the outlet straight pipe. Through the inlet straight pipe section, the streamwise and cross-stream velocities are defined as:

$$\overline{U}_s = \overline{U}_x, \tag{7}$$

and

$$\overline{U}_c = \overline{U}_y, \tag{8}$$

Through the pipe bend, the tangential and normal components of the velocity vector are defined as:

$$\overline{U}_s = \overline{U}_x \cos\Theta - \overline{U}_y \sin\Theta, \tag{9}$$

and

$$\overline{U}_c = \overline{U}_x \sin\Theta + \overline{U}_y \cos\Theta, \tag{10}$$

Through the outlet straight pipe section, the streamwise and cross-stream velocities are defined as:

$$\overline{U}_s = -\overline{U}_y, \tag{11}$$

and

$$\overline{U}_c = \overline{U}_x, \tag{12}$$

The heat transfer coefficient is non-dimensionalised as the Nusselt number. The Nusselt number is defined as:

$$Nu = \frac{D}{(T_w - T_b)} \frac{\partial \overline{T}}{\partial n}, \tag{13}$$

where D is the pipe diameter, T_w is the wall temperature, T_b is the bulk temperature at the inlet and $\partial \overline{T}/\partial n$ represents the wall-normal gradient of the temperature. The bulk temperature at the outlet increased by less than 1% compared to the inlet. Hence, Equation 13 is used for the formulation of the Nusselt number. A non-dimensional temperature field, known as the temperature coefficient T^*, is defined for post-processing analysis as:

$$T^* = \frac{T_w - \overline{T}}{T_w - T_b}. \tag{14}$$

Note that the temperature coefficient vanishes to zero at the wall. The non-dimensional temperature is always positive in the bulk flow as the wall heat flux is defined as positive if entering the fluid, and negative otherwise.

The wall shear stress vector is also defined at the wall. The wall shear stress is also converted into intrinsic components to represent better the evolution of skin friction through the bend. The wall shear stress is defined as:

$$\tau_w = \nu \frac{\partial \overline{U}_i}{\partial n}, \tag{15}$$

where ν is the kinematic viscosity and $\partial \overline{U}_i/\partial n$ is the wall-normal gradient of the velocity vector in intrinsic coordinates.

The velocity field in intrinsic coordinates U_i can be split into a mean part and a fluctuating component. This decomposition is defined as:

$$U_i = \langle U_i \rangle + u'_i, \tag{16}$$

where $\langle U_i \rangle$ is the mean velocity determined by time-averaging and u'_i is the fluctuating part of the velocity in intrinsic coordinates. Consequently, the components of the Reynolds stress tensor τ''_{ij} in intrinsic coordinates is defined as:

$$\tau''_{ij} = u'_i u'_j. \tag{17}$$

This work also calculates the tangential $\langle u'_s \theta' \rangle$, the flow normal $\langle u'_c \theta' \rangle$ and the spanwise $\langle u'_z \theta' \rangle$ components of the turbulent (Reynolds) heat flux $\langle u'_i \theta' \rangle$. The resolved turbulent heat flux is defined as:

$$\langle u'_i \theta' \rangle = \left\langle \overline{U_i T} \right\rangle - \left\langle \overline{U_i} \right\rangle \left\langle \overline{T} \right\rangle. \tag{18}$$

The SGS turbulent heat flux is defined as:

$$\langle u'_i \theta' \rangle_{SGS} = \frac{\nu_{SGS}}{Pr_t} \left\langle \frac{\partial \overline{T}}{\partial x_i} \right\rangle. \tag{19}$$

The total turbulent kinetic energy is the summation of the trace of the resolved Reynolds stress tensor and the subgrid-scale turbulent kinetic energy. The modelled turbulent kinetic energy is obtained from the subgrid-scale turbulence model and is defined as:

$$k_{SGS} = C_D \Delta^2 \times 2 \overline{S}_{ij} \overline{S}_{ij}, \tag{20}$$

where C_D is a coefficient that is dynamically computed. Hence, the mean total turbulent kinetic energy is defined as:

$$k = \frac{1}{2} \langle \tau''_{ii} \rangle + \langle k_{SGS} \rangle. \tag{21}$$

The computational grid contains 30 million hexahedral nodes and is multiblock structured. The grid has 700 cells along the centreline in the streamwise direction. The viscous sublayer of the pipe flow is well resolved. The non-dimensional near-wall grid spacings are specified as $\Delta\theta^+ \leq 15$ and $\Delta x^+ \leq 30$ in the circumferential and streamwise directions respectfully. The wall-normal grid spacing of the cell centres next to the wall is designed as $y^+ < 1$.

The ratio of the grid cell size to the Kolmogorov length scale (Δ/η) is computed to determine if the grid is well designed. The Kolmogorov length scale is estimated as $\eta = \left(\nu^3/\varepsilon\right)^{1/4}$. Fröhlich et al. (2005) recommends $\Delta/\eta \leq 12$ to ensure that the computational grid is designed to resolve a significant portion of the turbulence. Postprocessing the results shows that at the core of the pipe the ratio has a value of $\Delta/\eta \approx 3$ and increases to a maximum value of $\Delta/\eta \approx 9$ in some sections near the wall. The increased value of Δ/η is anticipated as the dissipation rate is expected to be higher near the walls. This work fulfils the criteria of $\Delta/\eta \leq 12$ throughout the grid. Further investigation of the resolution requirements of the LES reveals that the grid resolves at least 90% of the total turbulent kinetic energy. This result is in line with the criteria by Pope (2000) that the portion of the subgrid-scale turbulent kinetic energy to the total should be kept below 20%.

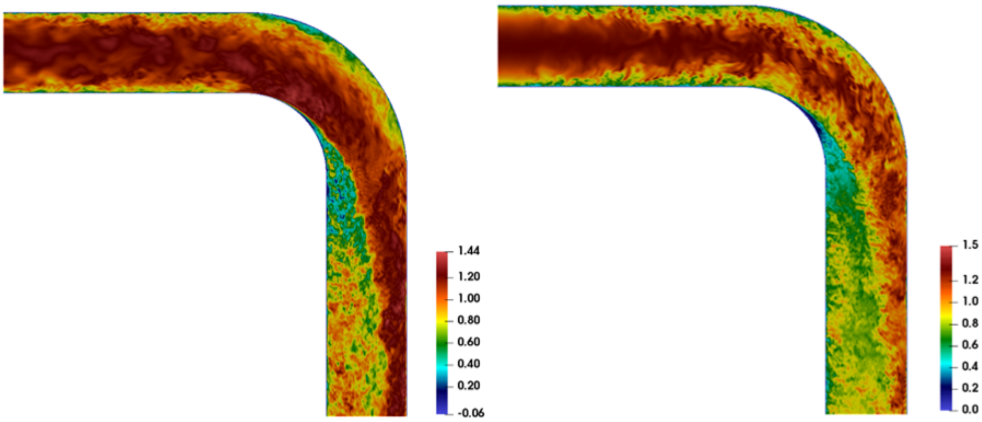

(a) Instantaneous streamwise velocity

(b) Instantaneous temperature

Figure 2: Contours of the instantaneous streamwise velocity and temperature coefficient fields.

2.1. Boundary conditions and numerical methods

Fully developed profiles of the velocity and temperature fields are specified at the inlet of the pipe, while a Neumann boundary condition of zero is specified for the pressure and SGS turbulent kinetic energy fields. A precursor RANS simulation is done with a straight pipe geometry, matching the diameter of the bent pipe, to generate fully developed inlet boundary conditions of the pipe bend. The precursor RANS simulation uses the elliptic blending RSM model of Manceau and Hanjalić (2002). The synthetic eddy method (SEM) of Jarrin et al. (2006) and Skillen et al. (2016) is used to instigate the fluctuating velocity from the specified fully developed velocity field at the inlet of the pipe bend. The mean profiles of velocity, Reynolds stress tensor and the dissipation rate obtained from the precursor RANS simulation provide the statistics for the synthetic eddy method. No method is used to produce the instantaneous temperature from the fully developed temperature field at the inlet. Instead, the fluctuating velocity instigates fluctuations in the temperature field $1D$ downstream of the pipe inlet as seen in Figure 2.

At the wall, a no slip boundary condition is specified for the velocity field. The wall thermal boundary condition is isothermal with a constant wall temperature defined. The Neumann boundary condition of zero is indicated for pressure.

At the pipe bend outlet, a Neumann boundary condition of zero is designated for the velocity and temperature fields. The pressure field at the outlet is specified with the scalar value of zero.

LES simulations are performed with the open-source toolbox OpenFOAM version 5. OpenFOAM uses a cell-centred finite volume method. The pressure algorithm with splitting operators (PISO) by Issa (1986) couples the momentum and pressure equations. Second-order central difference schemes are used to spatially discretise the convection and diffusion terms in the transport equations of momentum and temperature. In addition, an implicit second-order difference scheme is used for the temporal integration. The time step is automatically calculated to ensure that the maximum local Courant number is less than 0.6.

2.2. Pipe bend configuration

The bulk Reynolds number based on the diameter $D = 2R$ is defined as $Re_b = U_b D/\nu$, where U_b and ν are the bulk velocity at the inlet and the kinematic viscosity respectively. The bulk Reynolds number of this work is 40,000, which corresponds to the bulk Reynolds number used in one of the mass transfer experiments of Mazhar et al. (2013).

A large eddy simulation is done for a pipe of diameter D with a pipe bend of an angle of $90°$, and the distance between the pipe centreline and the bend pivot is $R_c = 1.5D$, as shown in Figure 1. The pipe diameter is taken as $D = 1$m. The Dean number determines whether the flow through the bend develops counter-rotating vortices, also known as Dean vortices.

The Dean number is defined as:

$$De = Re_b\sqrt{\frac{D/2}{R_c}}. \tag{22}$$

The Dean number for this case is 23,000, which indicates that Dean vortices are expected to be found in the flow.

The length of the computational domain is $8.4D$ with a straight pipe of $3D$ located upstream of the bend entrance, and a straight pipe of $3D$ attached downstream of the bend exit as illustrated in Figure 1. Holgate (2018) determined that the length of the inlet straight pipe of $3D$ is sufficiently long enough for the SEM to develop fluctuations in the flow.

The working fluid is air and is treated as incompressible. The Prandtl number of the fluid is taken as $Pr = 0.71$ with the turbulent Prandtl number specified as $Pr_t = 0.90$. The kinematic viscosity is defined as $\nu = 2.5 \times 10^{-5}$ m^2/s.

2.3. Numerical validation

The flow results on the plane at $z = 0.67D$ downstream of the bend exit are compared in Figure 3 against experimental data of Kalpakli and Örlü (2013) and LES data of Holgate (2018). The two reference data performed flow investigations for a slightly different ratio of curvature radius to diameter of $R_c/D = 1.58$. The bulk Reynolds number of the two investigations is also different at 34,000. Figure 3 shows the comparison of the velocity magnitude, the cross-stream velocity, the turbulent kinetic energy and the pressure coefficient. The profiles are taken along the symmetry centreline between the inner and outer walls at the cross-sectional plane $z = 0.67D$ downstream of the bend exit. The velocity magnitude result of this work is in good agreement with the reference experimental data. The disparities in comparisons are due to differences in the Reynolds numbers and curvature radius between the present LES and the experimental data. The absence of near-wall measurements makes it difficult to assess the performance of predicting the near-wall velocity gradient. However, when the results are compared with the wall-resolved LES of Holgate (2018) the velocity profiles are in excellent agreement, with the wall gradients of the present LES being slightly higher due to the higher Reynolds number. The present LES yields good results when the other profiles in Figure 3 are compared with the wall – resolved LES of Holgate (2018). Figure 4 shows the comparison of contour

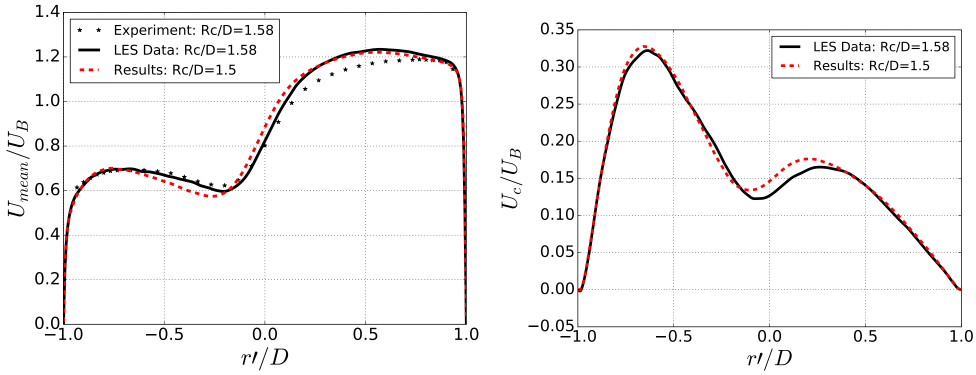

(a) Mean velocity magnitude

(b) Mean cross-stream velocity

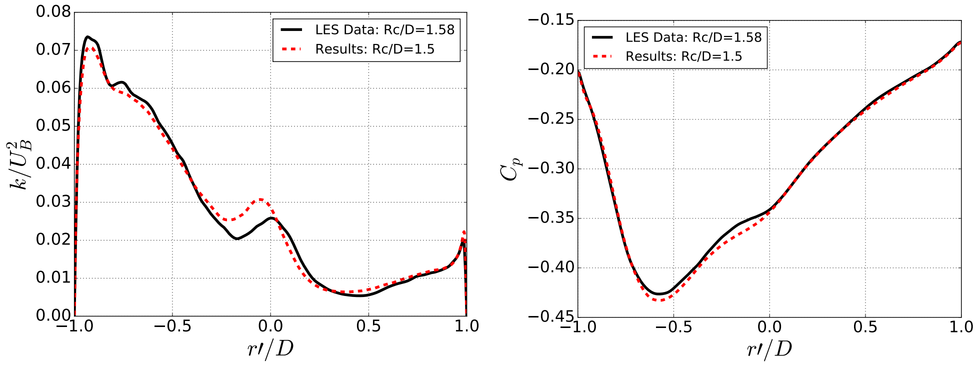

(c) Mean turbulent kinetic energy

(d) Mean pressure coefficient

Figure 3: Comparison of the non-dimensional profiles at the symmetry plane between the inner and outer walls at position $z = 0.67D$ downstream of the bend exit. The position $r'/R = -1$ refers to the inner wall of the bend while $r'/R = 1$ is the outer wall. Experimental data of Kalpakli and Örlü (2013) (• • •), LES data of Holgate (2018) (——), present LES result (- - -).

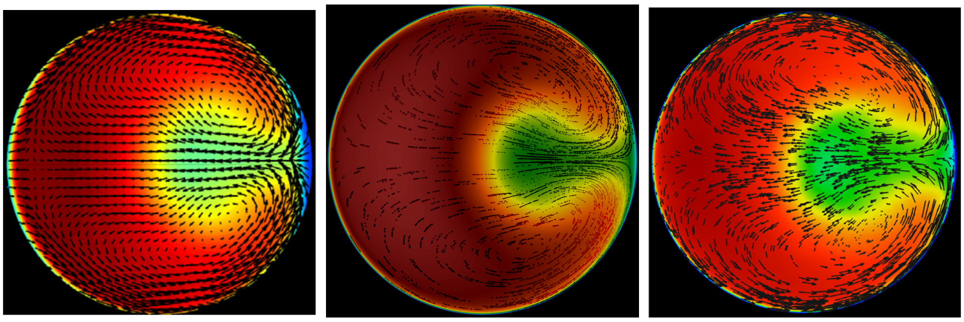

(a) Kalpakli and Örlü (2013) experiment ($R_c/D = 1.58, Re_B = 34,000$)

(b) Results of this present heat transfer LES ($R_c/D = 1.5, Re_B = 40,000$)

(c) Röhrig et al. (2015) numerical results ($R_c/D = 1.58, Re_B = 34,000$)

Figure 4: Contours of mean streamwise velocity at $z = 0.67D$ downstream of the bend exit.

plots of the mean streamwise velocity at the cross-sectional plane $z = 0.67D$ downstream of the bend exit. The velocity contour of this present work (Figure 4b) is compared with the plot obtained from the data of Kalpakli and Örlü (2013) and the LES investigation of Röhrig et al. (2015). The bulk Reynolds number and geometry of the numerical setup of Röhrig et al. (2015) is the same as Holgate (2018). The contour plot of this study is in very good qualitative agreement with the experimental results with the global in-plane behaviour of the flow being well captured. A close qualitative agreement is also observed with the LES contour of Röhrig et al. (2015). The vector array of Figure 4b illustrates the presence of a pair of counter-rotating vortices, which is typical for pipe bend flows. The close agreement with the quantitative and qualitative reference data underlines that the LES results presented in the later sections can be analysed with confidence.

3. Results & Discussion

3.1. Mean flow and thermal fields

Figure 5 shows the evolution of the pressure coefficient and the streamwise wall shear stress profiles through the pipe. The profiles are plotted in the symmetry plane intersecting the inner and outer walls with the streamwise wall shear stress normalised by the wall shear stress value of the inlet straight pipe. Along the inner wall, there is a strong favourable pressure gradient at the bend entrance. This strong favourable pressure gradient coincides with

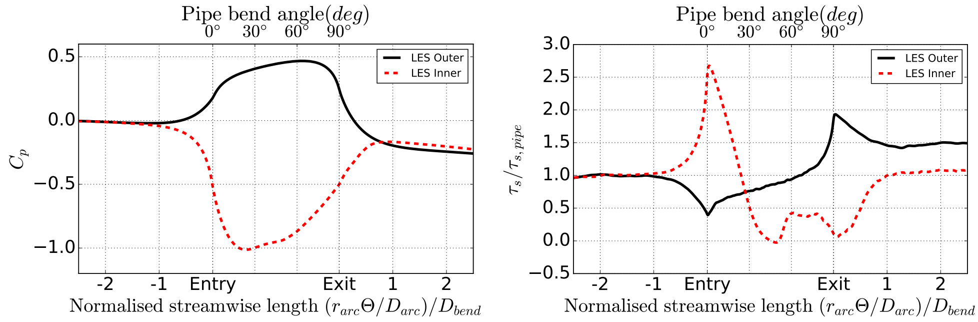

(a) Pressure Coefficient (b) Streamwise wall shear stress

Figure 5: Plots of the pressure coefficient and streamwise wall shear stress along the outer and inner walls of the pipe. The streamwise wall shear stress is normalised by the wall shear stress of the inlet straight pipe. Profile along *outer* wall symmetry plane (—), profile along *inner* wall symmetry plane (- - -).

the increase in skin friction at the bend entrance along the inner wall. After 20° of the bend, the gradient of the pressure switches sign and acts to retard the flow close to the inner wall, while the wall shear stress drops below the wall shear stress value of the inlet straight pipe. The streamwise wall shear stress becomes negative in the second half of the bend along the inner wall. The flow separates at 45.46° and reattaches at 51.38°. Along the outer wall, there is a mild adverse pressure gradient which turns to a favourable pressure gradient after 75° of the bend. At the bend entrance, the skin friction along the outer wall drops below the skin friction of the inlet straight pipe but increases along the outer wall. Downstream of the bend exit, the pressure coefficient and wall shear stress commence recovering to profiles of the inlet straight pipe.

Figure 6 shows the profiles of the streamwise velocity, cross-stream velocity and temperature at five cross-sectional planes through the pipe. The planes start upstream of the bend entry, go through the bend and end downstream of the bend exit. Upstream of the bend entry, the streamwise velocity and temperature profiles maintain axis-symmetry while the secondary velocity is negligible. Figure 7 illustrates the streamwise velocity, cross-stream velocity and temperature at the midplane section of the pipe. At the bend entrance, there is an acceleration of the flow next to the inner wall due to the strong favourable pressure gradient along the inner wall, as seen in Figure 5a. The increase in streamwise velocity leads to the rapid increment of

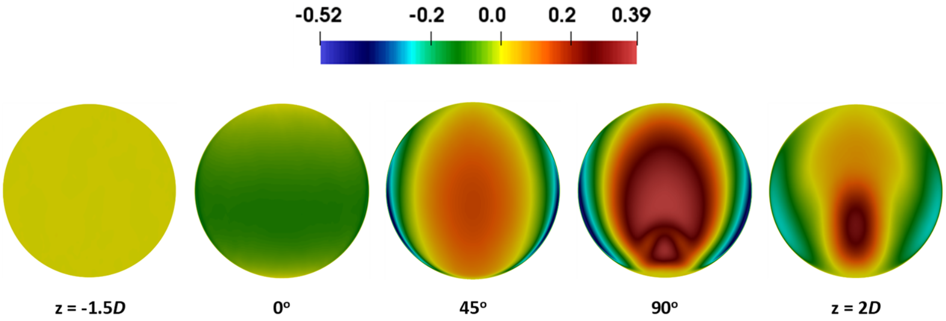

(a) Mean cross-stream velocity

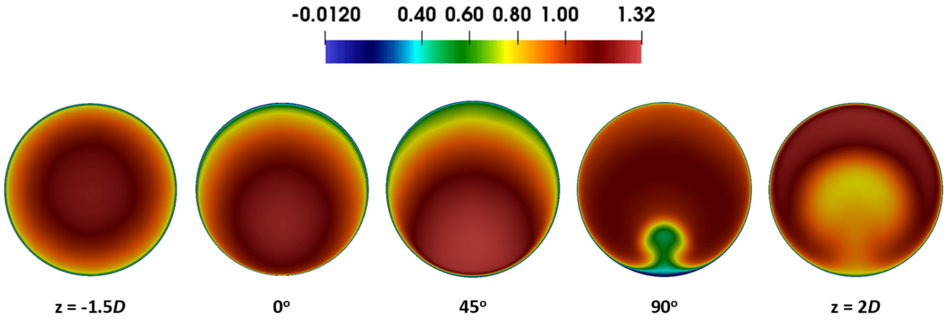

(b) Mean streamwise velocity

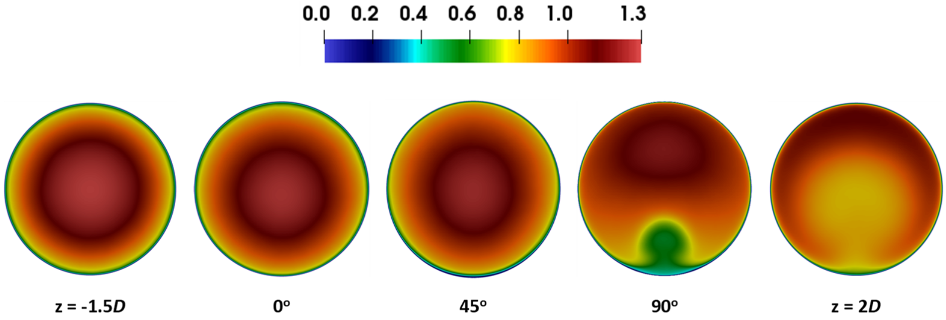

(c) Mean normalised temperature

Figure 6: Contours of cross-stream velocity, streamwise velocity and temperature at planes through the pipe.

the skin friction along the inner wall at the bend entrance as also seen in Figure 5b. However, the trend of the acceleration of the flow close to the inner wall is not observed for the temperature field at the bend entrance. The temperature profile retaining its symmetric nature for the first half of the bend is in line with what Baughn et al. (1987) reported in their heat transfer experiment of a U-pipe bend. The temperature maintains its symmetric profile as the flow convects the high temperature fluid close to the inner wall 'forward' at a faster rate (Note that from the definition of the temperature coefficient, higher values of T^* signify a higher temperature difference with the wall temperature. Therefore, with the assumption of $T_w > T_b$, hot fluid is located next to the wall, while the cold fluid is at the core of the flow for $0° < \Theta < 45°$). Hence, the flow acceleration along the inner wall makes negligible changes to the temperature profile, as the pressure gradient term is not included in the temperature transport equation like the momentum equation. Curiously, at the bend entry, the cross-stream velocity becomes negative for most of the cross-sectional plane. This leads to a light impingement of the flow on the inner wall at position $\Theta = 0°$ as illustrated in Figure 6b. The cross-stream velocity is negative due to the acceleration of the streamwise velocity at the bend entry. From continuity, the lateral acceleration of the streamwise velocity leads to the resulting normal gradient of the cross-stream velocity being below zero around the bend entrance.

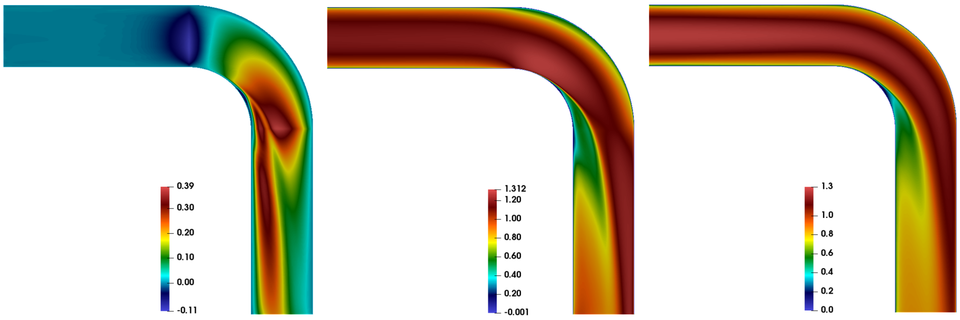

(a) Cross-stream velocity (b) Streamwise velocity (c) Temperature

Figure 7: Contours showing the evolution of the mean cross-stream velocity, mean streamwise velocity and the mean normalised temperature through the pipe. Contours are shown on the symmetry midplane.

Secondary velocity with positive values starts becoming more dominant by 45° of the bend. The secondary flow becomes increasingly significant in the second half of the bend due to the presence of centrifugal forces acting on the fluid. The imbalance of the centrifugal forces and the cross-stream pressure gradient leads to the formation of a pair of counter-rotating vortices, also known as Dean vortices. These Dean vortices act the move the high momentum fluid from the inner wall towards the outer wall and the low temperature part of the fluid from the centre of the plane towards the outer heated wall. This transport increases the normal gradients of the flow and thermal fields, thereby increasing the flux of momentum and heat transfer at the outer wall. As the temperature profile remained relatively symmetric for the first half of the bend, the low temperature core of the fluid is convected closer to the outer wall by the Dean vortices than the high momentum fluid. Also, the low momentum and high temperature fluid at the side walls are transported to the inner wall by the Dean vortices. This mechanism can be seen in the second part of the bend in Figures 7b and 7c. The low momentum fluid next to the inner wall is further retarded by the presence of the adverse pressure gradient. The transport of low momentum and high temperature fluid towards the inner wall leads to the increase of gradient of those two quantities in the radial and circumferential directions in that region. Downstream of the bend exit, the effect of the bend is still felt on the thermal and flow fields, with the low temperature and high momentum fields coalescing next to the outer wall. In the absence of centrifugal forces due to the bend, the secondary flow weakens downstream of the bend exit with the slow recovery to the symmetric thermal and flow fields commencing.

3.2. Velocity and temperature fluctuations (Turbulence and statistics)

Figure 8 shows the contours of the turbulent kinetic energy at different planes of the pipe. Figure 9 shows the plots of the composition of the Reynolds stresses and the variance of the temperature field at different sections of the pipe on the symmetry line between the inner and outer walls. At the bend entrance, the temperature variance and the turbulent kinetic energy are slightly lower at the inner wall due to flow acceleration suppressing turbulent mixing. At 45° of the bend, the peak turbulent kinetic energy near the inner wall moves towards the core of the flow as secondary flow shifts the production of the streamwise Reynolds stress due to shear towards the outer wall. The same trend is witnessed for the temperature variance at $\Theta = 45^\circ$. The spanwise and cross-stream Reynolds stresses are reduced near the inner wall at this position. In addition, the temperature variance decreases at the inner wall for $\Theta = 45^\circ$ as the streamline curvature around the convex surface acts to dampen thermal mixing, due to the local orientation of the Dean vortices coinciding with the direction of the mean angular momentum to stabilise turbulence. On the other hand, the concave outer wall acts to augment thermal mixing of the fluid in that vicinity. As the Dean vortices become dominant in the second half of the bend, the peak streamwise Reynolds stress and temperature variance due to production from the inner wall moves towards the centre of the flow as secondary flow shifts the high gradient sections of the velocity and temperature towards to the core of the flow. The enhanced production of the temperature fluctuations and the streamwise Reynolds stress is linked to the deficiency of the temperature and velocity flow fields, respectively, between the inner wall and the centre core of the flow. Furthermore, the counter-rotating vortices transport turbulence from the side walls towards the inner wall of the bend. This transport greatly increases turbulent kinetic energy at the inner wall as can be seen at $\Theta = 90^\circ$ of Figure 8.

Interestingly, the turbulent transport leads to turbulence being strongly anisotropic and leads to the spanwise component of the Reynolds stress being the most dominant component of the turbulent kinetic as can be seen in Figure 9 at the bend exit. The highly anisotropic nature of turbulence at the bend exit was also noticed by Röhrig et al. (2015) when the distribution of the flatness parameter in the near-wall vicinity was computed. The turbulent kinetic energy is maximum close to the inner wall in the second half of the bend where turbulent transport is pronounced, and there are substantial gradients of velocity in the radial and circumferential directions. Although the transport of temperature fluctuations to the inner wall can be seen in the temperature variance plots at the bend exit, the temperature fluctuations are most considerable at the outer wall where the Dean vortices impinge cold fluid on the heated outer wall. Downstream of the bend exit, the counter-rotating vortices push the peak streamwise and cross-stream Reynolds stresses and the temperature fluctuations due to the high strain rate at the centre of the plane closer to the outer wall. The temperature fluctuations reduce downstream of the bend exit as the Dean vortices weaken.

Figure 10 shows the qualitative and quantitative plots of the shear stress at different cross-sectional planes through the pipe. The shearing force acting on the fluid upstream of the bend entrance is symmetrical. At the bend entry of $\Theta = 0^\circ$, the shear stress slightly reduces near the inner wall as the profile of high streamwise velocity flattens in that region. The covariance of the streamwise and cross-stream fluctuations continue to be suppressed to zero

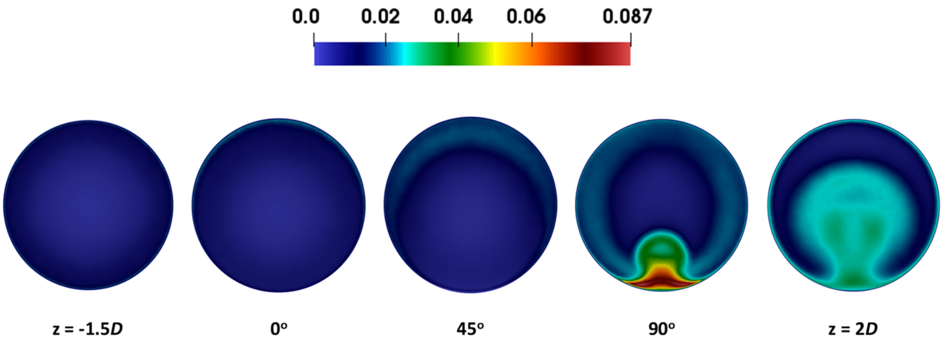

Figure 8: Contours of turbulent kinetic energy at cross-sectional planes through the pipe.

near the inner wall as the strain rate of the streamwise velocity in that area becomes negligible.

At $\Theta = 45°$, the Dean vortices become more prominent, leading to the strain rate of the cross-stream velocity making a significant contribution to the shear stress near the inner arc. The sign of the shear stress changes at this location.

In the second half of the bend, the Dean vortices move the core of the high momentum but flat distribution of high streamwise velocity towards the centre of the pipe ensuring that the shear stress in the centre of the plane becomes negligible. Towards the inner wall, the contributions from the strain rates of the streamwise velocity and the cross-stream velocity make the distribution of the covariance of the streamwise and cross-stream fluctuations complex. Also, it is observed that other components of the shear stress become non-zero due to the aforementioned contributions.

Downstream of the bend exit, the vortices push the section of the high momentum flow with the high strain rate closer to the outer wall. This movement brings a second peak of the shear stress into the vicinity of the outer wall. Closer to the inner wall, the intensity of the shear stress reduces as the secondary flow weakens downstream of the bend exit.

3.3. Heat transfer

The heat transfer coefficient represented by the non – dimensional Nusselt number is illustrated in Figures 11a and 11b. The distribution of the wall heat transfer is shown for the inner and outer walls. The contour of the streamwise wall shear stress is also demonstrated in Figures 11c and 11d.

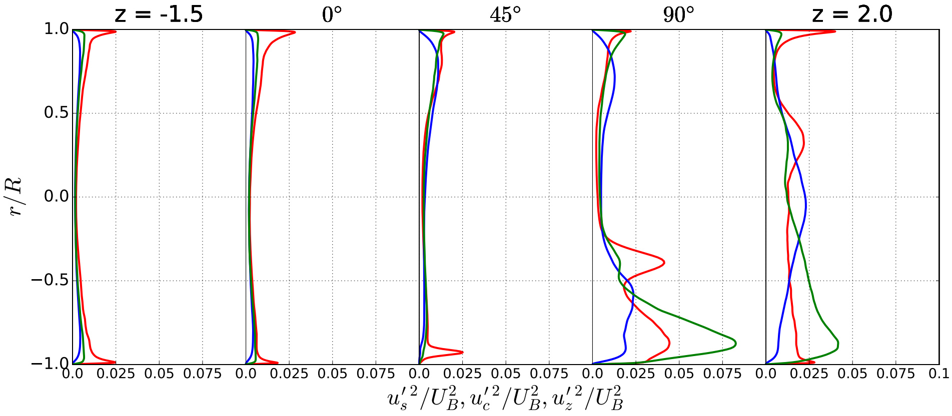

(a) Reynolds Stresses

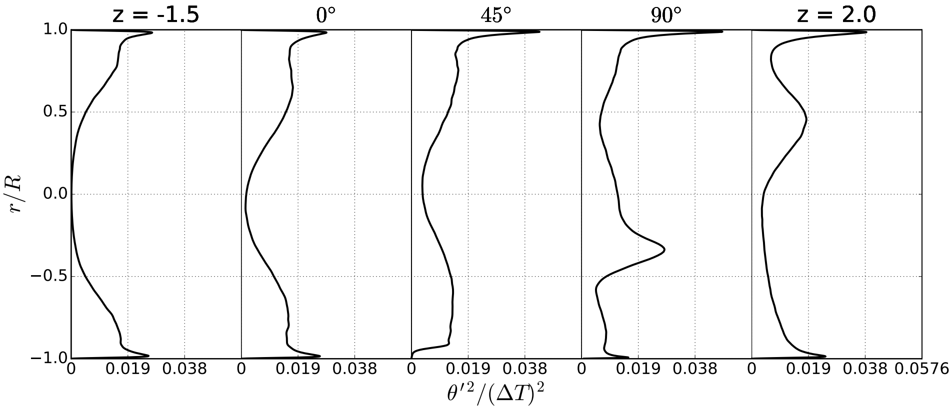

(b) Temperature variance

Figure 9: Plots of profiles of the Reynolds stresses and the temperature variance along symmetry lines between the inner and outer walls. Figure 9a Legend: streamwise Reynolds stress (—), cross-stream Reynolds stress (—), spanwise Reynolds stress (—).

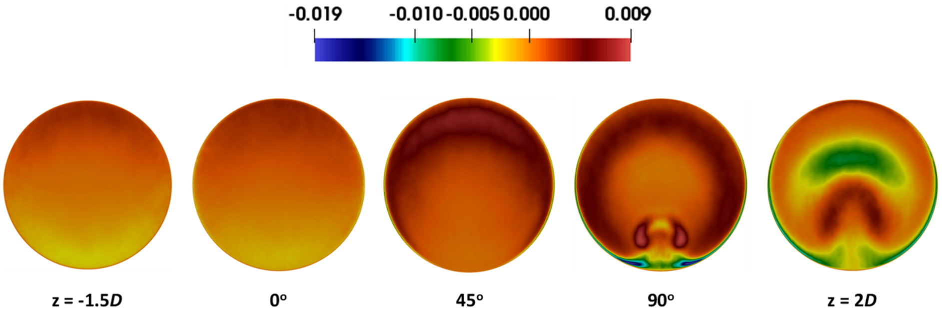

(a) Shear Stress – covariance of streamwise and spanwise fluctuations – $\overline{u_s u_c}$

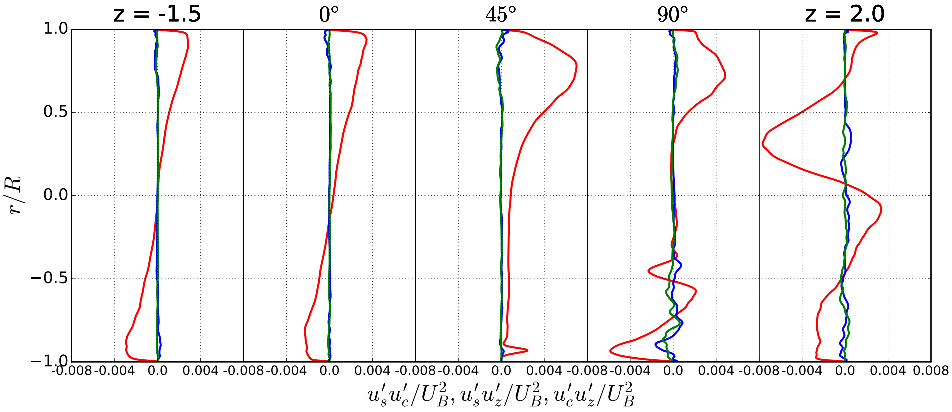

(b) Shear stresses

Figure 10: Contours and plots of profiles of the shear stress components at different sectional planes. Plots are along symmetry lines between the inner and outer walls. Figure 10b Legend: $u_s'u_r'$ (🟥), $u_s'u_z'$ (🟦), $u_c'u_z'$ (🟩).

Upstream of the bend entry, the heat transfer circumferential distribution is even. At the bend entrance, the Nusselt number increases along the side and outer walls. The heat transfer progressively increases along the outer wall as the flow goes through the bend. However, along the inner wall, the heat transfer decreases markedly in the first section of the bend. The value of the Nusselt number along the inner wall being lower than the value of the inlet straight pipe is similar to the observation of Baughn et al. (1987) in their heat transfer experiment of the 180° pipe bend. In the second half of the bend, $45^\circ \leq 90^\circ$, along the inner wall, the Nusselt number increases in value, as the skin friction decreases, although the increment does not match the intensity of the heat transfer along the outer wall.

Figure 12 shows the distribution of the Nusselt number on profile lines along the inner and outer walls. The Nusselt number values are normalised by the average Nusselt number of the inlet straight pipe attached upstream of the bend entrance. The LES heat transfer results are compared with the mass transfer experimental datasets of Mazhar et al. (2013) and Ikarashi et al. (2017). Like the heat transfer results, the mass transfer data through the bend are normalised with the averaged value of the Sherwood number of the inlet straight pipe section. Along the outer wall, the heat transfer results capture the trend of the mass transfer data of Mazhar et al. (2013). Differences between the two profiles are due to the wall roughening in the mass transfer experiment; thereby affecting the results of the experiment. The two profiles increase gradually through the bend reaching a maximum value at $\Theta = 90^\circ$. The maximum Nusselt number at the outer wall is about 1.85 of the inlet straight pipe value, which matches the peak Sherwood number of Mazhar et al. (2013). Downstream of the bend exit, there is a slight decrease then a flattening of the heat transfer coefficient, as secondary flow weakens and reduces the intensity of impingement on the heated outer wall. The trend of heat transfer downstream of the bend exit along the outer wall is also observed for the mass transfer profile of Mazhar et al. (2013). The skin friction along the outer arc matches the inclination of heat transfer through the bend with also the peak value being at the bend exit. On the other hand, the experiment of Ikarashi et al. (2017) shows a modest increase in mass transfer along the outer wall. There is a big difference between the mass transfer results of Ikarashi et al. (2017) and the heat transfer profile along the wall. The mass transfer profile reduces downstream of the bend exit then flattens, just like the heat transfer results, as the intensity of secondary flow weakens.

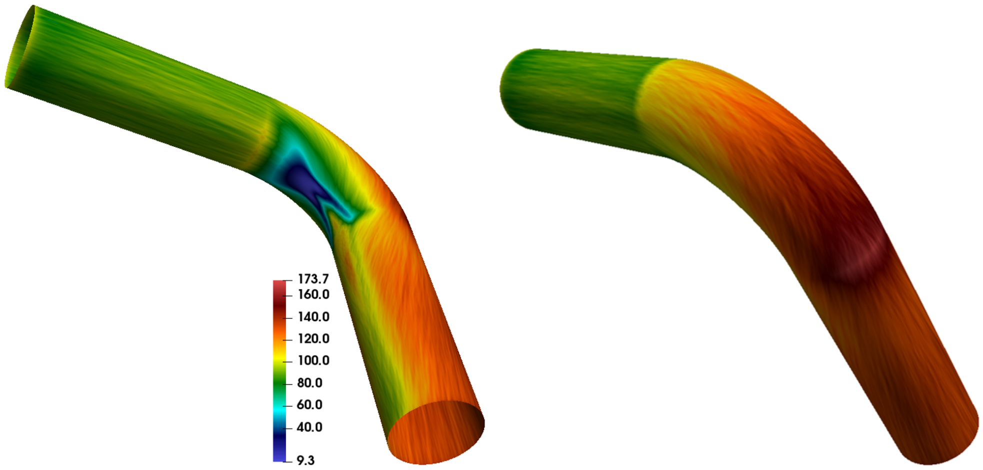

(a) Mean Nusselt number – Inner wall (b) Mean Nusselt number – Outer wall

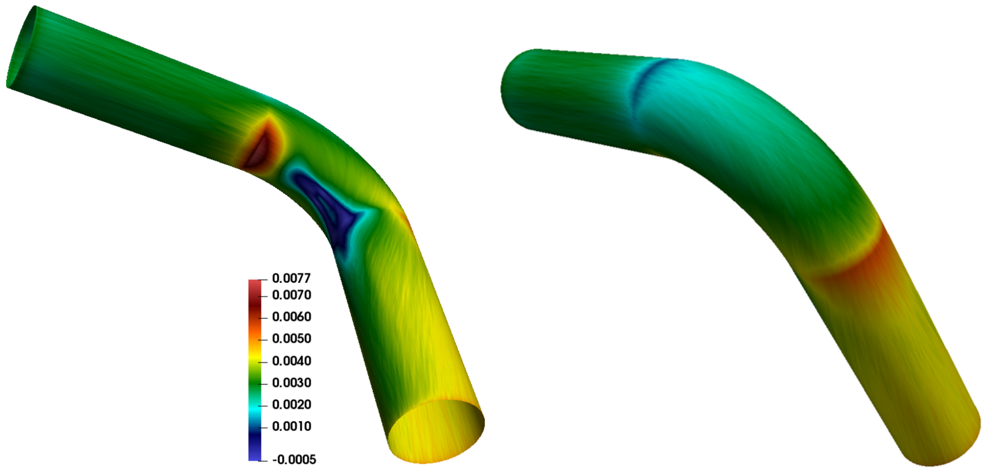

(c) Mean Wall shear stress – Inner wall (d) Mean Wall shear stress – Outer wall

Figure 11: Distribution of mean Nusselt number and mean streamwise wall shear stress on the walls. The contours show distribution either along the inner wall or the outer wall.

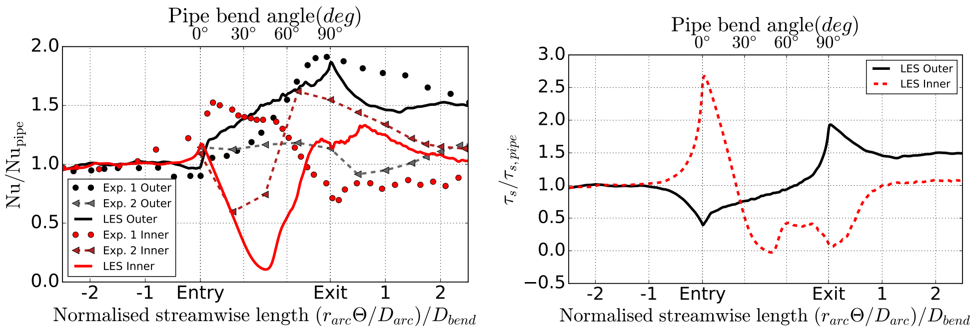

(a) Heat transfer coefficient

(b) Streamwise wall shear stress

Figure 12: Plot of the Nusselt number predicted by the numerical simulation and the Sherwood number predicted by the experiments of Mazhar et al. (2013) and Ikarashi et al. (2017) along the inner and outer walls. The Nusselt and Sherwood numbers are normalised by the axis-symmetric values of the inlet straight pipe upstream of the bend entry. The wall shear stress is shown for comparison. LES profiles represent the results of this heat transfer study. Exp. 1 profiles correspond to the results of Mazhar et al. (2013) mass transfer experiment, and Exp. 2 lines depict the results of Ikarashi et al. (2017) mass transfer experiment.

However, there is a different picture along the inner wall. Downstream of the bend entry, there is a big discrepancy between the mass transfer experimental data of Mazhar et al. (2013) and the heat transfer numerical results. The mass transfer of Mazhar et al. (2013) increases downstream of the bend entrance following the trend of the rapid increment in skin friction, as seen in Figure 11c where the flow accelerates near the inner wall. The mass transfer of Mazhar et al. (2013) reduces between positions $\Theta = 20^\circ$ to $\Theta = 90^\circ$ which correlates with the decrease in wall shear stress. On the other hand, the heat transfer along the inner arc follows the trend of Ikarashi et al. (2017). There is a slight increase of heat transfer at the bend entrance as a result of light impingement of the flow in that location due to near-inner wall flow acceleration. This increment is also noticed in the Ikarashi et al. (2017) profile. Through the bend between $\Theta = 0^\circ$ and $\Theta = 45^\circ$, the temperature profile remains symmetrical even though the flow accelerates in the near-wall region. The near-wall acceleration and streamline curvature due to the convex arc suppress turbulence, and consequently thermal mixing, in the near-wall region as seen in Figure 9, which leads to a decrease in wall heat flux in the inner wall region. The lowest Nusselt number occurs around $\Theta = 45^\circ$ where the flow separates, with the heat transfer coefficient being almost negligible at that location. The mass transfer profile of Ikarashi et al. (2017) matches the decrease along the inner wall of the heat transfer profile. Although, the lowest mass transfer coefficient occurs earlier than $\Theta = 45°$, probably due to increased surface roughness in the mass transfer experiment. As the Dean vortices become more prominent in the second part of the bend after $\Theta = 45°$ and the flow reattaches, transport of temperature fluctuations and turbulence from the side walls increases thermal mixing in the inner wall region, thereby significantly increasing heat transfer along the inner wall. The augmented heat transfer in this region is matched by the enhanced mass transfer of Ikarashi et al. (2017), though there is a detachment between the two profiles due to differences in the Reynolds number of the two datasets. Downstream of the bend exit, the is a slight decrease of the heat transfer coefficient along the inner wall with the profile converging with the mass transfer results of Ikarashi et al. (2017).

The two mass transfer datasets differ markedly along the inner and outer walls. The heat transfer results of this study correspond with the mass transfer profile of Mazhar et al. (2013) along the outer wall and with the data of Ikarashi et al. (2017) along the inner wall. The heat transfer profile maintains a correlation with the flux of momentum along the outer wall, but the comparison between heat transfer and skin friction is more complex along the inner wall. Heat transfer along the inner arc scales more with turbulence intensity as the counter-rotating secondary flow strongly influences thermal parameters in the inner wall region.

Figures 13a and 13b represent the distribution of the instantaneous heat transfer coefficient and the variance of the Nusselt number over the pipe wall. The outer and side walls display streak patterns of alternating low and high heat transfer as discovered by Di Liberto and Ciofalo (2013) in their DNS of toroidal pipes with periodic boundary conditions at the inlet and outlet. This trend also correlates to alternating patterns of low and high near-wall temperatures, which is akin to the distribution found in channel flows with heated walls. The heat transfer fluctuations on the outer and side walls increase significantly through the bend. The augmented wall heat flux fluctuations are linked with the Dean vortices transporting cold fluid in alternating circumferential directions and represented with the heightened temperature fluctuations next to the outer wall. Consequently, the outer and side walls are prone to higher thermal fatigue with the heightened levels of heat flux fluctuations. Continuing with the trend of previously discussed thermal or flow parameters, the variance of the heat transfer coefficient downstream of

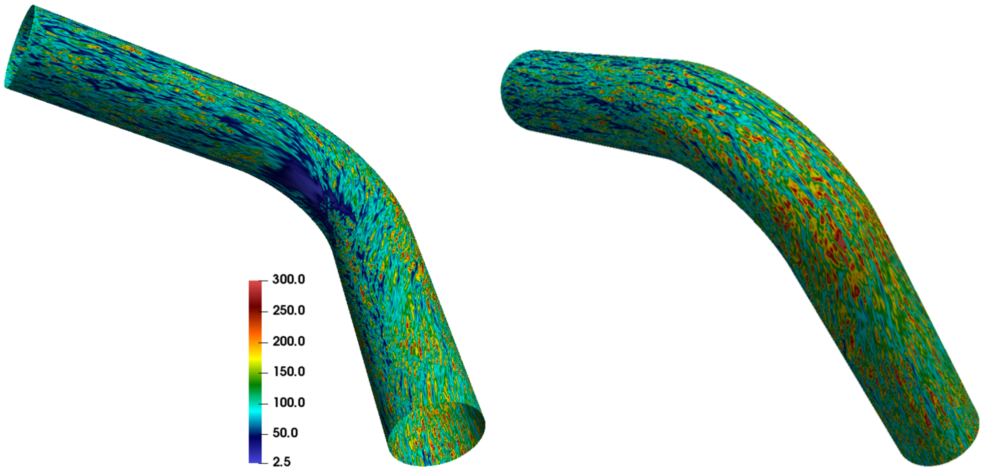

(a) Instantaneous Nusselt number – Inner wall (b) Instantaneous Nusselt number – Outer wall

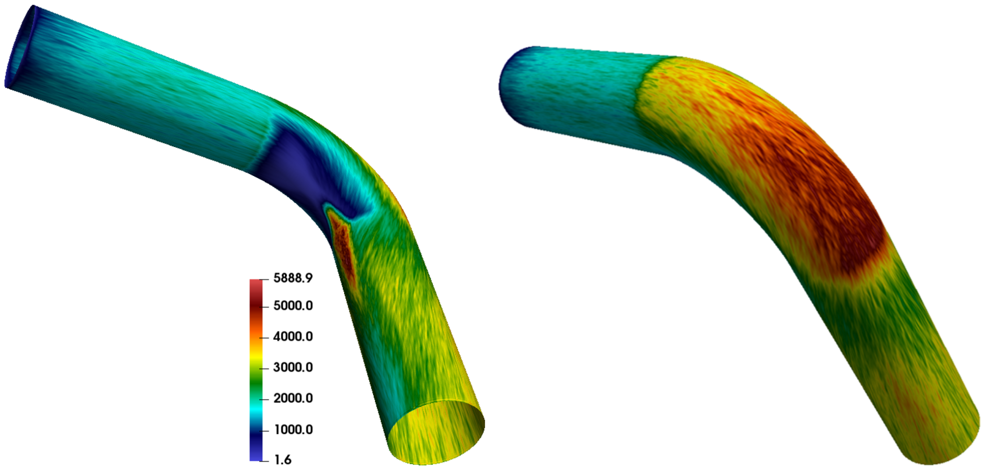

(c) Variance of Nusselt number – Inner wall (d) Variance of Nusselt number – Outer wall

Figure 13: Distribution of instantaneous Nusselt number and variance of the Nusselt number on the walls. The contours show distribution either along the inner wall or the outer wall.

the bend exit reduces as the Dean vortices lose strength.

On the other hand, the inner wall close to the bend entry has a large area with a flat distribution of instantaneous heat transfer coefficient. The impact of this even distribution is noticeable in the figure illustrating the negligible heat transfer fluctuations in that location shown in Figure 13c. A thin strip of significantly enhanced heat transfer fluctuations develops along the inner wall in the second half of the bend. The increased fluctuations suggest that both the inner and outer walls are subjected to elevated levels of thermal fatigue at the bend exit.

Figure 14 illustrates the evolution of the turbulent heat flux through the pipe. Upstream of the bend entry, the turbulent heat fluxes remain undisturbed by the influence of the bend. The peak of the streamwise turbulent heat flux near the inner wall moves towards the core of the pipe as the Dean vortices dominate. The cross-stream turbulent heat flux exhibits more complex behaviour. Between the bend entry at $\Theta = 0°$ and $\Theta = 45°$, the normal turbulent heat flux is suppressed near the inner wall as the flow acceleration suppresses turbulent mixing in that region (This feature is illustrated clearer in Figure 1). This suppressed normal heat flux is reflected in the reduced heat transfer coefficient between $\Theta = 0°$ and $\Theta = 45°$ illustrated in Figure 12a. The normal turbulent heat flux is mostly negligible in the lower half of the pipe next to the inner wall at $\Theta = 45°$, which matches the lowest value of the Nusselt number. In the second part of the bend after $\Theta = 45°$, the counter-rotating vortices bring high temperature fluid from the side walls towards the inner wall region, which forces the peak value of the normal turbulent heat flux to switch signs. Turbulent transport also increases thermal mixing in the inner wall region as earlier identified at $\Theta = 90°$ with the highest magnitude value of the cross-stream heat flux occurring at this location as seen in Figure 14a. The switched peak normal heat flux is transported towards the outer wall through the Dean vortices. On closer inspection, the contours of the cross-stream turbulent heat flux mimic the contours of the shear stress co-variance of streamwise and cross-stream fluctuations when Figure 14a and Figure 10a are compared.

4. Conclusions

A large eddy simulation is performed for turbulent flow through a 90° pipe bend. The ratio of the radius of curvature to pipe diameter is 1.5. The bulk Reynolds number of the case is 40,000. The simulation solves

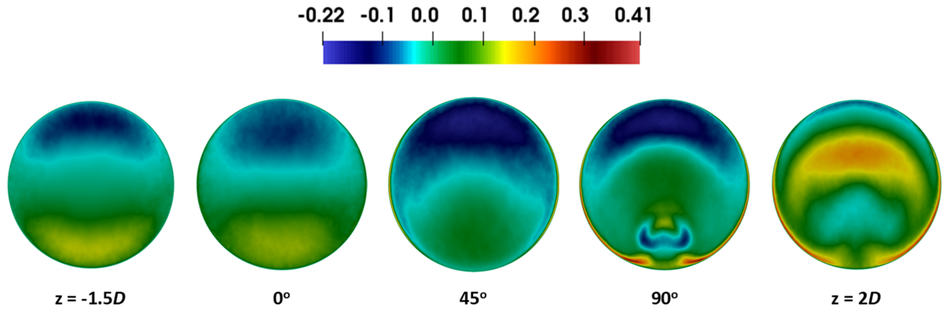

(a) Cross-stream turbulent heat flux – $\overline{u_c\theta}$

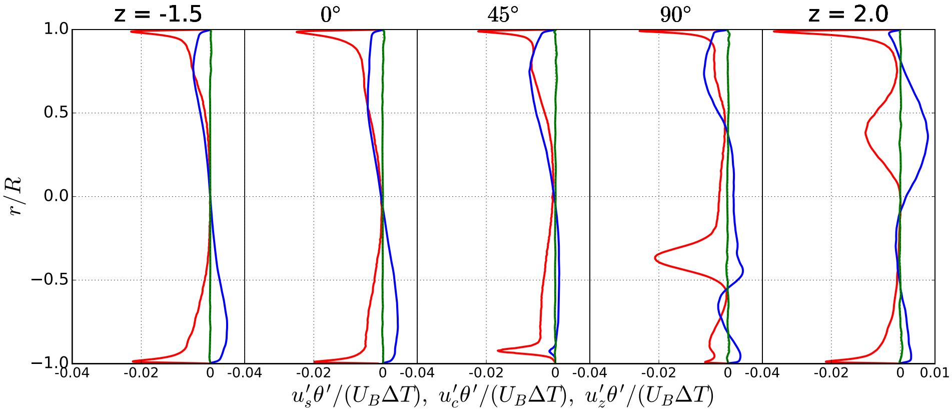

(b) Turbulent heat fluxes

Figure 14: Contours and plots of profiles of the turbulent heat flux components at different sectional planes. Plots are along symmetry lines between the inner and outer walls. Figure 14b Legend: $u'_s\theta'$ (🟥), $u'_c\theta'$ (🟦), $u'_z\theta'$ (🟩).

the energy transport equation with the temperature variable computed as a passive scalar. Existing literature on turbulent heat transfer through 90° pipe bends is limited. This work validates the heat transfer coefficient results with the mass transfer experimental data of Mazhar et al. (2013) and Ikarashi et al. (2017). The flow immediately downstream of the bend exit is validated with experimental data of Kalpakli and Örlü (2013) and the LES results of Holgate (2018). Also, qualitative contour plots of Kalpakli and Örlü (2013) and Röhrig et al. (2015) of the streamwise velocity downstream of the bend are compared with the results of this study. The simulation converts the Cartesian coordinate of the velocity field into intrinsic coordinates to enable the generation of an extensive database.

The thermal and flow fields are symmetric upstream of the bend entrance. However, The evolution of the thermal and flow fields differ downstream of the bend entrance. A strong favourable pressure gradient accelerates the flow next to the inner wall vicinity after the bend entry, which leads to an increase in skin friction. However, the temperature field remains relatively symmetric. By $\Theta = 45°$, the pressure gradient along the inner wall becomes unfavourable, and the skin friction reduces. The mean (time-averaged) flow separates at 45° and reattaches at 51°. Secondary flow becomes significant in the second half of the bend, which leads to the formation of a pair of counter-rotating vortices that act to move the high momentum - low temperature fluid towards the outer heated wall. This transport leads to an increase in the flux of temperature and momentum along the outer wall.

Downstream of the bend entry, the temperature and velocity fluctuations are suppressed close to the inner wall as the flow accelerates. The streamwise Reynolds stress remains the most significant stress component of the turbulent kinetic energy for the first half of the bend. As the Dean vortices become dominant in the second half of the bend, secondary flow transports turbulence from the side walls to the inner wall region leading to the enhancement of thermal mixing in that area, while peak thermal fluctuations due to production are deflected towards the core of the flow. The transport mechanism makes turbulence highly anisotropic around the inner wall. The spanwise Reynolds stress becomes the largest component of the turbulent kinetic energy when the counter-rotating vortices are active, while the concave outer arc augments the temperature fluctuations in the outer wall region.

Heat transfer increases along the outer wall of the bend and this increment matches the trend of the mass transfer experimental data of Mazhar et al. (2013). The maximum heat transfer occurs at $\Theta = 90°$ with the largest value being 1.85 of the inlet straight pipe Nusselt number. However, along the inner wall, the correlation between the heat and mass transfer of Mazhar et al. (2013) breaks down. Heat transfer reduces at the inner wall in the first half of the bend as thermal mixing is suppressed due to the convex flow streamlines. The heat transfer is the lowest at 45°, where the cross-stream heat flux is negligible. Heat transfer increases rapidly along the inner arc in the second half of the bend as Dean vortices greatly enhance thermal mixing. The trend of the decrease and subsequent increase in heat transfer along the inner wall is closely followed by the mass transfer dataset of Ikarashi et al. (2017). Heat transfer maintains scaling with the wall shear stress along the outer wall but scales more with turbulent intensity along the inner wall, due to the influence of secondary flow. Furthermore, fluctuations of the heat transfer coefficient are greatly augmented along the side and outer walls leading to an increase in wall thermal stresses in those areas. The enhanced heat transfer fluctuations are also observed in a thin strip area along the inner wall located at the bend exit.

The two mass transfer experimental datasets utilised by this study differ considerably along the inner and outer walls. This discrepancy leads to the heat transfer coefficient of this work comparing favourably with the data of Mazhar et al. (2013) along the outer wall, and with Ikarashi et al. (2017) along the inner wall. There is a crucial need to perform a direct numerical simulation of heat and mass transfer through a 90° pipe bend to address the discrepancies between the two experimental datasets.

Acknowledgements

The authors are profoundly grateful for the funding provided by the Department of Mechanical, Aerospace and Civil Engineering of The University of Manchester for this work. The assistance given by the IT Services and the use of the Computational Shared Facility at The University of Manchester are acknowledged. The authors would also like to thank EPSRC for the computational time made available on the UK supercomputing facility ARCHER via the UK Turbulence Consortium (EP/R029326/1).

References

Acharya, N., Sen, M., Chang, H.C., 2001. Analysis of heat transfer enhancement in coiled-tube heat exchangers. International Journal of Heat and Mass Transfer 44, 3189–3199. URL: `https://doi.org/10.1016/s0017-9310(01)00002-3`, doi:10.1016/s0017-9310(01)00002-3.

Azzola, J., Humphrey, J.A.C., Iacovides, H., Launder, B.E., 1986. Developing turbulent flow in a U-bend of circular cross-section: Measurement and computation. Journal of Fluids Engineering 108, 214–221. URL: `https://doi.org/10.1115/1.3242565`, doi:10.1115/1.3242565.

Baughn, J.W., Iacovides, H., Jackson, D.C., Launder, B.E., 1987. Local heat transfer measurements in turbulent flow around a 180-deg pipe bend. URL: `https://doi.org/10.1115/1.3248065`, doi:10.1115/1.3248065.

Carlsson, C., Alenius, E., Fuchs, L., 2015. Swirl switching in turbulent flow through 90° pipe bends. Physics of Fluids 27, 085112. URL: `https://doi.org/10.1063/1.4928971`, doi:10.1063/1.4928971.

Chilton, T.H., Colburn, A.P., 1934. Mass transfer (absorption) coefficients prediction from data on heat transfer and fluid friction. Industrial & Engineering Chemistry 26, 1183–1187. URL: `https://doi.org/10.1021/ie50299a012`, doi:10.1021/ie50299a012.

Colburn, A.P., 1964. A method of correlating forced convection heat-transfer data and a comparison with fluid friction. International Journal of Heat and Mass Transfer 7, 1359–1384. URL: `https://doi.org/10.1016/0017-9310(64)90125-5`, doi:10.1016/0017-9310(64)90125-5.

Cvetkovski, C.G., Reitsma, S., Bolisetti, T., Ting, D.S., 2015. Heat transfer in a U-bend pipe: Dean number versus Reynolds number. Sustainable Energy Technologies and Assessments 11, 148–158. URL: `https://doi.org/10.1016/j.seta.2015.01.001`, doi:10.1016/j.seta.2015.01.001.

Di Liberto, M., Ciofalo, M., 2013. A study of turbulent heat transfer in curved pipes by numerical simulation. International Journal of Heat and Mass Transfer 59, 112–125. URL: `http://linkinghub.elsevier.com/retrieve/pii/S0017931012009568`, doi:10.1016/j.ijheatmasstransfer.2012.12.011.

Ebara, S., Aoya, Y., Sato, T., Hashizume, H., Kazuhisa, Y., Aizawa, K., Yamano, H., 2010. Pressure fluctuation characteristics of complex turbulent flow in a single elbow with small curvature radius for a sodium-cooled fast reactor. Journal of Fluids Engineering 132. URL: `https://doi.org/10.1115/1.4002813`, doi:10.1115/1.4002813.

Enayet, M., Gibson, M., Taylor, A., Yianneskis, M., 1982. Laser-doppler measurements of laminar and turbulent flow in a pipe bend. International Journal of Heat and Fluid Flow 3, 213–219. URL: `https://doi.org/10.1016/0142-727x(82)90024-8`, doi:10.1016/0142-727x(82)90024-8.

Fröhlich, J., Mellen, C.P., Rodi, W., Temmerman, L., Leschziner, M.A., 2005. Highly resolved large-eddy simulation of separated flow in a channel with streamwise periodic constrictions. Journal of Fluid Mechanics 526, 19–66. doi:10.1017/S0022112004002812.

Germano, M., Piomelli, U., Moin, P., Cabot, W.H., 1991. A dynamic subgrid-scale eddy viscosity model. Physics of Fluids A: Fluid Dynamics 3, 1760–1765. URL: `https://doi.org/10.1063/1.857955`, doi:10.1063/1.857955.

Hellström, L.H.O., Zlatinov, M.B., Cao, G., Smits, A.J., 2013. Turbulent pipe flow downstream of a 90° bend. Journal of Fluid Mechanics 735. URL: `https://doi.org/10.1017/jfm.2013.534`, doi:10.1017/jfm.2013.534.

Holgate, J.W., 2018. Development and Application of Embedded Large Eddy Simulation for Internal Fluid Flows in Industrial Computational Fluid Dynamics. Ph.D. thesis. The University of Manchester.

Hufnagel, L., Canton, J., Örlü, R., Marin, O., Merzari, E., Schlatter, P., 2018. The three-dimensional structure of swirl-switching in bent pipe flow. Journal of Fluid Mechanics 835, 86–101. doi:10.1017/jfm.2017.749.

Ikarashi, Y., Taguchi, S., Yamagata, T., Fujisawa, N., 2017. Mass and momentum transfer characteristics in and downstream of 90° elbow. International Journal of Heat and Mass Transfer 107, 1085–1093. URL: `https://doi.org/10.1016/j.ijheatmasstransfer.2016.11.014`, doi:10.1016/j.ijheatmasstransfer.2016.11.014.

Issa, R., 1986. Solution of the implicitly discretised fluid flow equations by operator-splitting. Journal of Computational Physics 62, 40 – 65. URL:

http://www.sciencedirect.com/science/article/pii/0021999186900999, doi:https://doi.org/10.1016/0021-9991(86)90099-9.

Iyamabo, B.E.O., 2015. Numerical investigation of turbulent heat transfer through a circular 90-deg pipe bend. Dissertation. The University of Manchester.

Iyamabo, B.E.O., Afgan, I., 2018. Implementing numerical wall function for large eddy simulation in OpenFOAM, in: 5th MACE PGR Conference, Manchester.

Jarrin, N., Benhamadouche, S., Laurence, D., Prosser, R., 2006. A synthetic-eddy-method for generating inflow conditions for large-eddy simulations. International Journal of Heat and Fluid Flow 27, 585–593. URL: https://doi.org/10.1016/j.ijheatfluidflow.2006.02.006, doi:10.1016/j.ijheatfluidflow.2006.02.006.

Kalpakli, A., Örlü, R., 2013. Turbulent pipe flow downstream a 90° pipe bend with and without superimposed swirl. International Journal of Heat and Fluid Flow 41, 103 – 111. URL: http://www.sciencedirect.com/science/article/pii/S0142727X13000076, doi:https://doi.org/10.1016/j.ijheatfluidflow.2013.01.003. eTMM9.

Kang, C., Yang, K.S., 2015. Large eddy simulation of turbulent heat transfer in curved-pipe flow. Journal of Heat Transfer 138. URL: https://doi.org/10.1115/1.4030968, doi:10.1115/1.4030968.

Li, L., Lin, C., Ebadian, M., 1998. Turbulent mixed convective heat transfer in the entrance region of a curved pipe with uniform wall-temperature. International Journal of Heat and Mass Transfer 41, 3793–3805. URL: https://doi.org/10.1016/s0017-9310(98)00100-8, doi:10.1016/s0017-9310(98)00100-8.

Lilly, D.K., 1992. A proposed modification of the Germano subgrid-scale closure method. Physics of Fluids A: Fluid Dynamics 4, 633–635. URL: https://doi.org/10.1063/1.858280, doi:10.1063/1.858280.

Lin, C., Ebadian, M., 1999. The effects of inlet turbulence on the development of fluid flow and heat transfer in a helically coiled pipe. International Journal of Heat and Mass Transfer 42, 739–751. URL: `https://doi.org/10.1016/s0017-9310(98)00193-8`, doi:10.1016/s0017-9310(98)00193-8.

Manceau, R., Hanjalić, K., 2002. Elliptic blending model: A new near-wall Reynolds-stress turbulence closure. Physics of Fluids 14, 744–754. URL: `https://doi.org/10.1063/1.1432693`, doi:10.1063/1.1432693, `arXiv:https://doi.org/10.1063/1.1432693`.

Mazhar, H., Ewing, D., Cotton, J., Ching, C., 2013. Experimental investigation of mass transfer in 90° pipe bends using a dissolvable wall technique. International Journal of Heat and Mass Transfer 65, 280 – 288. URL: `http://www.sciencedirect.com/science/article/pii/S0017931013004614`, doi:https://doi.org/10.1016/j.ijheatmasstransfer.2013.06.001.

Noorani, A., Schlatter, P., 2016. Swirl-switching phenomenon in turbulent flow through toroidal pipes. International Journal of Heat and Fluid Flow 61, 108–116. URL: `https://doi.org/10.1016/j.ijheatfluidflow.2016.05.021`, doi:10.1016/j.ijheatfluidflow.2016.05.021.

Passalacqua, A., n.d. Implementation of the Dynamic Smagorinsky Model as Proposed by Lilly (1992) for OpenFOAM. URL: `https://github.com/%0AAlbertoPa/dynamicSmagorinsky`.

Pope, S.B., 2000. Turbulent Flows. Cambridge University Press. doi:10.1017/CBO9780511840531.

Röhrig, R., Jakirlić, S., Tropea, C., 2015. Comparative computational study of turbulent flow in a 90° pipe elbow. International Journal of Heat and Fluid Flow 55, 120–131. doi:10.1016/j.ijheatfluidflow.2015.07.011.

Rütten, F., Meinke, M., Schröder, W., 2001. Large-eddy simulations of 90° pipe bend flows. Journal of Turbulence 2, N3. URL: `https://doi.org/10.1088/1468-5248/2/1/003`, doi:10.1088/1468-5248/2/1/003.

Rütten, F., Schröder, W., Meinke, M., 2005. Large-eddy simulation of low frequency oscillations of the Dean vortices in turbulent pipe bend flows. Physics of Fluids 17. doi:10.1063/1.1852573.

Sakakibara, J., Machida, N., 2012. Measurement of turbulent flow upstream and downstream of a circular pipe bend. Physics of Fluids 24, 041702. URL: `https://doi.org/10.1063/1.4704196`, doi:10.1063/1.4704196.

Salimpour, M., 2009. Heat transfer coefficients of shell and coiled tube heat exchangers. Experimental Thermal and Fluid Science 33, 203–207. URL: `https://doi.org/10.1016/j.expthermflusci.2008.07.015`, doi:10.1016/j.expthermflusci.2008.07.015.

Skillen, A., Revell, A., Craft, T., 2016. Accuracy and efficiency improvements in synthetic eddy methods. International Journal of Heat and Fluid Flow 62, 386 – 394. URL: `http://www.sciencedirect.com/science/article/pii/S0142727X16305604`, doi:https://doi.org/10.1016/j.ijheatfluidflow.2016.09.008.

Sudo, K., Sumida, M., Hibara, H., 1998. Experimental investigation on turbulent flow in a circular-sectioned 90-degree bend. Experiments in Fluids 25, 42–49. doi:10.1007/s003480050206.

Tunstall, R., Laurence, D., Prosser, R., Skillen, A., 2016. Large eddy simulation of a T-Junction with upstream elbow: The role of Dean vortices in thermal fatigue. Applied Thermal Engineering 107, 672–680. URL: `http://dx.doi.org/10.1016/j.applthermaleng.2016.07.011`, doi:10.1016/j.applthermaleng.2016.07.011.

Vashisth, S., Kumar, V., Nigam, K.D.P., 2008. A review on the potential applications of curved geometries in process industry. Industrial & Engineering Chemistry Research 47, 3291–3337. URL: `https://doi.org/10.1021/ie701760h`, doi:10.1021/ie701760h.

Vester, A.K., Örlü, R., Alfredsson, P.H., 2015. POD analysis of the turbulent flow downstream a mild and sharp bend. Experiments in Fluids 56. URL: `https://doi.org/10.1007/s00348-015-1926-6`, doi:10.1007/s00348-015-1926-6.

Vester, A.K., Örlü, R., Alfredsson, P.H., 2016. Turbulent flows in curved pipes: Recent advances in experiments and simulations. Applied Mechanics Reviews 68. URL: `https://doi.org/10.1115/1.4034135`, doi:10.1115/1.4034135.

Wang, Z., Örlü, R., Schlatter, P., Chung, Y.M., 2018. Direct numerical simulation of a turbulent 90° bend pipe flow. International Journal of Heat and Fluid Flow 73, 199–208. URL: `https://doi.org/10.1016/j.ijheatfluidflow.2018.08.003`, doi:10.1016/j.ijheatfluidflow.2018.08.003.

Chapter 9

Paper III: *Implementing Numerical Wall Function for Large Eddy Simulation in OpenFOAM*

This paper is published in the proceedings of the 5^{th} MACE PGR Conference 2018.

Note that the author's accepted manuscript is included rather than the published version, as its larger margins are more suited to the binding requirements of the thesis.

Implementing numerical wall function for large eddy simulation in OpenFOAM

Brendan Ehimen Omozopia Iyamabo
School of Mechanical, Aerospace and Civil Engineering
The University of Manchester
Manchester, UK
brendan.iyamabo@manchester.ac.uk

Imran Afgan
School of Mechanical, Aerospace and Civil Engineering
The University of Manchester
Manchester, UK
imran.afgan@manchester.ac.uk

Abstract— **This paper presents the methodology of a new wall function for large eddy simulation (LES) where two regions are solved simultaneously. The first region solves the LES for the entire domain, but the grid is coarse and under-resolved in the near-wall area. The second region is embedded in the near-wall area of the LES grid, solves transient Reynolds Averaged Navier Stokes (RANS) transport equations and supplies the LES with a corrected wall shear stress. In return, the RANS grid obtains partial time-averaged quantities from the LES domain. This enables the use of more advanced turbulence models in the RANS region. This paper presents results of the new method for a plane channel flow and the more challenging 90º pipe bend case.**

I. INTRODUCTION

Large eddy simulation (LES) has become a popular tool for analysing turbulent flow in academia. The grid requirements for LES increases modestly with Reynolds number (Re) as $N \approx O(Re^{0.4})$, which suggests that LES could be used more in industry. However, this requirement is only valid for regions that are far from the wall. The near-wall region of a turbulent flow requires a much finer numerical discretisation to resolve the flow. Reference [1] estimates that the grid size required to resolve the viscous sublayer increases as $Re^{1.8}$, thereby limiting the usage of LES in engineering applications. Hence, high-Re turbulent flows for LES is only realistic in combination with near-wall corrections that allows the use of a coarser near-wall grid.

Log-law-based wall functions were developed initially to compute the instantaneous skin friction or velocity of the first cell in a coarse near-wall LES grid. However, these approaches remained applicable to flows in near-equilibrium conditions like the channel flow. Later, a wall-layer model for LES was developed by [2] where a separate domain was embedded in the first cell of the LES grid. The embedded domain solved unsteady Reynolds averaged Navier-Stokes transport equations (RANS) and supplied the LES with wall shear stress information to correct the first cell at the wall of the LES grid. The top boundary of the RANS subdomain received information from the LES. This approach demonstrated some clear advantages over the standard wall function methods, but there are still some limitations. First, the RANS turbulence models used in most cases were limited to an algebraic mixing length model to overcome the difficulties of prescribing boundary conditions at the RANS domain interface when using RANS closure methods. This reduced the usage of wall-layered models in complex flows. Second, the instantaneous filtered velocity of the LES was matched with the Reynolds time-averaged velocity at the interface of the RANS domain. This is obviously an inconsistent approach which has led to the development of several empirical corrections such as equating the subgrid scale (SGS) viscosity of the LES to the eddy viscosity of the RANS at the interface, which is unphysical, or numerically solving only the diffusion term in RANS domain. This work looks to improve the consistency of coupling the RANS and LES fields at the interface of the RANS domain. Furthermore, the work develops approaches which permit the use of more advanced turbulence models in the RANS domain to enable the usage of LES for more complex geometries.

II. METHODOLOGY

This numerical wall function for LES (LES-NWF) is implemented in an opensource code OpenFOAM and solves two regions concurrently as shown in Figure 1. The LES grid is intended to be well refined except in the near-wall area where the grid does not resolve the dynamic motions. The RANS grid overlaps the coarse inner region of the LES domain, and the RANS grid is biased towards the wall. The RANS grid computes the wall shear stress which corrects the near-wall region of the LES domain. On the other hand, the interface of the RANS grid receives information from the LES to complete the boundary conditions of the RANS grid. The top boundary of the RANS domain is designed to bypass at least the first three cells of the LES grid to ensure that the information received from the LES at the interface is well resolved.

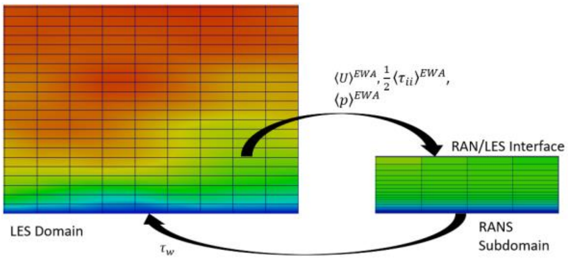

Figure 1: Schematic showing the setup of the new wall function for LES

The momentum equation for an incompressible flow for the LES domain can be written as follows:

$$\frac{\partial \overline{U_i}}{\partial t} + \frac{\partial \overline{U_i U_j}}{\partial x_j} = -\frac{\partial \bar{P}}{\partial x_i} + 2\nu \frac{\partial}{\partial x_j}\overline{S_{ij}} - \frac{\partial \langle \tau_{ij}^{r}\rangle}{\partial x_j} - \frac{\partial}{\partial x_j}(\tau_w * A_w), \qquad (1)$$

where τ_w is the wall shear stress calculated from the RANS domain and mapped to the LES grid as a source term, and A_w is the wall cell area.

The partial time average of the filtered fields of the LES domain is computed. The partial time averaged LES fields is coupled with the Reynolds time-averaged fields to improve consistency between the two regions. The exponentially weighted time-average (EWA) is used to compute the partial time-average of a quantity $\langle\varphi\rangle^{EWA}$, which is defined as follows:

$$\langle \varphi \rangle^{EWA} = \int_{-\infty}^{t} \left(\frac{1}{T} \varphi(t') e^{-(t-t')/T} dt' \right), \quad (2)$$

where T is the time-scale of the exponentially weighted average. The use of the exponentially weighted average prioritises recent events in the LES [3]. The EWA timescale is made to be long enough to ensure that the EWA fields will be smooth. Hence, the exponentially weighted average of the filtered velocity of the LES is assumed to be equivalent to the Reynolds-averaged velocity of the RANS domain ($\langle \overline{U_i} \rangle^{EWA} \approx \langle U_i \rangle$). The EWA of the filtered velocity field is then interpolated to the interface of the RANS domain. Also, the LES stress tensor can be determined by defining the resolved fluctuations about the EWA of the filtered velocity field as $u_i'' = \overline{U_i} - \langle \overline{U_i} \rangle^{EWA}$. The LES stress tensor is defined as:

$$\tau_{ij} = u_i'' u_j'' + \tau_{ij}^{r}, \quad (3)$$

where τ_{ij}^{r} is the modelled subgrid scale (SGS) stress tensor and $u_i'' u_j''$ is the resolved stress about the EWA of the filtered velocity field.

To make use of closure methods in the RANS domain, the boundary conditions at the interface for variables such as the turbulent kinetic energy and the rate of dissipation have to be defined. The interface boundary condition for the turbulence kinetic energy k^R is obtained by taking the trace of the EWA of the LES stress tensor which is defined as $k^R = 0.5\langle \tau_{ii} \rangle^{EWA}$. Then again, the interface boundary condition of the dissipation rate ε is found by calculating the EWA of the sum of the resolved dissipation rate linked with the large eddies of the LES and the modelled dissipation rate associated with the subgrid scales which is defined as:

$$\langle \varepsilon \rangle = 2\nu \overline{S_{ij} S_{ij}} - \tau_{ij}^{SGS} \overline{S_{ij}}. \quad (4)$$

This work makes use of the elliptic blending k-ε model of [4] in the RANS region, which solves the transport equations of two additional quantities: the elliptic blending parameter and the ratio of the normal Reynolds stress to the turbulent kinetic energy. The algebraic correlations used to define these extra variables at the interface can be found in [5].

III. RESULTS AND DISCUSSION

A. Results for a Re_τ = 1000 Channel Flow

We assess the performance of the new method for a fully developed $Re_\tau = 1000$ flow through a plane channel of half height δ and validate the results with DNS data of [6]. The sizes of the domain for the LES and RANS regions are $2\pi\delta \times 2\delta \times \pi\delta$ and $2\pi\delta \times 0.15\delta \times \pi\delta$ respectively, with periodic conditions on the inflow and sides. The LES grid has $50 \times 60 \times 30$ points with constant spacing in all directions, and the near-wall region being under-resolved, while the RANS grid has $50 \times 30 \times 30$ points that is biased towards the wall. The subgrid scale turbulence used in the LES domain is the dynamic one-equation model of [7], while the RANS domain uses the elliptic blending k-ε model. Also, a separate simulation is run on the same coarse LES grid without using a wall function. Figure 2 shows the plot of the mean streamwise velocity computed in the LES domain in the channel. The mean streamwise velocity of the LES domain is well predicted when the first cell of the grid is corrected by the wall shear stress supplied by the RANS subdomain. The friction Reynolds number predicted by the LES domain with wall function is 1039, which differs from the nominal value by under 4%.

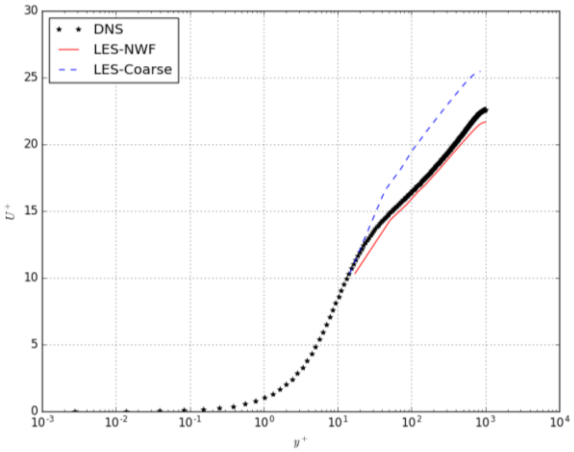

Figure 2: Plot of mean streamwise velocity in a plane channel of *Re*$_\tau$=1000

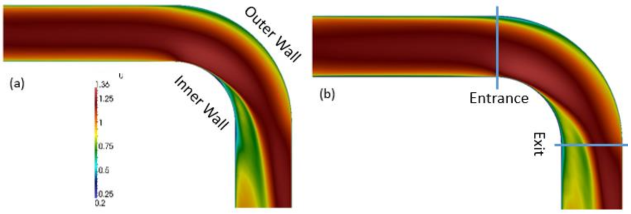

Figure 3: Contour plot of the mean streamwise velocity of a plane section - Left: Well resolved LES, Right: Numerical wall function with LES

B. Results for Flow through a 90^o Pipe Bend

Flow through a 90^o pipe bend is investigated (Figure 3). The presence of centrifugal forces and pressure gradients in different directions, which lead to the development of counter-rotating vortices in the bend, makes the pipe bend geometry a challenging case to simulate. The bulk Reynolds number of the case is 34,000. The ratio of the radius of curvature of the bend to the pipe radius is 1.58, signifying a sharp bend. The LES grid using the numerical wall function has 540,000 points with the viscous sublayer under-resolved. As with the channel flow case, the LES domain uses the dynamic one-equation SGS model, while the RANS domain uses the elliptic blending *k*-*ε* model. Results of the study are compared with data from a 19 million-cell well-resolved LES simulation, which have not been published. An added study is done on a 1.4 million-node grid using improved delayed detached eddy simulation (IDDES) as detached eddy simulation has become the most popular hybrid RANS/LES method used in industry. Figure 4 shows the profiles of streamwise and radial velocities plotted along a line between the inner and outer walls of the bend. At the bend entrance, the LES-NWF and IDDES accurately predict the acceleration of the flow around the inner wall due to the presence of strong axial favourable pressure gradient in that region. However, as secondary flow becomes more dominant, only the LES-NWF can predict the streamwise velocity at the bend exit in the inner wall vicinity. The IDDES predicts a high radial velocity in the inner-wall region which causes the high-momentum part of the fluid to be pushed further towards the outer wall, while the LES-NWF accurately computes the secondary velocity. Hence, the LES-NWF can maintain the trend of the streamwise velocity. Figure 5 shows the contour plots of the mean streamwise velocity at the bend exit section-plane. The NWF-LES contour plot compares favourably with the reference plot despite using a minute fraction of points in the computational grid.

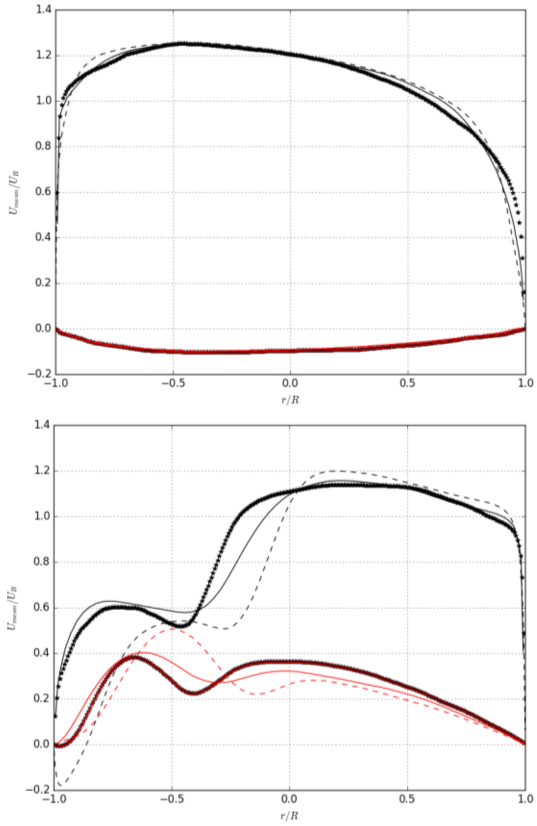

Figure 4: Plots of the mean streamwise and radial velocities along a line between the inner and outer walls of the pipe – Top plot: Plot line at bend entrance, Bottom plot: Plot line at bend exit – Black lines and markers: Streamwise velocity, Red lines and markers: Radial velocity – Solid line (—): LES-NWF, Dashed line (- -): IDDES, Star marker (*): Well-resolved LES (Reference Data) – x-axis: Outer wall (1.0), Inner wall (-1.0).

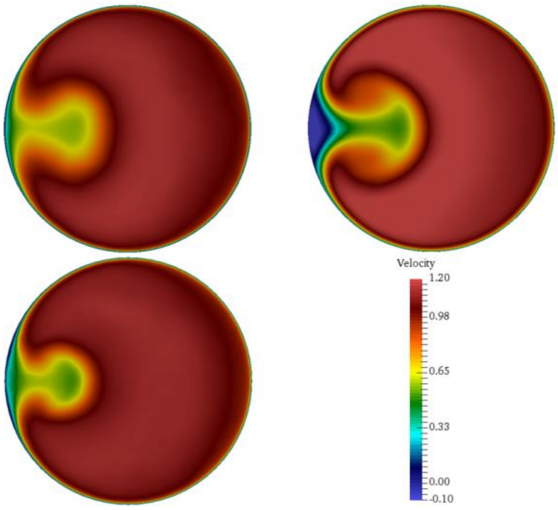

Figure 5: Contour plots of the mean streamwise velocity of a plane section at the bend exit - Top left: Numerical wall function with LES (LES-NWF), Top right: Improved delayed detached eddy simulation (IDDES), Bottom left: Well resolved LES (Reference data)

IV. CONCLUSIONS

A numerical wall function for LES was implemented in OpenFOAM. The LES domain received wall shear stress information from a separate near-wall RANS domain to correct the first cell of the coarse near-wall LES grid. A more consistent coupling of the LES and RANS regions was done by computing the partial time average of LES quantities. This coupling enabled the use of more advanced turbulence models compared to the algebraic mixing length approach that is commonly used in literature. The method was tested with success for plane channel flow. It also performed admirably for the demanding 90^o pipe bend.

ACKNOWLEDGEMENT

The authors thank Prof Dominique Laurence and Alistair Revell for their invaluable contributions to this paper. The authors are profoundly grateful for funding provided by the School of Mechanical, Aerospace and Civil Engineering of The University of Manchester.

REFERENCES

[1] D. R. Chapman, “Computational aerodynamics development and outlook,” *AIAA J.*, vol. 17, no. 12, pp. 1293–1313, 1979.

[2] E. Balaras, C. Benocci, and U. Piomelli, “Two-layer approximate boundary conditions for large-eddy simulations,” *AIAA J.*, vol. 34, pp. 1111–1119, 1996.

[3] R. Tunstall, D. Laurence, R. Prosser, and A. Skillen, “Towards a generalised dual-mesh hybrid LES/RANS framework with improved consistency,” *Comput. Fluids*, vol. 157, pp. 73–83, 2017.

[4] F. Billard and D. Laurence, “A robust $k - \varepsilon - v^2/k$ elliptic blending turbulence model applied to near-wall, separated and buoyant flows,” *Int. J. Heat Fluid Flow*, vol. 33, pp. 45–58, 2012.

[5] F. Billard, D. Laurence, and K. Osman, “Adaptive wall functions for an elliptic blending eddy viscosity model applicable to any mesh topology,” *Flow, Turbul. Combust.*, vol. 94, no. 4, pp. 817–842, 2015.

[6] M. Lee and R. D. Moser, “Direct numerical simulation of turbulent channel flow up to $Re_\tau \approx 5200$,” *J. Fluid Mech.*, vol. 774, no. 4, pp. 395–415, 2015.

[7] W.-W. Kim and S. Menon, “A new dynamic one-equation subgrid-scale model for large eddy simulations,” in *33rd Aerospace Sciences Meeting and Exhibit*, 1995.